Research and Technology

(NASA-TM-88753) RESEARCH AND TECHNOLOGY, FISCAL YEAR 1985 Annual Report (NASA) 150 p HC A07/MF A01 CSCL 05A
N86-25320
Unclas
G3/99 42916

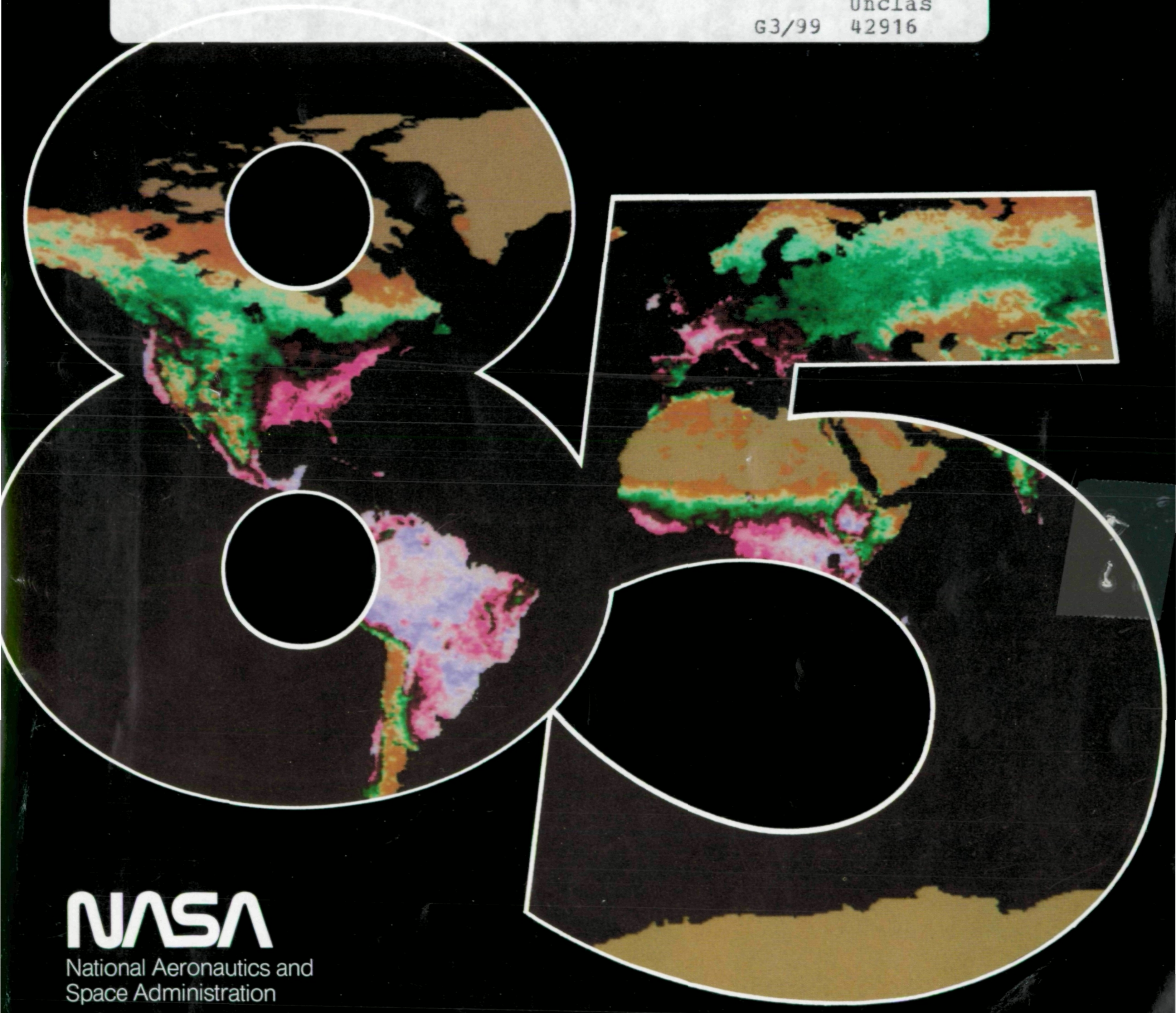

National Aeronautics and
Space Administration

Goddard Space Flight Center
Greenbelt, Maryland 20771

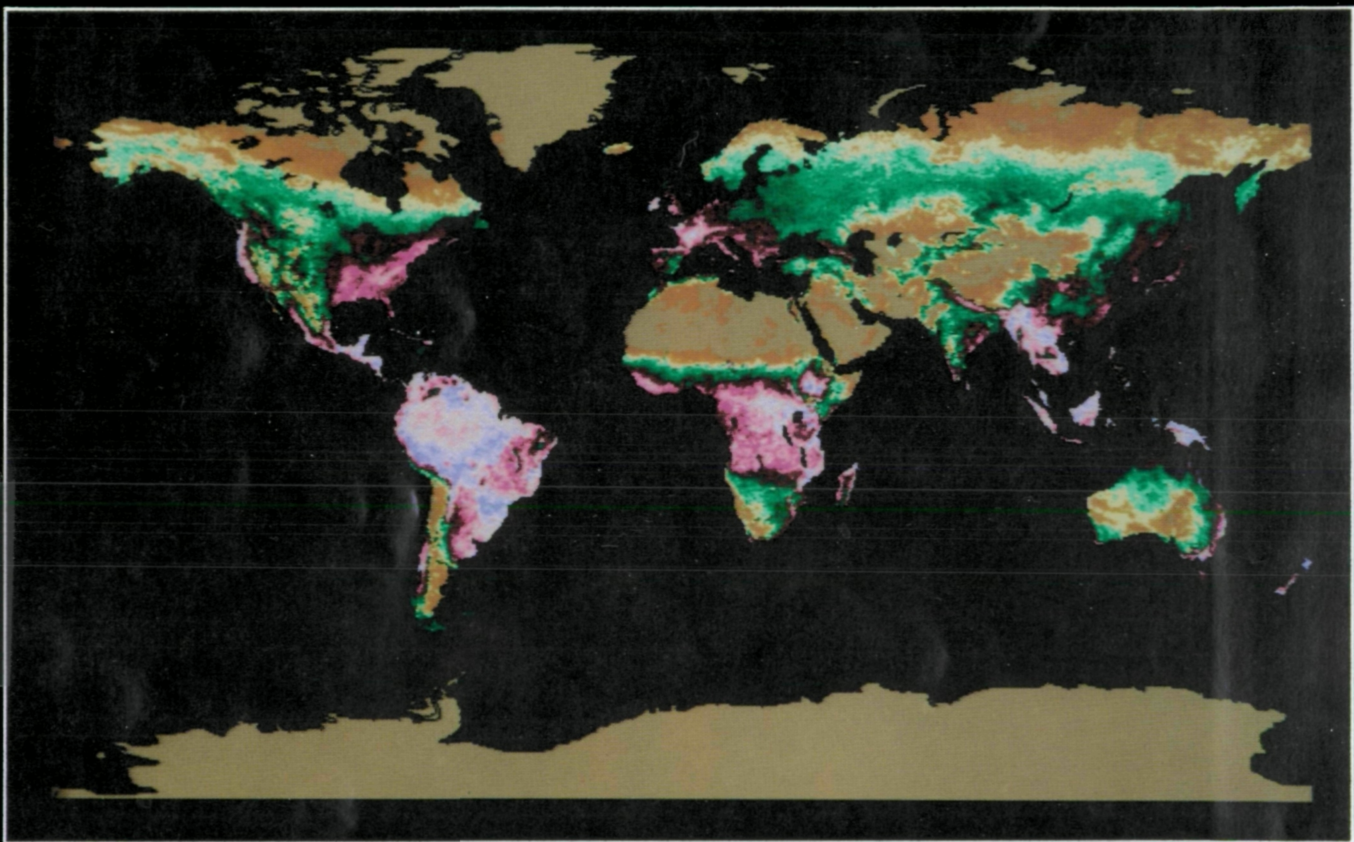

Cover photo: Global patterns can be observed by satellite. The cover shows the integral of the photosynthetically active radiation absorbed by the terrestrial vegetation for a 12-month period, 1982. It represents net primary production (or an index highly correlated with net primary production). Areas of desert and tundra which have integrated values and hence productivity values close to zero are represented by the **yellow-tan** *colors. The* **orange-tan** *colors represent areas with low amounts of primary production such as semi-arid grasslands and steppes. The* **white-cream** *and* **green** *colors represent areas of moderate productivity such as savanna, grassland and some forested areas. The* **red** *colors correspond to temperate forests as well as some equatorial forests and moist savanna areas and are areas of moderate to high primary productivity. The* **purple** *colors represent areas of high primary production. From the patterns in the cover photo one can clearly see the general pattern of the Earth's vegetation and the location of the forests. Through the use of remote sensing techniques, a potential for global environmental monitoring of the productivity of vegetation now exists. See article on p. 1. (Cover photo courtesy of C. Tucker, National Aeronautics and Space Administration/Goddard Space Flight Center.)*

1061

Research and Technology

Fiscal Year 1985

ANNUAL REPORT

of the

Goddard Space Flight Center

Foreword

Goddard Space Flight Center has had a rich year in research results. We are beginning to understand the Earth's continental changes of vegetation and their link to atmospheric carbon dioxide variation. The shift of continental plates has been measured to within a few centimeters, and a conceptual model of what drives the El Niño has been developed. The importance of some of the trace constituents of our atmosphere in influencing the incoming radiation has begun to get recognition. Winds, clouds, aerosols, and solar variations are finding a place in the large climate models of the Earth.

In planetology the IRIS data have been used to develop an inventory of the Jovian troposphere and to observe clouds of interstellar molecules. We are examining the chemistries of Io and Titan and have discovered the first organic ring compound in space. A great rotating gas cloud 300,000 light years across has been detected, and there is now evidence that hard X-rays in solar flares are produced by electron beams . . . . There is even a novel explanation of the disappearance of the dinosaurs!

Substantial advances were made this year in spacecraft technology, including the demonstration of new concepts for heat transfer systems and devices to greatly extend the orbital lifetime of cryogenic systems. In data systems excellent progress was made in processing tools and analysis techniques, including parallel processing, programming in ADA, coordinated interdisciplinary data presentation, and methods of analyzing long-term global phenomena.

September 11, 1985 was an important day in our history, for on that day the International Cometary Explorer (ICE) spacecraft, renamed from an earlier existence as the International Sun Earth Explorer (ISEE), completed its complex path from the Sun-Earth libration point L_1, having swung past the Earth and the Moon a dozen times on its way to intercept the tail of the comet Giacobini-Zinner. The intercept was a complete success. The spacecraft survived undamaged and returned outstanding data.

The point of contact within the Center for this report is Dr. George F. Pieper, Code 100 (344-7301), who provided overall editorial supervision. He was assisted by an editorial committee consisting of Dr. Stephen J. Paddack, Code 402; Ms. Karen L. Moe, Code 522; Dr. Gerald A. Soffen, Code 600; and Mr. Robert S. Kraemer, Code 700. Detailed editorial support and production of the report were supervised by Mr. Jerry R. Hodge, Code 253; Mr. Mark H. Allen, and Ms. Elaine Armstrong, Engineering and Economics Research, Inc., Beltsville, Maryland.

Noel W. Hinners

Noel W. Hinners
Director

Contents

Space and Earth Sciences

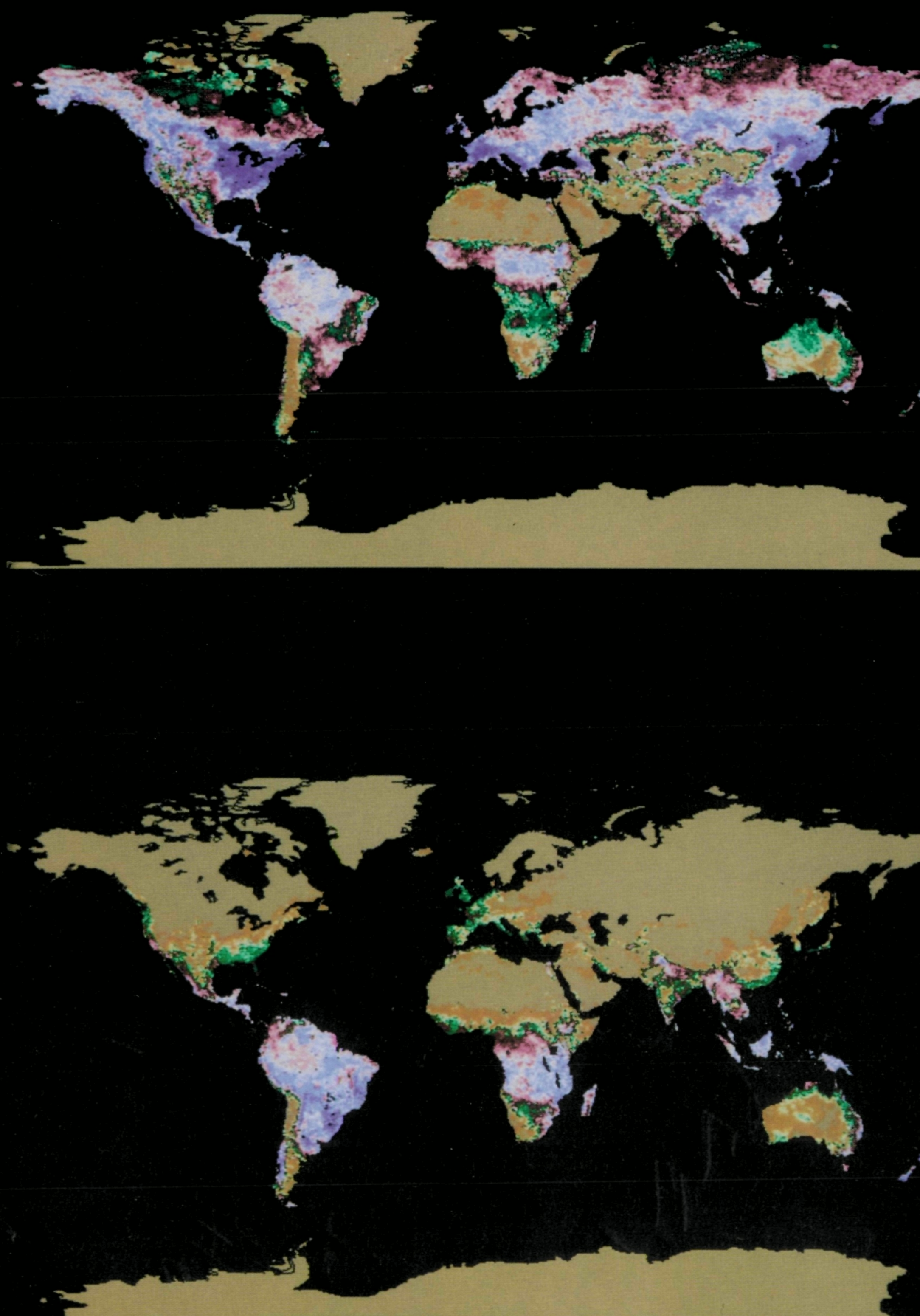

GSFC's program in Earth Science in recent years has emphasized the basic science involved in the study of the Earth's atmosphere, oceans, and land masses, and the interactions among them. Satellite data have been particularly useful in studies of the Earth's atmosphere and climate, the dynamics of its crust, and in the monitoring of its land and water resources.

In the Space Sciences, activities are directed toward the investigation of the Earth's space environment, the Sun, the solar system, the interplanetary medium, galactic and extragalactic phenomena, and the interrelationships among them.

GSFC scientists continue to pursue a wide variety of research studies, instrument developments, measurement projects, and data analysis efforts to increase our understanding of the universe.

TERRESTRIAL PHYSICS

THE RELATIONSHIP OF A GLOBAL SPECTRAL VEGETATION INDEX AND ATMOSPHERIC CO_2 CONCENTRATIONS

The biosphere absorbs CO_2 from the atmosphere via photosynthesis and incorporates the absorbed carbon into simple carbohydrates giving off O_2 in the process. CO_2 absorption by the terrestrial biosphere occurs in the green leaves of plants where incident photosynthetically active radiation (0.4 to 0.7 μm) is absorbed by the chlorophylls, carotenoids, and other accessory photosynthetic pigments. The energy of the absorbed photons is used to drive the reaction of photosynthesis and to produce carbohydrates for primary production. A direct relationship exists between the intercepted photosynthetically active radiation, CO_2 uptake, and gross primary production. Because incident radiation in the 0.4 to 0.7 μm region is strongly absorbed by green leaves (i.e., scattering and photosynthetic pigment absorption), and radiation in the 0.7 to 1.1 μm region is strongly backscattered or reflected, combinations of reflected radiance from the red and near-infrared spectral regions are used to estimate nondestructively the green leaf biomass of plant canopies. The reflected radiance combinations are highly correlated to the intercepted fraction of photosynthetically active radiation (IPAR), the photosynthetic capacity, and the resistance to water vapor transfer of plant canopies.

The ability to monitor global changes in vegetation IPAR through time provides the ability to estimate CO_2 drawdown and primary production, all as a consequence of the relationships of leaf structure, leaf density, light relations in plant canopies, and the relationship between intercepted photosynthetically active radiation and photosynthesis.

Monthly atmospheric CO_2 concentrations for 1982-1984 were obtained for Point Barrow, Alaska (147°W, 71°N) and Mauna Loa, Hawaii (156°W, 20°N); monthly atmospheric CO_2 concentration data were obtained from 1982 through September 1984 for the South Pole (90°S). These stations are operated by the Global Monitoring for

◀ *Facing page: Satellite-recorded global patterns are illustrated by monthly composite aggregated normalized difference images for August 1982 (top) and February 1983 (bottom). Note the dramatic difference between these two months, especially in the northern hemisphere.*

Climatic Change (GMCC) program of NOAA, and the CO_2 flask samples were analyzed at the Scripps Institution of Oceanography (SIO). The accompanying figure shows CO_2 concentrations for twenty monitoring stations operated by the NOAA/GMCC obtained for the time period 1982-1983.

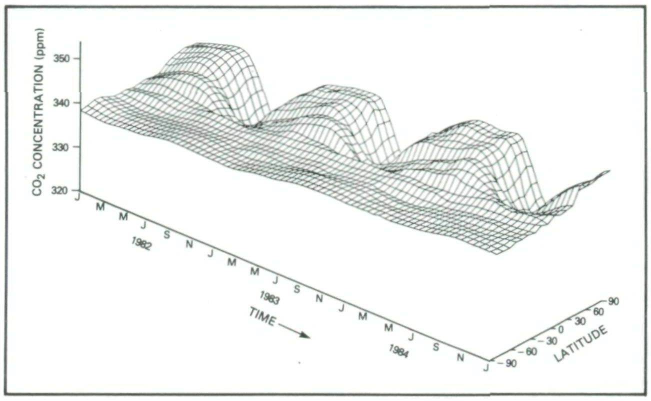

Atmospheric CO_2 concentration plotted against time and latitude. Note the highly seasonal response of the northern hemisphere, the generally constant response in equatorial areas, and the influence of the low portion of land area south of 30°S.

Global weekly vegetation composite satellite data were obtained from April 12, 1982 through January 31, 1985. The monthly terrestrial normalized difference data were used to compute zonal averages values for 5° latitude zones. The zonal averages were then multiplied by the land area within each zone to weight the averages by the land area involved. The second illustration displays the latitudinal and temporal variation of the aggregated vegetation index from April 1982 to January 1985. Consistent with considerations of the growing season, the maximum zonally aggregated vegetation index occurs in summer at middle to high latitudes in the northern hemisphere. This is a consequence both of the large land surface and the highly seasonal behavior of vegetation at these latitudes. The southern hemisphere south of 30°S has a low aggregated vegetation index because the southern hemisphere vegetation is not as seasonal and the land area is not appreciable when compared to other latitude zones north of 30°S. The aggregated vegetation index in the equatorial areas is high throughout the year, and a desert belt is apparent as a depressed aggregated vegetation index from ~20°N to ~30°N. The second figure shows differences between the aggregated vegetation index from 1982 to 1984. The 1982 global peak occurred in August, while the 1983 and 1984 global peaks occurred in July. These data are also being used to

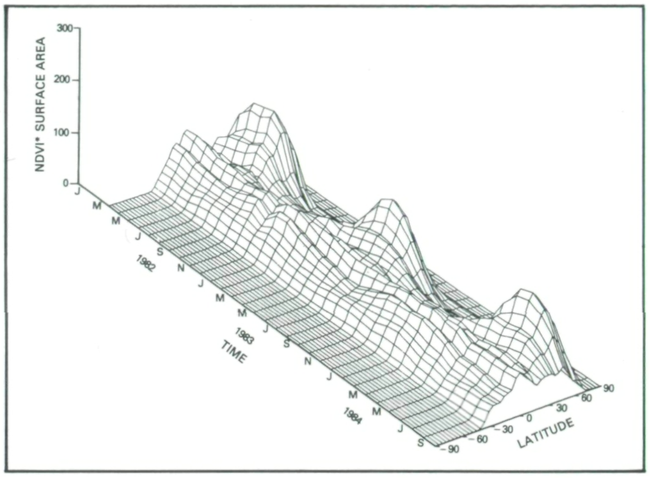

Aggregated vegetation index data plotted against time and latitude zone. Note the opposite effects in the northern latitudes, the generally constant response in equatorial areas, the influence of deserts in the ~20°N to 30°N latitude zone, and the influence of the low proportion of land area south of 30°S.

develop a quantitative relationship between satellite-derived vegetation indices and total terrestrial primary production.

Contact: Compton Tucker and Inez Fung
Codes 620, 640

Sponsor: Office of Space Science and Applications

AIRBORNE LASER DATA FOR BIOMASS ASSESSMENT

Global assessments of biomass using digital data from space platforms must, at some point, tie into a reliable estimate of current ground conditions. The gross spatial resolution of globally synoptic sensors (1 to 4 km) precludes the use of point estimators to assess ground conditions reliably. An aircraft laser system offers the unique capability of a very intensive sampling rate (as often as one pulse every 0.25 meter) and rapid data collection along ground transects covering tens or hundreds of kilometers; therefore, precise transect data that might be used to characterize and quantify vegetation quickly may be acquired over areas spanning many pixels of satellite imagery.

Researchers have shown that two pieces of information must be combined in order to derive forest biomass

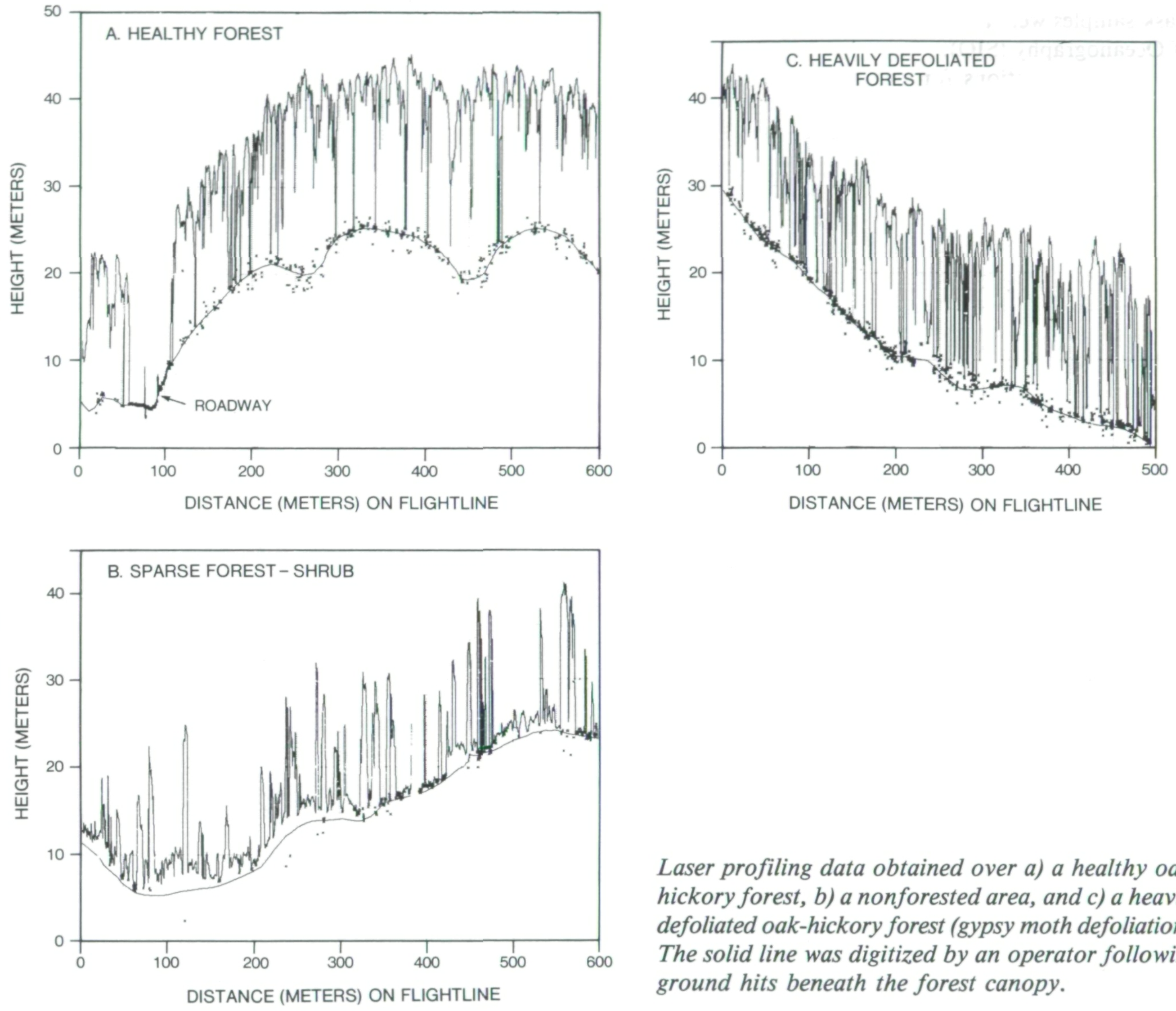

Laser profiling data obtained over a) a healthy oak-hickory forest, b) a nonforested area, and c) a heavily defoliated oak-hickory forest (gypsy moth defoliation). The solid line was digitized by an operator following ground hits beneath the forest canopy.

remotely using laser data: 1) canopy height or canopy profile (that cross-sectional area described by the top of the canopy and the ground, integrated over distance); and 2) the plant species associated with the height measure. An airborne laser system may be used to acquire data that address both aspects of the biomass assessment problem.

The airborne laser system collects tree height data and, in addition, illuminates the target with enough light to induce fluorescence in vegetation. The laser acts as the light equivalent of radar, precisely measuring distances between the aircraft and the target. After the initial return, 36 sequential measurements are taken on the return strength of that single laser pulse. The measurements are taken at 5-nanosecond intervals, which is the time it takes light to travel 2/3 meter through the canopy. The 36 measurements constitute a waveform, and a strong response in this waveform connotes a return from the ground beneath the canopy. Hence if ground is found, then tree heights may be estimated directly from the laser pulse. Canopy profiles, obtained over different forest types, are illustrated.

Fluorescence measurements may be obtained; 90 percent of the initial light return is directed into a fluorosensor which measures the flourescent response of the target between 400 to 800 nm. Research in the laboratory using a 337-nm laser has shown that flourescent peaks at 440, 525, 685, and 740 nm may be used to differentiate species or species groups. Thus a single pulse may yield data on

tree height and species groups, and pulses may be acquired up to 400 times per second.

Previous research using bathmetry (tree height) data has shown that laser and photogrammetric estimates of tree heights agreed within 0.60 meter, on the average. Additional work has shown that strong, logarithmic regressions (R^2 = 0.60-0.90) between canopy profile and timber volume may be established if tree species are known. Laser data have been acquired over a study site near Bainbridge, Georgia, to determine if, with limited ground sampling, laser data may be used to accurately predict timber volume. These data will be assessed to determine the utility of airborne laser fluorescence and passive spectral data for differentiating hardwoods from conifers, and distinguishing conifer species.

Contact: Ross Nelson
Code 620

Sponsor: Office of Space Science and Applications

REMOTE SENSING OF SUSPECTED ACID DEPOSITION DAMAGE IN HIGH ELEVATION FORESTS LOCATED IN VERMONT

Materials emitted into the atmosphere as a result of anthropogenic activities, principally the combustion of fossil fuels, are transformed into acidic substances, such as sulfur and nitrogen oxides, which are then returned in a wet or dry form to the Earth's surface. The deposition of acidic materials from the atmosphere is referred to as "acid rain" or "acid deposition," and the impact of the phenomenon on terrestrial and aquatic systems is a topic of international concern. The effects of acid rain are not fully understood, but damage has already been observed in lakes, forests, soils, crops, and building materials. It is hypothesized, for example, that trees in high-elevation spruce/fir forests may suffer from water stress due to a reduced capability to uptake and retain water because of acid rain-induced damage to their roots and leaves.

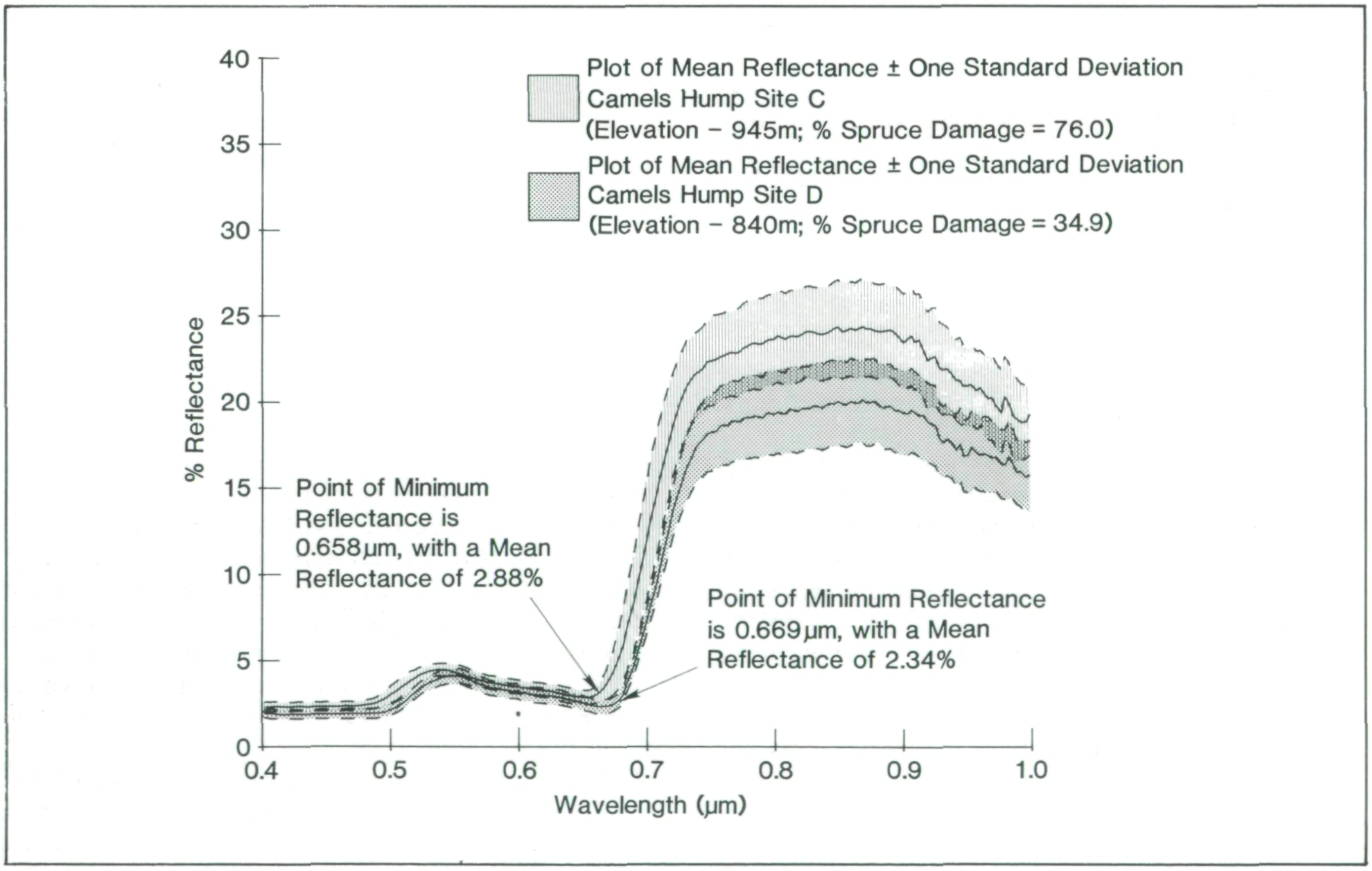

Comparison of spectral reflectance characteristics for two red spruce stands depicting higher (Site C) and lower (Site D) stress conditions. [Note: SI or stress index values are related to the average percentage of dead branches within the live crown of the spruce component of a forest stand. Therefore, the higher the value, the greater the stress.]

Members of Goddard's Earth Resources Branch are currently involved in a cooperative effort with the University of Vermont, the Jet Propulsion Laboratory (JPL), and the University of Maryland to determine the feasibility of using quantitative remote sensing techniques to detect forests under stress due to acid deposition. This research activity was initiated in 1984, and the geographic area of interest centers around Camels Hump Mountain and the Green Mountain National Forest in west-central Vermont.

Based on detailed ground observations, twelve red spruce stands were selected as study areas for this project. These stands represented a continuum of vigor classes, ranging from healthy to very stressed. In mid-August 1984, spectral data were collected over four sites on Camels Hump Mountain under ideal solar illumination conditions using a spectrometer and radiometer mounted on a helicopter that hovered some 300 meters above the forest canopy. The 300-m altitude, coupled with 1° field of view (FOV) lens, yielded a ground sample area approximately 5.5 m in diameter. Botanists from JPL and the University of Vermont acquired *in situ* spectral data of branches with needles attached, along with plant water potential measurements (i.e., a measure of plant water stress) using Scholander pressure bombs.

Illustrated is a representative plot of mean spectral reflectance ± one standard deviation, as acquired over a high damage site and a moderate damage site from the helicopter-mounted spectrometer. A significant shift in the point of minimum reflectance (maximum absorption) in the chlorophyll absorption region typically centered at approximately 0.670 μm is noticeable when comparing the two curves. The point of minimum reflectance in the spectra from the high damage site occurred at 0.658 μm, whereas the minimum for the moderate damage site occurred at 0.669 μm, a difference of 11 nanometers. This shift in reflectance minima toward shorter wavelengths for stressed vegetation, known as the "blue shift," has been documented in geobotanical studies of coniferous forests growing under stress due to high concentrations of heavy metals in the soil. One of the key components of acid deposition is heavy metals, and University of Vermont studies have shown that over a 13-year period from 1966 to 1979, concentrations of copper, lead, and zinc found in the soil on Camels Hump increased by 23 percent, 79 percent, and 27 percent, respectively.

The *in situ* spectrometer data acquired by JPL scientists also indicate the presence of a 9-nanometer "blue shift" in the spectra from high damage sites versus low-to-moderate damage sites. Intersite comparisons of the Scholander pressure bomb data and shortwave IR reflectance data (as recorded by radiometers) indicate that high damage sites exhibit greater water stress and are more reflective (i.e., an indication of drier canopies) than low-to-moderate damage sites. At this point in the investigation, it is very encouraging that significant shifts in vegetative reflectance properties have been identified both from the air and on the ground, and that the hypothesis of plant water stress seems to be valid.

Contact: Darrel Williams
Code 620

Sponsor: Office of Space Science and Applications

LONG-TERM STREAMFLOW OBSERVATIONS IN RELATION TO BASIN DEVELOPMENT

Streamflow is a seemingly unchanging phenomenon from year to year, and aside from the inherent differences in seasonal flows, variation is seldom noticed. Runoff trends due to climatic and man-made changes in the surface character of a basin are generally subtle, and often masked by the cyclic nature of precipitation. Simple models that accept more limited past climatic data are best suited to analyze historical runoff data. The Thornthwaite Water Balance model was selected based on these criteria. The objectives established for a study addressing the subjects noted above were twofold: 1) detect suspected trends due to changing land use in historical streamflow records, and 2) determine the suitability of the Thornthwaite model for subsequent use in modeling basin runoff.

Control basins have been a popular tool for quantifying trends in streamflow through time. In the absence of a control basin, a runoff model may serve as an effective substitute. The Thornthwaite model computes runoff based *solely* on climatic input, without regard to changes in land cover. The changes in the ratio between observed and calculated streamflow over time can be analyzed, and any apparent change in that relationship may then be attributed to changes in the physical nature of the basin.

The Chester Creek basin, located in southeastern Pennsylvania, is typical of rapidly developing areas within the Northeast. It is an excellent catchment for analysis due to its continuous 51-year streamflow history and its lack of diversions and significant impoundments. Historical land use classification was accomplished by acquiring aerial photography for years 1937, 1952, 1958, 1964, and

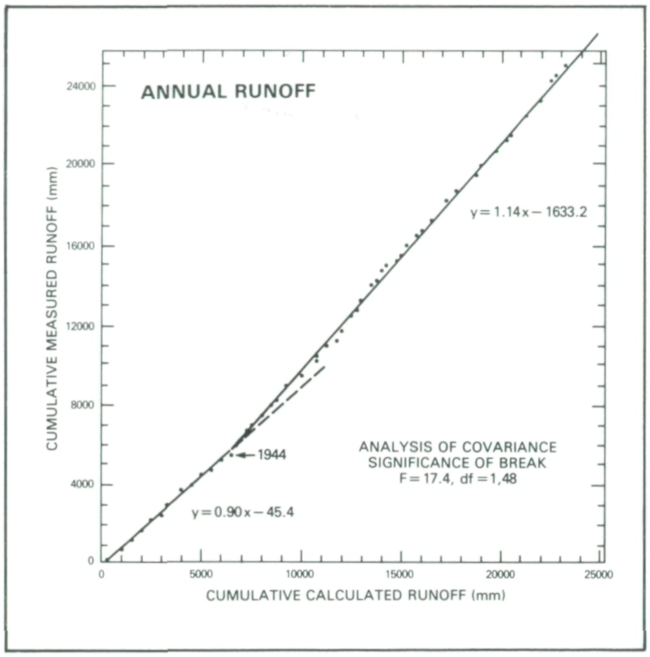

Cumulative calculated versus cumulative measured annual runoff with the break in the initial relationship indicated.

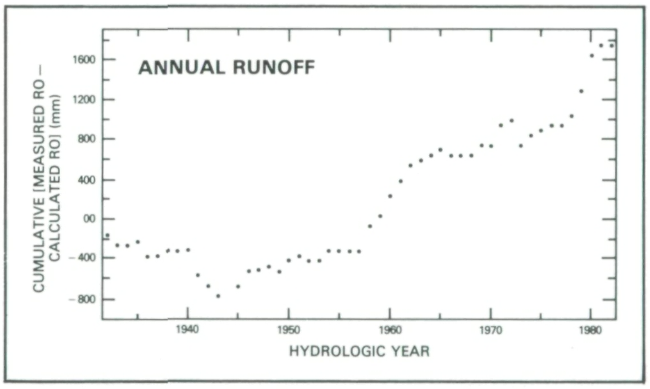

The annual runoff residual-mass curve depicting the difference between cumulative measured and cumulative calculated annual runoff versus time.

1975, in addition to a 1982 Thematic Mapper scene. The physical nature of the basin was classified into five land uses: urban, residential, forest, row crop, and open fields.

To demonstrate the historical trend in the observed streamflow data, a double mass analysis was performed, in which the cumulative annual runoff as estimated by the model was plotted against the observed value. The residual mass curve is the result of cumulating the residuals of the observed runoff values minus the calculated values, and plotting them against the year of occurrence. As long as the relationship between the two values remains constant, the points will plot as a straight line. A break in either plot indicates a change in the proportionality between them, and subsequently a deviant trend in the observed runoff. Growing season and dormant season runoff were analyzed in the same manner.

Stepwise multiple regression analyses were performed on the observed runoff values using their respective seasonal climatic values and the land use parameters previously quantified. Using the derived equations as the model, seasonal runoff was calculated for each year. To account for climatic variability, precipitation was held constant by inserting the 51-year mean values for each year, while the actual annual values for the land use variables were used. The resultant dynamic range displayed for each runoff parameter during the period of record is indicative of the net change in streamflow, which can be attributed to land cover.

Annual, dormant, and growing season runoff were subsequently found to exhibit increases of 51, 46, and 57 percent, respectively, during the period of observation. The evidence suggests that these increases are the direct result of changes in the surface character of the basin. It has previously been shown that land cover derived by remotely sensed methods is more cost effective than conventional techniques while achieving comparable levels of accuracy in hydrologic models (Rango et al, 1983). This study further corroborates the results of that research and, furthermore, shows that through the use of the procedures described (including the use of the Thornthwaite Runoff Model), the specific effects of land use can be isolated and explained.

Contact: Manfred Owe
Code 620

Sponsor: Office of Space Science and Applications

ESTIMATING SOIL HYDRAULIC PROPERTIES WITH PASSIVE MICROWAVE DATA

Hydraulic properties of soil are of primary importance in determining the rate of water and energy flow in the soil, and information about these properties is essential to most water balance, plant growth, and watershed runoff models. Although point measurements of soil properties such as saturated hydraulic conductivity and matric potential (a measure of the strength with which water is

held by the soil matrix) have been taken in the field, their number is limited due to cost and manpower constraints, and their extrapolation to large areas is questionable due to spatial heterogeneity. Remotely sensed data, when used to calibrate physically based hydrologic models, may provide useful estimates for these properties over large areas. Values for soil hydraulic parameters have been estimated by using remotely sensed surface temperature and L-band passive microwave brightness temperature with the models.

Moisture and temperature profiles in the soil are modeled by a computer program which solves coupled diffusion equations for heat and moisture flow in soils. The moisture flux is controlled primarily by the soil matric potential (ψ) and hydraulic conductivity (K) which are parameterized as functions of soil moisture (θ) as follows:

$$K(\theta) = K_s\ (\theta/\theta_s)^{2b+3} \qquad \psi(\theta) = \psi_s\ (\theta/\theta_s)^{-b}$$

in which θ_s, K_s, and ψ_s are, respectively, moisture content, conductivity, and matric potential at saturation, and b is related to soil texture.

Microwave emission from the soil was calculated with a radiative transfer model that describes the propagation of electromagnetic energy in a stratified soil, assuming that the radiation is coherent, that internal reflection of the radiation within the soil due to the gradient in the moisture profile is negligible, and that scattering within the soil can be neglected. The soil moisture and temperature profiles from the soil physics model are input to the microwave emission model, which calculates the brightness temperature.

The fitting procedure developed for estimating soil hydraulic properties consists of varying the parameters until the root mean square errors (RMSE) between the predicted and observed values of soil physical temperature and microwave brightness temperature were each minimized. The surface temperature is used to calculate the surface energy balance which provides the heat and moisture flux boundary conditions. The microwave data, being sensitive mostly to the soil moisture distribution, is used to calibrate the hydraulic parameters which control the subsurface moisture flux.

This procedure was tested on data from a 1984 field experiment at the USDA Beltsville Agricultural Research Center. Two 6 m x 6 m bare plots (labeled T1 and T4) were saturated and then allowed to dry naturally. The plots differed in the amount of sand present so their hydraulic properties were expected to be somewhat different. For this study 38 hours of data were used, with

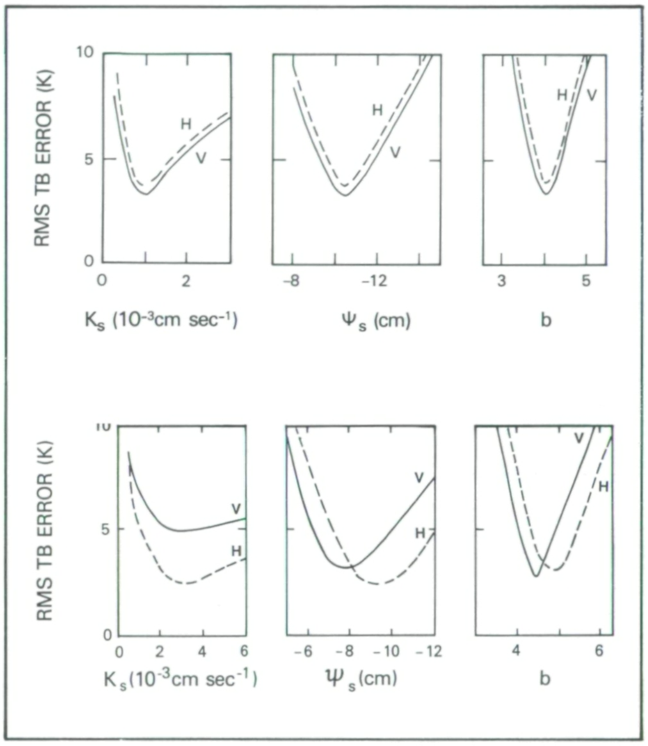

RMS error of predicted minus observed microwave brightness temperatures versus soil hydraulic parameters K_s, ψ_s, and b for horizontal (H) and vertical (V) polarizations at a 20° look angle. The minima of the plotted curves correspond to the best fit values for these parameters. The top and bottom sets are for fields T1 and T4, respectively. The minimum RMSE of 3K is on the order of the instrument error for the microwave radiometer.

Table 1

	K_s (cm sec^{-1})	ψ_s (cm)	θ_s	b	Infiltration Rate (cm sec^{-1})
T1	0.001	-10.5	0.40	4.0	0.0024 ± 0.0005
T4	0.003	-10.0	0.36	5.0	0.0033 ± 0.0007

about 40 remotely sensed measurements taken in that time. An automatic weather station adjacent to the plots provided the data needed to evaluate the surface energy balance.

The figure summarizes the results of estimating the soil hydraulic parameters from the microwave measurements. The RMSE of the predicted and observed brightness temperatures (both vertical and horizontal polarizations) are plotted against the parameter value varied in the simulation. The other three parameters were given their best fit values as defined by the minimum of the RMSE curves. The minimum RMSE in most cases is on the order of 3K, which is the same magnitude as the instrument error for the microwave radiometer. Table 1 summarizes the values of the parameters for each plot. They are in agreement with values found in the literature for these soil types.

At the end of the experiment, double-ring infiltration measurements were made in each plot in the area directly examined by the remote sensors. These values are given in Table 1. There is some disagreement as to whether these should equal K_s in value or should in fact be somewhat larger. Given these uncertainties, it can be said at least that the estimates for K_s from remote sensing agree qualitatively with the infiltration data.

Contact: P. J. Camillo, R. J. Gurney, and P. E. O'Neill
Code 620

Sponsor: Office of Space Science and Applications

LANDSAT STUDY OF LINEAMENTS ON THE CANADIAN SHIELD

It was proposed early in the 20th century by the geologist, W. H. Hobbs, that the Earth's crust is broken by a relatively simple "primary" fracture pattern reflecting uniform global stress conditions. The concept has since been advocated by many scientists under the term "regmatic shear pattern," the word "regmatic" referring to a master system of fractures. European geologists, in particular, interpret many geologic features as such a regmatic system of lineaments. The availability of Landsat pictures, providing synoptic viewing of large areas with uniform lighting, greatly stimulated interest in lineaments and the concept just described.

In 1982, a study of lineaments was begun, the purpose of which was to test the regmatic shear concept by mapping lineaments with Landsat imagery on the Canadian Shield. The Shield was chosen because it is a cratonic, i.e., old stable crust, and should thus be free from localized fracture patterns resulting from recent deformation. In addition, lineaments there are also abundant and well-expressed by lakes, streams, and other depressions. Finally, there are few artificial land-use patterns such as section lines to confuse interpretation. Sixty Landsat frames covering all parts of the Shield were selected and lineaments mapped by five interpreters. Field-checking was carried out in 1984 and 1985 in Manitoba and Ontario. Major conclusions reached at this time are the following:

- Most of the lineaments mapped represent a natural class of brittle fracture, characterized by straightness, steep dip, and length of tens of kilometers. This is mentioned simply to stress that the investigators have not made an arbitrary selection, thus creating an artificial class.

- Many of the lineaments mapped, particularly in northwest Ontario and Manitoba, are diabase dikes or fractures parallel to such dikes. The dikes of the Canadian Shield tend to occur in distinct "swarms," and have been well-mapped and radiometrically dated by Canadian geologists. Field checking has shown that these dikes, or related fractures, are susceptible to differential erosion and thus tend to form linear stream segments or lakes.

- The lineaments for the most part are extensional fractures (whether filled by dikes or not): joint zones, megajoints, or normal faults. This is inferred from the fact that, as seen on Landsat pictures, geologic maps, and outcrops, they do not show lateral offset. Strike separation does occur locally, but this can be explained by vertical motion. The conclusion that the lineaments are of an extensional nature is a qualified one, since such features will be more susceptible to erosion, and are more likely to be mapped than compressional fractures (reverse or strike-slip faults).

- Most of the fractures mapped are of Precambrian age, although some have been reactivated since. Evidence for this age comes both from radiometric dike ages and from field relations.

- There is no evidence that lineaments on the Canadian Shield are part of a regmatic pattern of continental

Landsat scene covering southern Ontario; Georgian Bay at lower left, Lake Nipissing at upper right. Note lineaments visible on Canadian Shield. French River is at left center.

View to west along French River, Ontario, from Route 69 bridge south of Sudbury. Course of river controlled by tension fractures, visible as lineaments on the Landsat figure. Outcrops at left show fractures parallel to the French River to be joints, with no visible offset.

or global extent. Domains covering two or three Landsat scenes in which a unified pattern is obvious can be delineated, but the Shield as a whole shows nothing like the postulated regmatic shear system. Furthermore, the absence of significant strike slip by itself contradicts the existence of a shear system, although not decisively. There is some evidence of systematic rotation of fracture patterns between adjacent tectonic provinces, which may reflect microplate collisions.

Contact: P. D. Lowman
Code 620

Sponsor: Office of Space Science and Applications

TEMPORAL CHANGES OF THE GEOMAGNETIC FIELD

Geomagnetic field models are expressed in terms of series of spherical harmonics wherein the coefficients of the spherical harmonics constitute the model. These coefficients are called Gauss coefficients because the method was first elucidated by Gauss in 1839. Since the geomagnetic field varies with time, to model more than one epoch requires inclusion of time dependence in the Gauss coefficients. The standard procedure is to expand each coefficient in a Taylor series in time around the epoch of interest. Such expansions normally include only the first time derivative, or secular variation (SV), although several have included the second derivative, and a recent GSFC model went as far as the third derivative. This approach is successful in describing the field only for short periods of time.

In cooperation with the British Geological Survey in Edinburgh, a series of yearly first derivative models or SVs were derived for 1903-1982. The resulting series for each SV coefficient was then fit with a cubic spline function for the entire interval. The series of annual SV coefficients for the main dipole term—the points—and some of the better Taylor series solutions—the lines labeled GSFC(12/66) and IGS75, and the curve labeled GSFC (9/80), are shown in the first illustration.

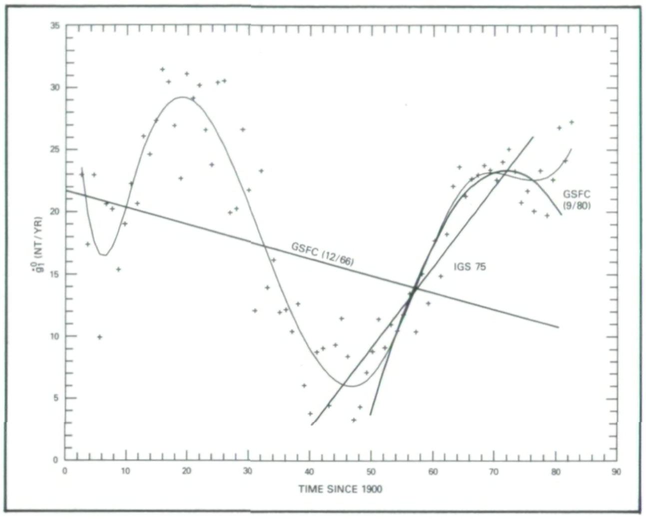

The rate of change of the Gauss coefficient, g_1^0, corresponding to the centered geomagnetic dipole. Units are nT/yr.

The thin curve through the points is the result of the spline fit. The spline representation has the advantage of being simple, smooth, and continuous for a period of time measured in decades, and is able to represent the major features of the geomagnetic temporal change with uniform accuracy for the entire time span. One may study trends with the spline representation, and it provides a tool with which to extrapolate main field models over long periods of time.

Using the spline representation and the 1980 Magsat main field model, geomagnetic westward drift was computed, and its correlation with decade fluctuations in length-of-day was tested. Recent discussions in the literature have suggested that this is an important correlation. However, we find that the correlation is *not* high; it is a maximum of 0.56 when westward drift leads fluctuations in the length-of-day by 10 years. Further investigation showed a higher correlation, 0.75, between changes in the geomagnetic dipole and changes in length-of-day, with changes in length-of-day leading by 13 years. This indicates that core-mantle coupling depends upon the strength of the main dipole as suggested by Yukutaki, (1965), but the detailed theory remains obscure.

A spectral analysis was carried out for each series of yearly Gauss secular variation coefficients. Table 1 shows the main periods found together with these found in an analysis by Currie (1976). The time span of data is too short to conclude that periods 70-80 years are really present, but the other periods found are believed to be real and to reflect time changes of fields within the Earth. These include changes probably originating in the core (e.g., 21-23 years, 16 years) and those induced in the mantle from external source (e.g., 9-13 years and harmonics).

Table 1
Groups of Periodicities

Period Range (years)	Coefficients where Present*
40 - 80	g_1^0(53.5), h_1^1(71), g_2^0(42.6), g_2^2(70.9), g_3^0(58.1), g_3^1(58.1), g_3^2(70.9), g_3^3(64)
29 - 32	h_2^2(32), h_3^2(29.1)
21 - 23	c(22.9), g_2^1(21.3), g_2^2(21.3), h_3^3(21.3)
16	g_2^0, h_2^1, g_3^0
9 - 13	c(11.5), h_1^1(10.7), g_2^1(10.7), g_2^2(10.7), h_2^2(12.8), g_3^0(10.7), h_3^1(12.8), g_3^2(12.8), h_3^2(10.7), g_3^3(9.1), h_3^3(10.7)
4.2 - 4.6	c(4.35), g_1^0(4.3), g_2^0(4.3), g_2^1(4.4), h_2^1(4.6), g_3^3(4.3)
4.0	g_2^2, g_3^0, g_3^1
3.6 - 3.8	c(3.75), h_1^1(3.8), g_2^1(3.6), h_2^2(3.8), h_3^1(3.6), h_3^3(3.8)
3.4	c, g_2^0, g_3^0, h_3^2, g_3^3
3.0	c, g_1^0 h_2^2, g_3^2, g_3^3
2.6 - 2.8	c(2.75), g_1^1(2.8), h_1^1(2.8), g_2^1(2.8), h_2^1(2.8), g_2^2(2.7), g_3^0(2.6), g_3^1(2.6), h_3^1(2.7), g_3^2(2.7), g_3^3(2.6), h_3^3(2.8)
2.2	c(2.27?), g_1^1(2.2), h_1^1(2.2), h_2^1(2.2), g_3^0(2.2), h_3^1(2.2), h_3^2(2.2)

*c = present in Currie's (1976) results.

A wealth of information is present if really adequate correlation with external sources can be carried out. This would include information on the variation of mantle conductivity not only with depth but also laterally.

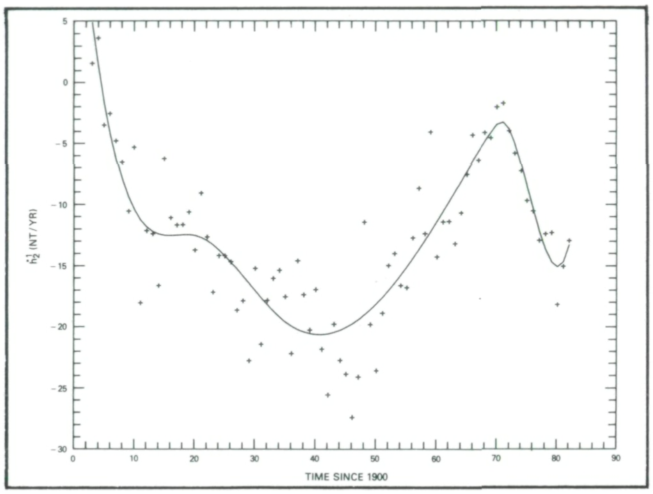

The rate of change of the Gauss coefficient h_2^1 in the spherical harmonic representation of the geomagnetic field.

Prominent in the results of the spline model is the presence of a substantial change in secular variation near 1970. (See the second figure.) This change has been called a "geomagnetic jerk" because it appears to be well represented by a discontinuity in the second time derivative of selected coefficients. It has been hypothesized that such a discontinuity might be the result of some sort of "event" in the core, such as the onset of a "kink" instability. Dr. Backus (UCSD) has developed the theory of the way the mantle would filter the results of a field event at the core-mantle boundary (CMB) as it is transmitted to the Earth's surface. The theory is in terms of a mantle filter for each Gauss coefficient characterized by an attenuation factor, delay time, and smoothing time. If the 1970 event is a true "jerk," i.e., discontinuity in second derivative, then the field behavior can be used to determine the mantle smoothing time. In practice, the available data for the 1970 "jerk" includes no satellite vector data. The quality of the observatory data is marginal for such a study. Yet, in collaboration with Dr. Backus, a study was undertaken with the available data which shows that the field change at 1970 can be satisfactorily presented as a quintic in time with fewer parameters than required for the biquadratic needed to model a true "jerk." Thus, within present data accuracy, the 1970 event is shown not to be a true "jerk." Because of the data shortcomings, this is not a definitive result. Hopefully, the future will bring accurate satellite data for a period spanning a jerk so that a definitive analysis can be accomplished.

Contact: R. Langel
Code 620

Sponsor: Office of Space Science and Applications

MAGSAT DATA OVER THE KURSK REGION, U.S.S.R.

It is generally believed that the source of the long-wavelength magnetic anomaly field of the Earth recorded by Magsat is produced by induced magnetization; that is, magnetization resulting from the Earth's current magnetic field. This magnetization would vanish if the present Earth field went to zero. In a recent study the possibility that some of the largest crustal magnetic anomalies are the result of remanent magnetization, or magnetization produced by a previously existing or "fossil" magnetic field, has been explored. If the Earth's present magnetic field went to zero, remanent magnetization would remain.

The largest magnetic anomaly in the world, the Kursk magnetic anomaly (KMA), was chosen for this search. This feature was named after the city of Kursk, U.S.S.R., which lies some 400 kilometers south of Moscow, and is the largest known source of iron ore in the world. Geologically, the KMA is situated on a large northwest-southeast trending crustal upwarp. This crustal dome, called the Voronezh bulge, extends 900 km along its long axis by 500 km on its short axis. Its origin is believed to be a failed crustal rift; it is situated between two aulacogens or incipient rifts. In their classic reference, Chapman and Bartels (1940), suggested that the Kursk magnetic anomaly could possess a significant component of remanent magnetization. The objective of the study was to determine if this remanent component can be detected from satellite data. Since the Magsat data represent a global data base, other large amplitude anomalies could be studied for remanence.

In order to study this singular magnetic anomaly, a new technique for reducing Magsat data to anomaly form was developed. This method, which utilizes the orbital intersection (between dawn and dusk orbits) to remove time varying fields, is similar to Seasat data reduction schemes. The resulting map is given in the first figure. This anomaly relationship is confirmed by the KMA section of the aeromagnetic map of the U.S.S.R. in the second figure.

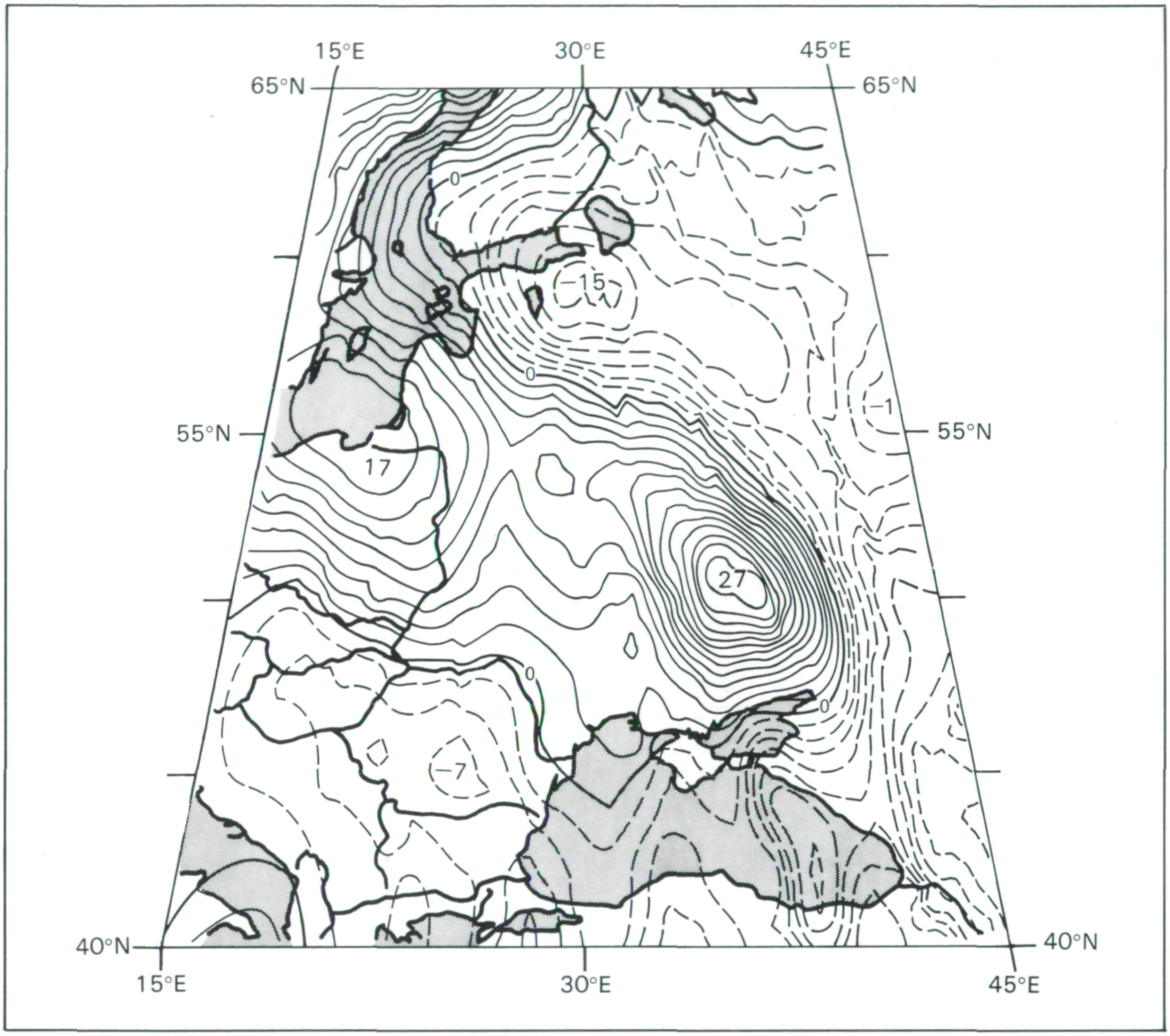

Total intensity magnetic anomaly map of the study area from Magsat data. Contour interval is 2 nt, zero contour is labeled, and dashed contours are negative values. Five degrees latitude equals 555 km. The city of Kursk is located at 51°40′N latitude, 36°12′E longitude.

If this magnetization vector is in the direction of the Earth's present magnetic poles, then the KMA is most likely a result of induction. Magnetization in a significantly different direction would indicate magnetization by remanence. Two different and previously developed methods were used to determine this magnetization vector. One assumes nothing about the shape of the body producing the anomaly, but operates on the magnetic anomaly vector components. With this method it is necessary to isolate the anomaly under study from any nearby features which might interfere. In practice, this may be difficult to do. The second method assumes a simple prismatic body and fits a magnetization by a least-squares analysis. A simple geometry must be assumed for the causative body. While this may be a geologically unrealistic assumption at satellite altitude, the field is insensitive to small changes in body shape. Both methods produced vectors which were significantly different from

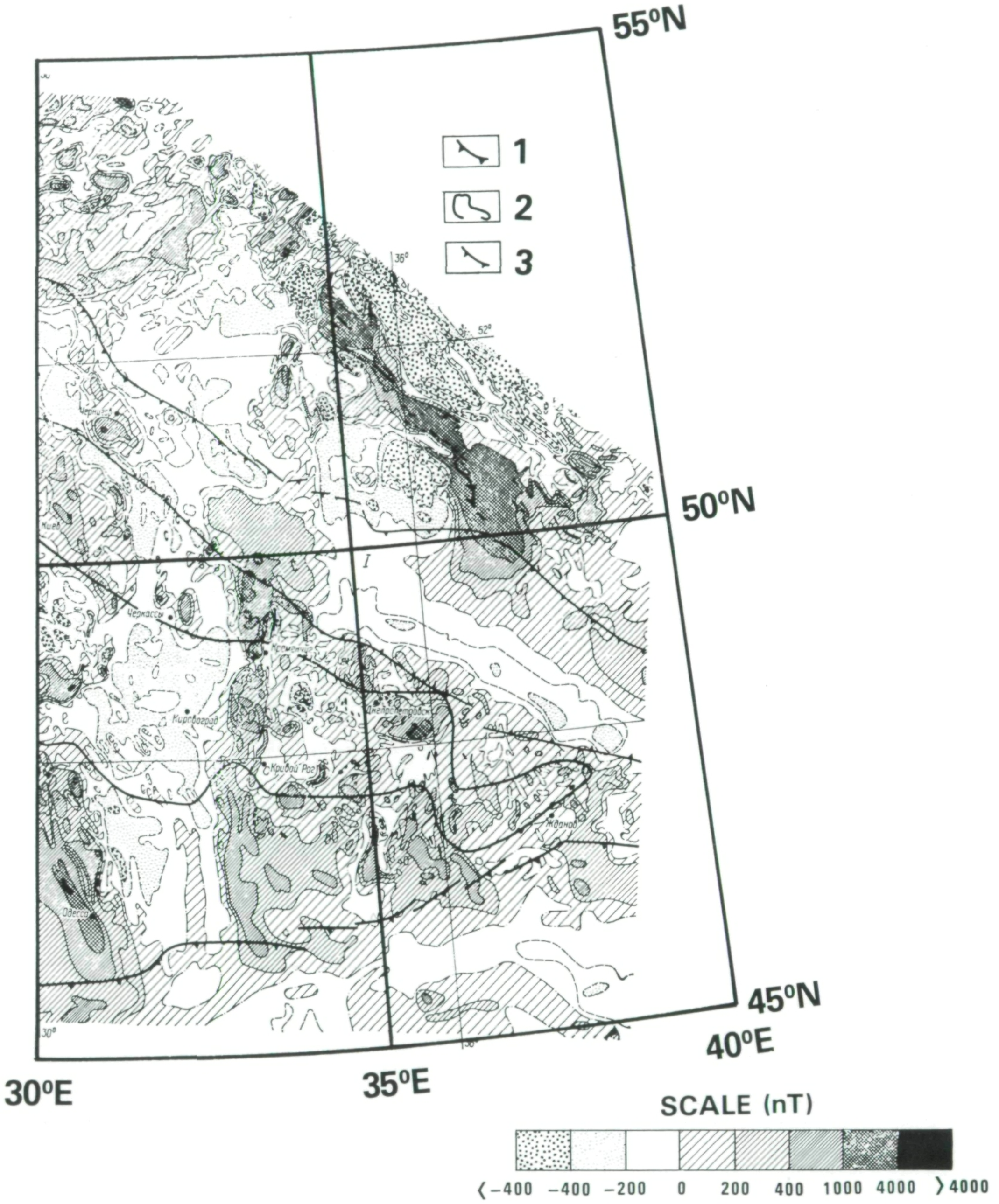

Part of the aeromagnetic map of the Soviet Union. Structure contours are: (1) western European platform; (2) Ukrainian Shield; and (3) Pripyat-Dniper-Donetsk aulacogen. (From Makarovoi, 1977.)

the present field, but they were relatively self-consistent. These vectors were converted into virtual paleomagnetic poles. They plot near the magnetic polar wandering path for Eurasia at 300 million years before present. While we cannot state that this represents the time the magnetization has acquired, we can conclude that the KMA has a significant component of remanent magnetization; and therefore the Magsat anomaly field is more complex than previously believed.

Contact: P. Taylor
Code 620

Sponsor: Office of Space Science and Applications

POLAR MOTION

To properly understand polar motion, one must define three auxiliary physical axes running in the general north/south direction. The first axis is known as the Conventional International Origin (CIO) and passes through a fixed point on the surface of the Earth near the North Pole. The second axis is the axis of maximum moment of inertia, known as the Figure Axis (FA) and is defined by the Earth's mass distribution. The third axis is the total angular momentum vector of the Earth which, to a very good approximation, coincides with the Earth's Instantaneous Rotation Axis (IRA) or simply the spin axis. (See accompanying figure.)

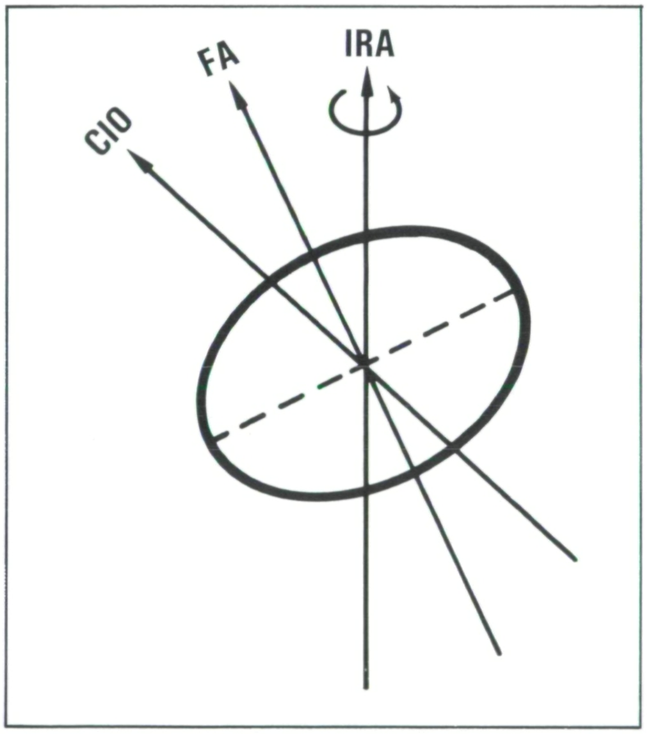

The Earth's auxiliary physical axis.

The Earth rotates about the spin axis which, due to internal or external excitations, does not coincide with its FA and therefore, according to Euler's rigid body theory, the FA will precess about the spin axis with a period of 305 days. Elastic yielding of the Earth, however, is enough to lengthen the period of this Eulerian free precession to about 14 months. This precession of the FA about the spin axis is known as the Chandler Wobble. A problem of great interest to geophysics is the explanation of the random excitations of this wobble. According to one theory, for example, large earthquakes may be associated with these excitations. Another problem associated with this wobble is the estimation and explanation of its period and damping. This problem, however, involves parameters describing the mechanical properties of the Earth's solid mantle as well as fluid hydrosphere and core, and is particularly difficult to fully explain using present Earth models.

The FA also precesses about the spin axis with a period of 1 year due to the torques exerted on the solid Earth by the seasonal movements of the atmosphere and hydrosphere. The amplitude of the annual wobble is about the same as that of the Chandler Wobble; however, its spectral peak is much sharper than the broad peak found at the Chandler period.

Since we live on our planet, we prefer to say that it is the spin axis that precesses about the FA. The CIO, fixed on the Earth's crust, doesn't move in this Earth-fixed coordinate system. If the mass distribution of the total Earth never changed, the separation between the CIO and the FA would remain constant in time. Assuming, however, that the almost circular path that the spin axis traces out has the FA at its center, the observations indicate that the FA drifts away from the CIO in the direction between Greenland and the Hudson Bay, at the rate of about 13 cm/yr. (See figure.)

The coordinates of the observatories and tracking stations around the world are referred to the CIO (by convention).

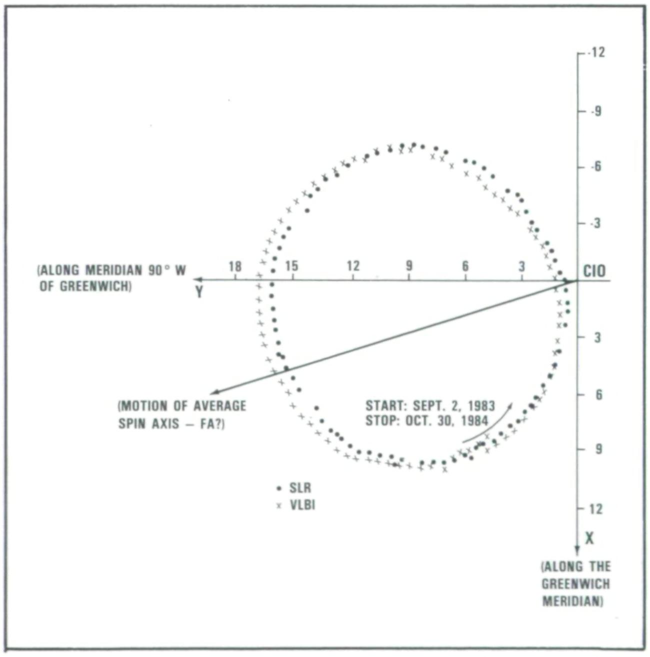

Path of Earth's instantaneous rotation axis from September 1983 to October 1984 (units in meters).

Due to the motion of the spin axis, however, the coordinates at any point on the Earth's surface will change with time (mostly latitude). It is through the observation of these coordinate variations of the observatories that we can define the relationship between the CIO and the IRA. Continuous monitoring of the movements of the spin axis is of importance both to theoretical geophysics (mechanical properties of the Earth's interior, excitation processes, etc.) and to very precise space geodesy.

In the past, observations of latitude variations were made exclusively with optical astrometery (i.e., through observations to the stars). Current technological advancements, however, provide these measurements with much better accuracy through the space geodesy techniques known as Satellite Laser Ranging (SLR) and Very Long Baseline Interferometry (VLBI). Under the direction of NASA's Crustal Dynamics Project, both techniques were furthered in order to satisfy the Project's very ambitious objectives, i.e., the use of space geodesy for the observation, confirmation and modeling of global kinematics of the tectonic plates, modeling of regional crustal deformations, and investigation of the possible relation between earthquakes and polar motion. It is apparent that the very precise positioning required by the Project (1 to 2 cm over distances of thousands of kilometers) can never be realized without securing polar motion parameters of comparable accuracy.

VLBI uses the simultaneous passive reception of intergalactic radio signals to infer the relative positions of observing antennas. SLR uses the known motion of near-Earth orbiting satellites to position in three dimensions sites on a global scale. These two diverse technologies are to a large measure independent and susceptible to differing error sources. Intercomparison of the Earth rotation parameters obtained by SLR and VLBI provides an excellent means for assessing the accuracy of state-of-the-art polar motion determinations.

The accuracy of space technology for monitoring the motion of the Earth's spin axis has been fully tested by an internationally coordinated project. During the latter part of 1983 and running through the end of 1984, the MERIT campaign (Monitor Earth Rotation and Intercompare the Techniques of Observation and Analysis) has taken an unprecendented amount of data to assess the quality and accuracy of space-derived measures of the Earth's spin axis. Initial results are promising. The positions of the pole from both SLR and VLBI techniques agree with one another over 5-day averages to better than 5 cm (Figure 2). Measurements of the Earth's spin axis on a 12-hour and daily basis have also been made. These space results are 10 times more finely resolved in time than those acquired from older optical methods and several times more accurate. A new era of Earth observations, with the ability to monitor the Earth's response to internal and external phenomena through changes in the Earth's rotation, is now emerging from these space measurement systems.

Contact: D. C. Christodoulidis
Code 620

Sponsor: Office of Space Science and Applications

A COMPARISON OF SATELLITE LASER RANGING AND VERY LONG BASELINE INTERFEROMETRY DERIVED BASELINE LENGTHS

One of the objectives of NASA's Crustal Dynamics Project is to improve knowledge and understanding of the regional deformation and strain accumulation at the plate boundary in western North America. An important item in this understanding involves precise determination of position or rate of change of position in three dimensions and at places separated by hundreds to thousands of kilometers on the surface of the Earth. The rates of change of position expected from geophysical and seismological considerations are approximately several centimeters per year, implying that over reasonable time scales, observational systems must be able to detect position changes of a few centimeters. The Crustal Dynamics Project collects these measurements to analyze and interpret. Currently only two systems are capable of making these measurements, Satellite Laser Ranging (SLR) and Very Long Baseline Interferometry (VLBI).

In order to ensure that the measurements are correct, it is desirable to compare the results obtained by these two independent techniques. The SLR technique uses ground-based lasers to range to satellites which orbit the Earth. The laser instrument emits a pulse of laser light toward the satellite, which reflects it back toward the laser by means of a retroreflector array on the satellite surface. From the time difference between the emitted and received pulse, a range to the satellite can be calculated. Using precision orbit determination programs, the orbit of the satellite and the position of the laser on the surface of the Earth can be determined. If several lasers are used, the distance between them can be calculated. The VLBI technique uses pairs of antennae located on the surface of the Earth for the reception of radio signals from quasars. The distance between the sites can be calculated

SLR and VLBI Baselines and Their Differences:
Ordered by Length (cm)

From	To	Length	SLR	VLBI	SLR-VLBI
Westford	Pasadena*	405702200+	3	7	-4
	Owens Valley	392972500+	83	77	6
	Goldstone	390059500+	76	76	0
	Fort Davis	313863600+	10	16	-6
	Platteville	275321900+	14	18	-4
Fort Davis	Quincy	184183700+	85	79	6
	Owens Valley	150127300+	80	76	4
	Pasadena*	138369700+	73	63	10
	Goldstone	129433300+	100	98	2
Platteville	Owens Valley	122172600+	61	67	-6
Fort Davis	Monument Peak*	119828300+	84	76	8
	Platteville	105568500+	89	85	4
Quincy	Monument Peak*	88360100+	80	79	1
	Pasadena*	68574300+	28	32	-4
	Goldstone	63970200+	98	94	4
Owens Valley	Monument Peak*	51088100+	1	8	-7
	Quincy	38206700+	79	71	8
	Pasadena*	33604200+	82	79	3
	Monument Peak*	26365300+	71	76	-5
Goldstone	Owens Valley	25828900+	76	78	-2
	Monument Peak	21828200+	80	80	0
Pasadena	Goldstone*	17137400+	82	79	3
	For 22 baselines	rms about 0			5.2
		mean			1.0 ± 1.1

*Baselines crossing tectonic plate boundary

by comparing the time difference in the receipt of a signal at each antenna.

Beginning in October 1979, the SLR and VLBI elements of NASA's Crustal Dynamics Project began to occupy the same sites in the continental United States. These eight sites were: Westford, Massachusetts; Fort Davis, Texas; Platteville, Colorado; and Quincy, Owens Valley, Goldstone, Pasadena, and Monument Peak, California. The first six sites are on the North American Plate, and the remaining two are on the Pacific Plate.

Of the 28 possible baselines between the eight sites, 22 were determined by both systems. The 22 baseline lengths determined by SLR were differenced from the corresponding VLBI determinations. These results are shown in the accompanying table. The rms scatter about zero for the length differences is 5.2 cm with a mean of 1.0 ± 1.1 cm, and there is no apparent scale factor between these two distance determinations. For this result, the Monument Peak-to-Quincy baseline has been adjusted for tectonic plate motion by using the SLR determined baseline rate. For the eight other baselines crossing a plate

boundary, tectonic plate motion was not modeled. If a model for this motion based upon baseline changes derived from strain rates is applied, the rms scatter about zero for the 22 differences becomes 7.2 cm, with a mean of 1.0 ± 1.1 cm. These results are within the combined error budgets of the SLR and VLBI baseline length determinations. Both technologies are capable of providing accurate geophysically meaningful measures of transcontinental baseline distances. A few more years of measurements of this type should aid geophysicists in understanding the distribution of crustal deformation and the temporal character along portions of the North American/Pacific Plate boundary.

Contact: R. Kolenkiewicz and J. W. Ryan
Code 620

Sponsor: Office of Space Science and Applications

OCEANS

DIRECT OBSERVATIONS OF THE WIND-DRIVEN OCEAN CIRCULATION

Oceanographers have made several attempts in this century to relate atmospheric forcing to the energetic long time period (days to years) currents in the ocean. Early efforts derived a mechanism for momentum transfer from the atmosphere into the surface layers of the ocean. The divergence of this wind-driven surface flow causes a vertical motion near the base of the oceanic surface mixed layer that forces the underlying ocean and is termed Ekman pumping. This surface pumping action causes horizontal flow at depth because of mass conservation. Steady Ekman pumping caused by the easterly trade winds in the tropics and the westerly winds at midlatitude has been shown to be responsible for the general pattern of the large-scale ocean circulation. Measurements of time-dependent, wind-driven deep ocean currents have been possible only in the last decade because of improvements in the analysis of available marine surface observations and developments in instruments to measure currents. To date, however, only a few observations of time-dependent ocean currents have suggested any direct relationship to the winds. In the past year, in a cooperative effort with the Scripps Institution of Oceanography, the first conclusive evidence for wind-driven deep ocean currents has been found (Niiler and Koblinsky, 1985).

For the past 5 years, deep ocean current measurements have been made at a variety of mooring locations across the North Pacific by investigators at Woods Hole Oceanographic Institution and Scripps Institution of Oceanography. (See the illustration.) In general, currents were recorded every 15 minutes at depths of 4000 m, 1000 m, 600 m, and 300 m below the surface. Depths at a few moorings varied because of desired objectives. Most observations were made for at least 1 year at any given location but none more than 3 years. Estimates of the surface wind field over the North Pacific for this time period have been made by the National Meteorological Center for every 12 hours, and by the U.S. Navy Fleet Numerical Ocean Center for every 6 hours. Both estimates make use of all available surface and satellite observations in the context of a dynamic forecast model. For the purpose of comparison, both the winds and currents were low-pass filtered to remove fluctuations with periods less than 10 days. For the wind field this removes unwanted high frequency noise, and for the ocean current measurements it removes tidal and inertial oscillations which are not relevant to this study. The wind vectors are then converted to wind stress vectors through an empirical formula. The curl of the wind stress vector, which is directly proportional to deep horizontal currents caused by Ekman pumping, is computed with simple differences.

The estimated wind-forced deep ocean currents, derived from the curl of the wind stress, have been compared with direct observations of the currents at several locations. The second figure shows this comparison at 42 N, 152 W during 1982-83. A strong correlation (99 percent significant) is found at all locations where the wind fields are highly variable (usually latitudes north of 35 °N), and the background ocean kinetic energy is small (i.e., away from strong currents such as the Kuroshio). In addition, true seasonal variations are found that appear to be related to the movements of large atmospheric pressure systems (e.g., Aleutian Low, Hawaiian High) around the Pacific.

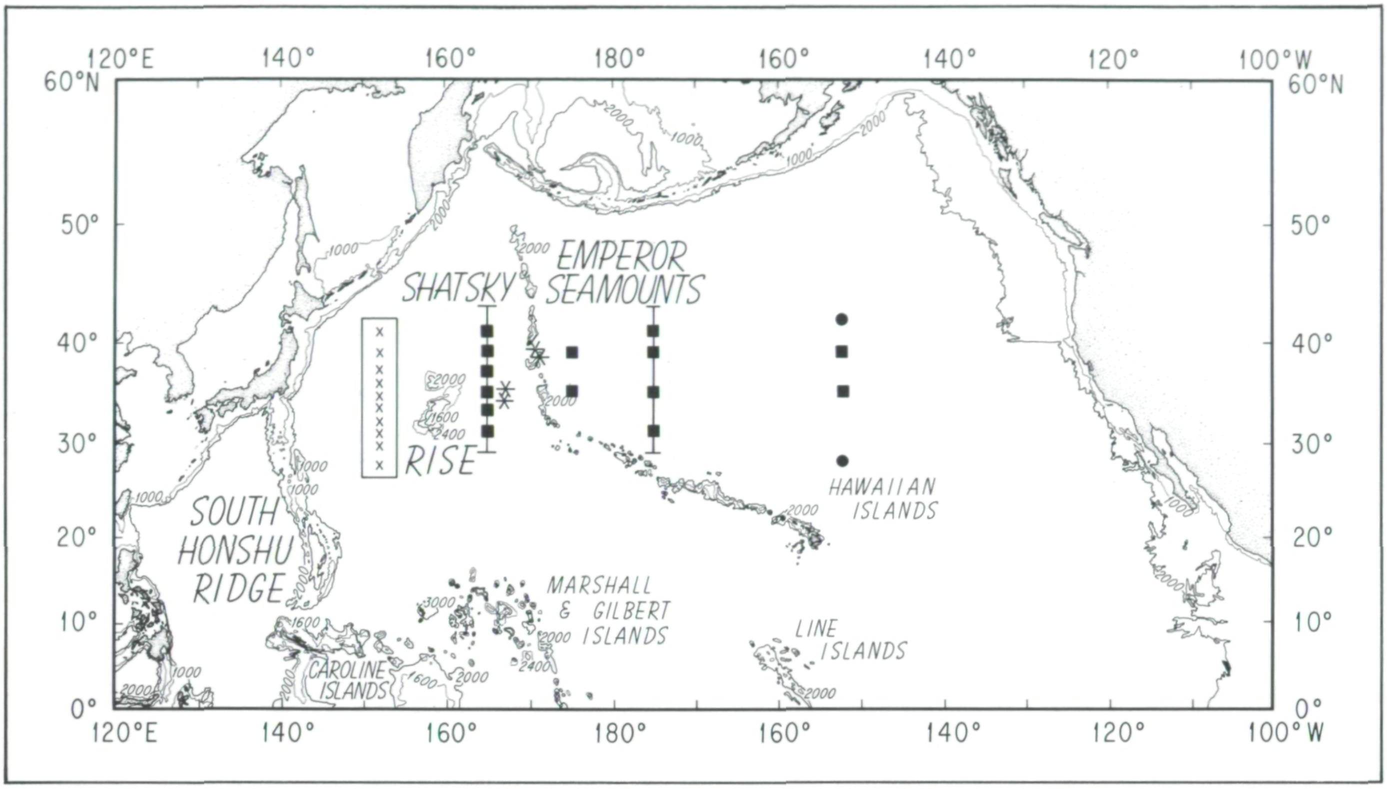

Locations of current meter moorings which measure the horizontal ocean currents at various depths used in this study.

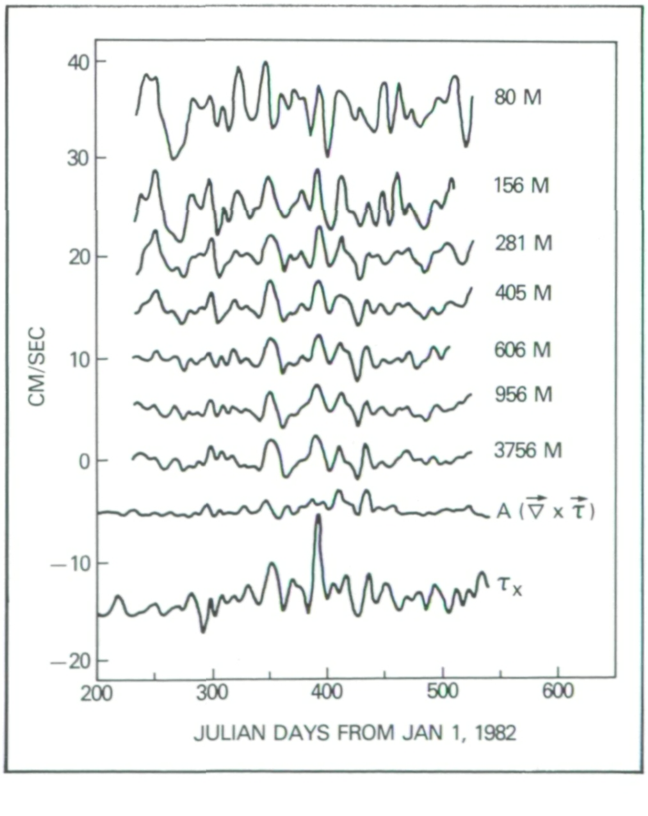

◀ *The observed horizontal currents at a variety of depths measured at 42°N, 152°W. The direction of the currents is perpendicular to the local potential vorticity gradient as expected for wind-driven currents. The bottom two curves are the curl of the wind stress $A(\nabla x\tau)$) scaled appropriately to estimate the deep flow in cm/sec, and the zonal wind stress (τ_x) in dynes/cm^2.*

In the early 1990's NASA will fly a scatterometer instrument on the Navy NROSS satellite to measure surface winds over the oceans. These results suggest a direct method of calibration for this instrument in addition to supplying a dynamical basis for wind-driven ocean circulation models. The numerical models will be able to compute the shape of ocean surface generated by large-scale wind forcing, which can be verified or compared with sea height measurements proposed to be taken by NASA's TOPEX Mission in the same time period.

Contact: C. J. Koblinsky
Code 620

Sponsor: Office of Space Science and Applications

MODEL STUDIES OF EL NIÑO AND THE SOUTHERN OSCILLATION

The tropical ocean and atmosphere undergo semiperiodic vacillations through a coupled process known as El Niño/Southern Oscillation (ENSO). This phenomenon manifests itself through anomalously warm sea surface temperatures (SST) in the eastern tropical Pacific, anomalous tropical winds, and large-scale disturbances of the extra-tropical atmosphere, with a period of 3 to 4 years. These perturbations persist for about one year and can significantly affect seasonal climates as far away as Europe.

As yet a complete theory for the existence and nature of these events is lacking. This work consists of a search for the energy source and governing physics to provide the basis for monitoring and prediction of ENSO. To this end, we have constructed a model of the tropical ocean and global atmosphere to look for similar vacillations. The model allows for the simplest features of interaction and feedback: SST anomalies drive the atmosphere through surface heat flux anomalies; surface wind stress anomalies drive ocean currents.

The model does produce vacillations similar to those observed in ENSO events. The energy source of the vacillations has been identified as due to a linear instability of the coupled system in the eastern portion of the basin. SST anomalies alter the surface heat flux into the atmosphere which drives anomalous surface winds. The winds so generated are essentially those needed to reinforce the SST anomaly itself, and the feedback is strong enough to be unstable.

The system vacillates through a nonlinear process similar to a delayed-action oscillator. In the western portion of the basin, the nature of the ocean state eliminates the coupling between surface winds and sea-surface temperature, thereby breaking the feedback loop. Waves shed from the warm (or cold) active instability in the east therefore propagate undisturbed through the western/ocean, reflecting at the boundary. When they return to the east, they induce cooling (warming). Since nonlinear effects limit the magnitude of the initial warm (cold) instability, these newly arrived signals can drive the system to a cold (warm) state. The system then repeats through a cold (or warm) phase.

Further experiments have established that: (1) neither the ocean nor atmosphere models have an inherent model of oscillation at these frequencies; (2) the oscillation is not a subharmonic on the annual cycle (there is none in these experiments); (3) the interevent variability is due to the presence of natural variability in the atmosphere.

This model system demonstrates that the tropical atmosphere/ocean system may vacillate for some relatively simple reasons. Complications, such as the addition of annual cycle, moisture effects in the atmosphere, migrations of the intertropical convergence zone, may be important in a faithful simulation of the system, but are not necessary conditions for the existence of ENSO.

Contact: P. Schopf and M. Suarez
Codes 670, 610

Sponsor: Office of Space Science and Applications

OCEAN COLOR REMOTE SENSING OF MORE THAN PIGMENT

The Coastal Zone Color Scanner (CZCS), a sensor on the Nimbus-7 satellite, has long exceeded its design lifetime of one year. Launched in 1978, the CZCS is still collecting data over the world's oceans in the visible region of the spectrum. The primary purpose of the sensor has been to provide estimates of phytoplankton pigment concentrations in surface waters. From the limited amount of data that has been processed, much has been learned about ocean dynamics and circulation, as well as the variability of oceanic productivity.

The Laboratory for Oceans is in the process of producing summaries of the photosynthetic pigment fields in the North Atlantic basin from CZCS data. The pigment concentrations are derived from ratios of the first three CZCS bands, after the atmospheric signal has been removed. The upwelling water radiances in these bands, centered at 443, 520, and 550 nm, are a function of the scattering and absorption properties of the particles suspended in the water. Phytoplankton are primarily absorbers, while suspended sediments and other particulates are mainly scatterers. However, there are situations in which the water radiances are anomalous, that is, outside the normal range of values. Two of these are illustrated in the accompanying figure showing the atmospherically-corrected ocean-leaving radiances at 443, 520, and 550 nm. The CZCS data were acquired on May 7, 1981. A dump site in the New York Bight appears as a plume of high radiance (light gray area) in bands 2 and 3 and low radiance (dark gray) in band 1. Just north of the clouds at the bottom of the scene is an area of slightly elevated radiances in all three bands, probably due to a

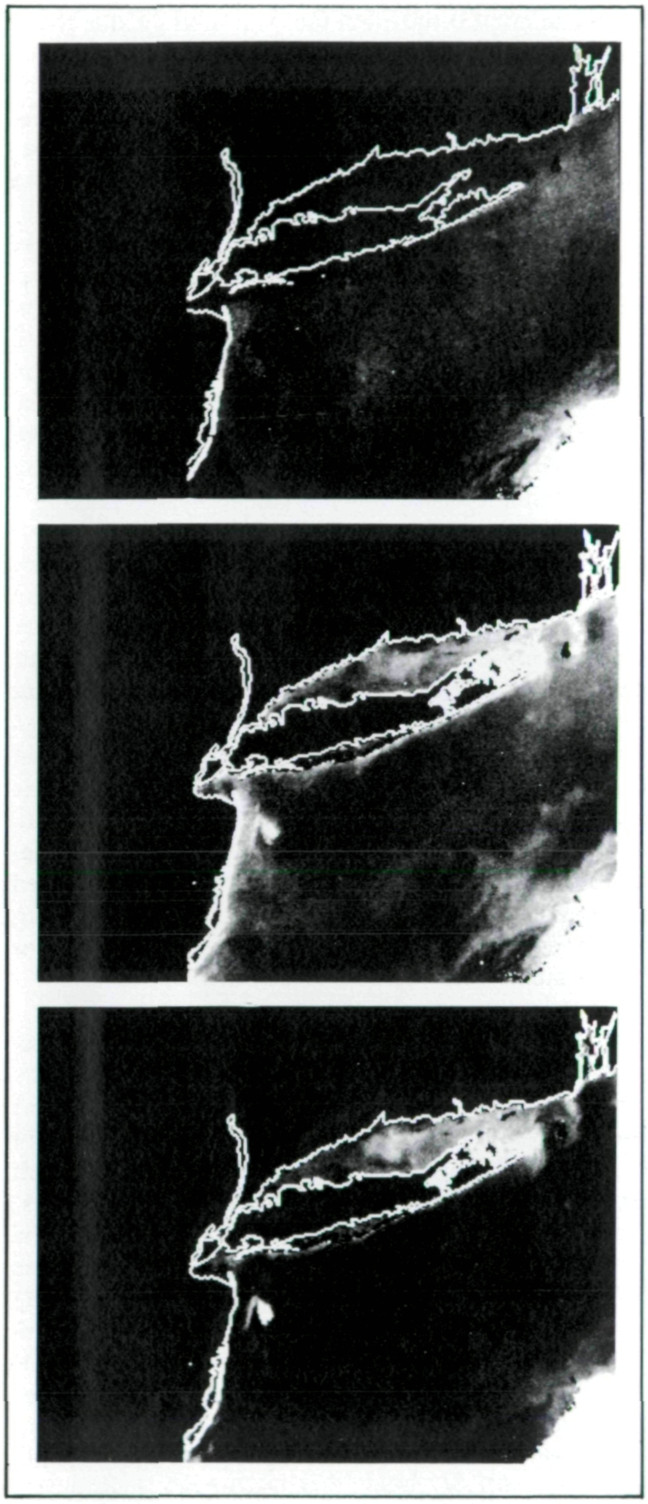

Atmospherically-corrected CZCS bands 1 through 3 for May 7, 1981, showing the Middle Atlantic Bight. Land is masked in black and outlined in white. Clouds are masked in white. (a) Band 1 at 443 nm. (b) Band 2 at 520 nm. (c) Band 3 at 550 nm.

bloom of coccolithophores, a group of phytoplanton covered with tiny calcium carbonate platelets which produce unusually high scattering of sunlight. These two anomalous regions can be distinguished by their spectral signatures, since the dump plume has low reflectance in band 1 and the bloom has high reflectance in the same band. In both instances, the pigment estimates derived from the radiances are in error.

Monthly and regional composites of pigment fields will be adversely affected by erroneous pigment estimates occurring in areas such as the two illustrated here. In order to produce valid pigment summaries, these and other anomalous regions will be initially identified by high radiance in band 3. The source of the anomalous radiances can be broadly classified by the spectral signatures in all three bands. In addition, ratios or differences of the plume/bloom radiances with radiances in the surrounding waters will provide a means of quantifying the effect on pigment estimates.

Contact: Dr. Jane Elrod
Code 670

Sponsor: Office of Space Science and Applications

OBSERVATION OF OCEAN EDDIES IN THE MARGINAL ICE ZONE

A large-scale international field experiment was carried out in the summer of 1984 in the marginal ice zone of the Fram Strait/Greenland Sea (MIZEX'84) in an effort to obtain more detailed knowledge of the air-sea-ice energy and momentum transfers important to the understanding of the climate system. One mechanism thought to be important is the formation of ocean eddies due to bottom topography and/or pycnocline structure; such eddies are capable of accelerating the transport of sea ice into the warmer seas, where the ice melts more rapidly. During MIZEX'84, seven research vessels were utilized to obtain detailed oceanic sections, weather data, physical and local radiometric measurements on the sea ice pack, and acoustic measurements. Five different aircraft were used for mesoscale observations of the marginal ice zone with the aid of synthetic and real aperture radars, altimeters, and multispectral microwave radiometers, including imagers. One of these was the NASA CV-990, equipped with the GSFC microwave imagers operating at wavelengths of 1.55 and 0.3 cm, and dual-polarized microwave radiometers operating at 1.7 and 0.8 cm.

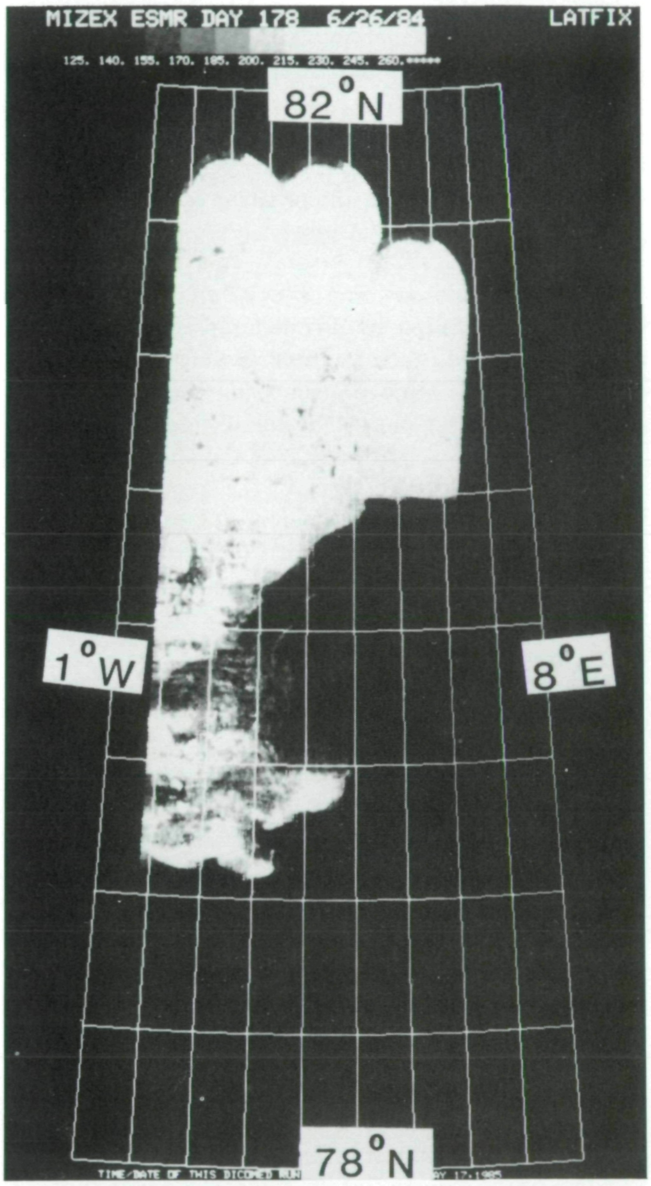

ESMR mosaic, June 26, 1984.

MIZEX'84 proved to be fruitful for observation of ocean eddies. Over the course of the two-month expedition, numerous eddies were seen in various stages of development with spacecraft images from the AVHRR, the airborne active and passive microwave imagers, and the surface sections. One hypothesis being scrutinized proposes that the Molloy Deep, an abyss more than 5,000 meters in depth located at 79° 10′N 3E, is the center of a permanent gyre which sluffs off eddies that propagate away with the ocean currents. Some of the AVHRR observations have lent credence to this idea, but it is still under study.

A related event is shown in the figure, a 1.55 cm microwave radiance image produced from data from one of the microwave scanners on board the CV-990, which flew a mosaic pattern in the MIZEX'84 area on June 26, 1984. Here, open ocean is represented by black, and increasing sea ice concentrations by lighter shades of gray. The center of the Molloy Deep gyre, a feature about 100 km in extent, is ice-free in this image. The southernmost ice, which had propagated eastwards about 50 km since an earlier image was made on June 22, 1984, may have been projected by the northern part of this gyre. An associated eddy, as indicated by a circular spiral of ice floes, can be seen centered at 79° 75′N, 1° 10′E. By the time the next image was formed, on June 29, only traces of these ice floes remained in the area, the bulk of the ice having either melted or been transported outwards.

The foregoing represents but an initial and partial view of the comprehensive data set acquired during MIZEX'84. The ongoing detailed analysis of these data shows promise of making valuable contributions to our understanding of the contributions of this marginal ice zone to the climate system.

Contact: Dr. P. Gloersen
Code 670

Sponsor: Office of Space Science and Applications

EXPERIMENTAL STUDIES OF RADAR SCATTERING BY WATER WAVES

Radar altimetry provides several measurements of interest to the geophysical community. In addition to the topographic information of primary importance and the backscattered power from within the radar's footprint, the shape of the backscattered waveform can yield accurate measurements of the sea state, a statistical measure of the roughness of the ocean. There is theoretical evidence that other parameters of interest can also be deduced from waveform analyses. Until now, efforts to accomplish this have been hindered by a lack of knowledge about the microscale scattering properties of the sea surface. Radar theory holds that microwave scattering is mainly accomplished by properly oriented facets on the wavy surface that are of a size comparable to the radar wavelength (i.e., in the 1 to 5 centimeter wavelength range). The location of these features in relationship to the wave crests and troughs has not been known previously.

Recently, a capability to simultaneously measure backscattered power and range in a controlled laboratory wave tank environment has been developed. This unique radar instrument features a 0.43 m diameter dielectric lens that focuses the radiation into a 1.5 cm diameter illuminated spot on the surface. This produces high resolution for examining the 10 to 50 cm wavelength water waves generated in the tank. Ranging is accomplished via a phase comparison between the reflected signal and a reference signal. A range resolution of about 1 mm is derived by use of the delta-K modulation technique, and an unambiguous range interval of 31.25 cm results from the use of a 480 MHz if signal. Both 13.5 and 35.0 GHz operation is possible.

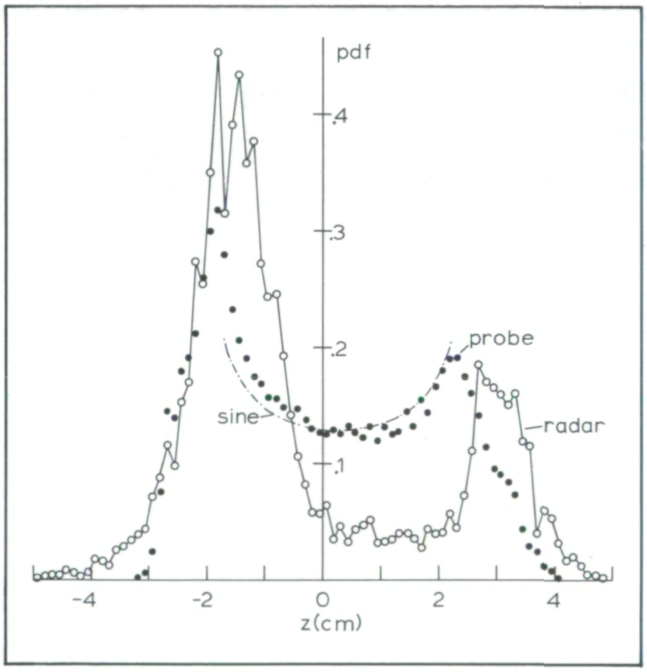

Probability density functions measured by a focused-beam radar and a capacitance probe for a 1.25 Hz sinusoidal wave field in the wind-wave tank facility.

The figure shows a typical experimental result using this radar set. The tank's mechanical wave generator was set to produce a 1.25 Hz sine wave of substantial amplitude. The radar probability density function (pdf) shows that the microwave instrument's backscattered signal was primarily the result of scattering from the troughs (negative range) and the crests. The troughs were clearly dominant; virtually no return was detected from the regions of high slope. A conventional capacitance probe, on the other hand, produced data that closely matched the pdf expected from a sinusoidal waveshape. The departure from the expected form suggests that the wave troughs were broader than were the crests, which is reasonable for a water wave that has propagated about 16 m down the tank.

These results are reasonable and consistent with expectations. Studies are underway to determine the distribution of scattering facets for various mechanically- and wind-generated wave fields. In turn, the results will be factored into radar altimeter waveform analyses. The goal will be to find out if new remote measurements of oceanographic parameters such as water wavelength can be extracted from altimeter-measured waveforms.

Contact: Chester L. Parsons
Code 670

Sponsor: Office of Space Science and Applications

AIRBORNE LIDAR STUDIES OF AIR-SEA INTERACTIONS

The planetary boundary layer (PBL) is the important link between the oceans and the free atmosphere. The atmospheric PBL along with the ocean mixed layer act as controlling influences on the surface flux of momentum heat and moisture. Knowledge of the structure of the PBL and vertical mixing processes can prove valuable in understanding this link.

Organized convection plays an important role in vertical motion and transport in the PBL. Woodcock's (1942) observation of the soaring characteristics of sea gulls was an early indication that convection frequently is organized into cellular and/or long linear patterns. It was obvious that these features had coherence in the vertical and occupied much of the PBL depth. Satellite-acquired images of clouds obtained in the early 1960's demonstrated that the convective patterns, made visible by cloud condensation, were prevalent around the globe.

An airborne downward looking lidar system has been used to observe organized cellular convection in the PBL. The cells, several kilometers in diameter, have been interpreted as consisting of central updrafts extending to the top of the PBL with compensating downdrafts around their periphery. Lidar (light detection and ranging) is able to visualize the cells due to sharp light scattering discontinuities associated with the updrafts containing moist aerosol-laden air compared with otherwise clean dry air aloft.

The research has demonstrated that an airborne lidar can provide a unique observation of the PBL structure showing both microscale (few kilometers) and mesoscale (tens of kilometers) variation of the PBL top. The lidar data shown as constant backscatter insopleths in the figure clearly provide a visual indication of the presence of vertically organized convective cells. The convective elements were determined to have aspect ratios (width to height) of 1.7 to 3.3 with 3.3 representing the most fully developed convection. This is in agreement with previous investigations of organized convection. Comparisons of the lidar-derived PBL structure were made with both a conceptual model of the PBL and recent laboratory simulations of a developing convective PBL. The comparison showed that the observations are consistent with a model of mixing in the PBL consisting of a field of organized updrafts separated by downdrafts. The entrainment rate at the PBL top inferred from the lidar data was found to be greater than expected when compared with laboratory measurements, and it was postulated that the difference was due to wind shear at the interface between the PBL and free atmosphere. Wind shear was also suggested as a possible controlling influence on convective cell spacing.

The study concluded that an airborne downlooking lidar is a powerful diagnostic tool for investigating the structure and dynamics of the PBL and for detailed studies of air-sea interactions. Also, that the PBL is highly variable on scales ranging from a few kilometers to several tens of kilometers, and therefore conventional soundings may be inadequate in describing its structure. Finally, the

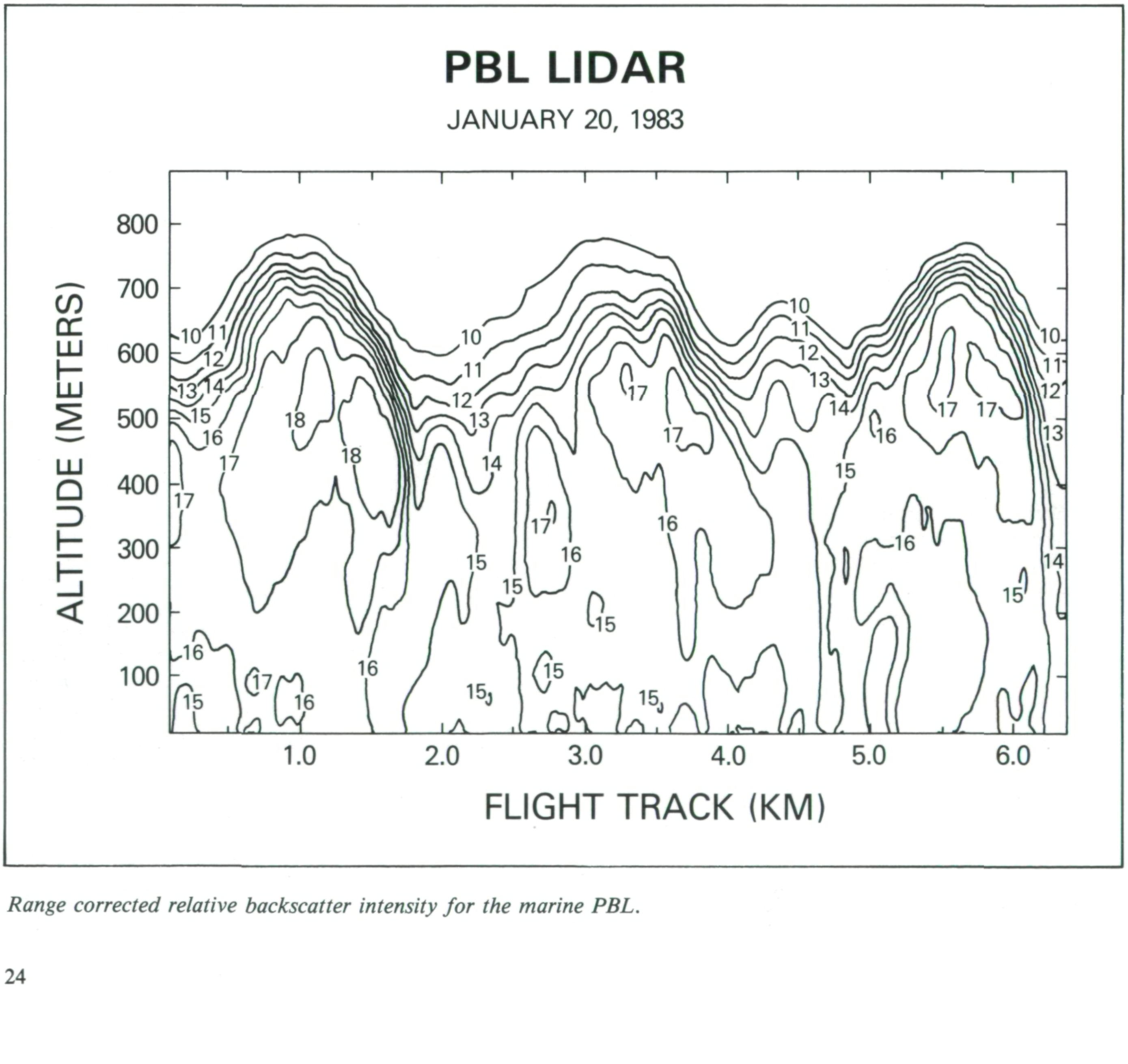

Range corrected relative backscatter intensity for the marine PBL.

presence of wind shear at the PBL top may be important in both determining entrainment rate and in controlling the horizontal size and spacings of organized convective cells.

Contact: Dr. S. H. Melfi
Code 670

Sponsor: Office of Space Science and Applications

ATMOSPHERES

CLIMATE RESPONSE TIME

The time required for the climate at the Earth's surface to adjust to a change in climate forcing (e.g., a change of solar irradiance) is a fundamental characteristic of climate which must be understood if we are to analyze successfully past climate change and predict future climate. Knowledge of the climate response time is particularly important today, in view of known and potential anthropogenic forcings of the climate system.

The upper layers of the ocean are the principal source of thermal inertia, and it has generally been assumed that they delay full climate response by of the order of a decade. Such a response time is sufficiently long to severely dampen the climate effects of a short-term perturbation, such as that due to aerosols from a single volcanic eruption, but not to substantially delay the greenhouse warming of the CO_2 which has been added gradually to the Earth's atmosphere over the past 130 years.

The climate modeling group at the Goddard Institute for Space Studies has investigated the factors which determine the climate response time using simple models and scaling statements. The results show that the response time is particularly sensitive to the amount that the climate response is amplified by feedbacks and to the representation of ocean mixing.

A chief implication of this information on the climate response time is that, if the equilibrium climate sensitivity is 3 °C or greater for a doubling of atmospheric CO_2, then most of the expected warming due to trace gases added to the atmosphere by man probably has not yet occurred. This is shown in the figure, based on calculations for which it was assumed that CO_2 increased linearly from 270 ppm in 1850 to 315 ppm in 1958 and thereafter, as observed by Keeling.

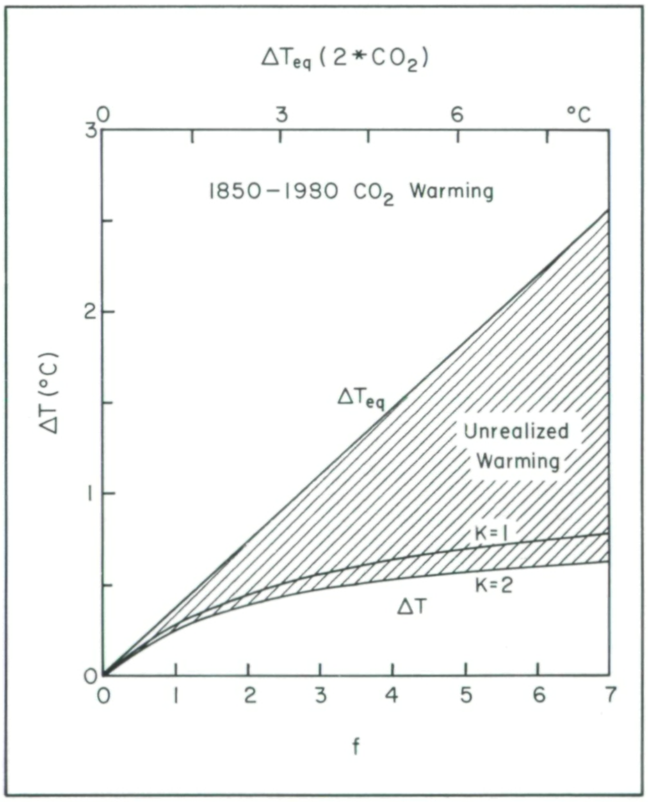

Ocean surface warming (ΔT) and the equilibrium warming (ΔT_{eq}) due to CO_2 added to the atmosphere in the period 1850 to 1980 for a 1-D box diffusion ocean model as a function of climate feedback factor, f, or climate sensitivity to doubled CO_2, ΔT_{eq} ($2{*}CO_2$). k, in $cm^2\ s^{-1}$, is the diffusion coefficient beneath the ocean mixed layer.

The potentially large amount of unrealized warming complicates the CO_2 and trace gas issue and limits the near-term effectiveness of reductions in greenhouse gas emissions. It calls into question a policy of "wait and see"

and "if necessary, make midcourse corrections" regarding the question of how to deal with increasing atmospheric CO_2 and other trace gases.

The strong dependence of the unrealized warming on equilibrium climate sensitivity emphasizes the importance of narrowing uncertainties about the strength of climate feedback processes. This will require better understanding of many components of the climate system including clouds, the cryosphere, biogeochemical cycles, ocean mixing, vegetation, and the land surface.

Contact: Dr. James E. Hansen
Code 640

Sponsor: Office of Space Science and Applications

ICE AGE TERRESTRIAL CONDITIONS AND CLIMAP SEA SURFACE TEMPERATURES: A GENERAL CIRCULATION MODEL INVESTIGATION

Paleoclimate sea surface temperatures are estimated by retrieving fossils from ocean sediments and relating the species distribution to a temperature distribution. This procedure has been employed by Climate Long Range Investigation Mapping and Predictions (CLIMAP) to determine ocean temperatures for 18,000 years ago, at the peak of the last ice age. The reconstructed temperature field indicates that low-latitude ocean temperatures were as warm as or slightly warmer than those which exist today. This primary conclusion has lent support to the concept that low-latitude temperatures are relatively insensitive to climate change.

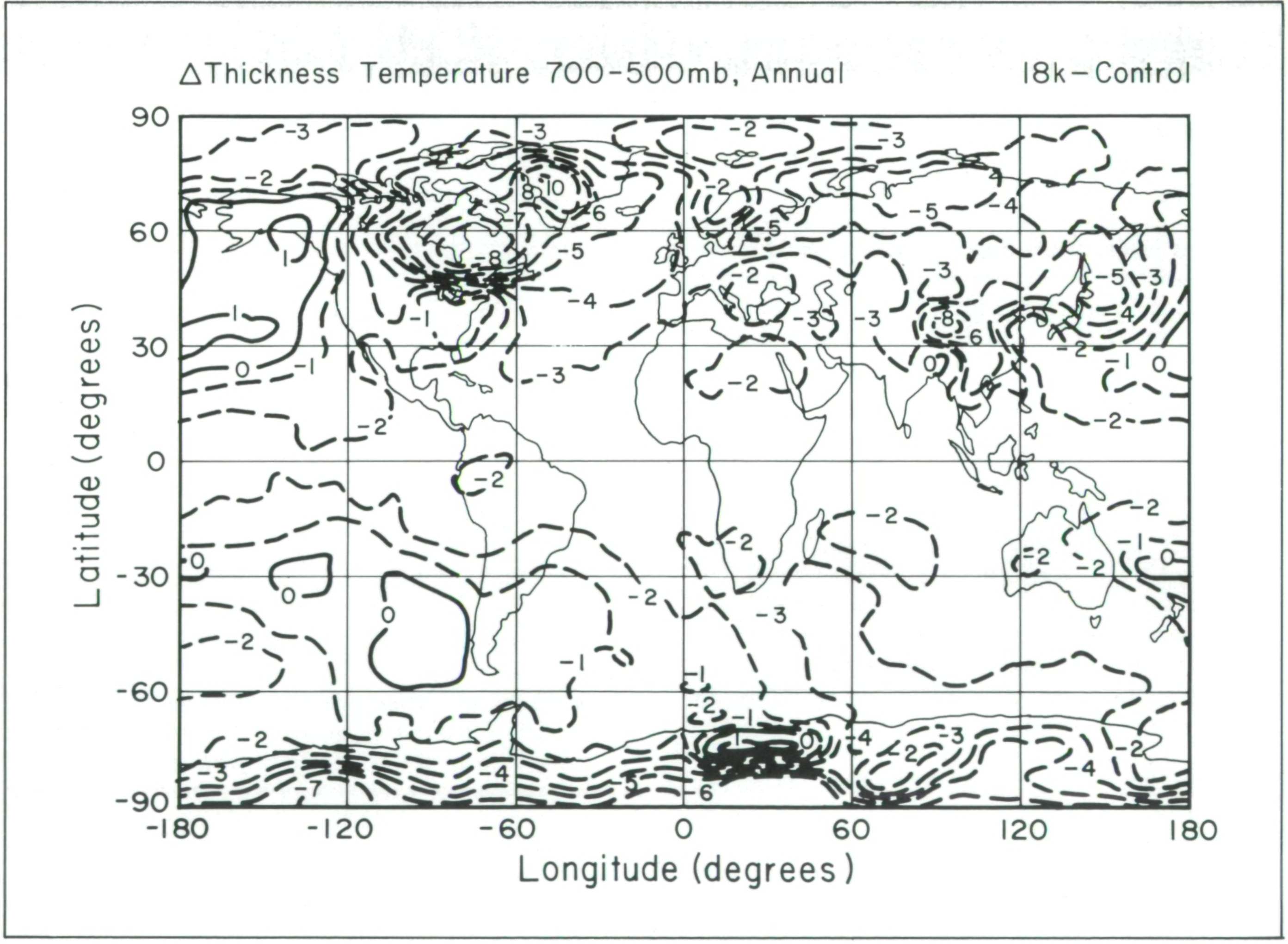

Change in the annual mean (thickness) temperature of the 700-500 mbar layer, which represents 4.5 km altitude from 30°N to 30°S, 18,000 yr B.P. climate — control.

Over the past 20 years there have been numerous investigations of terrestrial conditions at low and subtropical latitudes during the last ice age. Both glacial and palynological studies seem to imply that temperatures over land at heights of approximately 2 to 5 km were cooled by about 5 to 6 °C at a wide variety of locations.

Are these two lines of evidence consistent? Is it possible that warm ocean surface waters and substantial continental temperature depression were both characteristic of the last ice age at low latitudes? To explore this question, the GISS global climate model was run with the ice age boundary conditions, including the CLIMAP estimated sea surface temperatures, and the results over land were compared with those deduced by the glacial and pollen studies (Rind and Peteet). At the four widely dispersed locations studied in detail, Hawaii, Columbia, East Africa, and New Guinea, the model did not produce the magnitude of cooling implied by the terrestrial evidence. As shown in the figure, the model-generated cooling was at most half the nominal 5 to 6° estimate. With the CLIMAP sea surface temperatures, the modeled ice age climate was 3.6 °C colder than the current climate; to reproduce the terrestrial evidence the sea surface temperatures had to be reduced by an additional 2 °C, making the ice age climate 5 to 6° cooler, and implying a greater climate sensitivity. There thus appears to be an error or misinterpretation in either the model, the terrestrial data set, or the CLIMAP sea surface temperatures. As the questions of climate sensitivity and of the relative sensitivity of low and high latitudes are central to the estimation of the rapidity and size of future climate changes, the topic deserves especially close scrutiny.

Contact: Dr. David Rind
Code 640

Sponsor: Office of Space Science and Applications

OPTIMAL WEIGHTING OF DATA TO DETECT CLIMATIC CHANGE

Predictions of climatic change are necessarily probabilistic in nature, since incomplete knowledge of initial conditions of the atmosphere and limitations of atmospheric models prevent detailed predictions of the day-to-day evolution of the atmosphere beyond a few weeks. Detection of predicted climatic changes is not easy, because the changes are small compared with the day-to-day variability of atmospheric variables; but it is important to do it as effectively as possible, in order to verify our understanding of what affects the climate, and, in the case of the predicted "greenhouse effect" due to increasing carbon dioxide and other trace gases in the atmosphere, to provide concrete evidence of the change as early as possible. It is only by averaging data over time and space that the unpredictable variability (referred to as "climate noise") can be reduced enough for there to be a chance of seeing the predicted changes ("climatic signal"). But how should the averaging be done?

A method of averaging atmospheric data has been developed that is optimal for detecting a given climatic signal. The method is well known in the statistical literature, but has not been developed when the time span of data prior to the change is short, as is often the case with satellite data. These problems have now largely been solved.

To test the method, it was used to try to detect the climatic effects attendant on the eruption of the volcano El Chichón in Mexico in 1982. Climate models predicted that, in the absence of other anomalous influences on the climate, average surface temperatures should fall 0.2 to 0.5 °C over the globe during 1983. Since one of the explanations for our failure to see clear signs of the greenhouse effect on surface temperatures has been the confusing effect of intermittent volcanic eruptions, this seemed an ideal opportunity to verify quantitatively our understanding of how a well documented volcanic eruption affects surface temperatures. It was found that if the only climatic signal occurring during 1983 had been El Chichón's, the optimal weighting method would have increased our chances of seeing the signal from 2 out of 3, to 3 out of 4, when compared with conventional methods of detecting the cooling: the detection method works well, in principal.

However, average surface temperatures actually *rose* globally to unprecedented levels in 1983, and no signs of the volcanic cooling were observed. This was presumably due to the simultaneous occurrence of an unusually strong El Niño/Southern Oscillation (ENSO) episode during 1982/83. Ability to predict the extratropical effects of ENSO events is unfortunately not yet well developed, and so the ENSO and volcanic effects in 1983 cannot be disentangled with any confidence. Verification of our understanding of volcanic effects on climate will therefore have to await progress in understanding the ocean's influence on global climate, or another strong volcanic eruption in a less eventful year.

Contact: Thomas L. Bell
Code 610

Sponsor: Office of Space Science and Applications

REMOTE SENSING OF WEATHER AND CLIMATE PARAMETERS FROM TIROS-N SATELLITES

HIRS2 and MSU are the 20-channel infrared and 4-channel microwave passive sounders on the operational low-Earth orbiting satellites. They monitor emission arising primarily from the Earth's surface and the atmosphere up to the midstratosphere. These, together with the SSU, a 3-channel pressure modulated infrared radiometer, which monitors emission from the mid and upper stratosphere, comprise the TIROS Operational Vertical Sounder (TOVS) system. The TOVS data are analyzed operationally by NOAA NESDIS to produce vertical temperature-humidity profiles using a method based primarily on statistical regression relationships between observed radiances and atmospheric parameters.

HIRS2 and MSU data are analyzed at the GSFC Laboratory for Atmospheres in a research mode using a direct physical inversion method. In this approach, atmospheric and surface conditions are found which, when substituted in the appropriate radiative transfer equations, give rise to values consistent with the observed radiances. The parameters currently determined are global atmospheric vertical temperature-humidity profiles and total ozone burden, sea or land surface skin temperature, fractional cloud cover and cloud top pressure, and ice and snow cover.

Recent verification studies have centered on the accuracy of retrieved sea-surface temperatures and cloud parameters. Detailed studies show rms errors of monthly mean sea-surface temperatures, averaged over a $2° \times 2°$ grid, to be lower than 0.5 °C compared to ship measurements. In all cases, the rms errors were lower than those obtained using climatology as a guess, which sometimes is as low as 0.35 °C, and the anomaly correlations were all better than 0.6, even for every small anomalies.

Cloud fraction and cloud top pressure, for up to two cloud layers, are retrieved from infrared data at 125 km spatial resolution. Comparison of retrieved single day fields with visible (1 km resolution) and infrared (8 km resolution) geostationary imagery from GOES not only shows excellent consistency of all features, but also gives detailed cloud top pressure information not easily obtainable from the imagery. In addition, the use of IR only data allows for accurate cloud field determination day and night. Monthly mean zonally averaged cloud fraction and cloud top pressure are shown in the first figure for June 1979. The location of the intertropical convergence zone at 8 °N is clearly observed. The global mean

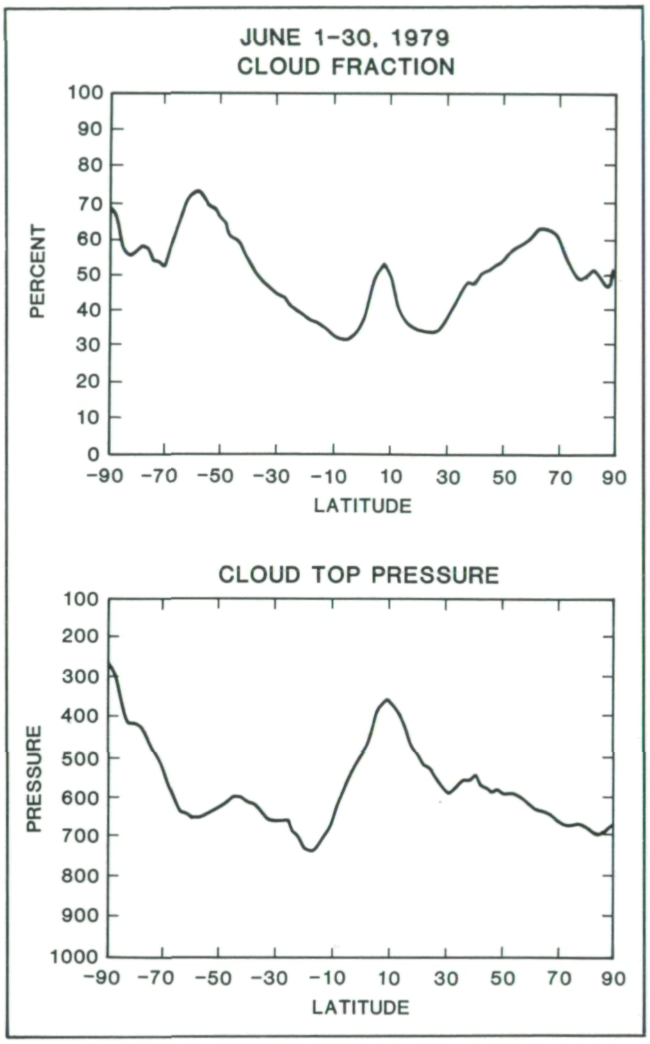

Zonal mean cloud fraction and cloud top pressure for June 1979 retrieved from HIRS/MSU sounding data. The global mean cloud fraction is 47 percent, and the global mean cloud top pressure is 580 mb.

effective cloudiness (cloud fraction times cloud emissivity) is 47 percent, and the average cloud top pressure is 580 mb. The effective cloud fraction is somewhat less than the "true" cloudiness because thin clouds such as cirrus clouds have emissivities less than 1. The effective cloud cover is the appropriate value for computing outgoing long-wave radiation from the Earth's atmosphere.

Experiments assimilating GLA temperature retrievals into the GCM have resulted in improved forecasts both with respect to those generated using no satellite data and those which had the benefit of operational NESDIS retrievals. The second figure (a) shows the anomaly correlation coefficient for an ensemble of 1- to 5-day forecasts from May

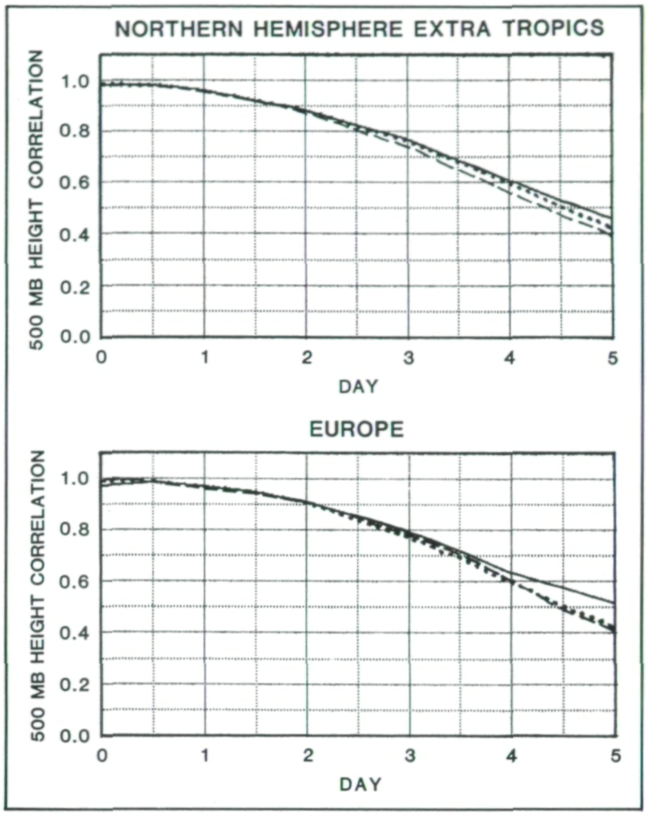

Ensemble 500 mb height anomaly correlation coefficients for Northern Hemisphere extratropics and Europe. Solid for forecasts with GLA retrievals, dotted for forecasts with NESDIS retrievals, and dashed for those with no satellite data.

1979 verified over the Northern Hemisphere extratropics. Useful predictability is associated with a correlation coefficient of 0.6 or greater. It is observed that use of the GLA retrievals improves forecasting skill by about 6 hours on the average. Similar results are shown in (b), verified only over Europe. The improvement in the Southern Hemisphere, which has much less conventional data, is the order of 2 1/2 days of forecasting skill. We are currently investigating the impact of assimilation of humidity profiles, sea-surface temperatures, and cloud fields into the GCM, to further improve forecasts and also to improve diagnostic quantities such as computed latent heat flux.

The European Centre for Medium Range Weather Forecasting (ECMWF) has requested that GLA process all of the FGGE year, December 1978 - November 1979, for their use in an improved FGGE year analysis. Currently, May, June, and July of 1979 have been processed and sent to ECMWF. Preliminary assessment of the GLA retrievals by ECMWF shows improved temperatures and humidities compared to the operational product, which constituted the original FGGE data base. ECMWF also plans to use the GLA-derived cloud fields and diurnal variation of ground temperatures, which is related to soil moisture, to help verify their model parameterizations.

Contact: Joel Susskind
Code 610

Sponsor: Office of Space Science and Applications

MODELING STUDIES OF THE ATMOSPHERIC RESPONSE TO TROPICAL SST ANOMALIES

Considerable progress is being made in understanding the atmosphere's response to anomalies in tropical sea-surface temperatures (SST's). The response appears to be quite large in the tropics, and evidence is mounting that there may also be a significant remote response that affects weather patterns in middle latitudes. Ocean surface temperature anomalies change relatively slowly, and there is some potential predictability in simply knowing how the atmosphere is affected by observed SST's. But even more important, the atmosphere may not be just passively responding to SST anomalies, but changing the surface winds so as to enhance and maintain them. Thus, the connection between SST anomalies and changes in surface winds may be a crucial leg in the feedback processes affecting the interannual variability of the tropical ocean/atmosphere.

Recent work at Goddard has sought to study this connection through detailed atmospheric modeling. Two long integrations of an atmospheric general circulation model (GCM) were performed. In the first, SST's were prescribed at normal values, including their normal seasonal change. In the second, the SST's were prescribed as the same normals *plus* the pattern of anomalies observed in the tropical Pacific during the 1982/83 El Niño event. This pattern is shown on the left panel of the figure. On the right panel is a sampling of computed atmospheric response. The model showed many of the anomalous patterns observed in the atmosphere during the fall and winter of 1982/83. In particular, it shows much heavier than normal rainfall in the central and eastern tropical Pacific and associated changes in surface winds. These wind changes supply the moisture for the additional precipitation and are qualitatively as one expects would drive the ocean currents to maintain the SST anomaly that produced them.

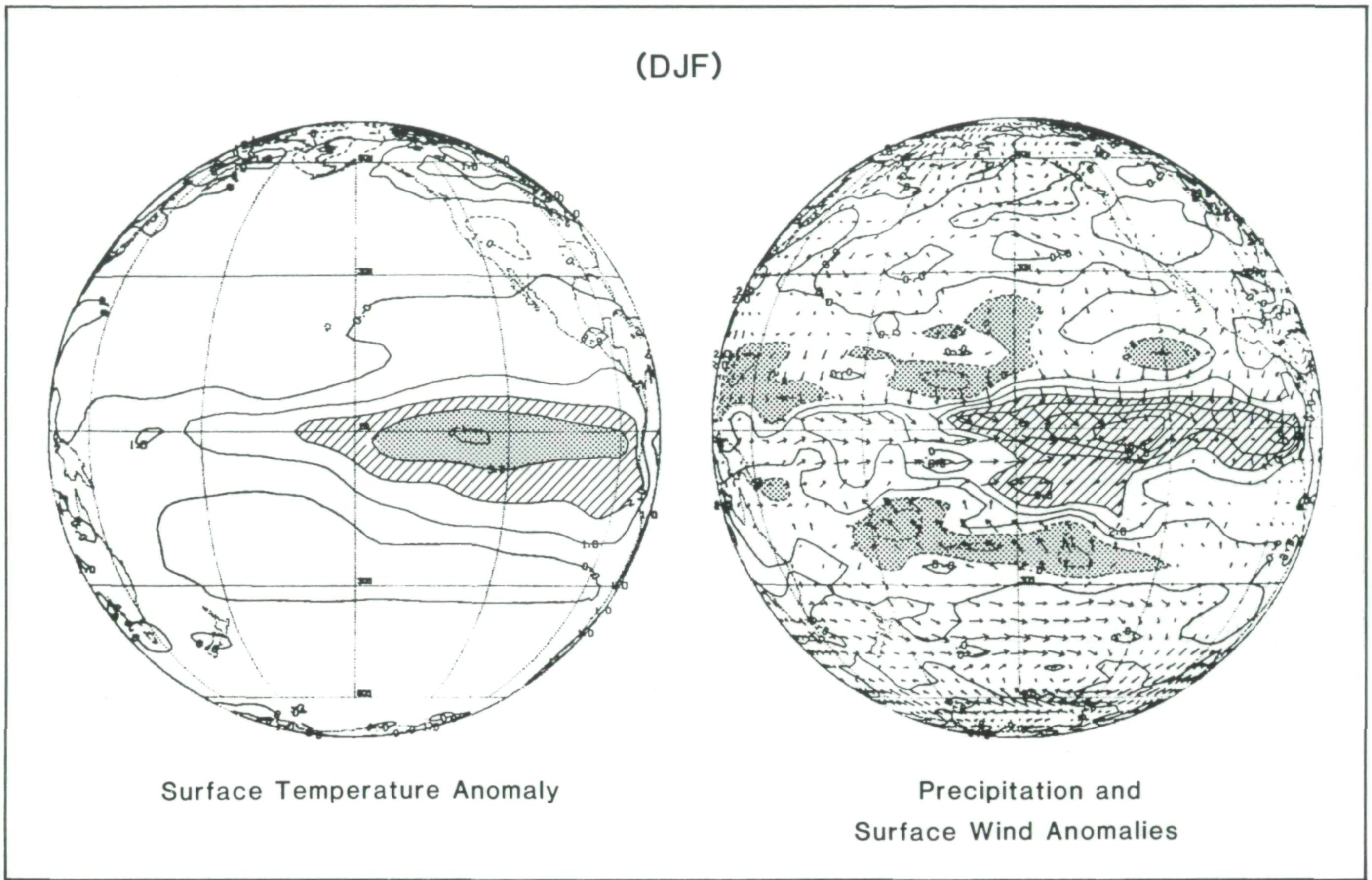

Left panel: Observed sea-surface temperature (SST) anomalies during the winter of 1982/83. Right panel: Atmospheric model's response to the SST anomalies. Arrows are vector wind differences between a case with and a case without anomalies. In shaded regions rainfall decreased when the anomaly was introduced, and in hatched regions it increased.

The results suggest this crucial link between ocean and atmosphere is sufficiently well simulated by the GCM to attempt large-scale ocean/atmosphere coupled simulations of the whole phenomenon.

Contact: M. Suarez
Code 610

Sponsor: Office of Space Science and Applications

EXTENDED-RANGE PREDICTION OF HEAT WAVES AND DROUGHT

A diagnostic study and numerical experiments are being conducted with the Goddard Laboratory for Atmospheres (GLA) fourth-order general circulation model in order to study the initiation, maintenance, and decay of heat waves, as well as the predictability of such events. This has consisted of: 1) an analysis of the wave structure associated with the severe summer 1980 heat wave and a comparison of this wave structure with climatology and with other anomalous years, 2) the development of an index for the diagnosis of heat wave patterns using 500 mb geopotential height analyses, and 3) numerical experiments to test the predictability of the initiation, maintenance, and decay of this heat wave and the sensitivity of the model predictions to anomalous sea-surface temperature and soil moisture patterns.

Current operational nondynamical prediction methods all failed to forecast the summer 1980 heat wave, which produced $16 billion in economic losses and caused nearly 1300 deaths in the United States. To test the model's accuracy in forecasting the initiation of the heat wave, extended-range (130-day) predictions for the summer of 1980 were generated from May 15, 1980 initial conditions. These experiments showed skill in predicting 10-day averages of a heat wave index for 50 days and 30-day

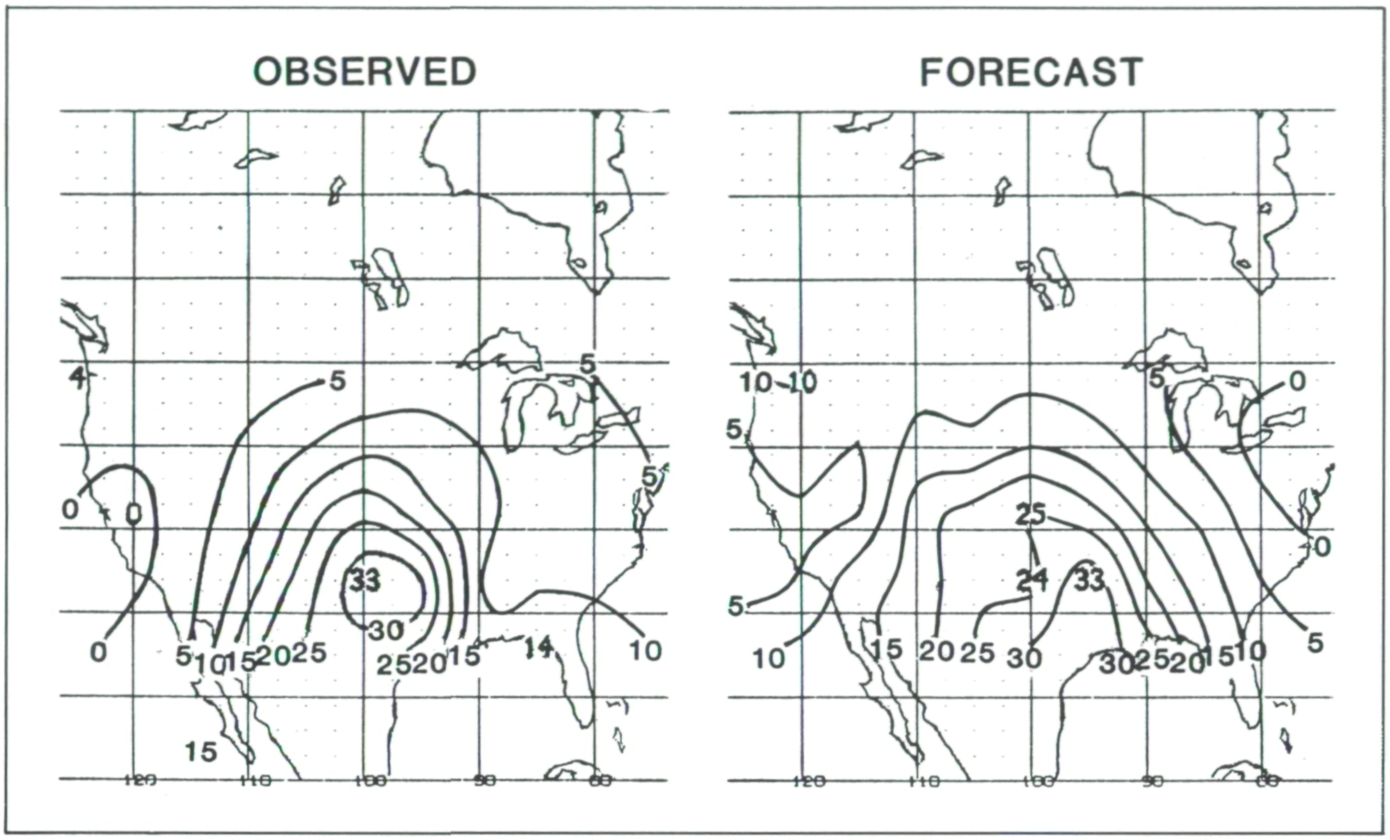

Observed and model predicted (from May 15, 1980 initial conditions) heat wave persistence index values for July 1980.

averages of the heat wave pattern for June and July of 1980. In addition, the experiments indicated that sea-surface temperature anomalies contributed to the initiation of the heat wave over the southern Great Plains.

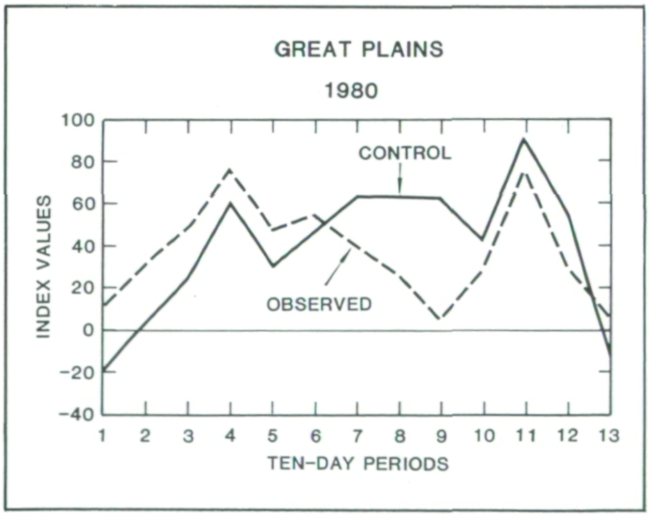

Observed and model predicted heat wave index values for May 15 to September 22, 1980.

Five 10-day numerical integrations with three different specifications of boundary conditions were carried out to study the maintenance of the heat wave. These experiments showed that soil moisture anomalies contributed to the persistence of heat wave once it was established over the Great Plains.

A series of shorter-range model integrations revealed the dynamics of the breakdown of the heat wave pattern and demonstrated the role of orography and lee cyclogenesis.

The results of these experiments indicate the possibility for current numerical models to forecast the occurrence and severity of heat waves more than 1 month in advance. The robustness of these results with respect to changes in initial conditions is currently being investigated.

Contact: Dr. Robert Atlas
Code 610

Sponsor: Office of Space Science and Applications

SURFACE RADIATION IN THE TROPICAL PACIFIC

Atmospheric and oceanic circulations are ultimately driven by solar radiation and modulated by orography and the rotation of the Earth. On the other hand, solar radiation is affected by clouds and other meteorological parameters, which are themselves dependent upon the general circulation of the atmosphere and oceans. Radiation is therefore an important component that causes the climate either to fluctuate or to maintain its current state.

A data set of monthly surface radiative fluxes in the tropical Pacific for the period from January 1970 to February 1978 has been created for studying the role of surface radiation in the tropical atmospheric circulation, such as the Southern Oscillation and El Niño. The efficient radiative transfer package developed at the Laboratory for Atmospheres/GSFC, which includes detailed treatments of the molecular and droplets absorptions and of the surface and cloud reflections, is used to compute solar and thermal radiation at the surface. The input data to the radiation package are surface measurements from the National Climatic Center, climatological temperature and humidity profiles from the National Center for Atmospheric Research, and cloud cover from the University of Hawaii.

As illustrated in the figure, results of the calculations show that the distribution of surface radiation follows

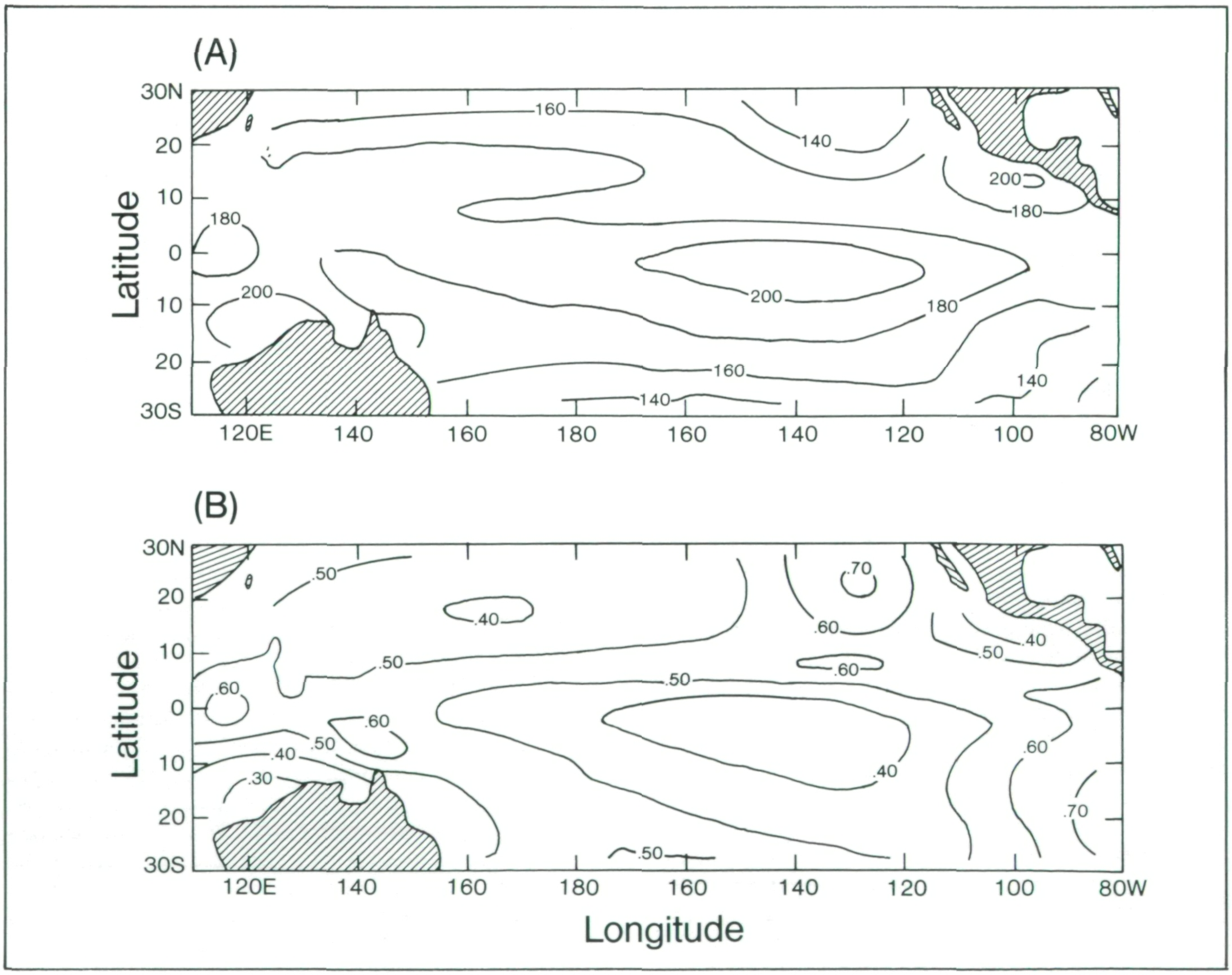

Annually-averaged absorption of solar (above) and loss of thermal infrared radiation (below) in the tropical Pacific for the period 1970-78. Units are in W/m^2.

closely that of cloudiness and, to a lesser extent, that of humidity. Surprisingly, the distribution of IR radiation can hardly be correlated to the surface temperature. The sensitivity of surface radiation to input data has also been studied. Based upon the expected range of uncertainties in the input data, the rms error in the calculated net surface radiation is estimated to be ~ 15 Wm^{-2} with the largest contributions from the uncertainties in cloud cover and humidity. This number is comparable to the interannual variation of the monthly net surface radiation, indicating a need to improve the quality of input data. The results of the sensitivity study can be used as guides for specifying the accuracy requirements for deriving atmospheric and cloud parameters from satellite measurements. In order to resolve the interannual variation of surface radiation, the accuracy of satellite retrievals should be within 2°C in temperature, 15 percent in specific humidity, 300 mb in cloud height, 0.05 in fractional cloudiness, and 50 percent in cloud optical thickness.

Contact: Dr. Ming-Dah Chou
Code 610

Sponsor: Office of Space Science and Applications

LIDAR OBSERVATIONS FROM A HIGH-ALTITUDE PLATFORM

A basic problem of passive remote sensing of the atmosphere is the difficulty in resolving the vertical structure of the atmosphere. For that reason the addition of active measurements such as lidar to passive observations can improve remote sensing interpretations. For the past several years, a remote sensing experiment has been flown on a high-altitude NASA aircraft, the ER-2 (U-2), that involves passive visible, infrared, and microwave observations in conjunction with an active lidar sensor. The lidar operation from a high-altitude aircraft serves as a test for problems, both technical and data interpretation, that would be associated with a satellite lidar experiment. The science objective of the aircraft experiment has primarily been the study of cloud remote sensing. An outstanding problem for passive cloud observations is the correct interpretation of thermal radiance measurements. The emitted radiance is a function of the cloud top height and also the existing atmospheric temperature profile and emissivity structure of the cloud top. Two examples may be given of research problems for which knowledge of the height-emissivity structure of cloud tops is important. Attempts have been made to apply satellite infrared observations for studies of the evolution of severe storm systems. Correct dynamical interpretations are possible only if cloud top emissivity effects are known. The second example is the climate influence of cirrus clouds. The radiative effect of cirrus may be either toward warming or cooling as a function of the height, temperature, optical thickness, and emissivity relationships. A direct inference of the cloud emissivity effects is possible from combined lidar and radiometer observations.

Overflights of high clouds, both cirrus and thunderstorms, have been made with the NASA ER-2 aircraft, most recently in May 1984. The cloud lidar system (CLS) and the multispectral cloud radiometer (MCR) have been on board the aircraft. The CLS is a fully automated lidar which incorporates a 150 mJ Nd:YAG laser and an 18 cm receiver. In order to accommodate the large dynamic range and fast spatial response of return signals, the lidar signals are compressed by three decade logarithmic amplifiers and are digitized at a 7.5 m range resolution. The airborne observations are such that a backscattered lidar return signal is received only in the nadir direction and at approximately every 70 m along the aircraft flight path. Both the signal intensity at two wavelengths and the signal depolarization are obtained. The MCR provides radiance measurements at 11.0 μm in the thermal infrared and at selected visible and near infrared wavelengths. The MCR scans cross track to the aircraft flight path and measures radiance to 45 degrees off nadir. The nadir pixel observation is precisely synchronized both in time and direction to the lidar signal return. The lidar signal and the nadir radiance measurement thus both correspond to the same cloud top area.

The analysis of the thermal radiance based on the lidar return data is possible since the thermal emission and the lidar return are dependent on vertical structure of the cloud particle density. The lidar return is a function of the backscattering cross section profile times the attenuation from transmission into the cloud. Multiple scattering serves to reduce the attenuation factor. The initial procedure of the combined analysis is a correction of the backscatter return signal for the apparent attenuation. The assumption must be made that the optical characteristics of the cloud particles are constant with altitude. The relative density into the cloud will be then proportional to the backscatter profile. A constant factor which relates the lidar backscatter cross section to the thermal absorption cross section may then be derived. The actual solution is an iterative procedure. The emitted radiance is found directly from the absorption cross section profile and the assumed vertical temperature structure.

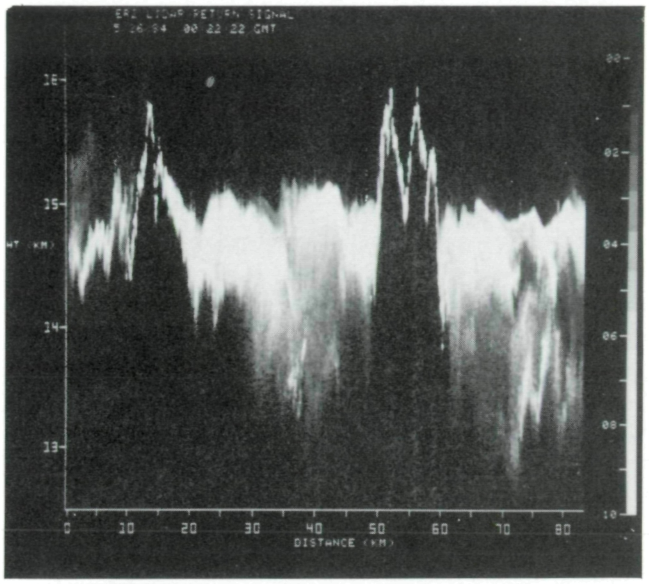

Lidar return from a severe storm top.

The accompanying figure shows an example of the lidar return data from a flight line over a severe storm system of tornadic intensity. There are two penetrating cells where a very strong lidar return is rapidly attenuated. The convective cells are surrounded by a diffuse anvil structure where return signals are received from several kilometers into the cloud. The coldest temperatures are at the location of the over-shooting cells. The combined analysis of the lidar and thermal observation as described were applied to the measurements along the flight line. Near the beginning of the flight line, the overlying cirrus was found to give rise to a warmer region. However, the particle density at the top of convective cells penetrating the tropopause is found to be such that the observed brightness temperature gives an accurate measurement of the cloud top temperature. For the diffuse areas between the cells, the equivalent temperature is a function of emission from an extended depth of the cloud top. Since the tropopause is near 14 km and the cloud top is above 15 km, colder equivalent blackbody temperatures are observed than would be indicated by only the cloud top height. These results may be applied to give a clearer dynamical interpretation from satellite observations of storm systems. A similar analysis has been applied to cirrus and other clouds for applications involving atmospheric radiation studies.

Contact: Dr. James D. Spinhirne
Code 610

Sponsor: Office of Space Science and Applications

ATMOSPHERIC AEROSOL PROPERTIES MEASURED FROM SATELLITES

Methods are being developed to derive atmospheric aerosol properties from the radiance of sunlight scattered to a satellite by the Earth-atmosphere system. The method used here is to relate the aerosol properties to the radiance by means of radiative transfer models that depend partially on assumptions of aerosol optical properties. Therefore, the satellite radiometer signals transmitted to the Earth require calibration, but no postlaunch calibration existed for the radiometers used in this study: the visible channel of the Visible Infrared Spin-Scan Radiometer (VISSR) carried by Geostationary Operational Satellites and by the visible and near infrared channels of the polar orbiting Advanced Very High Resolution Radiometer (AVHRR). The calibration depends on the very stable source of Rayleigh scattering by the atmospheric gas above the ocean with weak reflectance. The success of the method is shown by the stability of the calibration parameters for VISSR during three summers and by the accuracy of VISSR measurements of the aerosol optical thickness measurements.

Several investigators have derived the aerosol optical thickness over oceans from satellite measurements. The aerosol optical thickness is nearly linearly proportional to the radiance of the reflected sunlight. Deriving the optical thickness over land is difficult because of higher surface reflectance and variability. The land reflectance can be monitored with an accuracy of 0.01, however, by satellite measurements on cloudless days with small aerosol optical thickness, resulting in an optical thickness error of about 0.1 on hazy days. A comparison of aerosol optical thicknesses measured by VISSR (λ610 nm) and those derived from solar transmission measurements at the ground of five locations in the eastern part of the United States is given in the figure. One thousand regression lines for these measurements were computed by the bootstrap statistical method. The dashed lines on the figure include 68 percent of the regression lines and the mean value. The square of the mean correlation coefficient is 0.89, indicating the good accuracy of the calibration method and satellite measurements of aerosol optical thickness over land.

The aerosol mass is linearly proportional to its optical thickness for some air masses such as for the stagnant air that occupies the eastern third of the United States during the summer. Under such conditions, the aerosol mass can be mapped. With the aid of wind data the aerosol mass divergence and transport can be calculated.

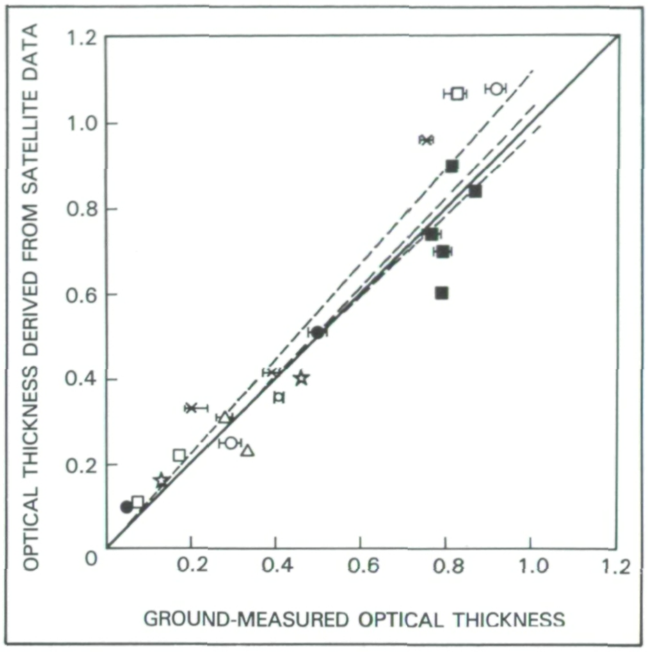

Comparison of VISSR and ground-based measurements of aeorsol optical thickness at 1400 GMT during the summers of 1981 and 1982 at five locations in the eastern United States. The three dashed lines include 68 percent of the regression lines and their mean.

Aerosol absorption is an important parameter in climate studies and for the effect of the atmosphere on Landsat investigations. Estimates of aerosol absorption from satellite measurements are based on the physical principal that an increase in aerosol amount results in increased radiance of scattered sunlight over dark surfaces but decreased radiance over bright surfaces, for example, where the surface reflectance exceeds 0.4. Thus, at some intermediate surface reflectance the radiance is insensitive to the aerosol optical thickness. The aerosol absorption is sensitive to such critical reflectance, at least if the absorption is less than 0.2 of the total aerosol extinction. As an example of one series of measurements, the absorption of smoke over Washington, D.C., from forest fires in northwestern Canada was estimated as 0.1 from Landsat measurements. No aerosol absorption data are known to exist for validating the satellite estimates.

Hence, validation was made with a laboratory experiment by Mekler and the authors to simulate radiative transfer within the Earth-atmosphere system. Latex spheres were suspended in water above two surfaces, one with low and the other with high reflectance. This system was illuminated by a solar simulator and absorption of the hydrosol was derived from the radiance of the reflected light. The absorption error was 0.02 when the absorption was less than 0.1, and 0.03 for absorption between 0.1 and 0.4. Such accuracy is comparable to that resulting from more direct laboratory measurements of aerosol absorption.

Another aerosol parameter, such as their mean size, can be estimated from satellite measurements of aerosol optical thickness in two wavelengths. There are relatively more small particles of tenths of a micron size than larger particles, if the optical thickness decreases with wavelength in the visible-near infrared spectrum. This principal was tested by applying it to AVHRR measurements near the Barbados Islands, where Langley Research Center personnel measured a vertical profile of the distribution of aerosol mass as a function of their size where AVHRR measurements were taken. Both the satellite and aircraft measurements of the geometric mean radius of Saharan dust were 0.9-μm, and the measured columnar masses agreed within 20 percent. Such close comparisons are based on only one aircraft profile. Additional independent measurements of aerosol absorption, mass, and size are required to validate the promising satellite techniques.

Contact: Robert S. Fraser and Yoram J. Kaufman
Code 610

Sponsor: Office of Space Science and Applications

MESOSPHERE-STRATOSPHERE-TROPOSPHERE GENERAL CIRCULATION MODEL

A grid-point global atmospheric general circulation model, extending in altitude from the Earth's surface to 90 km, has been constructed to study the circulation of the middle atmosphere. The starting point of this model is the GLAS Fourth Order GCM (Kalnay, et al., 1984). The earlier model was changed to alter the vertical coordinate from the terrain following formulation used in the earlier tropospheric model to a hybrid version where the terrain following form is used in lower layers, with pressure coordinates being used above. A new parameterization scheme, developed at NASA/GSFC, is used for the radiation calculation.

We have completed an 18-month run with annual cycle boundary conditions, a 9° (latitudinal) × 10° (longitudinal) horizontal resolution, and a 2-km vertical resolution. The results appear to show as good zonal mean

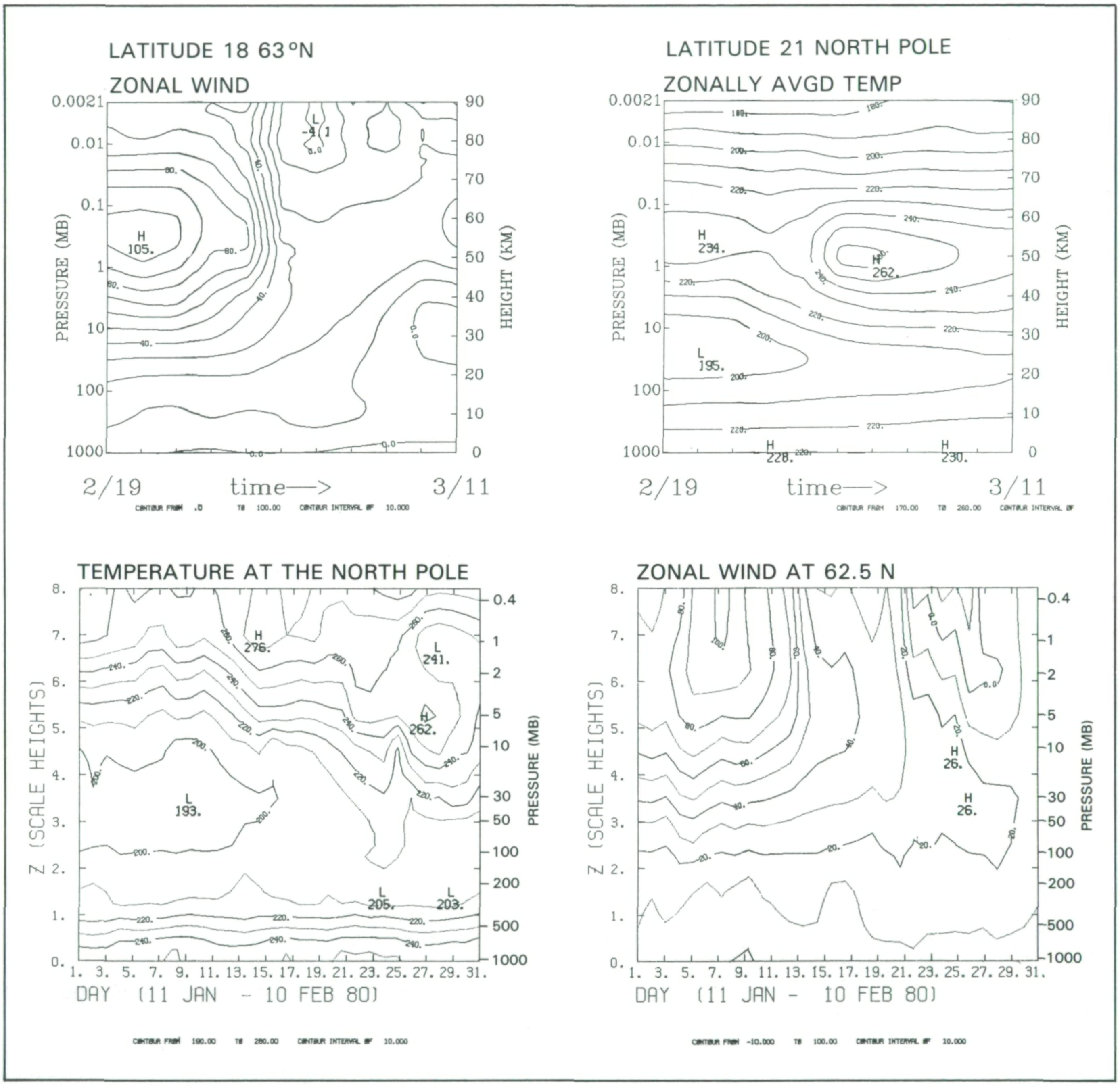

A global atmospheric general circulation model.

features as the NOAA Geophysical Fluid Dynamics Laboratory "SKYHI" model, with a higher (5° × 6°) horizontal resolution and similar vertical resolution. Moreover, in the second northern winter, a minor warming appeared in the model. Two figures of this event are presented as a sample of the model results; the first shows the time-height distribution of zonal mean wind at 63 °N. A 60 m/s change of the zonal mean wind at 55 km in less than 3 days occurred. Also in the model upper stratosphere and above, the deceleration appeared almost simultaneously. As shown below, these features are observed in the real atmosphere. The second figure shows the time-height distribution of temperature at the North Pole. A temperature change of 10° C/day at 50 km, which is a fairly realistic rate, occurred at the end of February.

For rough comparison two similar figures from observations are shown; one figure shows the time-altitude diagram of the atmospheric temperature at the North Pole for the January 11 through February 10, 1980 period, from satellite observations. The temperature at the 1-mb pressure level (about 48 km) was about 250 K on January 17 and rose to about 276 K on January 24. In response to this sudden increase in temperature in the upper stratosphere, the speed of the zonally-averaged zonal wind, deduced from satellite temperature data, dropped from about 100 m/sec to less than 40 m/sec at the same level and at 62.5 °N latitude during the same period (figure). Furthermore, the zonal wind has completely reversed its direction on February 1 from blowing toward the east to toward the west. The temperature data were taken from TIROS-S and NOAA-6 satellites.

The amplitudes of planetary waves in the 9° × 10° model are smaller than those observed by about 30 percent. We expect this deficiency will be greatly reduced when the horizontal resolution is increased. Currently, we are preparing a 5° × 6° resolution version of the model which is nearly completed.

Contact: Marvin A. Geller, Winston C. Chao, and Mark R. Schoeberl
Code 610

Sponsor: Office of Space Science and Applications

LOSS RATE OF ATMOSPHERIC ACETYLENE DUE TO REACTIONS WITH OH, O, CL, AND BR

Acetylene is an important hydrocarbon species that is present in trace quantities in the troposphere and lower stratosphere. Potential loss processes for atmospheric C_2H_2 include reaction with O, OH, Br, and Cl, as well as photodissociation. The rate parameters for the reaction of OH, Cl, and Br have been determined in this laboratory. Using these data, the rate data determined by Westenberg and deHaas for the reaction of oxygen atom with acetylene and known concentration profiles for OH, O, Cl, and Br, we have calculated loss rates for C_2H_2 as a function of altitude. For completeness we have also included the estimation of A. C. Aikin for the photodissociation rate, J.

The following conclusions may be reached:

- Reaction of C_2H_2 with OH dominates at lower altitudes, i.e., <20 km.

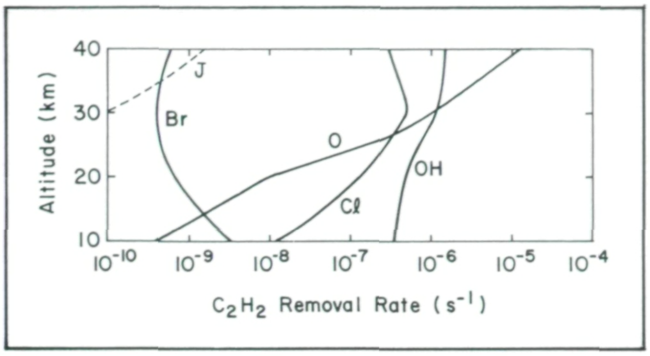

Comparison of acetylene removal in the atmosphere by photodissociation (J) and reaction with Br, O, Cl, and OH.

- Reaction of C_2H_2 with O dominates at higher altitudes, i.e., >30 km.
- Around 30 km, the loss rates of acetylene via reaction with OH, O, and Cl are similar.
- Removal of C_2H_2 by reaction with Br is slow and is thus unimportant.
- Removal of acetylene via photodissociation is of the same order of magnitude as the removal of C_2H_2 via reaction with Br.

The loss rates for C_2H_2 may be used to calculate a profile for C_2H_2 as a function of altitude. A comparison of the calculated profile, as well as profiles for other trace species with direct observation, is useful for verification of atmospheric models.

Contact: Dr. W. A. Payne
Code 690

Sponsor: Office of Space Science and Applications

SOLAR AND DYNAMICALLY INDUCED OSCILLATIONS IN THE STRATOSPHERE

We have studied the temporal and spatial characteristics of short-term fluctuations in stratospheric ozone using several years of ozone, solar ultraviolet, and temperature data from the Nimbus-4 and the Nimbus-7 satellites. Our study has shown that the ozone in the stratosphere is in a continuous state of oscillation with periods varying between 3 to 7 weeks. These oscillations are manifestations

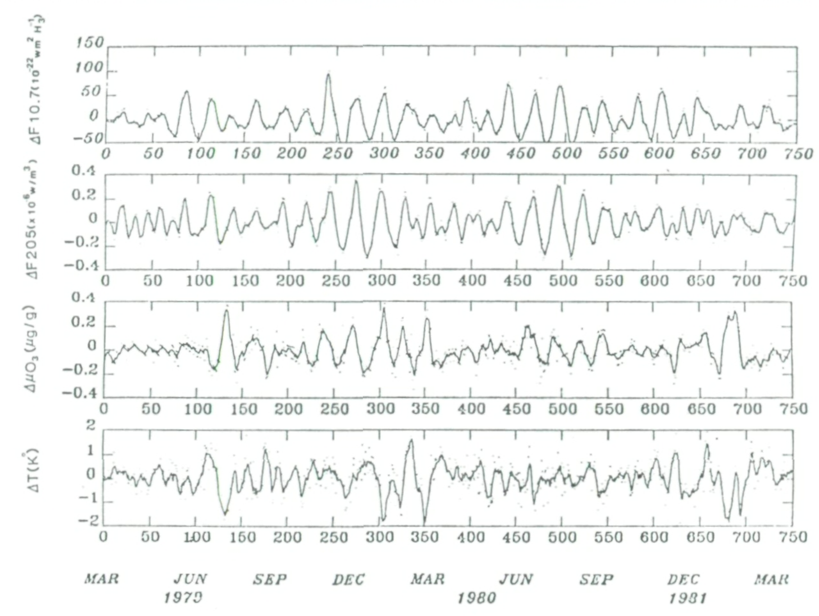

Comparison of daily fluctuations in ozone (third panel) and temperature (fourth panel) at 3 mb in the tropics with F10.7 (first panel) and F205 (second panel) assumed as proxy indices of the solar UV irradiance in the 180 to 400 nm range. F10.7 is the radio flux measured at 2800 MHz at Ottawa, Canada, and F205 the solar UV flux at 205 nm measured by the SBUV experiment on Nimbus-7. All the data are deseasonalized by subtracting 35-day running mean from the daily values. A cross spectral analysis of these data sets indicates a significant coherence between ozone and solar UV flux at 27-day solar rotation period, no coherence between solar flux and temperature, and strong coherence between ozone and temperature over a wide spectral range between 3 to 7 weeks.

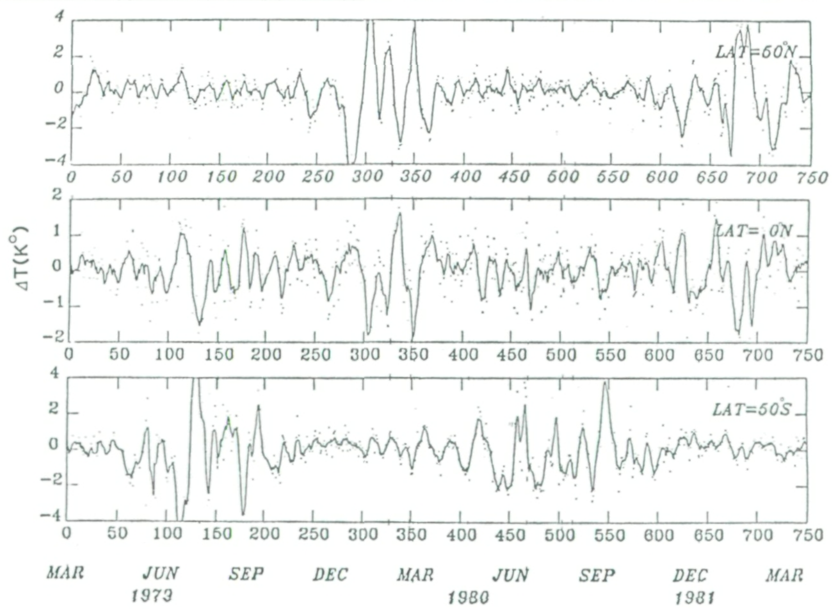

The daily fluctuations in temperature at 3 mb at three selected latitudes, 60° N, 0°, and 50° S. These plots clearly show the seasonal character of the high latitude oscillations in the two hemispheres and their out-of-phase relations with tropical oscillations.

of dynamically induced perturbations in temperature in the winter hemisphere and the 27-day modulation of the solar UV radiation. Whereas the solar UV flux in the 180 to 210 nm range of the solar spectrum primarily contributes to ozone production in the stratosphere, temperature perturbations tend to increase the loss rate of ozone through temperature dependent reaction rates. The two effects, therefore, cause ozone to vary in phase or out of phase, respectively. (See figure).

Temperature oscillations are global in extent and are independent of solar activity. In both the hemispheres, temperature oscillations begin at high latitudes during fall and persist through winter and spring. The oscillations manifest themselves at low latitudes with a phase change of about 180°. (See figure.) As a result, the peaks at high latitudes appear as troughs at low latitudes and vice versa. Since the seasons in the two hemispheres are complimentary, the oscillations at low latitudes remain uninterrupted even when the strength of the high latitude oscillations is considerably diminished with the onset of the summer.

The amplitude of low-latitude oscillations is typically less than 2 K and more often in the range of 1 K. Even though this is a factor of 3 to 4 less than the corresponding values at high latitudes, its effect on ozone is comparable to very large changes in solar UV flux. It takes about 8 to 10 percent increase in the 200 to 210 nm range of the solar UV spectrum to offset the effect of 1 to 2 K increase in temperature in the upper atmosphere. Such an increase in the solar UV flux is an upper limit of the 27-day cycles and typically corresponds to a change over a solar cycle. As a result, the 27-day signals in ozone, associated with the 27-day solar UV modulation, are detectable only under favorable circumstances, i.e., at low latitudes during periods of high solar activity.

The estimated change in ozone in the upper stratosphere is about 3 to 4 percent over a solar cycle and is comparable to a temperature-induced change of about 2 K of nonsolar origin over the same period. The latter may interfere constructively and destructively with solar cycle changes in ozone depending upon their relative phase. The interpretation of ozone data for solar cycle variation and long-term trends, therefore, depends critically on simultaneous monitoring of both ozone and temperature.

Contact: S. Chandra
Code 610

Sponsor: Office of Space Science and Applications

CASCADING OF DENSITY IRREGULARITIES IN THE EQUATORIAL IONOSPHERE

Dynamics Explorer-2 (DE-2) observations of equatorial spread-F have revealed a different behavior in the spread-F at early versus late times in the evolution of the phenomenon. The early time behavior, seen in DE-2 data from 300 to 1000 km altitude, shows: (1) large-scale density variations corresponding to plasma bubbles, (2) electric field fluctuations with frequencies in the 4-256 Hz range (corresponding to along-the-satellite-track wavelengths of 28 m to 1.8 km), and (3) a separate band of waves with frequencies in the range of 16-64 kHz that are interpreted as lower hybrid drift waves (LHD). Large ion velocities were observed in the DE-2 ion drift meter (IDM) data only at the location of the LHD instability. A calculation of the LHD growth rates using the DE-2 electron density data from the Langmuir probe (LANG) and the ion drift velocities from IDM (Hoegy et al., 1982) showed that the largest growth rates occurred at about 20 kHz—in the middle of the frequency band where the electric field turbulence was seen. Growth rates calculated at other frequencies and at other times in the DE-2 pass predicted no LHD waves, and no waves were seen in the data. Thus DE-2 data have been able to demonstrate that the lower hybrid drift waves are present in the early time spread-F observed in the equatorial region.

In contrast, the late time spread-F shows the behavior: (1) a comparatively smooth electron density profile with no sharp density variations (which are associated with newly formed bubbles), (2) electric field fluctuations with frequencies in the range 256 Hz to more than 1 kHz, and (3) strongly developed electric field turbulence in the 16-64 kHz regime (the frequency range associated with LH waves). These apparent LH waves occured for a long time during the pass (they had a large spatial extent), and no corresponding ion drift velocity was evident. This is in contrast with the early time spread-F. We attribute the differences between these early and late time observations to the relaxation of the initially large-scale density structures, which result from the nonlinear evolution of the Rayleigh-Taylor instability. In the early turbulence, there is some cascading from the large-scale density structures to the 4-256 Hz turbulence, but the LH waves at 16-64 kHz are driven by the drift velocity associated with the density gradients. In the late time turbulence, there are no density gradients to support large ion drift velocities; therefore, previously proposed inverse cascade mechanisms are not applicable for generating turbulence below the lower hybrid frequencies. The mechanism we believe to be responsible is cascading of wave energy from the larger wavelengths down to the wavelength regime of

the LH waves. The evidence that cascading is the wave source is that the intermediate electric field turbulence is at higher frequency than in the early time spread-F, indicating the transport of energy to shorter wavelengths and hence higher measured frequencies. The current evidence is for absorption and hence damping at the lower hybrid frequency at late times. The overall picture is analogous to a ship's wake with the gradual cascading of characteristic wake scales to shorter wavelengths. The additional effect here is due to kinetic plasma processes at the lower hybrid resonance.

Contact: W. Hoegy
Code 610

Sponsor: Office of Space Science and Applications

LABORATORY MEASUREMENTS OF SATELLITE DRAG COEFFICIENTS

A study was begun recently to estimate the drag coefficient of the spacecraft of NASA's Geopotential Research Mission (GRM). The spacecraft proposed for this mission are cylinders with a length roughly equal to 5 diameters, and they are to fly with attitude control to minimize aerodynamic drag. As a spacecraft moves through the rarefied upper atmosphere, it is struck by all molecules whose trajectories intercept its projected area along the flight path, and that projected area determines the drag force. Thus, the drag is minimized when the spacecraft projects the smallest possible area in the direction of flight, and this is accomplished by keeping the cylinder axis parallel to the direction of flight. Accordingly, most of the drag force should arise from molecular impacts of the air with the front surface (nose cone) of the spacecraft. However, for long cylindrical spacecraft, additional drag is exerted on the lateral surface by grazing angle collisions. For very long cylinders the lateral surface drag may exceed that of the front surface. Therefore, it is necessary to know the force (momentum transfer) per molecule for grazing angle collisions. An important part of this study involves laboratory experiments designed to determine the momentum transfer per molecule upon surface impact. The results obtained thus far are highlighted as follows.

The GRM spacecraft will be flying in Earth orbit at 160 km altitude or higher. The spacecraft velocity (about 8 km/s) and the air temperature (about 1000 °K) determine the average angle of incidence for the grazing angle collisions. For this case, the average angle of incidence is about 85 °, measured with respect to the surface normal. The corresponding impact energy is about 10 eV.

We have measured the angular and energy distributions of molecules reflected from likely spacecraft surfaces. Experiments have been done for angles of incidence from 30 ° to 85 °, and at energies from about 1 eV to 40 eV. The first figure shows the angular distribution for N_2^+ molecules incident at 60 ° upon a Molybdenum surface. The second figure shows the same for 85 ° incidence and for two energies, 8 and 15 eV. There is a trend for the angle of reflection to increase with increasing impact energy, as evidenced by the second figure. This is found to be the case as the impact energy increases from 1 to 40 eV for grazing angles (80 ° and 85 °). The narrow angular distribution of the reflected molecules is indicative of small momentum transfer. Also, the fraction of momentum transferred is larger at lower energies where the reflection angle is much smaller than the angle of incidence.

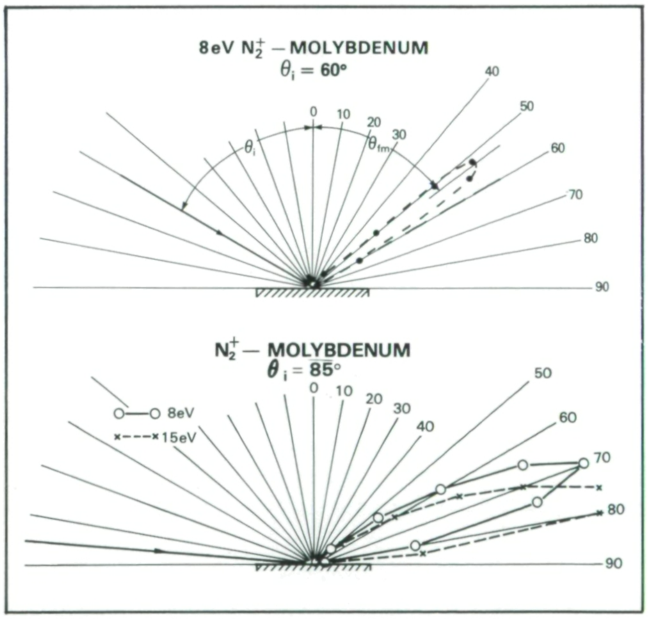

The angular and energy distributions of molecules reflected from likely spacecraft surfaces.

In addition to the angular distribution, the energy distribution of the reflected molecules was obtained using electrostatic potential retardation analysis. The angular and energy distributions have been used to obtain the average reflected energy and momentum for a given impact energy. For 10 eV impact energy and 85 ° incident angle, the average reflected energy is found to be 8.3 eV, and the average reflection angle is 74 °. With these numbers the fractional momentum transferred in the

direction of flight, which is needed to compute the drag force, is about -0.83. A value of -1.0 represents perfectly elastic collisions with the surface and zero drag force on the lateral surface.

The contribution of the lateral surface impacts to the total drag increases with the length of the cylinder, and it is possible to obtain a simple analytical expression for the total drag coefficient as a sum of the drag due to the front face and the drag due to the grazing angle impacts on the lateral surface. As may be expected, the lateral surface drag depends on the cylinder length L and its radius R, and its contribution to the total drag is proportional to the ratio L/R. The drag coefficient for the front face is likely to be between 1.5 and 2.0. With a fractional momentum transfer ratio of -0.83, as indicated previously, the contribution of the lateral surface of the GRM spacecraft will be about 0.3 for a total drag coefficient between 1.8 and 2.3 for the main cylinder of the spacecraft.

Experiments planned for the immediate future include measurement of angular and energy distributions using neutral molecules incident upon typical spacecraft surfaces, including nonmetallic surfaces. Previous studies, like this one, have relied upon the assumption that molecular ion impacts transfer the same momentum as neutral molecule impacts at the same impact energy and angle, and that therefore molecular ion impact data may be used in computing satellite drag coefficients. We hope to test the validity of this assumption with the next set of experiments.

Contact: F. A. Herrero
Code 610

Sponsor: Office of Space Science and Applications

SOLAR VARIATIONS IN THE THERMOSPHERE

An important link in the chain of arguments relating solar activity variations to variations in thermospheric density has recently been verified with data from the Atmospheric Explorer-E satellite. Early in the satellite era it was found that the drag on satellites by the neutral atmosphere (thermosphere) varied with solar sunspot activity. It was further found that measurements of the solar decimetric (10.7-cm wavelength) radio flux, which can be measured from a ground-based observatory regardless of weather, were an excellent indicator of solar activity and correlated closely with thermospheric density. However, the long wavelength radio waves do not carry enough energy to act directly on the thermosphere, and so it was assumed that the Sun increased its emission of extreme ultraviolet radiation (EUV) with increasing solar activity. Calculations have shown that there is sufficient EUV flux to account for the average temperature of the thermosphere (about 1000 K).

The Atmospheric Explorer-E satellite carried both a spectrophotometer for measuring EUV flux and a mass spectrometer for measuring *in situ* density. Simultaneous measurements were obtained during the rising portion of the last solar cycle from mid-1977 through 1980. It was found that the shorter wavelength solar EUV fluxes, which are most effective in heating the thermosphere, are indeed highly correlated with the solar 10.7-cm radio flux. Both the short wavelength EUV and long wavelength radio emissions are believed to originate primarily in the coronal region of the Sun. It was also found that variations in thermospheric density correlated better with the directly measured variations in solar EUV flux than with the radio flux, particularly over time periods of a few days. Thus, both of the links in the chain of reasoning relating ground-based measurements of solar activity to satellite measurements of density variations were verified.

This study also clarified the well known observation that day-to-day changes in solar radio flux of a given magnitude are associated with much smaller density changes than a similar magnitude change in radio flux over a longer time period. It was noted that changes in solar EUV flux are similarly larger when associated with longer time period changes in solar radio flux than with shorter time periods. Thus, while solar emissions at widely different wavelengths can have a high degree of similarity when they arise in similar regions of the solar atmosphere, they do not correlate perfectly.

With this verification that measured solar EUV fluxes are directly related to thermospheric variations, it must also be recognized that the more readily obtained 10.7-cm radio flux correlates remarkably well with thermospheric densities as well as solar EUV fluxes and is an essential datum for predicting thermospheric densities for the foreseeable future.

Contact: A. Hedin
Code 610

Sponsor: Office of Space Science and Applications

INTRACAVITY LASER DETECTION OF ATMOSPHERIC SPECIES

Over a decade ago preliminary studies indicated that industrial release of chlorofluoromethanes could have a significant and potentially detrimental effect on the Earth's ozone layer. Since then, a concerted effort has been made to understand the impact on the stratosphere of both natural and anthropogenic perturbations. Progress has been outstanding because this concentrated activity fostered close interaction and cooperation by those involved in model studies, laboratory experiments, and field measurements. As a result our understanding of the stratosphere has become more sophisticated with an attendant need for more detailed laboratory experiments and field experiments. Whereas conventional measurement techniques were adequate previously, the pressure for more detailed data has necessitated the development of newer detection methods.

Intracavity laser detection is an example of a nonlinear optical technique which is being developed as a complement to other methods for application to the detection of atmospheric species in laboratory experiments. Briefly, the laser cavity is extended by moving the output mirror so that a cell can be accommodated, and the spectral output of the laser is scanned with a narrowband monochromator. Since the shape of the laser spectral profile is extremely sensitive to any cavity loss, trace quantities of an absorber can easily be detected. The fact that the technique is based on absorprtion rather than fluorescence offers several advantages, among these ease of detection of nonfluorescing species and operation at high pressures where quenching of fluorescence can significantly reduce signal strength. The sensitivity is such that even very weakly absorbing species can be detected.

An intracavity dye laser spectrometer has been assembled in the laboratory for application to detection of atmospheric species. The extremely weak red atmospheric bands of O_2 and intercombination bands of H_2O have been observed in ambient room air. As an indication of the sensitivity of this technique, previous attempts to detect the red atmospheric system of O_2 required an atmospheric path length of 100 km, whereas the intracavity path length was just 50 cm. An extensive sensitivity study has been made using NO_2 as the absorber, and an example of the laser profile with and without NO_2 is illustrated in the accompanying figure. Note the sharp line-like structure that develops when an absorber is present. Experiments to measure the rate for the atmospherically important reaction $NO + NO + O_2 \rightarrow 2NO_2$ by NO_2 detection are presently in progress. In the next phase of the program the method will be extended to detection of transient species such as $O(^1D)$, formed from ozone photolysis, and HCO. The $O(^1D)$ atom is particularly difficult to monitor using conventional techniques because of its long radiative lifetime and related weak absorption strength. However, it plays a pivotal role in atmospheric chemistry, and refinement of our knowledge of $O(^1D)$ reactions will be beneficial in modeling the upper atmosphere.

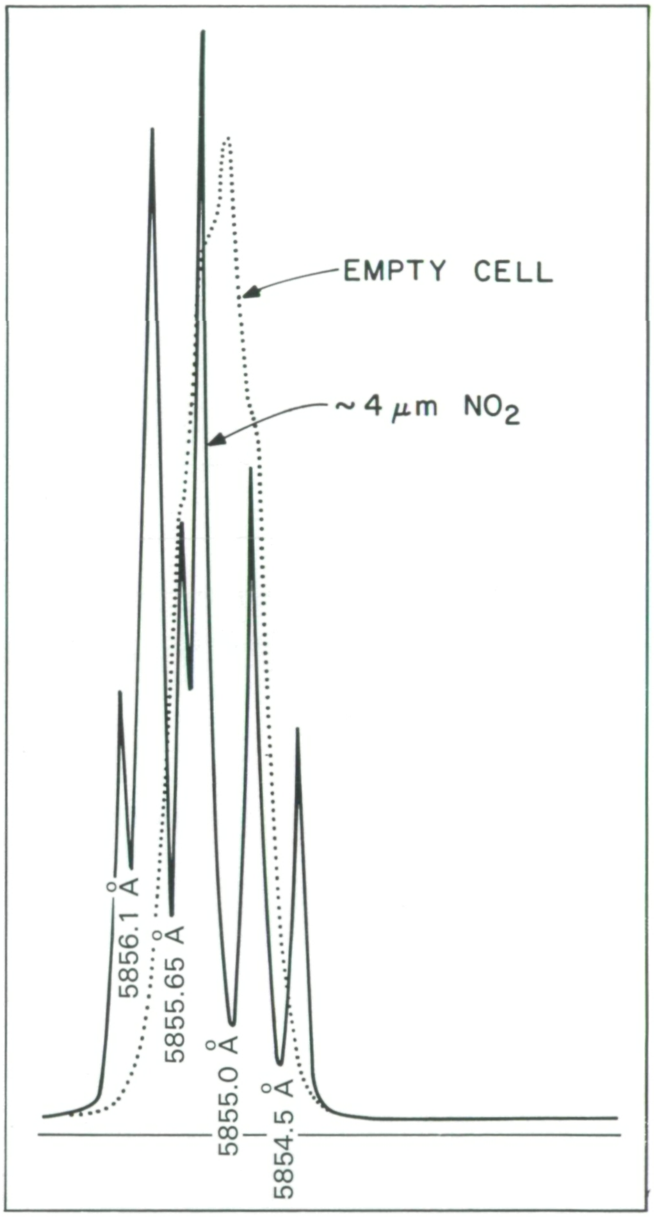

Intracavity absorption by NO_2 ($\tilde{X}\,^2A_1$).

The development nature of this project has provided an opportunity for collaboration with the Johns Hopkins

University through support of Mr. W. D. Brobst, who is working at GSFC under the NASA Graduate Student Researchers program.

Contact: Dr. John E. Allen, Jr.
Code 690

Sponsor: Office of Space Science and Applications

VISIBLE AND ULTRAVIOLET LASER SPECTROSCOPY FOR ATMOSPHERIC MEASUREMENTS

Optical measurements of trace atmospheric gases require accurate spectroscopic data which are often unavailable in the scientific literature. Such information is critical for both the interpretation of data from existing instruments as well as feasibility studies for new generations of scientific experiments. Current or planned instruments utilize fluorescence, absorption, and emission optical techniques from satellite and balloon platforms. This spectroscopy laboratory has supported instruments in all of these categories.

We have recently concluded two separate studies which have provided spectroscopic information necessary to expand the capabilities of existing satellite instruments. The first arose out of a mesospheric emission spectrum (illustrated in the first figure) recorded by the BUV instrument on board Nimbus-7 in which several bands were assigned to emission from excited levels of nitric oxide (NO). Emission rate data available in the literature for NO were contradictory. The second figure shows the experimental apparatus setup to record the fluorescence

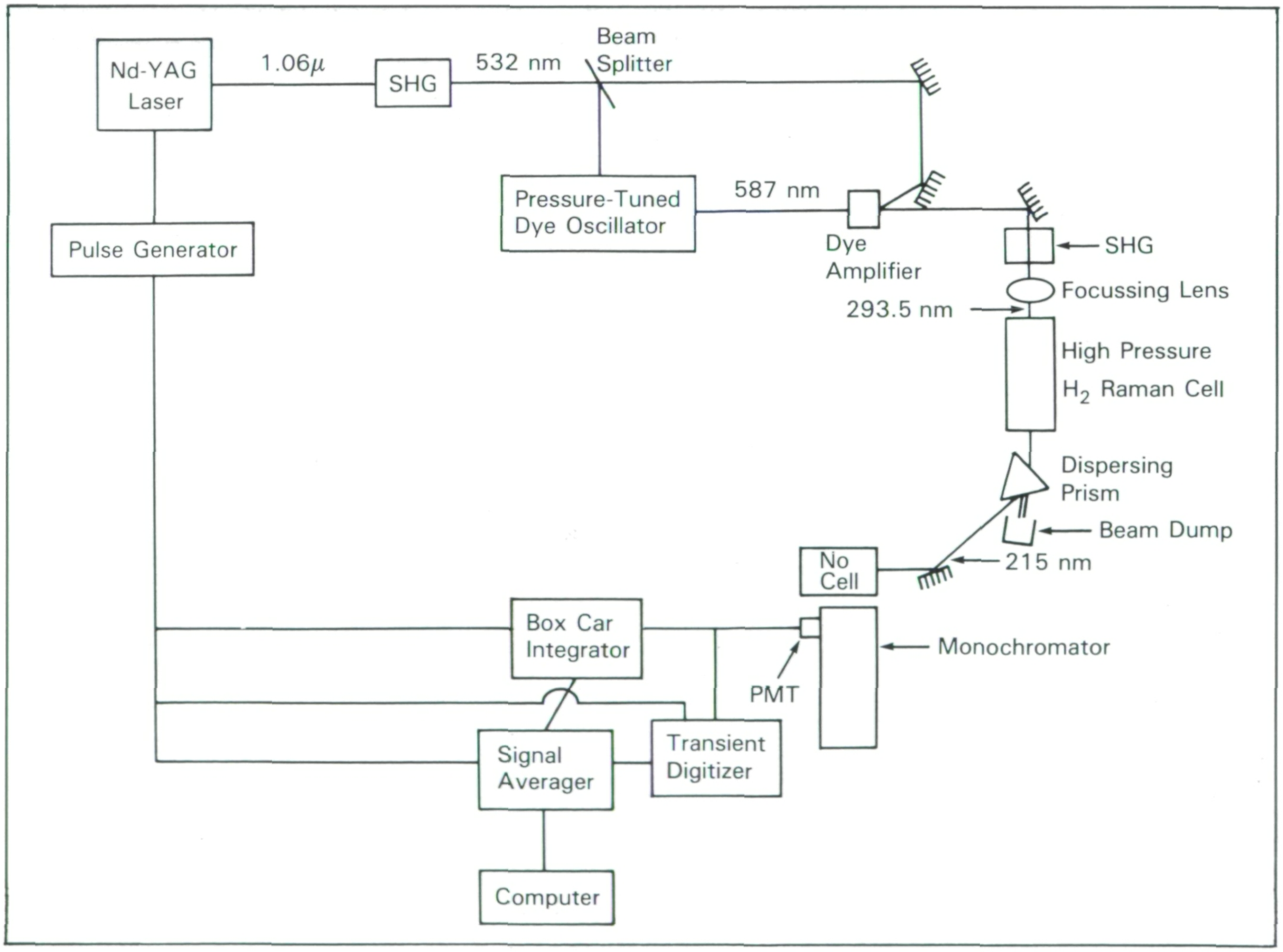

Experimental apparatus for measurement of spectrally or temporally resolved nitric oxide fluorescence.

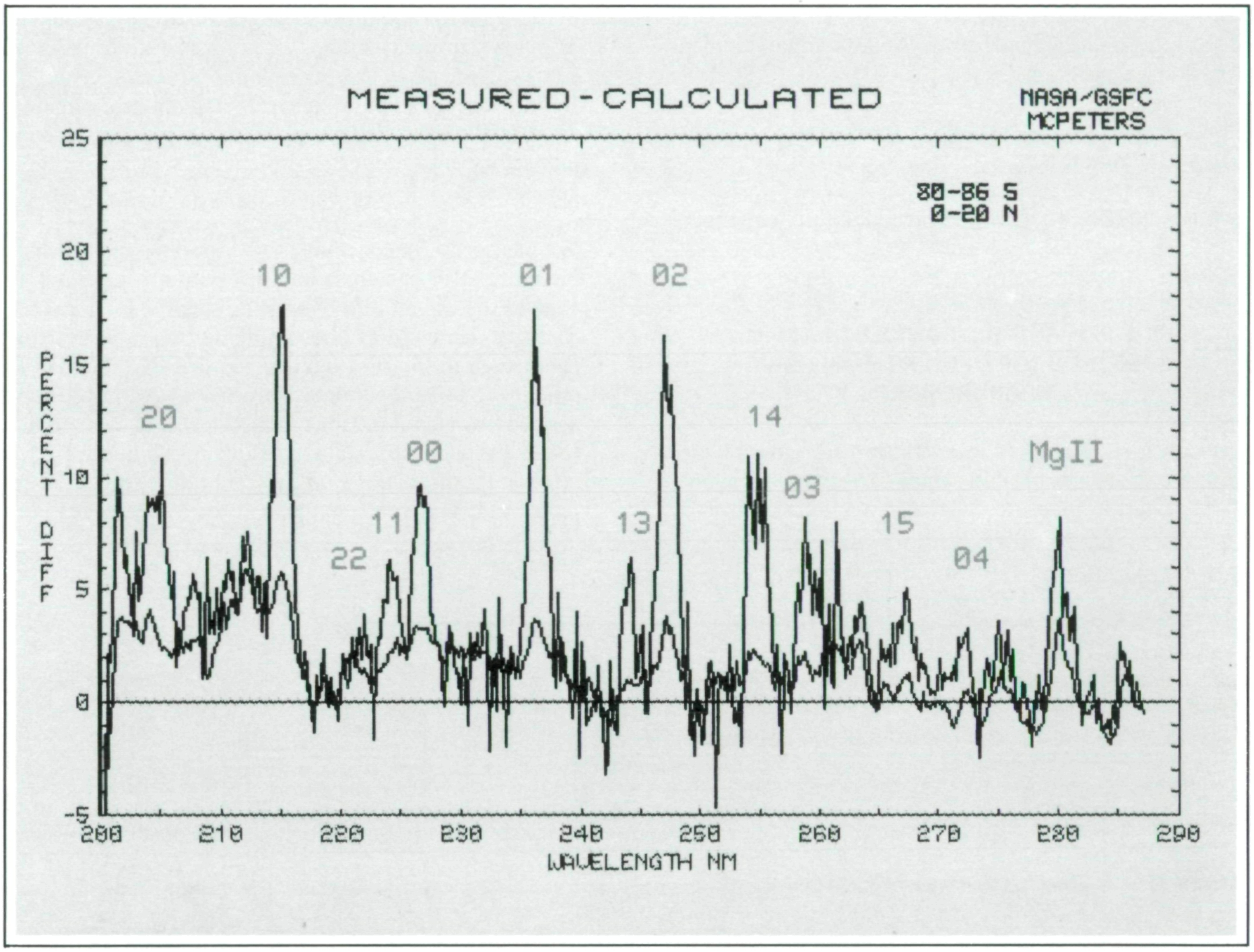

The percent difference between the measured albedo and the theoretical albedo (Rayleigh-ozone-oxygen model atmosphere). Scans made on June 20, 1979, near 60°S (large amplitude curve: 80-86°ZA), and near 20°N (small amplitude curve: 0-20°ZA). Wavelengths of NO gamma band (v'v'') transitions have been marked.

branching ratios, lifetimes, and quenching rates for collisions with N_2 and O_2. The third illustration is the collision-free emission spectrum from the $A^2\Sigma^+(v'=1)$ state of NO excited by a narrowband, Raman-shifted laser emitting at 215 nm. From this and other similarly recorded spectra the most complete set of experimentally determined branching ratios and Franck-Condon factors for the $A^2\Sigma^+(v'=0,1)$ levels in NO have been determined. Time resolved emission studies have also been made yielding NO radiative lifetimes and quenching rates for collisions with N_2 and O_2. This entire set of data has been used to extract mesospheric NO abundances from satellite data and has also demonstrated the feasibility of stratospheric measurements of NO via fluorescence lidar. The second study concerned sulfur dioxide (SO_2). Absorption cross sections for SO_2 between 3000 and 3200 Å have been measured both at room temperature and -70 °C. The recent eruption of El Chichon sent large clouds of SO_2 into the stratosphere, which were observed by the Total Ozone Mapping Spectrometer (TOMS) aboard Nimbus-7. Existing spectroscopic data were not in good agreement, and low temperature data did not exist at all. Spectra were recorded with a resolution on the order of 0.3 Å, and cross sections were measured at 0.3 Å intervals at both temperatures. The low temperature spectra show marked differences from the room temperature spectra in both wavelength position and intensity. This SO_2 spectral data, which are of higher resolution than previously published and recorded near the actual satellite observation temperatures, have

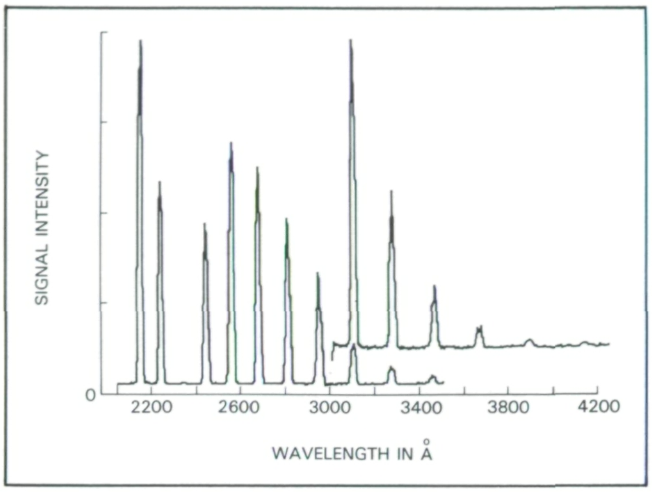

Emission spectrum of nitric oxide [$A^2\Sigma^+(v' = 1)$].

been used in the analysis of TOMS data taken at the time of the El Chichón eruption.

Contact: T. J. McGee
Code 610

Sponsor: Office of Space Science and Applications

REMOTE SENSING TECHNIQUES TO MAKE VAS SOUNDING IMAGES OF ATMOSPHERIC STABILITY PARAMETERS

The Geostationary Operational Environmental Satellites (GOES) launched before 1980 carried an instrument called the Visible and Infrared Spin-Scan Radiometer (VISSR) designed to aid meteorologists by providing day-night pictures of the cloud patterns over the western hemisphere. After 1980, the instrument was upgraded to 12 infrared channels to become the VISSR Atmospheric Sounder (VAS). Since 1980, VAS has been used experimentally to provide atmospheric temperature and moisture soundings at selected points in cloud-free regions. However, manual production of point-by-point soundings is tedious, and the individual values must pass through an objective analysis scheme in order to produce the gridded and contoured fields required by meteorologists. Atmospheric soundings by automated methods often prove to be of little value to meteorologists because of the difficulty in writing algorithms that are robust in the face of the errors in satellite data, the difficulty in dealing with clouds, and the space-time variations from the surface of the Earth. Because VAS data are collected in a rasterized format (like a 12-color television picture), frequent views of the thermodynamic structure of the atmosphere could be provided. The problem is to invent fast but accurate algorithms which calculate parameters of meteorological interest and present the results in an easy-to-digest form. The first illustration presents the conceptual data flow for calculating either point-by-point temperature-moisture profiles or horizontal fields of atmospheric stability parameters from VAS and conventional data.

We have developed remote sounding and imaging techniques for presenting VAS satellite retrievals of atmospheric moisture and stability parameters as though they were GOES images at 60-km resolution. These sounding images vividly display the enormous volume of numerical information about mesoscale weather developments over the United States. Multilinear regression is used to retrieve the atmospheric fields from a combination of rasterized satellite radiances and conventional surface reports interpolated into satellite coordinates. Accuracy with respect to radiosonde data is good for

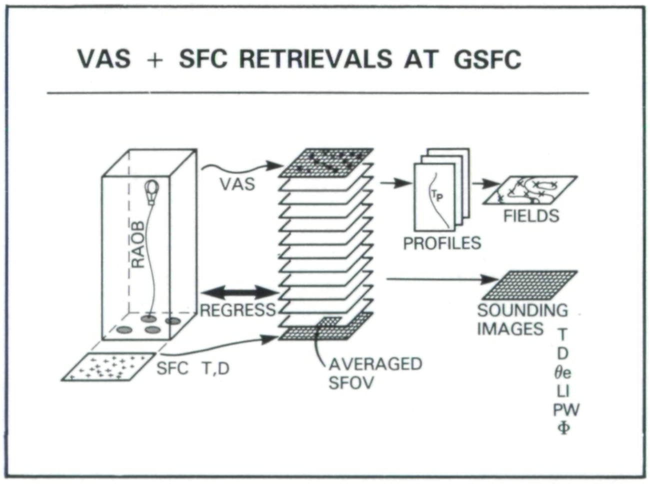

Schematic flow for data processing of VAS point-by-point retrievals or of VAS sounding images. Conventional low-resolution radiosonde data about the 3-dimensional atmosphere are used in regression with high-resolution 2-dimensional VAS radiances and gridded surface reports. Random noise is reduced by horizontal averaging sounding fields of view (SFOV). Traditionally, quality-controlled remote soundings must be retrieved manually at selected points as vertical temperature-moisture profiles, which must then be converted to stability indices and analyzed as contour maps. Current digital technology and automated quality-control techniques now make it practical to produce real-time fields of stability indicators at satellite resolution.

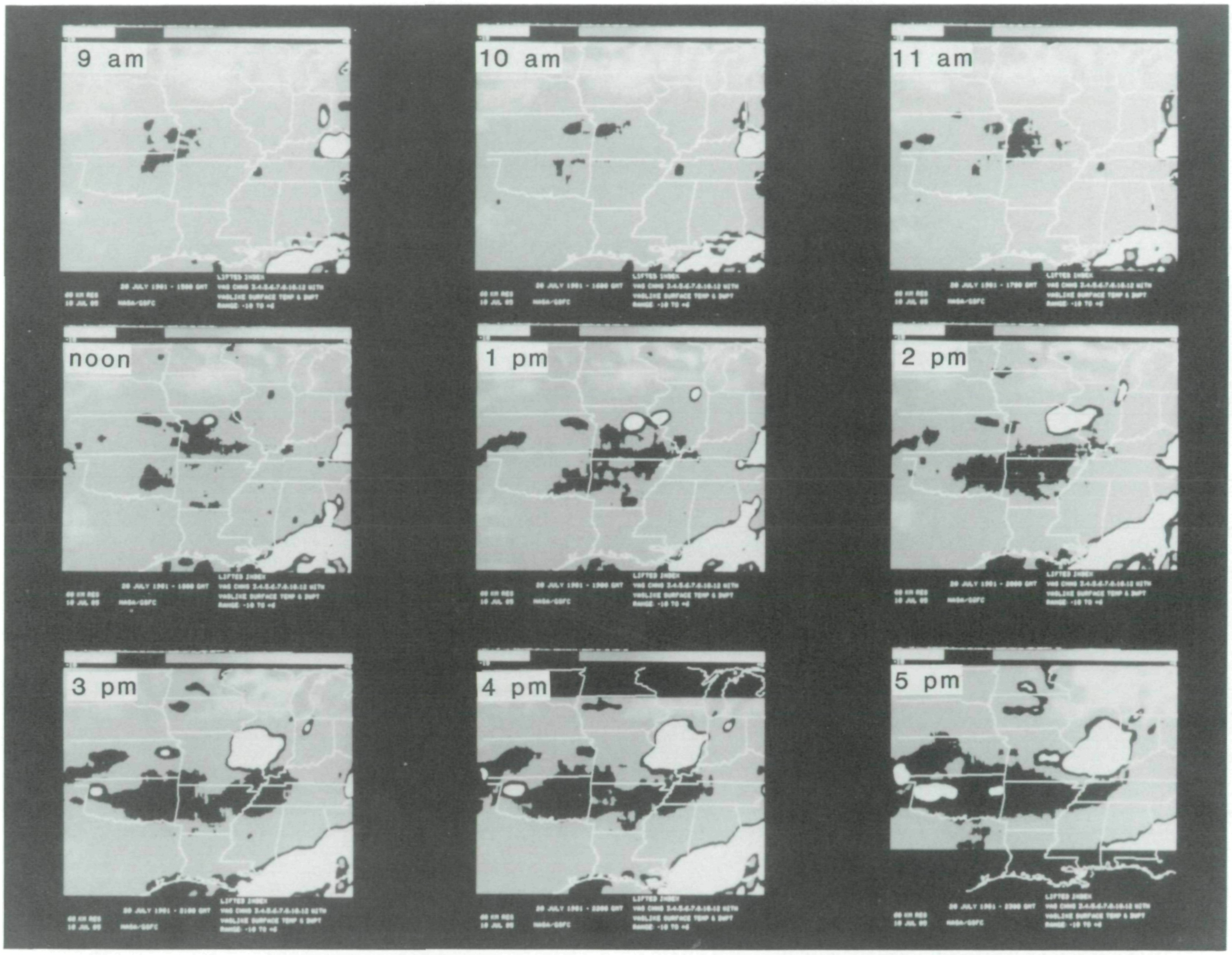

A graphic demonstration of the resolution and continuity in VAS sounding images for lifted index (LI) at hourly intervals over the midwest on July 20, 1981. The darker shades indicate more negative (more unstable) values for LI in areas with a greater thermodynamic potential for convection. Overcast areas appear white, and broken clouds are readily identified as hazy gray areas across the northern midwest. Errors due to unwanted diurnal and surface effects have been eliminated. Note the significantly unstable values which are reliably obtained prior to the development of severe thunderstorms over Missouri at midday and over Oklahoma-Arkansas by late afternoon.

temperature, dewpoint, precipitable water, lifted index, layer thickness, and equivalent potential temperature. Gray-level digital images (easily color-coded to highlight the significant values) at 1- to 3-hour intervals correctly determine the location and magnitude of potential convective instabilities for two midsummer case studies over the United States. The second figure presents one such series of gray-level images for lifted index (LI) at hourly intervals prior to the development of severe thunderstorms in the midwest. The significantly unstable air is indicated with darker shades of gray (potentially buoyant because it is very hot and humid near the surface compared to the midtroposphere). The illustration demonstrates the effectiveness of the techniques that were developed to make VAS retrievals insensitive to random noise, unresolved clouds, space-time variations in skin temperature, scanline dropouts, reflected sunlight, and sparse statistical training. The techniques were designed to be practical for the distribution of VAS sounding images in real time with a minicomputer workstation, such

as the MCIDAS system developed by the University of Wisconsin for NOAA to distribute this kind of useful meteorological product.

Contact: D. Chesters, A. Mostek, and D. Keyser
Code 610

Sponsor: Office of Space Science and Applications

GENERATION OF SEVERE, EAST COAST WINTER STORMS

Occasional but crippling snowstorms along the east coast of the United States are a research topic that presents many challenges to the research and satellite meteorologist. An international field program, Genesis of Atlantic Lows Experiment (GALE), is planned for early 1986 that is designed to examine many aspects of atmospheric processes that result in the formation of cyclones along the Atlantic coast. In preparation for the field program, recent analysis and modeling investigations have shown how the interactions of isolated wind maxima, also known as jet streaks, at various levels in the troposphere can influence the development of wintertime cyclones.

A study of a selection of major winter storms during the past quarter-century along the northeastern United States urban corridor has shown how the production of heavy snowfall is related to the juxtaposition of vertical circulations associated with jet systems in the upper troposphere. A particular configuration of jet streaks and associated circulations appears to be a common feature in many of these systems as shown in the first figure. The rising branches of the circulations produce a broad region of ascending air necessary for the production of widespread precipitation. The lower horizontal branches of the circulations are responsible for both the maintenance of low-level cold air necessary for low temperatures to support snowfall and for the transport of warm, moist air over the cold air toward the region of heavy snowfall.

Recent work with the Total Ozone Mapping Spectrometer (TOMS) and the 6.7 μm water vapor channel on the Temperature-Humidity Infrared Radiometer (THIR) aboard the Nimbus-7 polar-orbiting satellite has contributed to the understanding of jet streak interactions in winter storms. When combined with conventional radiosonde data and visible and infrared imagery from the GOES satellite, these data have shown how subsidence associated with vertical circulations in the vicinity of upper-level jet streaks can act to extrude stratospheric air

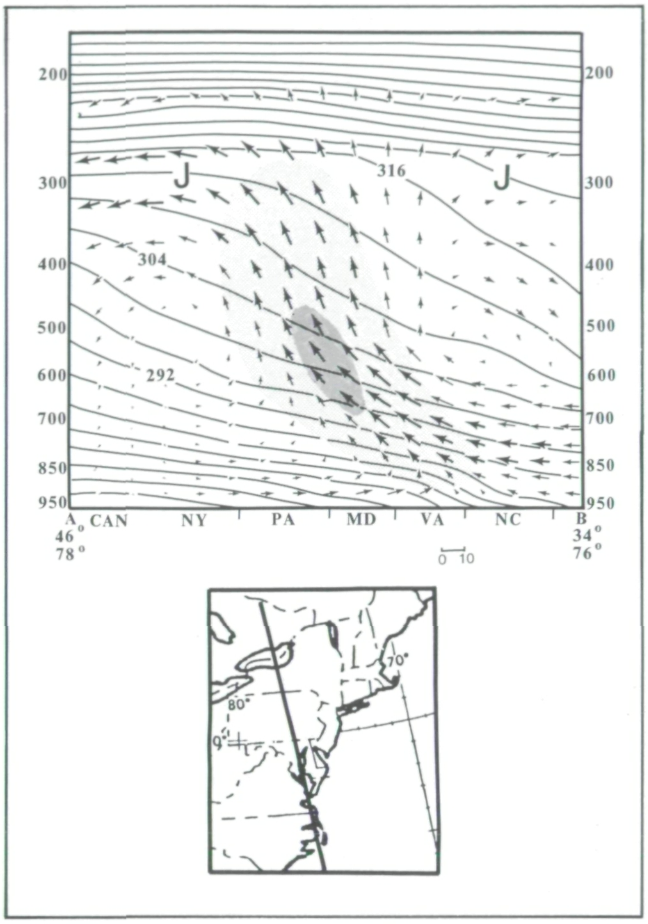

A particular configuration of jet streaks appears to be common in many jet systems in the upper troposphere.

into the troposphere prior to and during cyclogenesis with the February 18-19, 1979, Presidents' Day snowstorm along the Atlantic coast (shown in the second illustration). As stratospheric air descends, the static stability of the atmosphere decreases and, subsequently, the vorticity increases, an important element for the development or intensification of cyclones. The TOMS and THIR data indicated that the descent of stratospheric air can occur prior to significant cyclogenesis, indicating that the satellite data may have great prediction potential for identifying conditions conducive for cyclone development.

Additional analyses of the Presidents' Day snowstorm indicate that an intensification of the subtropical jet located in the upper troposphere was linked to an increase in upper-level divergence and coincided with the development of an area of heavy snow. The intensification of the upper-level jet was due to the confluence of the mass and wind fields as an upper-level trough impinged upon the prevailing flow field and as the distance between the

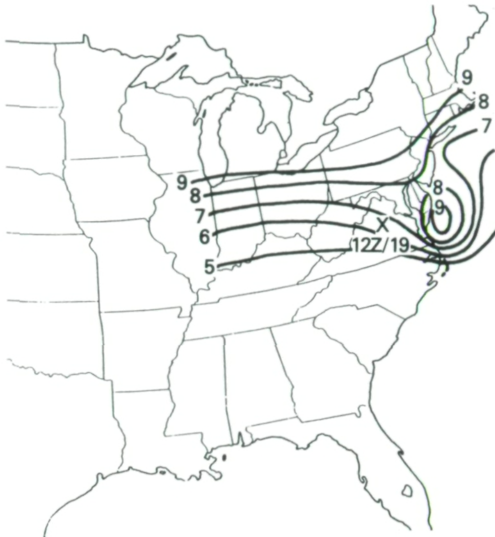

1637 GMT 19 FEBRUARY 1979
TOMS OZONE DISTRIBUTION

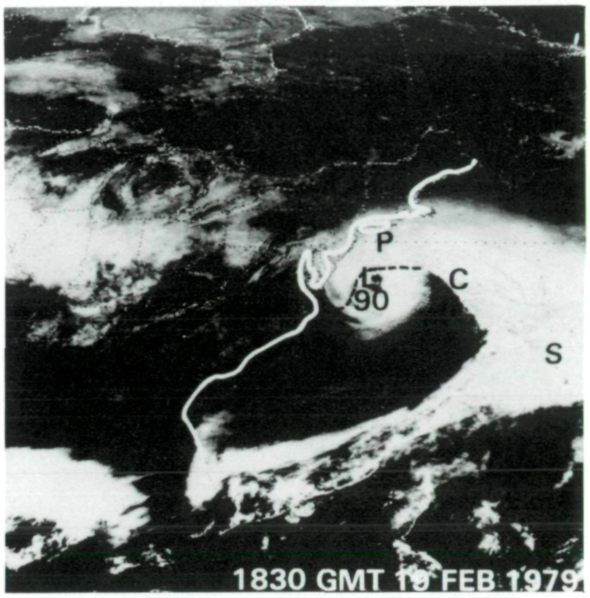

- TOTAL OZONE MAPPING SPECTROMETER (TOMS) USED TO DIAGNOSE TROPOPAUSE FOLDING PRIOR TO AND DURING RAPID DEVELOPMENT OF PRESIDENTS'S DAY SNOWSTORM
- TOMS CONFIRMS THAT DESCENDING STRATOSPHERIC AIR WAS INVOLVED WITH RAPID CYCLOGENESIS
- TOMS IS A POTENTIALLY USEFUL DIAGNOSTIC TOOL FOR INFERRING ANTECEDENT CONDITIONS FOR RAPID CYCLOGENESIS

Stratospheric — tropospheric exchange during rapid cyclogenesis.

trough and ridge located further downstream decreased. A transverse vertical circulation was associated with the intensifying jet streak and a low-level jet developed within the lower branch of the circulation along the coast of the southeastern United States. The low-level jet was responsible for increased heat and moisture transports and low-level convergence, which further aided in the development of snowfall and subsequent cyclogenesis.

These complex interactions between multilevel jet streaks and associated vertical circulations, in association with diabatic processes near the Earth's surface, contribute greatly to the formation of cyclones that result in heavy snowfall. Observational and modeling studies of these interactions have and can further aid in understanding the interrelationships of these processes and have and can further improve our capability to diagnose and forecast snowstorms capable of crippling the urban regions of the northeastern United States.

Contact: Dr. L. W. Uccellini
Code 610

Sponsor: Office of Space Science and Applications

MICROWAVE OBSERVATIONS OF PRECIPITATION

The measurement of precipitation is important in a variety of meteorological, hydrological, and climatological applications. For climatological purposes, global or regional coverage of monthly means with a spatial resolution of 200 to 500 km is sought. Daily totals with higher spatial resolutions are desired for hydrological and

agricultural purposes and for verification of regional and global numerical weather prediction (NWP) models. Higher spatial and temporal resolutions (20 km, 1 hr) are required for NWP model initialization, short-term forecasting, nowcasting, and warnings (e.g., flash flood warnings).

The need for a satellite component to the measurement or estimation of precipitation is obvious from the global coverage requirement—the need for precipitation information in areas not covered by conventional (rain gauge) or ground-based remote sensing (radar) techniques. This is especially true of oceanic areas, remote land areas, and even areas (such as mountainous terrain) where other techniques may have limitations. Because of the high time variability of precipitation in general and the existence of a diurnal cycle which needs to be defined for climatological purposes, deducing precipitation information from geosynchronous satellite data is also required.

Recently, we have examined data from a microwave radiometer (92 and 183 GHz) and have made observations on a high-altitude aircraft to determine the potential of these frequencies in the detection of precipitation and the estimation of rainfall rate. These frequencies are to be flown in low-Earth orbit and, because of the relatively high frequency, are candidates for a future geosynchronous satellite. The high frequencies are necessary because of limits on antenna size and the desire for reasonable resolution (20 km) from 35,000 km in space (geosynchronous orbit).

Results of examining the aircraft microwave data indicate that distinct convective features can be seen in the visible and 11 μm channels and also at the 92 and 183 GHz channels as areas of cold (100 to 230 K) microwave T_B (brightness temperature). The cold T_B values have been shown to be related to scattering by the precipitation ice in the convective cloud. In addition, the microwave channels have identified convective features that do not appear in either the visible or IR images because of overlying clouds indicating that these microwave frequencies may prove useful in delineating convection embedded in a large cirrus shield. Similar very cold features with intense convection have also been noted with an ocean background, despite the somewhat lower emissivity of the ocean at this frequency. The aircraft observations from flights in Montana and the midwestern United States clearly indicate that the 92 and 183 GHz channels can delineate cores of active convection.

The accompanying figures give plots of brightness temperature versus radar-determined rain rate for 92 and 183 ±9 GHz, respectively. The dots connected by the solid line are calculated values of brightness temperature from a radiative transfer model. It assumed realistic ice and liquid water profiles for various intensities of convection and rain rates. The x's, triangles, and circles represent a combination of the aircraft microwave observations and ground-based radar-estimated rain rates. The observations and the modeling results agree fairly well with a sharp drop in brightness temperature with increasing rain rate, especially between rain rates of 15 and 50 mm h^{-1}. The observations seem to reproduce the range of brightness temperatures from approximately 280 K to below 100 K that the radiative transfer calculations also show. The relationships between brightness temperature and rain rate are essentially independent of whether the observation is made over a land or ocean background,

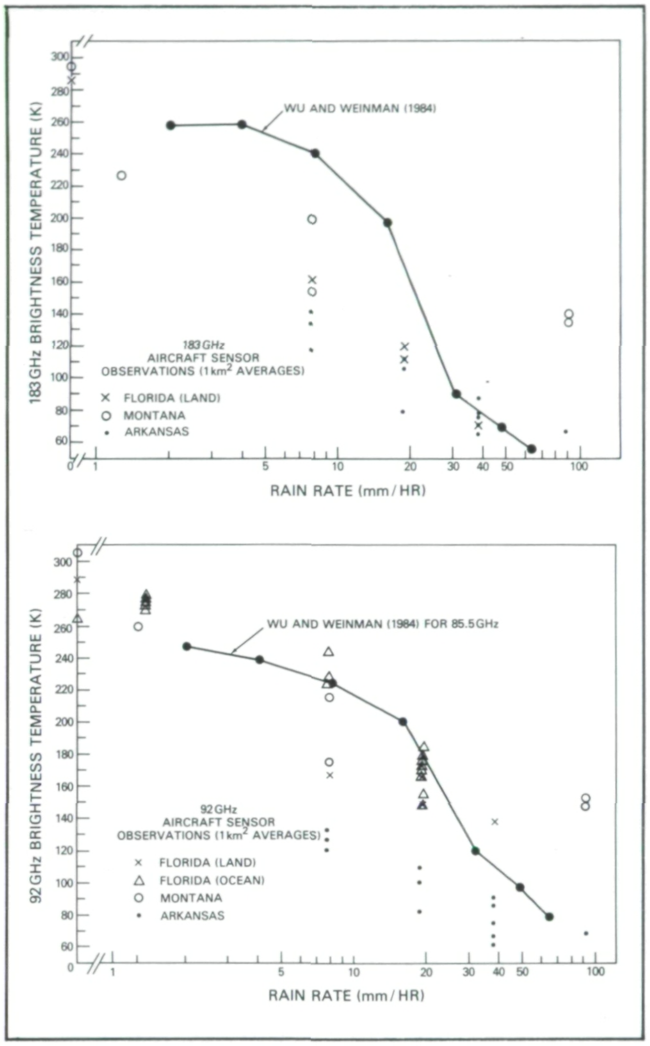

Plots of brightness temperature versus radar-determined rain rate.

except for a slight increase in brightness temperature from the no-rain situation over ocean to the very light rain rate (approximately 1.5 mm h^{-1}) situation. However, there are indications in both diagrams that there might be significant differences between the various locations or climatological regimes that may have to be taken into account by a more detailed examination of the relationships between rain rate, amount of cloud ice, etc. These two graphs represent the first observational results linking 92 and 183 GHz brightness temperature to observed rain rates. However, the upwelling radiance in these frequencies is a function of the amount and depth of ice in the cloud and is primarily coming from the upper few kilometers of the cloud, not the precipitating layer at the bottom of the cloud.

The theoretical and observational results indicate that the high-frequency microwave observations have great potential in identifying rain and estimating rain rate from space, even from geosynchronous altitude.

Contact: Dr. R. F. Adler
Code 610

Sponsor: Office of Space Science and Applications

SOLAR SYSTEM

RELATIONSHIP BETWEEN SOLAR RADIUS AND LUMINOSITY VARIATIONS FROM THEORY

From extensive work done by our group and elsewhere we have studied the relationship between changes of the solar radius and luminosity for solar models that use the mixing length theory of convection. A recent paper (Endal, Sofia, and Twigg, 1985) presents the most complete set of calculations carried out to date and also summarizes the results from previous work. We find that in order to identify the origin and the physical nature of the mechanism capable of producing radius changes as large as reported from the analysis of the solar eclipses of 1925 and 1979, i.e., $\Delta \ln R \approx 6 \times 10^{-4}$, it is necessary to compute, for each model, the quantities

$$S(t) = \frac{\delta \ell n\ R(t)}{\delta X}$$

where R is radius, and δX is the perturbation amplitude;

$$W(t) = \frac{\delta \ell n\ R}{\delta \ell n\ L}$$

where L is solar luminosity;

$$V(t) = \frac{\delta \ell n\ R/\delta t}{\delta \ell n\ L/\delta t}\,'$$

The first quantity, S(t), measures the sensitivity of the radius to a given perturbation. In particular, the results show that this sensitivity is so small for most physical perturbations that only one mechanism, a large, variable magnetic field at the base of the solar convection zone, can produce a $\delta R/R \gtrsim 10^{-4}$. W or V measure the relative changes of radius and luminosity depending on the nature of the perturbation. If two measurements are made before and after the perturbation, W applies; whereas, if the measurements are both made after the perturbation (i.e., if we are observing the system relaxing to the unperturbed state), then V applies. These are the most important of the parameters defined because they can be measured most accurately, and also because they link measured past radius changes with otherwise unmeasurable past changes of the solar luminosity.

An important result of our modeling work has been the unexpected finding of a prominent time scale in the perturbation phenomena of about 100 years. This is very different from the known time scale of billions of years for evolution, 10^5 years thermal time scale of the convection zone, a month for eddy turnover time, and a half-hour dynamical time scale.

The theoretical result that it is a variable (presumably dynamo-induced) magnetic field that is responsible for changes in the solar radius, as well as the newly identified time scale, is supported by our work on the determination of solar radius variations from eclipse observations. This work shows that, for the last two centuries, the

radius variations are, phasewise, the mirror image of the Zurich sunspot number which shows, as is well known, the ~ 90 year Gleissberg cycle variation.

The main conclusions from this work are:

1. The solar luminosity-radius link is indeed a fruitful way to look at the past history of the solar luminosity.

2. Theory is extremely useful in guiding our measurements and interpreting their meanings, but it cannot, alone, provide a unique answer for the radius-luminosity relation.

3. Observations required are: repeated simultaneous measurements of R and L accurate enough to obtain meaningful second-order differences.

Contact: S. Sofia
Code 610

Sponsor: Office of Space Science and Applications

AN ENSEMBLE OF SOLAR WIND DATA SETS

Theories of magnetohydrodynamic fluid turbulence are usually developed in terms of ensemble averages because the evolution of a turbulent fluid is never exactly repeatable. Ensemble averages represent those properties of the medium that remain essentially the same from one example (or "realization") of a system to another. Ensemble average quantities of interest in solar wind research include average values of the speed and magnetic field intensity, the two-point correlation function, and power spectra. However, spacecraft data are not usually compiled as ensemble averages, but rather as time averages. Thus, for example, the "average solar wind speed" refers to an average over a certain time interval and represents the value of the solar wind speed in a particular realization of conditions. This value will not necessarily be the same as an ensemble average speed which might, for example, be computed for high-speed solar wind streams. An ensemble of solar wind data sets is also useful for computing some two- and possibly three-dimensional properties of the solar wind. This can be done by accumulating measurements when the mean solar wind magnetic field for a specified length of time is directed, say, radially outward from the Sun, or perpendicular to the Earth-Sun direction, or in some intermediate direction.

We have constructed an ensemble of solar wind magnetic field and plasma velocity data sets using approximately 16 months of nearly continuous ISEE-3 data. Individual subintervals of these data, ranging from 15 hours to 15.6 days comprise the ensemble. The sole condition for including each subinterval in the averages is the degree to which each subinterval represents a weekly time-stationary process satisfying an ergodic theorem. From this ensemble average values of magnetic field variance and correlation length, and average solar wind speed have been computed. Both the correlation length and variance were found to have a systematic variation with subinterval duration, reflecting the important role of low-frequency fluctuations in the interplanetary medium due in part to the rotation of the Sun. The average value of the variances of the magnetic field components are in the approximate ratio 8:9:10, where the third component is the local mean field direction. This is in marked contrast to the time average values found during periods in which the solar wind contains large amplitude Alfvén waves. During those periods, the ratio of variances is closer to 5:4:1. Our results suggest that Alfvénic fluctuations may not be representative of the ensemble average properties of the solar wind, which appear to be closer to isotropy.

Contact: Dr. Melvyn L. Goldstein
Code 690

Sponsor: Office of Space Science and Applications

NEW INFORMATION ON THE COMPOSITION OF THE SOLAR WIND

Previous measurements of the solar wind, which is simply the outer part of the solar corona, have established in broad outline its chemical composition. However, 4 years of observation using the first interplanetary mass spectrometer on the spacecraft ISEE-3, have added considerably to our detailed knowledge. Observation has shown that fractionation takes place in the upper chromosphere and solar corona and allows the testing of theories describing the acceleration of material from the chromosphere of a star into its stellar wind. A new value for the He/O ratio indicates that oxygen may be depleted in the solar wind by approximately 40 percent, and the oxygen ions behave less like hydrogen than like the much more variable helium. Table 1 shows the best of the new numbers now available.

Table 1
Elemental Ratios in the Solar Wind

	Solar Wind	Ref	Solar Energetic Particles	Photosphere
He/O	75 ± 20		72 ± 6	108
Ne/O	0.17 ± .02		0.167 ± 0.015	0.187
He/Ne	470 ± 150**		429 ± 37	580
C/O	0.70 * 0.55		0.47 ± 0.04	0.060

*With the assumption that the ionization of C freezes in at a temperature $2 \cdot 10^5$ K below the oxygen freezing-in temperature. The first value is derived with a solar Mg/O ratio. For the second value, we assume an enrichment by a factor of 3 of the Mg/O ratio in the solar wind.

**Geiss et al., Apollo 16 Preliminary Report, NASA SP-315, 1972.

Contact: Keith Ogilvie
Code 690

Sponsor: Office of Space Science and Applications

POLAR WARMING IN THE MIDDLE ATMOSPHERE OF MARS

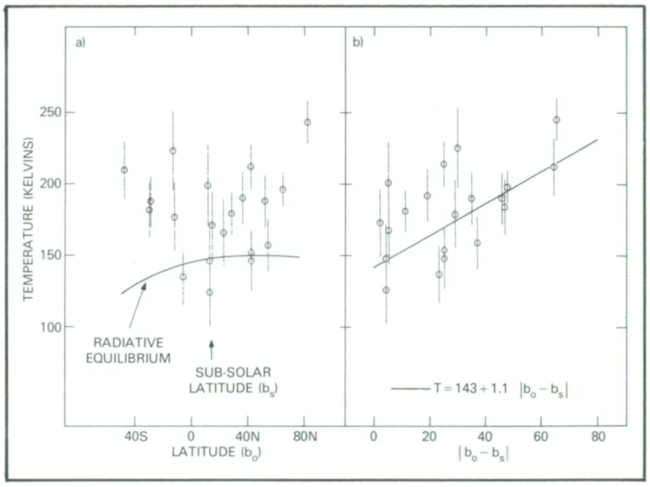

Latitudinal temperature dependence, where temperatures have been derived from the total intensity of the emission.

Common experience tells us that the atmosphere of the Earth becomes colder as we progress toward the poles, due to the lower solar insolation at high latitudes. However, this normal latitudinal gradient in the Earth's atmospheric temperature is not present at all altitudes. In the terrestrial mesosphere, near 80-km altitude, the highest temperatures are seen near the winter pole, and the lowest temperatures are observed near the summer pole in a region where noctilucent cloud formation occurs. This pole-to-pole temperature gradient is due to heating and cooling by a dynamical process. Insolation in the summer hemisphere heats the atmosphere at low altitudes, causing parcels of gas to rise and cool adiabatically. Subsidence in the winter hemisphere causes a corresponding adiabatic heating, and this dynamical process results in a high-altitude reversal of the temperature gradient.

A latitudinally reversed temperature gradient has now been observed in the middle atmosphere of Mars, near 70-km altitude. This has been determined from ground-based observations of nonthermal CO_2 emission which occurs in the 10-micron spectral region. These observations utilized the ultra-high-frequency resolution available with the laser heterodyne technique. Although this emission is nonthermal in origin, it is sensitive to the atmospheric temperature in several ways. First, the frequency width of the emission is a direct measure of the magnitude of molecular thermal motions. Also, the total intensity in the emission is temperature sensitive through the temperature sensitivity of its near-infrared pumping source. After correction for viewing geometry and other effects, both the frequency width of the emission and its total intensity are found to increase toward the Martian poles. This results in the latitudinal temperature dependence shown in the figure, where temperatures have been derived from the total intensity of the emission. The radiative equilibrium temperature for a pure CO_2 atmosphere is shown in comparison. Large departures from the radiative equilibrium temperature, particularly in the southern hemisphere near 40° S latitude, can be seen. The minimum temperature occurs near the subsolar latitude, and this is attributed to adiabatic cooling on the rising branch of a circulation which is symmetric about the subsolar latitude. This symmetry about the subsolar

point does not occur in the terrestrial case, because the dust-laden CO_2 atmosphere of Mars absorbs incident sunlight on a much faster time scale than does the relatively transparent atmosphere of Earth.

Contact: Dr. Drake Deming
Code 690

Sponsor: Office of Space Science and Applications

COMPOSITION AND STRUCTURE OF JUPITER'S TROPOSPHERE

The Voyager infrared experiment (IRIS) returned thousands of spectra of Jupiter covering the 4- to 5-μm wavelength region. One portion of this spectrum provides unique information about the state of Jupiter's atmosphere well below the visible clouds. At 5 μm the major gases H_2, CH_4, and NH_3 absorb very weakly, and, in selected hot spot regions, the cloud opacity is also very small. We therefore can "see" about 10 times deeper into Jupiter's atmosphere at 5 μm than at visible or other infrared wavelengths. In addition, a number of molecules important in Jovian chemistry have very strong vibration-rotation transitions at 5 μm. This permits the detection of some molecules at the parts-per-billion level.

Thus far seven molecules have been detected in Jupiter's 5-μm spectrum. These can be divided into three categories to emphasize their role as tracers of physics and chemistry in Jupiter's atmosphere. The abundance of CH_4, NH_3, H_2O, and CH_3D at deep levels in Jupiter's atmosphere can provide us with a measure of the total inventory of carbon, nitrogen, oxygen, and deuterium in Jupiter. Comparing these elemental and isotopic abundances with the solar atmosphere constrains models of Jupiter's formation from the solar nebula. Two of the molecules NH_3 and H_2O, condense to form clouds in Jupiter's troposphere. Knowledge of their abundance below the clouds determines the pressure level where condensation takes place as well as the cloud mass. Finally, three additional gases PH_3, CO, and GeH_4 are not expected to be detectable at all in the upper troposphere. Their presence can best be explained by rapid vertical transport from great depths.

Analysis of the IRIS spectra of Jupiter's belts and zones, in conjunction with airborne spectra obtained by Dr. Harold P. Larson of the University of Arizona, has led to a greatly improved model of Jupiter's deep atmosphere. Jupiter is enhanced in carbon and nitrogen by factors of ~ 3 and 1.5, respectively, compared to the Sun. Oxygen, on the other hand, appears to be depleted by a factor of 40 with respect to the Sun, at least in the observable part of Jupiter's atmosphere. A massive cloud composed of NH_4SH, and perhaps H_2O ice, is inferred to be present at the 2-bar level on Jupiter in order to fit the IRIS data. This cloud is very thick in Jupiter's zones but is much thinner in belts and hot spot regions. A deeper H_2O cloud at 5 bars, proposed in some previous models, is inconsistent with the IRIS data.

Contract: Virgil G. Kunde and Gordon Bjoraker
Code 690

Sponsor: Office of Space Science and Applications

DISEQUILIBRIUM OF ORTHO AND PARA H_2 ON JUPITER

Molecular hydrogen is the dominant constituent of the atmospheres of Jupiter, Saturn, Uranus, and Neptune. In order to establish the thermodynamic properties of these atmospheres, it is necessary to understand the behavior of H_2 under conditions appropriate to these planets. The molecule possesses two modifications: the ortho state, corresponding to parallel proton spins; and the para state, with antiparallel proton spins. The spin states are quantum mechanically coupled to the rotational energy levels of the molecule such that the triplet ortho and singlet para states are paired with levels of even and odd rotational quantum numbers, respectively. Since transitions between adjacent rotational states are highly forbidden, a parcel of pure H_2, transported from deeper layers where the temperature exceeds 300 K, will tend to retain its "normal" 3:1 high temperature limit associated with the proton spin statistical weights rather than achieving the thermal equilibrium value associated with the cooler temperatures of the higher atmospheric levels. The thermal equilibration time for pure H_2 is $\sim 10^8$ s, but this time can be substantially shortened by catalytic effects associated with admixtures of paramagnetic molecules or paramagnetic sites on surfaces such as might occur on atmospheric cloud particles. The specific heat of H_2 is strongly dependent on the degree to which thermal equilibration occurs. In addition, when H_2 is transported from a region of higher temperature to a lower temperature region and then permitted to

equilibrate, energy is released in the form of heat. Thus, under appropriate conditions, the equilibration of H_2 can play a role similar to the latent heat release of water in the Earth's atmosphere. Since the thermodynamic behavior of the atmospheres of the giant planets is dependent on the relative magnitudes of the equilibration and dynamic transport times, neither of which is well known, it is of considerable importance to determine observationally the ortho-para ratios in these atmospheres.

The infrared spectrometers carried on the Voyager spacecraft obtained measurements over a spectral region which includes the pressure-induced lines of H_2 centered at 354 cm^{-1} and 602 cm^{-1}. The lower frequency line corresponds to transitions associated with para states while the line at 602 cm^{-1} results from transitions between ortho states. By combining measurements from the two lines, it was possible to obtain estimates of the ortho-para ratio in the upper troposphere of Jupiter. It was found that at low latitudes substantial departures from thermal equilibrium occur, while at higher latitudes the ratio approaches the equilibrium value. No obvious correlation was found between the ortho-para ratio and indicators of atmospheric cloudiness, suggesting that the equilibration time is long, probably approaching that of pure H_2.

The measurements have implications for the meteorology of the upper tropospheric levels where the disequilibrium is observed and also by inference for the deeper levels which are not directly observed. In the upper troposphere, the disequilibrium at low latitudes suggests the presence of a large-scale meridional cell with upwelling near the Equator on a time scale comparable to or less than the H_2 equilibration time, with poleward horizontal transport and descending motion at high latitudes. Such a cell could occur in response to differential absorption of solar energy in the upper troposphere. At deeper levels, the dynamic behavior is believed to be dominated by buoyancy-driven convection, which provides the outward heat flux associated with the internal heat source which the planet is known to possess. The long thermal equilibration times for H_2 suggested by the observations will result in an enhanced efficiency for the convection process since most of the heat will be transported in the form of a latent heat flux. As a consequence, less vigorous overturning is required to provide the necessary heat transport.

Contact: B. J. Conrath
Code 690

Sponsor: Office of Space Science and Applications

ANALYSIS AND MODELING OF ATMOSPHERIC DYNAMICS ON JUPITER AND SATURN

Voyager imaging and infrared observations of Jupiter and Saturn have provided detailed global maps of their cloud-top winds and thermal fields aloft. Both planets show super-rotating equatorial currents, and at higher latitudes, an axisymmetric and apparently long-lived pattern of alternating westward and eastward jet streams. The observations also suggest the presence of planetary wave activity, eddy momentum exchange, and small-scale convection. Altogether, these observed or inferred features of the Jovian meteorology span at least four decades in space and time as indicated schematically in the accompanying figure.

The analysis of these phenomena must take account of the internally heated, fluid structure of Jupiter and Saturn, which may more nearly resemble a stellar interior than a terrestrial atmosphere. It is puzzling that a fully three-dimensional, deeply convective fluid planet would be so dominated by a zonal jet system with horizontal scales more typical of two-dimensional motion. The special nature of the implied coupling between the presumably rapid, small-scale convection of the interior and the apparently permanent large-scale flow at the cloud tops poses an outstanding challenge to theoretical understanding. One line of investigation assumes that in fact the wind patterns are the effect of interior convection organized into multiple counter-rotating cylinders, concentric with the planetary spin axis, and extending for thousands of kilometers throughout the full depth of the molecular fluid envelopes. This picture does not by itself, however, account for such nonzonal structures as Jupiter's equatorial plumes and Great Red Spot. It also fails to take account of several potentially strong phase change effects such as cloud condensation and the ortho-to-para conversion of hydrogen which are expected to occur at shallow atmospheric levels.

We are developing dynamic models designed to explore the alternative picture of large-scale Jovian meteorology within a thin atmospheric layer. Unlike previous thin layer models for Jupiter, ours does not assume a rigid lower boundary or a strongly stable lapse rate for the potential temperature. Instead, the wind layer is assumed to be very weakly stratified in potential temperature, and vertical motions are constrained by convective mixing of sensible and latent heat across a level of thermodynamic phase changes. We have shown that the resulting system maintains a two-dimensional structure by a self-similar variation of horizontal winds with altitude. The model predicts

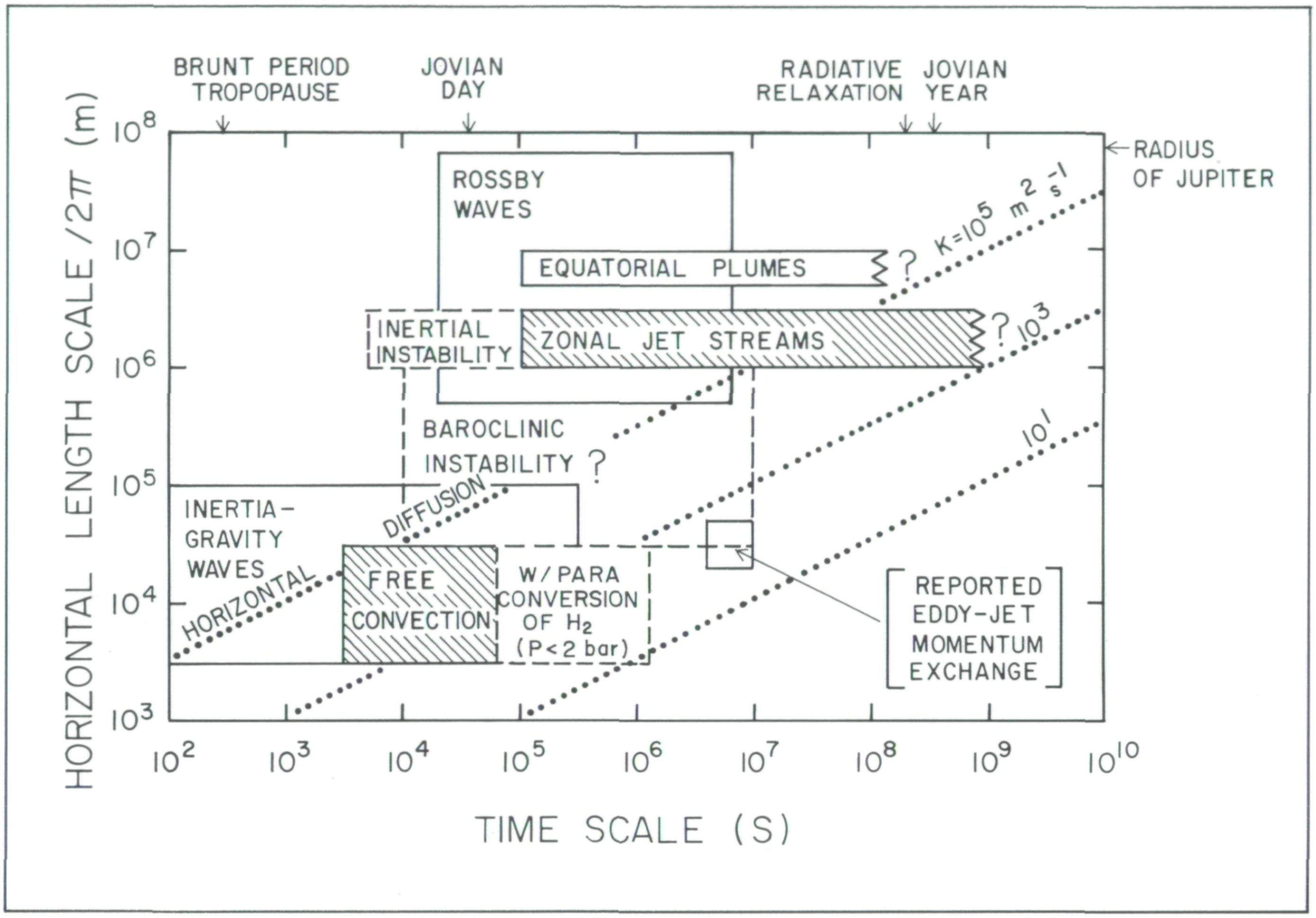

Space-time regime diagram for dynamic features in Jupiter's atmosphere.

that the onset of horizontal shear instability will occur for westward jet stream curvatures almost three times as high as in terrestrial wind systems but close to the observed maximum values on Jupiter and Saturn. The assumed thermodynamic forcing prescribes an instability to vertical motions for low-frequency oscillations but reduces to statically stable control of vertical motions for high-frequency oscillations. Numerical solutions of the thermally forced model, corresponding to neutral stability for horizontal wind shear, bears a remarkable resemblance to the observed latitudinal profile of Jupiter's jet streams.

If the thin layer picture for Jovian meteorology is correct, then the observed wind patterns may be the equilibrium state of continual horizontal shear adjustment to convective forcing of the planetary interior. Continuing studies with these models should provide an important guide to the further analysis of Voyager data, as well as the expected reconnaissance of the Jupiter meteorology by the Galileo mission.

Contact: Dr. Michael Allison
Code 640

Sponsor: Office of Space Science and Applications

IO PLASMA TORUS ELECTRONS: VOYAGER 1

The Io plasma torus is a giant cloud of ionized gas that extends all the way around Jupiter with Io, situated 5.9 R_J from Jupiter's center (1 R_J is one Jovian radius = 72,000 km), near its center. The plasma torus can be subdivided into two distinct regions, the cold inner torus (4.9 $R_J < r < 5.4$ R_J), and the hot outer torus (5.4 $R_J < r <$ 7.7 R_J) with the cold and hot parts having vertical half widths relative to the centrifugal equator of about 0.25

R_J and 1.0 R_J, respectively. Nearly spatially coincident with the plasma torus is a neutral cloud of Na, K, S, O, and SO_2 which can also extend around Jupiter with doughnut geometry. This cloud of neutral and ionized gas is believed to originate from Io as a result of tidal interactions between Jupiter and Io with subsequent volcanic emission of neutral gas. The Io torus is unique because of the large radiative ultraviolet emission $> 2 \times 10^{12}$ W, complex ion and neutral composition (0 to 0^{+3}, S to S^{+4}, Na, Na^+, K and K^+), and the fact that it represents the first analog of an astrophysical object, interstellar cloud or nebula, that is close enough to be well observed from the Earth and probed by spacecraft. The Voyager 1 Plasma Science Experiment (PLS) has provided *in situ* observations of the ion and electron components of the torus plasma. After a lengthy analysis, the electron observations, covering the energy range from 10 eV to 5950 eV, are now providing new and exciting results. They show the presence of a neutral cloud centered on Io with radial extent ≈ 1 R_J inferred from the localized cooling of the electrons measured during the outbound pass when the spacecraft came within 11 Ionian radii of Io. It is believed that this neutral cloud is the source of the plasma torus. The primary energy source for the UV emission is believed to be electron impact or charge exchange between the neutrals and the ions which are picked up by Jupiter's corotating magnetic field. Within the hot torus the thermal electrons have temperatures $T_c \approx 5$ eV, while $T_c < 1$ eV is observed within the cold torus. These conclusions allow better modeling of line-of-sight observations of the torus made by ground-based and satellite instruments at Earth. The suprathermal electrons with characteristic temperatures $T_H \approx 500$ eV make up $\lesssim 0.1$ percent to the total electron density. Even so, they contribute significantly to the ionization of S^{++} and 0^+ and almost all the ionization of S^{+++} and 0^{++} within the hot torus. Since no suprathermals are observed within the cold torus and a large drop in suprathermal electron fluxes outside Europa's L shell at 9.4 R_J is observed, the hot electrons are believed to be locally produced within the hot torus. The inner boundary is caused by cooling resulting from Coulomb collisions between the thermal and suprathermal electrons as they diffuse radially inward, and satellite "sweeping" by Europa as they diffuse radially outward. Overall, the plasma electron observations are providing new constraints upon theoretical models to provide a more consistent picture of the Io torus.

Contact: Edward C. Sittler, Jr.
Code 690

Sponsor: Office of Space Science and Applications

SATURNIAN KILOMETRIC RADIATION AND THE CENTRIFUGAL FLUTE INSTABILITY

A striking difference between the kilometric radiation emitted by the Earth's plasma environment and that of Saturn is the very different peak emission regions in the two planets' magnetospheres. Whereas the Earth's kilometric radiation originates in the near-midnight auroral zone, radiation from Saturn comes from a high-latitude near-noon source. From an examination of Voyager radio emission, magnetometer, and plasma data, an explanation has been developed for this difference. The figure summarizes the observations and shows how the observed source region of the radio emissions may be mapped using the Z3 magnetic field model into the Saturnian equatorial plane in the vicinity of what plasma observations indicate are detached regions of the plasmasheet. Large amplitude MHD waves are also detected by the magnetometer in the region of detached plasma and peak near the outer edge of the plasmasheet. The waves are primarily azimuthal near the Saturnian equatorial plane but are field-aligned at higher latitudes.

The plasma mass density measured at the edge of the plamasheet indicates that centrifugal force is sufficient to cause plasmasheet detachment and loss down the Saturnian magnetotail. The plasma detachment causes a sharp gradient at the plasmasheet edge and also eliminates the free energy source of planetward hot electron transport that drives auroral kilometric emission at the Earth. As the sharp plasmasheet edge is rotated toward the noon meridian, the density gradient steepens owing both to magnetic field compression and enhanced plasma mass density due to photoionization of the exospheric neutrals of Saturn's moons. Near the noon meridian the steepened density gradient and centrifugal force of Saturn's rapid rotation combine to drive the centrifugal flute instability, which produces the detached regions and large-amplitude azimuthal MHD waves. At higher latitudes, due to the limited latitude extent of the plasmasheet, the instability gives rise to large-amplitude field-aligned MHD waves. These waves can accelerate electrons along field lines and provide a free energy source for Saturnian Kilometric Radiation (SKR) similar to that which powers the Earth's Auroral Kilometric Radiation. Solar wind control of SKR follows as a direct consequence of the need for keV shock-heated electrons to exist outside of the plasmasheet.

Contact: Steve Curtis
Code 690

Sponsor: Office of Space Science and Applications

ORIGINAL PAGE IS
OF POOR QUALITY

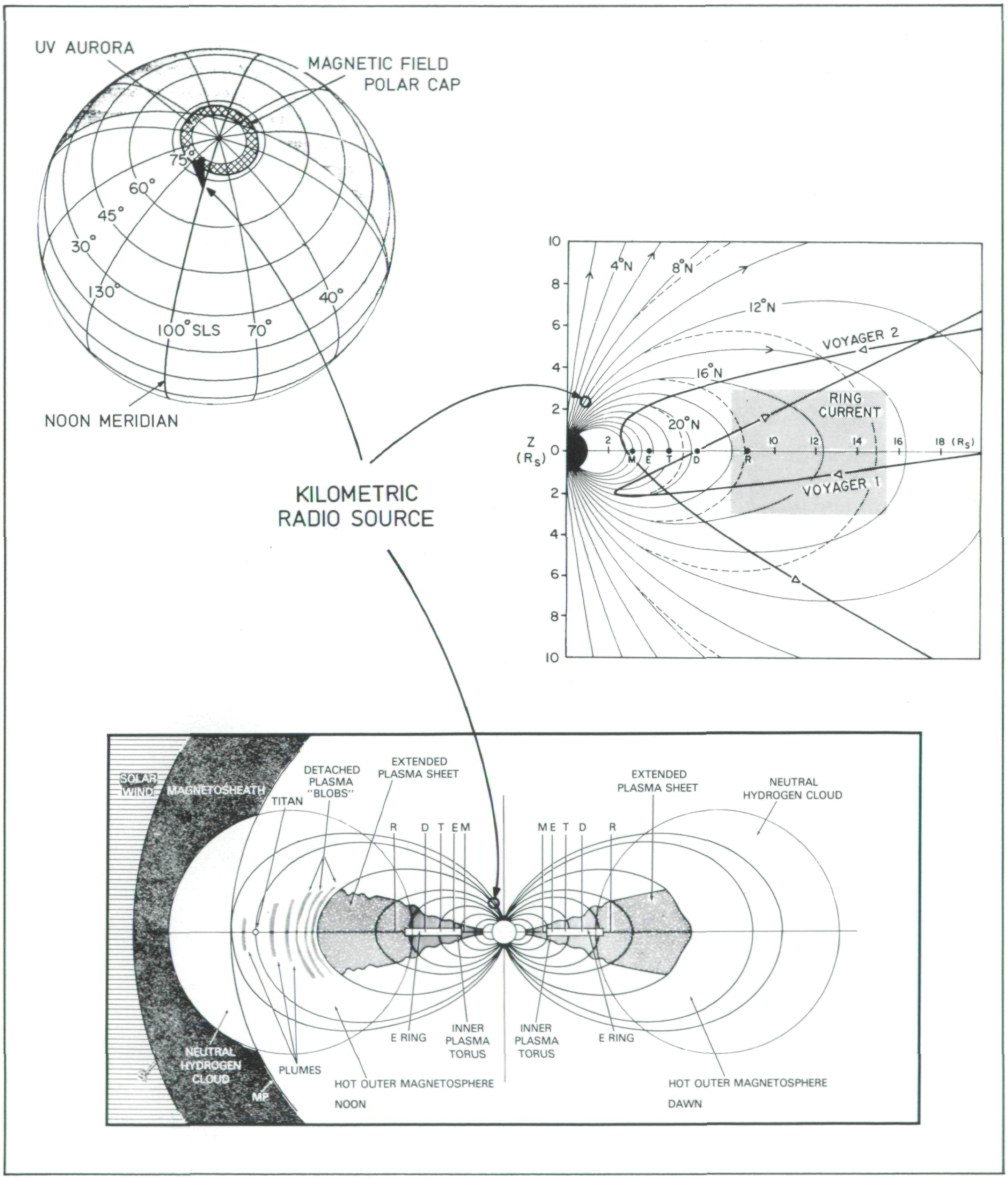

Saturnian kilometric radiation, source region.

SATURN AND THE RING RAIN

Saturn is unique among all the magnetized planets for which measurements are available in the intriguing spin symmetry of its magnetic field. The magnetic field thus provides a natural coordinate system with which locations at any point on Saturn's surface can be mapped uniquely to corresponding locations in the ring plane. A remarkable relationship exists between features in Saturn's rings and atmosphere, when both are examined in the magnetic coordinate system that links them.

Latitudinal variations in images of Saturn's disc (see figure), upper atmospheric temperatures, and ionospheric electron density anomalies are found in magnetic conjugacy with (i.e., magnetically linked to) features in Saturn's ring plane. We suggest that these latitudinal variations are the result of a variable influx of water, transported along magnetic field lines from sources in Saturn's rings. The enhanced water influx at specific latitudes leads to a localized depletion of stratospheric haze, evident as narrow dark bands in visual images of Saturn's disc; a locally depleted ionosphere, deduced

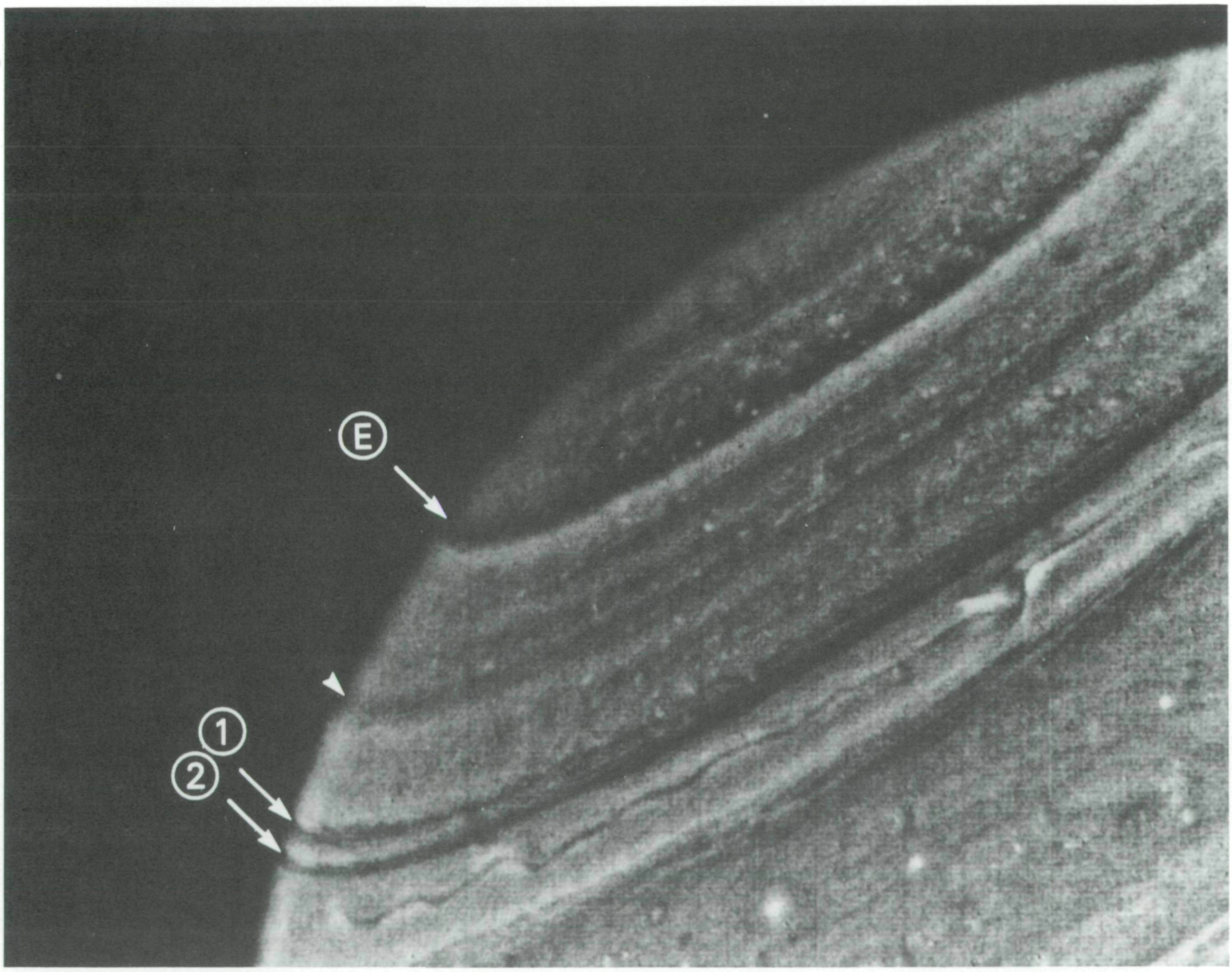

Voyager 2 high contrast (green) image of Saturn's northern hemisphere. The North Pole is at the top of the figure; just visible at the bottom of the figure lies a dark band of the north equatorial belt at ~20°N latitude. The two parallel dark bands near 50°N map to the inner edge of Saturn's B ring at 1.525 Saturn radii (2) and 1.62 Saturn radii (1), where an electromagnetic erosion process transports water from the rings, along magnetic field lines, to the planet's surface. An additional dark band to the north (dart) marks the inner edge of Saturn's A ring. Further northward, a wide dark band (E) is found where field lines link the icy satellite Enceladus and the E ring with the planet's surface.

from escaping radio emissions; and (locally) elevated upper tropospheric temperatures, observed by the Voyager infrared investigation. Quantitative estimates of the water influx deduced from a detailed ionospheric model (*Nature 312*, 136 1984; with H. Waite at MSFC) lead to an erosional time constant of 30 $\times$ 10^6 years for the inner B ring. This erosion process can evidently be observed directly in images of Saturn's disc, suggesting that present-day observations of Saturn's disc (e.g., space telescope) may potentially reveal details of the erosion history that formed the rings.

Contact: J. E. P. Connerney
Code 690

Sponsor: Office of Space Science and Applications

REACTION RATE KINETICS OF H + C_4H_2 AND IMPLICATION FOR ATMOSPHERIC MODELING OF TITAN

A greater variety of larger hydrocarbon species is observed on Titan compared to Jupiter or Saturn, because hydrogen molecules, an abundance of which inhibits larger hydrocarbon formation, are mainly lost from the atmosphere of Titan rather than being retained as in the atmospheres of the giant planets. The conversion of hydrogen atoms into hydrogen molecules is the key reaction process which brings about this contrast in atmospheric constituency. Diacetylene (C_4H_2), an intermediary product from the photodecomposition of methane in the atmosphere of Titan, has been postulated to be the major catalyst in this conversion process. Consequently, in collaboration with M. Mitchell and L. Stief, we have determined the absolute rate constant for the reaction of H + C_4H_2 as a function of temperature and pressure. The method involved flash photolytic production of hydrogen atoms, followed by time-resolved measurement of resonance fluorescence signal of the hydrogen atoms as they decay by reaction with diacetylene. Results from the rate constant data show the reaction of H + C_4H_2 to be temperature dependent, moderately rapid, and independent of total pressure.

Implications of this laboratory study for modeling the atmosphere of Titan are: (1) Low-temperature data relevant for the atmospheric conditions are provided; (2) Relative to the slower reaction rate of hydrogen atoms with acetylene, the reaction of hydrogen atoms with diacetylene is an effective pathway for conversion of hydrogen atoms to hydrogen molecules; and (3) C_4H_2 is important in both the formation and survival of larger unsaturated hydrocarbon species.

Contact: Dr. David F. Nava
Code 690

Sponsor: Office of Space Science and Applications

THE CLOSE APPROACH OF COMET IRAS–ARAKI–ALCOCK

IRAS detected a comet on April 26, 1983, at less than half the distance to the Sun. Later designated Comet IRAS-Araki-Alcock, this rather low-mass object would become important only because its orbit brought it to within 12 times the Earth-Moon distance, the closest approach of any comet in modern times. This close approach afforded a unique opportunity to spatially resolve molecular and atomic gaseous emission emanating

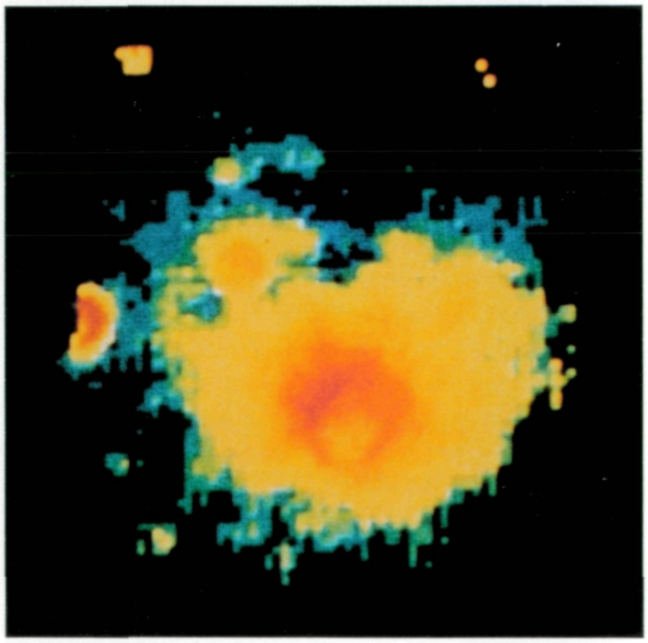

Shown is the spectral line emission of diatomic carbon observed in Comet IRAS-Araki-Alcock with the colors blue, yellow, and red in order of increasing molecular abundance. Note that the red central region contains a "yellow hole" which is ~2000 km across at the distance of the comet and represents a deficiency of diatomic carbon molecules. The "ear-like" object on the left of the comet is a nearby bright star whose residual image is distorted due to the telescope's tracking of the comet which was moving relative to the star.

from the region known as the inner coma, which immediately surrounds the comet's nucleus.

The differential photometry camera developed at GSFC was used on May 10, 1983, to observe Comet IRAS-Araki-Alcock to determine the spatial distribution and abundance of diatomic carbon, an important species of the inner coma. The preliminary results revealed the unexpected discovery of a deficiency of diatomic carbon within a radius of ~1000 kilometers of the nucleus, which itself is at most a few kilometers in diameter. The next few years were spent analyzing these results to determine if the observations could be explained by some unknown instrumental effect or an artifact of the data reduction process; upon submission to the international journal *Icarus*, another independent observing team confirmed the GSFC results.

No cometary model to date explains the results, but there are at least several alternative explanations which may account for the central depression of diatomic carbon: (1) Sufficient dynamical activity may give rise to "chunks" of material which fly off and finally sublime far from the nucleus, producing diatomic carbon, or (2) the central diatomic carbon deficiency may represent unobserved progenitor molecular production processes, or (3) if the production rate of diatomic carbon is not a constant but, in fact, decreases with time, then a central deficiency could occur. In any event, these fortuitous observations of an unspectacular comet's close approach to Earth tell us that we have much more to learn of the evolution of comets and that the closer we can get to them through space-borne missions, the better.

Contact: Dr. Jan M. Hollis
Code 680

Sponsor: Office of Space Science and Applications

WHAT KILLED THE DINOSAURS?

In recent years, abundant evidence has been brought forward to show that the disappearance of the dinosaurs and many other forms of life some 65 million years ago was associated with a deposit of excess iridium and other noble metals. These elements are thousands of times as abundant in meteorites as in the Earth's crust; and it has been widely believed that both the extinctions and the noble metals resulted from the impact of a giant meteorite, which formed a huge crater that cannot be found.

Further studies have found evidence connecting the extinction of the dinosaurs (and at least one smaller extinction some 34 million years ago) with the fall of showers of tektites. Tektites are small glass meteorites, which often contain excess amounts of the noble metals. This fact has led to the development at Goddard of a very different theory for the extinction of the dinosaurs.

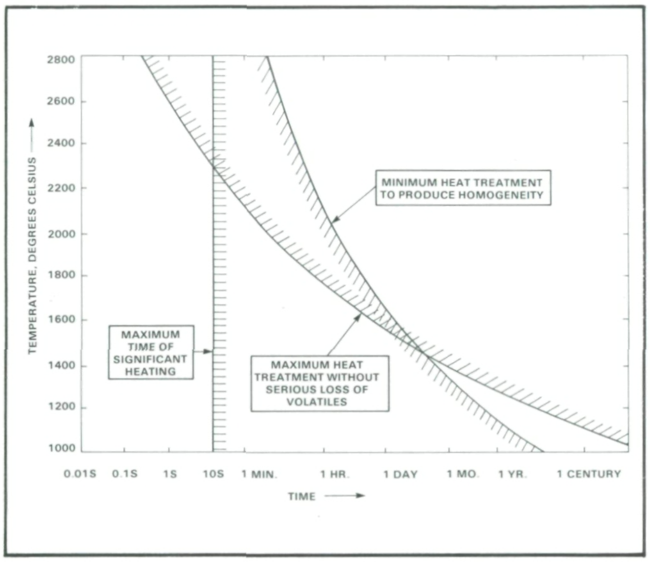

The thermal problems of tektite production.

The fundamental point is that most tektites are composed of homogeneous, water-poor, bubble-free glass, often in centimeter-sized pieces. The evidence that the process which destroyed the dinosaurs was also responsible for the origin of tektites is an important clue to the nature of the process. Although it is widely believed that tektites are made by shock heating during the impact of giant meteorites on the Earth, the fact is that studies at Goddard indicate that the period of heating during an impact is too brief, by a factor of 10,000 or more, to produce tektite glass from the appropriate (sandy) sediments. The elimination of bubbles while the tektite is following a ballistic trajectory from the hypothetical impact crater is also inexplicable, since buoyant forces would be zero. The impact idea does not work. The only hypothesis which appears to be capable of explaining this

glass is that of ejection from a lunar volcano. Some of the ejecta would fall to the Earth (the tektites) while some would go into orbit around the Earth. The orbiting dust and pebbles would evolve into a ring system like the rings of Saturn. (In a similar way the E ring of Saturn is thought to be forming from matter ejected by the Saturnian satellite Enceladus.) Probably the volcano erupted more than once. Each of the rings so made would be destroyed by air drag and radiation drag over a period of 100,000 years or so; thus, the lifetime of the system would be a few hundred thousand years.

The ring system altered the environment, it is thought; the dinosaurs did not respond to the challenge as well as the mammals, and so were driven to the wall by competition.

Contract: Dr. John A. O'Keefe
Code 680

Sponsor: Office of Space Science and Applications

ATLAS OF COMET HALLEY, 1910 II

As we prepare to study Comet Halley, 1986, knowledge of the behavior of the comet in 1910 will be very valuable. An atlas of photographs from 1909-1911 of the 1910 apparition compiled from observations made at 15 observatories around the world is being compiled. On some days there are up to 50 images from 10 observatories, yielding nearly continual coverage. These show characteristics of the ion and dust tails as well as details near the nucleus. Visual observations from 1835 and 1910 show structure at high spatial resolution in the head of the comet and complement the photographic images. For the first time there will be a record of the gradual development and of sudden changes in Comet Halley during the nearly 2 years of observation.

Contact: Dr. B. Donn
Code 690

Sponsor: Office of Space Science and Applications

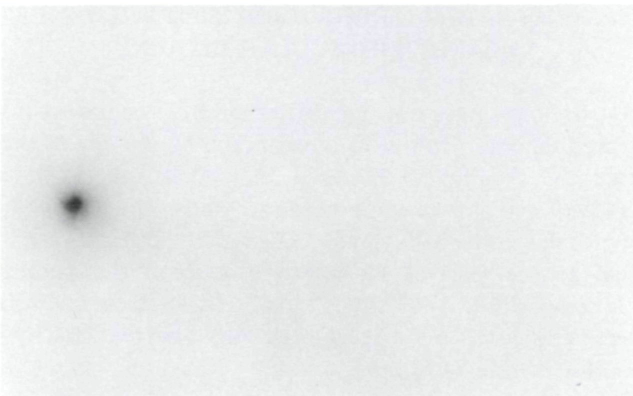

(May 13, 1910) Lick Observatory showing details of structure near the comet nucleus.

(May 22, 1910) Lick Observatory showing details of structure near the comet nucleus.

(April 21, 1910) Harvard Observatory photograph showing complex tail structure.

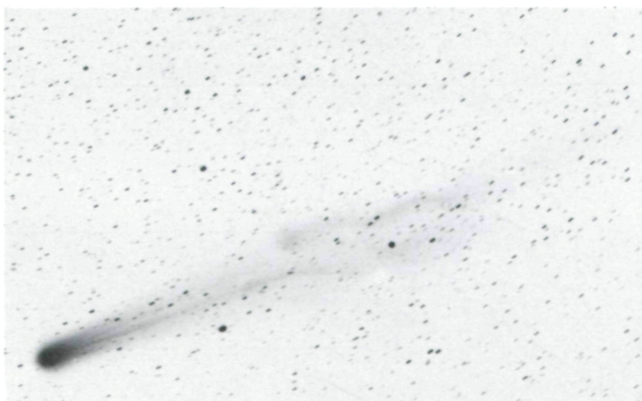

(June 7, 1910) Córdoba Observatory, Argentina, showing another variety of complex tail structure.

ASTRONOMY

INTERSTELLAR MOLECULES: THE FIRST ORGANIC RING IN SPACE

The cyclopropenylidine molecule C_3H_2 (shown in the figure), a highly reactive planar ring long sought by organic chemists, has been identified by the Goddard Institute for Space Studies (GISS) astrophysics group in many molecular clouds in the Milky Way, and in a laboratory discharge as well. The ring is so conspicuous in one of its strongest transitions at a wavelength of 1.64 cm that it may already have been detected in an extragalactic object, the peculiar dust-rich galaxy M82.

In spite of its highly exotic character, C_3H_2 ranks as one of the most securely identified molecules in interstellar space. The GISS investigators have assigned a total of 27 rotational lines: 22 in a laboratory glow discharge through acetylene and helium, 11 in astronomical sources, 6 in both, and have measured the spectroscopic constants so accurately that the most important spectral lines in the radio and far infrared can now be calculated to an accuracy of better than 1 part per million (or in terms of radial velocity to better than 300 m/sec—adequate for all contemplated astrophysical applications).

There is reason to believe that C_3H_2 in the interstellar gas is the daughter of another three-membered ring not yet observed, the $C_3H_2^+$ ion, a symmetrical, nonpolar equilateral triangle according to theory, which is thought to be the carrier of the well known peak at a molecular weight of 39 in mass spectrometers. The reaction leading to C_3H_2 is simple dissociate recombination, which has a very large cross section: $C_3H_3^+ + e \rightarrow C_3H_2^+ H$. There is no hope of finding $C_3H_3^+$ with radio telescopes (because of its lack of a dipole moment and hence a rotational spectrum), but there are vibrational transitions which may be detectable in the IR. $C_3H_3^+$ is the simplest conceivable aromatic system, and is of particular interest to theoretical chemists for this reason.

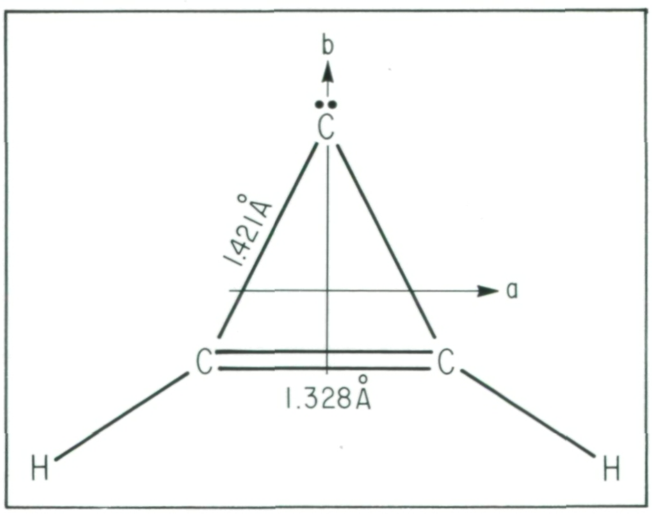

Molecular geometry of C_3H_2.

Contract: Dr. Patrick Thaddeus
Code 640

Sponsor: Office of Space Science and Applications

INFRARED CIRRUS IDENTIFIED WITH NEARBY MOLECULAR CLOUDS

Astronomers have now identified some of the patchy infrared emission found to cover much of the sky in the recently completed Infrared Astronomical Satellite (IRAS) sky survey with nearby clouds of interstellar molecules in the Milky Way Galaxy. These results show that at least part of the mysterious ubiquitous patchy emission, dubbed as "cirrus" by the IRAS scientists, will serve as a guide to the nearest regions of current star formation within our Galaxy.

One of the intriguing discoveries of the IRAS satellite, flown in 1983 as a joint US/Netherlands/United Kingdom project, was patchy clouds of very cold cosmic dust (typically 30 Kelvin or -405 Fahrenheit) similar in appearance to clouds in the Earth's atmosphere. The immediate challenge was to determine the location of the dusty material: Is it within the solar system, or in interstellar space within our Galaxy? The question of whether any of the material lies within the solar system has yet to be answered. Initial comparisons by IRAS scientists with the known distribution of clouds of interstellar atomic hydrogen gas showed that some of the "cirrus" emission does arise from dust in these interstellar atomic gas clouds.

Recently, several groups have used different approaches to show that some of the cirrus emission also arises in interstellar clouds of molecular gas near the Sun. This

is particularly exciting because star formation is invariably associated with molecular gas clouds. One group (Michael Hauser, Goddard Space Flight Center and a member of the IRAS Science Working Group; Janet Weiland, Applied Research Corporation; Loris Magnani and Leo Blitz, University of Maryland; Richard White, Computer Sciences Corporation; and Lee J. Rickard, Sachs/Freeman and Naval Research Laboratory) has shown that known nearby molecular clouds coincide with strong cirrus emission. These molecular clouds were discovered by Blitz, Magnani, and Lee Mundy using a ground-based radio telescope at the University of Texas in a search for interstellar carbon monoxide (CO) molecules conducted at the same time as the IRAS survey. The CO observations suggested that these clouds were relatively recently formed and lie within a few hundred light years of the Sun. Magnani, Blitz, and Cor deVries (University of Leiden, Netherlands) have made a direct determination of the distance of several of these clouds, confirming them to be within about 300 light years of the Sun. One example of a recently formed star is known in one of these clouds, and others may yet be identified.

In an independent effort, Hendrik W. deVries and Patrick Thaddeus of Columbia University and the Goddard Institute for Space Studies used their CO survey telescope in New York to sample some locations of strong cirrus in the recently-released IRAS data. Having found CO emission at these locations, they mapped several clouds over sky areas of many square degrees. Their observations also support the notion of very nearby material, with a close correspondence between the location of the molecular gas and the dust, giving rise to the infrared emission. The gas and dust emission data are being studied by all groups to characterize physical conditions in these clouds and attempt to understand their evolutionary state.

Contact: Dr. Michael G. Hauser
Code 690

Sponsor: Office of Space Science and Applications

OPTICAL POLARIZATION OF X-RAY BINARIES

Currently accepted theories of stellar evolution predict that all stars will eventually exhaust their nuclear fuel. Depending on their original mass, stars will ultimately become a white dwarf, a neutron star, or a black hole. Neutron stars contain the mass of the Sun in a volume of space the size across of the District of Columbia.

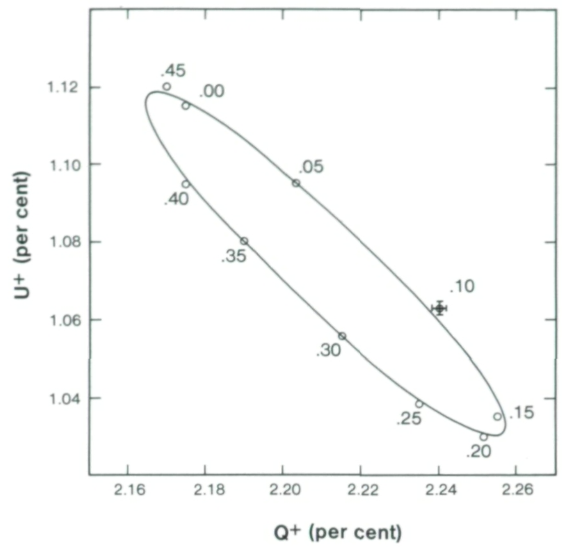

A representation of the orbit of the neutron star in 4U1700-37 about its primary. The orbit is nearly circular; it appears flattened because the orbital plane is tilted nearly 85° with respect to our line of sight to the star. The primary is at the center of the resulting ellipse. The numbers on the data points (the open circles) are related to the position of the neutron star in its orbit as a function of time.

About a hundred binary systems are known in which a neutron star is in a close orbit about a "normal" star, one still burning its nuclear fuel. These systems emit X-rays when material from the primary, or normal star, is pulled over to the neutron star by the tidal force of the neutron star's gravity. The study of X-ray binaries is of value to astronomy both for what it can reveal about the neutron stars themselves, and for what it can tell us about the mechanism by which the X-rays are produced.

A new method of studying X-ray binaries has recently been developed, which analyzes the linear polarization of the light emitted by the system. The light emitted by the primary is reflected off the gas streams carrying matter between the stars. The scattered light can be strongly polarized. By measuring the amount of polarization in the starlight as a function of wavelength, and by observing how that polarization changes with time (i.e., with the relative position of the neutron star in its orbit about the primary), we are able to determine such important properties of the system as the temperature, density, and ionization state of the material in the gas streams, the

amount of matter being transferred, and the orbital parameters of the binary. Polarimetric observations are the only effective method of determining the inclination of many of these systems, i.e., whether the neutron star revolves clockwise or counterclockwise around the primary as seen from the Earth. In fact, these observations often allow us to construct a picture of the binary orbit, representative of what we would see if we looked at the system with a telescope millions of times more powerful than any now in existence.

Recent work has concentrated on Cygnus XR-1, Vela XR-1, 4U1700-37, and HD152667. All of these systems show variable polarization characteristic of light scattering off of gas streams, which appears to be a common characteristic of the optical counterparts of X-ray binaries.

Contact: Dr. Joseph F. Dolan
Code 680

Sponsor: Office of Space Science and Applications

BETA CEPHEI - NOT LIKE ALL THE REST

Among the variable stars, one particular group is the Beta Cephei type. There are about 25 of these stars, which have the following facts in common: 1) They are all about 10 to 15 times the mass of the Sun; 2) Their temperatures are about 25,000 degrees Kelvin; and 3) They vary in brightness and in radius with a period of about 4 or 5 hours—it is not clear why they do this. Although many variables have easily observed intensity variations, these stars change their brightness by only about 3 percent when seen in visible light and by no more than 10 percent when observed in the ultraviolet (UV).

Several spectra taken in 1971 with the Copernicus satellite showed that Beta Cephei has another type of variation associated with it. Over a period of about 6 days, which is 30 times its 4.5 hour "normal" Beta Cephei period, this star changes a few, but not most of the lines in its spectrum. While the photosphere, or "surface," of the star is so hot that the star appears violet, the atoms in question for this 6-day variation are about 5 times hotter and are several times ionized.

Some of the questions raised by these early observations were:

- Which lines change with the 6-day period?
- What is the exact period?
- Do these same lines change in other Beta Ceph's?

The analysis of 58 observations of Beta Cephei with the IUE satellite shows that the period is 6.10 days and that the only notable changes were in the strength of absorption by carbon, nitrogen, silicon and possibly chromium. More specifically, the amount of absorption and emission of light by C IV (1550), N V (1240), Si III (1393), and Cr III (1208) change by as much as a factor of two or three. Here the Roman numeral is one more than the number of electrons missing, and the number in parentheses is the wavelength, in Angstroms, of the light absorbed.

Goddard Space Flight Center scientists developed a new technique for measuring the changes in the UV behavior of Beta Cephei, using an interactive spectral analysis system written in the language FORTH and implemented on a PDP 11/44 computer. Many spectra of Beta Cephei, evenly spaced in time, were smoothed with a low-pass digital filter, then normalized so all have the same light flux in a wavelength region which did *not* vary in brightness. (See illustration.) The amount of absorption by the changing features could then be accurately measured and compared. (See figure.) Note that the shape of the C IV feature in the illustration changes from symmetric to asymmetric, indicating periodic motion of parts of the outer atmosphere of the star.

Study of a total of 67 IUE observations of 7 other Beta Cephei type stars shows that Beta Cephei itself is unique in having this 6-day period. The implication is that *some*

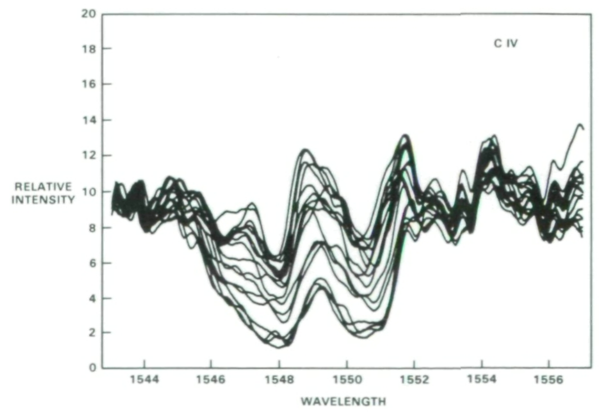

Superposition of normalized intensities of C IV (1550 A) from 18 spectra of Beta Cephei taken at one-day intervals.

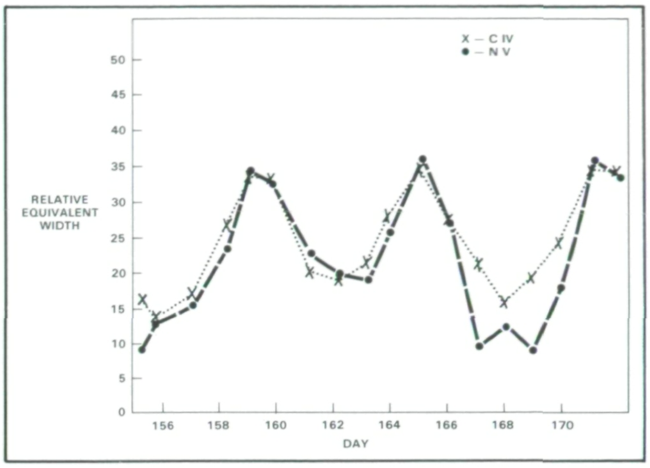

Normalized absorption strengths of C IV (1550 A) and N V (1239 A) as a function of time.

hot stars have atmospheric conditions quite different from otherwise identical stars. These differences are probably due to some material being contained, at very high temperature, by magnetic fields.

Contact: Dr. R. P. Fahey
Code 680

Sponsor: Office of Space Science and Applications

THE AGES OF THE GLOBULAR CLUSTERS

Our Milky Way Galaxy contains over a hundred compact spherical stellar systems known as globular clusters. These systems are comprised typically of several hundred thousand stars and are found throughout the galactic halo. They are believed to have formed during the initial collapse of the proto-galactic cloud and thus represent the oldest stellar systems in our Galaxy.

The globular clusters play a crucial role in studies of our Galaxy's formation and early evolution. Since our Galaxy formed shortly after the big-bang explosion, the ages of the globular clusters should be close to the age of the universe. Thus the dating of the globular clusters also has considerable cosmological significance. For these reasons the globular clusters have been the focus of much theoretical and observational research. One of the first key projects recommended for the Hubble Space Telescope is to determine the globular-cluster ages more accurately than currently possible.

A globular cluster contains stars in many evolutionary phases. Most of the stars are in an early evolutionary phase known as the main-sequence phase during which the energy is produced by the fusion of hydrogen into helium at the center. A few percent of the stars, however, are in more advanced phases. One important class of evolved stars is the class of variable stars known as the RR Lyrae stars. These stars pulsate with a period of about 0.5 day and are considerably brighter than the main-sequence stars.

The best current method for dating the globular clusters is based on the luminosity difference between the RR Lyrae and main-sequence stars. This luminosity difference can be calibrated as a function of the age from theoretical stellar-evolution calculations. Recent observations by Sandage, Katem and Sandage (Ap. J. Suppl., 46, 41, 1981) have shown that RR Lyrae stars in the most metal-poor globular clusters pulsate more slowly than those in the metal-rich clusters. These observations suggest that the metal-poor RR Lyrae stars are more luminous than the metal-rich ones. This result has raised serious questions about how well we know the RR Lyrae luminosity and consequently the ages of the globular clusters.

We have undertaken several studies in order to determine the theoretical properties of the RR Lyrae stars more accurately. In particular, we have constructed an extensive grid of evolutionary sequences over the range of input parameters appropriate for the RR Lyrae stars. In this research we have included a number of effects ignored in most previous calculations and have extended the metallicity of the theoretical models into the domain of the metal-rich RR Lyrae stars. Our calculations, obtained with the computer facilities at the Goddard Space Flight Center, provide the most detailed grid of RR Lyrae sequences currently available. Such sequences are an essential prerequisite for estimates of the globular-cluster ages.

Additional calculations involving a total of 10,000 stellar models have also been made to study the change in the RR Lyrae period with metallicity. Our results indicate that the observed period change is not caused by evolutionary effects during either the RR Lyrae phase or the preceding evolution. Rather, we find that the observed period change might arise from an increase in the opacity at temperatures around a few million degrees. It is at these temperatures that the opacity, which governs the flow of

energy from the interior, is most uncertain. Thus the RR Lyrae observations might also lead to a better understanding of the physical processes operating in the stellar interior.

Contact: Dr. Allen V. Sweigart
Code 680

Sponsor: Office of Space Science and Applications

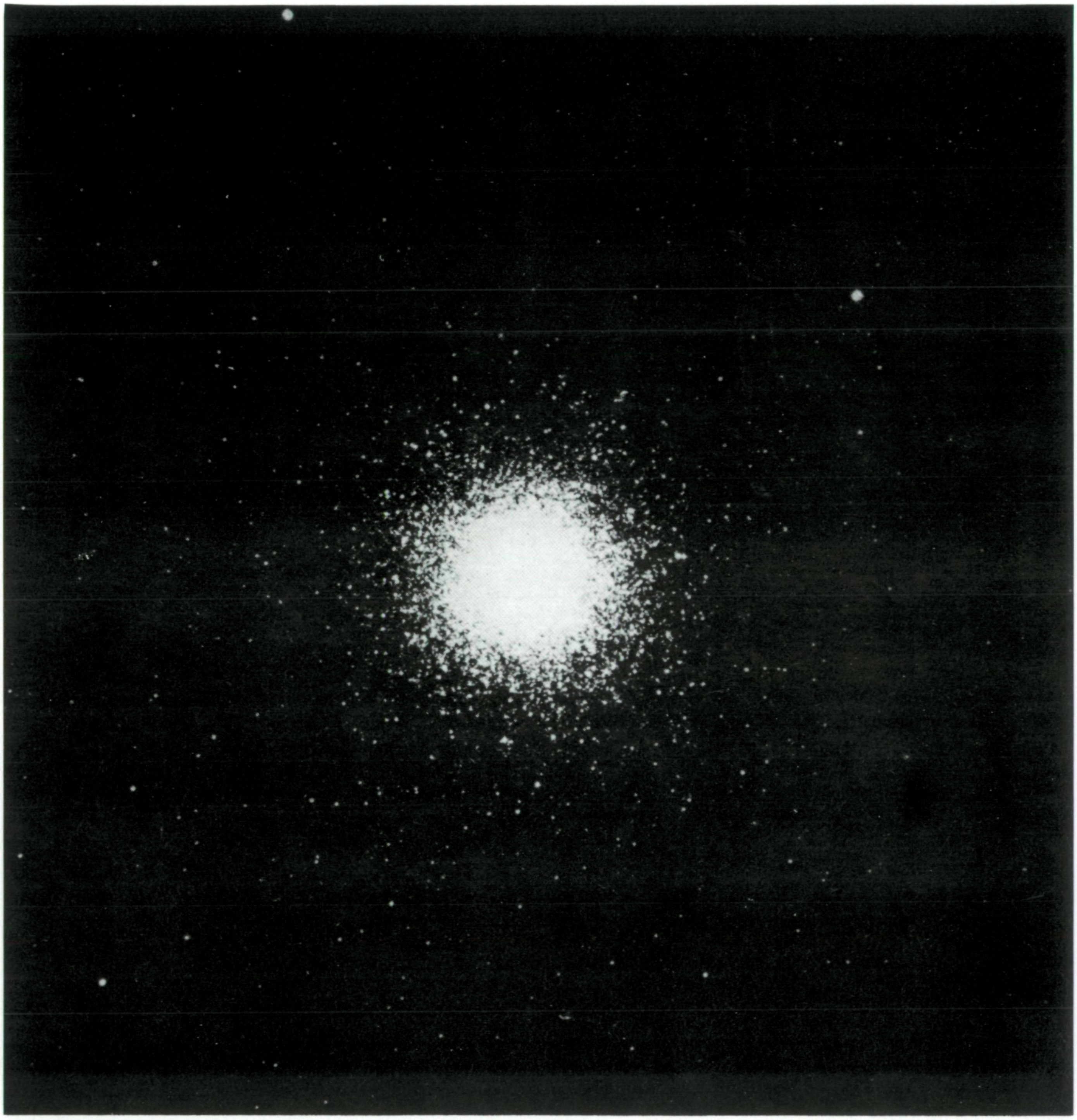

Globular star cluster M_3.

DISCOVERY OF A ROTATING GAS CLOUD 300,000 LIGHT YEARS DIAMETER UNDERLYING A DISTANT QUASAR

Scientists observing with the 4-meter telescope at Kitt Peak National Observatory have detected an enormous rotating gas cloud 300,000 light years in diameter surrounding a distant quasar. Earlier observations of the quasar, called 3C275.1, demonstrated that it lies at the center of an extremely rich cluster of galaxies, the first such case discovered in 20 years of quasar research. Many scientists had previously predicted that quasars would never be found in rich clusters of galaxies because of the high density of matter in such regions.

The cluster surrounding 3C275.1 is about 7 billion light years from Earth, so the light which was detected at Kitt Peak left this distant cluster 2 billion years before our Earth and solar system were even formed. Observations of the cluster can therefore reveal what the universe was

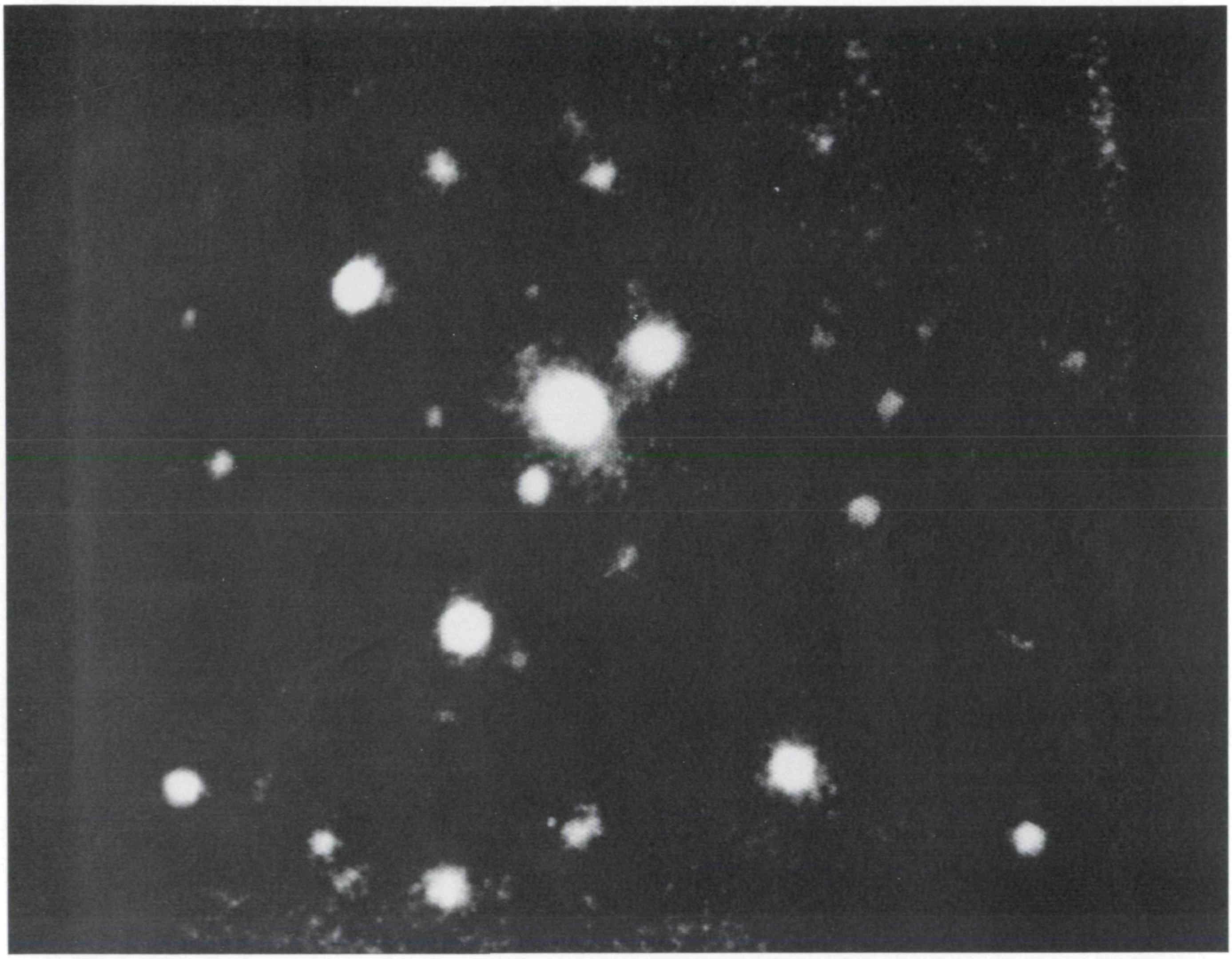

This deep photograph centered on the quasar 3C275.1 demonstrates that the quasar lies at the center of an extremely rich cluster of galaxies, the first such instance identified in 20 years of QSO research. The quasar, the brightest object at the center of the photograph, is surrounded by an elliptical nebulosity which was originally suspected to be a giant galaxy. Recent spectroscopic observations carried out at Kitt Peak demonstrate that this nebulosity is actually an enormous rotating gas cloud. Its rotation curve is very different from those of spiral galaxies, and the authors suggest that the nebulosity consists of infalling gas from the cluster surrounding the quasar. This gas may eventually spiral in and feed the black hole which many scientists believe powers the quasar nucleus.

like 7 billion years ago, more than one-third of the way back to the big bang explosion that began the universe.

The same deep photographs that detected the 3C275.1 cluster also showed that the quasar is surrounded by a faint elliptical glow which is much larger than any of the galaxies in the cluster.

Paul Hintzen, of NASA's Goddard Space Flight Center, and John Stocke, of the University of Arizona, have now obtained detailed observations which show that the nebulosity primarily consists of a hot, rotating gas cloud. This is the first quasar nebulosity in which rotation has been detected, and the nebulosity's rotation curve demonstrates that 3C275.1 is not the superluminous nucleus of a spiral galaxy. This result is especially important because it provides the first definitive test of the "spiral galaxy model" of quasars.

Since the rotation observed in 3C275.1 does not fit the rotation characteristics seen in galaxies, the authors have suggested that the gas cloud may consist of material which is falling in from the surrounding cluster. This material might eventually feed the black hole which many scientists believe powers the quasar nucleus.

Contact: Dr. Paul M. N. Hintzen
Code 680

Sponsor: Office of Space Science and Applications

HIGH ENERGY ASTROPHYSICS

IMAGES OF HIGH-ENERGY ELECTRON INTERACTIONS IN SOLAR FLARES

Hard X-rays produced by interactions of energetic electrons accelerated in solar flares can be observed from satellites or from high-altitude scientific balloons. Observations obtained with the hard X-ray imaging instruments flown during the solar maximum which peaked in 1980 demonstrated the potential of such observations for answering the most fundamental questions on the nature of solar flares. In particular, the Hard X-ray Imaging Spectrometer (HXIS) on the Solar Maximum Mission (SMM) and the Solar Hard X-ray Telescope (SXT) on the Japanese Hinotori spacecraft have shown that hard X-rays with energies up to 40 keV appear to come from the footpoints of flaring magnetic loops. This result has been used to argue that the X-rays must be produced by beams of high-energy electrons incident on the thick target of the lower solar corona and chromosphere. If this conclusion could be substantiated, it would be a major advance in understanding the phenomenology of the energy release mechanism and particle acceleration in solar flares.

There is, in fact, considerable supporting evidence for the existence of electron beams:

- The simultaneous brightening of loop footpoints separated by 70,000 km. The hard X-ray image of the footpoints which brightened within approximately 10 seconds of each other is shown as a contour plot in the first figure. Only signals traveling between the footpoints with velocities close to the speed of light could give the observed simultaneity. This same observation is shown in the accompanying false-color image.

- The absence of any significant hard X-ray brightening between the footpoints. Explicitly, the emission between the footpoints is at least a factor of 3 weaker than the intensity from the footpoints. The relatively low density in the region of the loop between the footpoints means that the electron beam produces very few bremsstrahlung X-rays except at the footpoints.

- The temporal coincidence between the brightening of ultraviolet lines and the brightening of hard X-rays. The ultraviolet lines are produced in the transition region which lies between the corona and the chromosphere.

In spite of the evidence for beaming, it is still not clear whether most of the energetic electrons appear in beams or in hot plasmas. Some investigators have argued that only a small fraction of the hard X-rays actually come from footpoints; most of the X-rays may come from a more diffuse region around and between the footpoints.

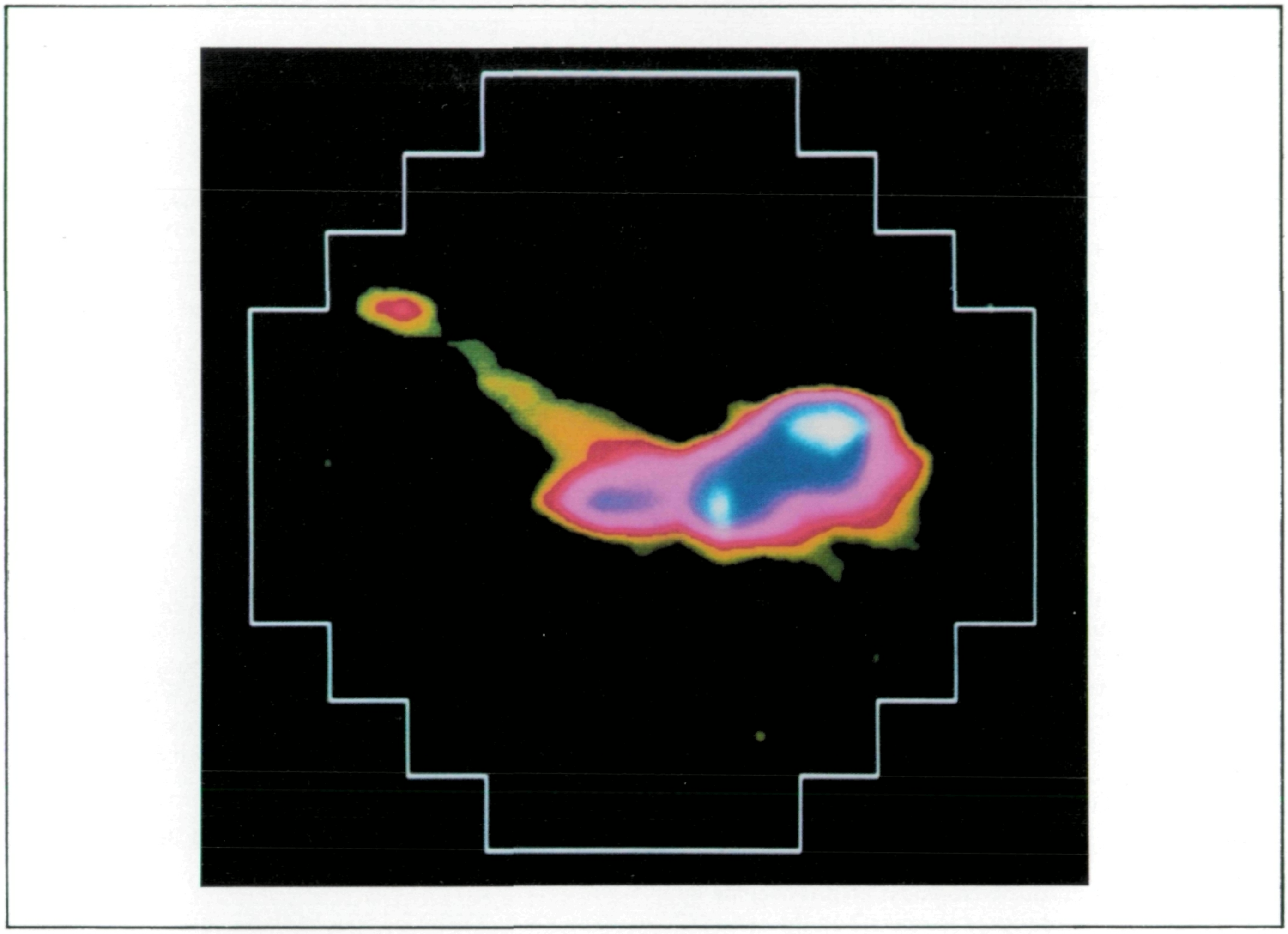

Observations from the Solar Maximum Mission of a major solar flare on November 5, 1980. The image shows the "foot-point brightening" seen in 16 to 30 keV hard X-rays (white), together with the structure of the 3.5 to 8 keV soft X-ray sources (colored contours), using data from the Hard X-ray Imaging Spectrometer. Such observations strongly suggest that flares derive their energy from the coronal magnetic structures connecting the foot-points (courtesy B. Dennis and the HXIS experiment team).

Contour plot of an X-ray image obtained with HXIS on SMM for a flare that occurred on November 5, 1980, at 22^{h}33^m UT. The contours show the intensity of the X-ray emission in the energy range from 3.5 to 8 keV, and the three cross-hatched regions marked A, B, and C show the location of the brightest emission in the energy range from 16 to 30 keV. The exposure time for the image was 13.5 seconds during the most intense part of the hard X-ray flare. ▶

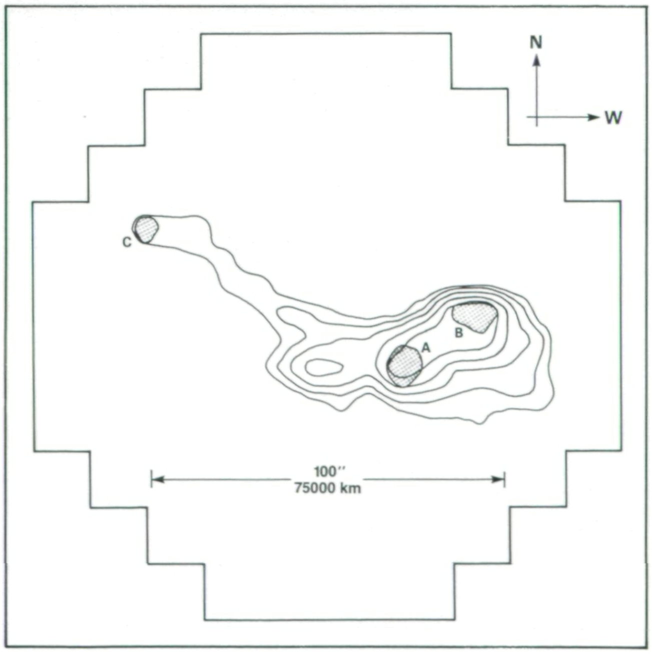

They also question the requirement for beams based on the simultaneity of the brightening of two footpoints, claiming that the HXIS images may all be consistent with hard X-ray emission from a magnetic arch filled with hot plasma.

The beam interpretation, as illustrated, shows two loops interacting, annihilating some of their magnetic field, and accelerating particles which stream along the remaining field lines. The hot thermal plasma interpretation is illustrated showing conduction fronts traveling down the legs of a magnetic arch and confining the hard X-ray emitting plasma. The ambiguities which prevent us from distinguishing between these two interpretations, or variations in between, are due to the limitations of the observations presently available. The critical instrumental parameters that must be improved to resolve the ambiguities are sensitivity, time resolution, and angular resolution. The sensitivity and time resolution must be increased so that the simultaneity of footpoint brightening can be determined to better than 1 second. Improved angular resolution of better than 1 arc second is needed to resolve the bright patches and to determine the distribution of emission from the different parts of the magnetic arches. Most critically, the sensitivity and dynamic range must be sufficient to produce high-contrast images, because the emission from footpoints may be a factor of 10 or more brighter than the emission from the tops of loops.

Our current instrument-development efforts include a hard X-ray telescope designed to operate on the concept

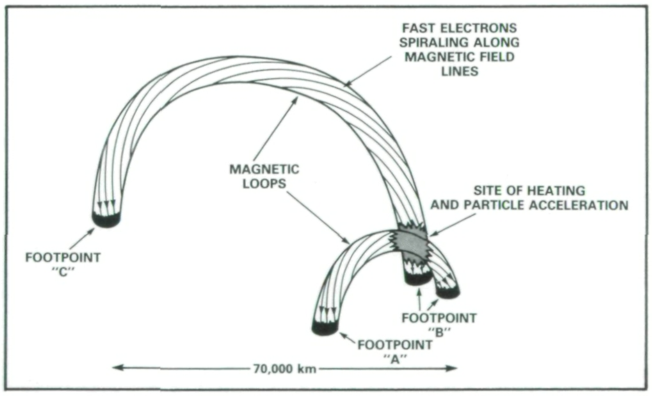

Interacting magnetic arches. Magnetic field is annihilated at the point of contact of the two magnetic arches resulting in the acceleration of electrons up to energies of 100 keV or more. These electrons spiral along the magnetic field lines of the two loops and produce X-rays as they penetrate the higher density plasma of the lower corona and chromosphere at the footpoints of the loops.

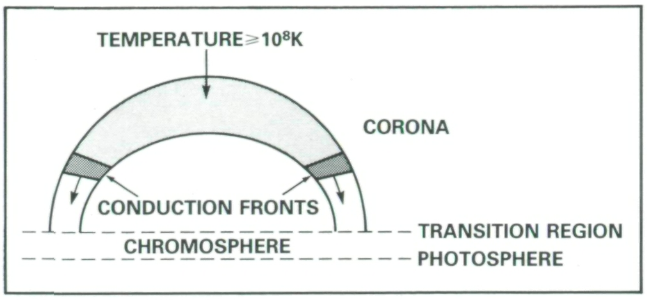

Flaring coronal arch. Plasma, confined by the magnetic fields and the conduction fronts, is being heated to temperatures in excess of a hundred million degrees Kelvin. The conduction fronts are moving down the arch at speeds of a few hundred kilometers per second.

of spatial Fourier transforms. This imaging technique will enable us to obtain the required sensitivities and resolution with low-cost components and to extend the range of observable energies above 100 keV. The hard X-ray images in this extended energy domain can be compared directly with spatially resolved microwave observations such as those obtained with the VLA because both emissions are due to high-energy electrons. With such observations we can hope to locate the energy release site and to determine the division of the released energy between electron beams and hot plasma.

Contact: Drs. Carol Jo Crannell and Brian R. Dennis
Code 680

Sponsor: Office of Space Science and Applications

SOLAR FLARE PARTICLES

Using data from the IMP-8 and ISEE-3 spacecraft, we have investigated the association of impulsive and long-duration solar flare soft X-rays with energetic charged particle events. We find that the particle populations associated with the impulsive flares have substantially different properties than the particle populations associated with the long-duration flares. The events originating with impulsive flares are associated with intense meter wavelength Type III radio bursts with associated Type V continuum. The impulsive events have high electron-to-proton ratios and are almost never associated with interplanetary shocks. In contrast, the events associated with long-duration flares extend to much higher proton energies and are closely associated with coronal and interplanetary shocks. Apparently the two classes of particle events arise because different acceleration processes operate preferentially for the two

classes of flares. In impulsive flares the acceleration is rapid. In some energetic events very high energy electrons are accelerated along with the lower energy electrons that are responsible for Type III emission and other impulsive phenomena. The reported correlation of so-called electron-rich events with SMM gamma-ray events is consistent with this suggestion. In long-duration flares the acceleration is more gradual; the acceleration appears to take place at extended shocks. These differences are attributed to the fact that impulsive flares occur low in the corona, are compact, and have high energy densities, whereas long-duration flares occur high in the corona in extended regions. Occasionally, a single-flare event exhibits strong impulsive acceleration and also generates strong coronal and interplanetary shocks with their associated large fluxes of protons.

Contact: Dr. Hilary V. Cane
Code 660

Sponsor: Office of Space Science and Applications

OBSERVATIONS OF STELLAR X-RAY FLARES

Photographic observations of the stars, DH Car in 1924 and UV Ceti in 1947, first recorded stellar brightening by several visual magnitudes for only a few minutes. These objects became known as flare stars. The majority turned out to be red dwarfs within 25 parsecs of the Sun. Advances in instrumentation have allowed measurements of flare star activity to be made in a range of energies, from radio to X-rays. Though individual stellar flares are not very energetic by X-ray standards (the brightest X-ray flare observed, at an intensity of 100 millicrabs, had an intrinsic luminosity 5 orders of magnitude less than the Crab Nebula), the large number of active flare stars (about 1 every 25 cubic parsecs) implies they could contribute significantly to the galactic environment. Current theories suggest they are the initial source of particles that are eventually accelerated into cosmic rays, for example.

In 1974, flares from YZ CMi and UV Ceti that were observed by the United States/Netherlands cooperative satellite ANS confirmed that stellar flares can indeed produce X-rays like their solar counterparts, occasionally even 3 order of magnitude more energetic. Surveys of data from all sky scans of HEAO-1 have produced 17 bright transients, which are likely to be very bright flares, from stars like YZ CMi. The flare rates are such that an observer near Earth would see typically 10 to 50 X-ray flares per day over the whole sky above our search threshold of 4 millicrabs. This number is consistent with what one predicts using the known frequencies of optical flares.

The imaging optics used in HEAO-2, the Einstein Observatory, allowed unambiguous identification of sources of flares. From 45 known flare stars, 10 flares were observed, with luminosities closer to those of solar X-ray flares and about 1,000 times fainter than the most energetic ones observed by HEAO-1. The temperatures were 10 times lower. The system H0449-55, in particular, was detected by HEAO-1 during a 15-keV flare at one-fortieth the Sun's bolometric luminosity. The HEAO-2 observation detected a rather ordinary flare with a temperature of less than 2 keV. It was 1,000 times weaker, but still 10 times more energetic than large flares on the Sun. The few successful correlated optical and X-ray observations show a range of ratios of X-ray-to-optical emission from 1 to 100. The variety of stellar flares may correspond to those of solar flares, although they have not been so well classified yet. As on the Sun, the very intense hot flares of long duration may originate on quite large magnetic loop structures. The shorter, lower temperature flares that are much less intense may originate on much more compact magnetic loops.

The higher sensitivity of the Einstein Observatory also made it possible to measure quiescent coronal emission from flare stars, which are 10,000 times brighter than active regions on the Sun. Though both presumably originate from plasma confined in similar magnetic loop structures, their active regions seem to cover a greater percentage of the surface. Studies of X-ray emission from rapidly rotating stars indicate a trend for total X-ray surface flux to rise with the rotation rate. However, this is still an active area of investigation, as other stellar parameters such as spectral type play a role.

The X-ray properties of stellar flares are being pursued in observations with the European X-ray satellite EXOSAT. The temperatures and decay rates of flares will indicate the strength and dimensions of magnetic field configurations. Optical, ultraviolet (IUE) and X-ray (EXOSAT) observations together are being sought to explore the rates of energy supply during a flare. Sizes of the quiescent coronae are being studied with observations of special systems in which eclipses occur.

Contact: Jean H. Swank and Alanna Connors
Code 660

Sponsor: Office of Space Science and Applications

X-RAY CONSTRAINTS ON THE DARK MATTER IN CLUSTERS OF GALAXIES

The problem of "missing mass" in astronomy seems to exist at three scales of increasing size: galaxies, clusters of galaxies, and the Universe. On the largest scale, astronomers have been searching for a mass component which will be sufficient to halt the expansion of the Universe. However, on the scale of clusters of galaxies the missing mass problem is slightly different; clusters appear to be gravitationally bound, based on optical observations, but as was noted over 5 decades ago, the mass in stars is not sufficient to bind them. Therefore the total cluster mass must be about 10 times the mass in stars and is not visible at optical wavelengths. For the past 50 years, this "dark" matter has eluded detection and consequently astronomers have invented many exotic forms that the matter might take.

The data acquired, using the HEAO-1 and Einstein (HEAO-2) Observatories, have enabled us to determine the density and temperature structure of the hot, X-ray emitting gas associated with clusters. The hot gas, which is trapped in the gravitational field of rich clusters of galaxies, is believed to reach an equilibrium state much more quickly than the galaxies themselves, making it a more reliable tracer of the cluster gravitational mass than the optically observed galaxies.

As shown in the accompanying figure, the total mass for the Coma cluster of galaxies, derived from X-ray measure ments, is a factor of 3 to 4 less than the optically determined mass. This reduction in the total cluster mass reduces the density parameter (the ratio of cluster mass to closure density for the Universe) to below 0.2. Big bang nucleosynthesis requires the neutron and proton component of the density parameter to be less than 0.19. Therefore, the cluster mass derived from the X-ray data does not require large amounts of other types of matter (such as neutrinos) as does the optical analysis.

Of greater importance may be the reduction of the total mass-to-blue-light ratio from a number of nearly 200 to the range 50 to 70. (The mass-to-light ratio (M/L) is defined in units of solar mass and total radiative luminosity such that M/L for the Sun is equal to 1.) The latter value is similar to that found for galaxies. This would imply that clusters do not require significantly larger amounts of dark matter than do galaxies. The distribution of the residual mass in the cluster (in excess of the galaxy and gas components) is more centrally concentrated then either the gas or galaxy components. This disagrees with the long-held belief that the dark matter is distributed like the galaxies in the Coma cluster. The gas is also a significant fraction (26 percent) of the total mass and is a significant contribution to the gravitational mass, contrary to what had previously been assumed.

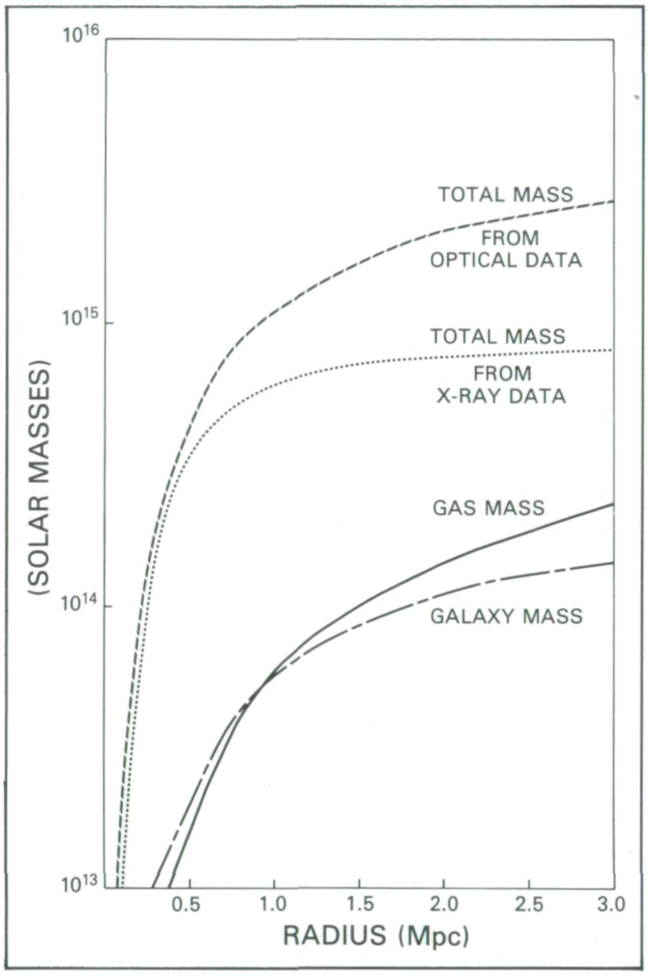

The total mass for the Coma cluster of galaxies is a factor of 3 to 4 less than the optically determined mass.

Contact: Dr. Mark Henriksen
Code 660

Sponsor: Office of Space Science and Applications

HIGHEST ENERGY MEASUREMENT OF COSMIC RAY IRON

For some years there has been a controversy about the amount of iron in high-energy cosmic radiation. Determinations of the iron content, based on atmospheric air showers, has not yielded a clear answer. A direct measurement of the cosmic ray iron spectrum around 10^{13} eV (energy/nucleus) has been made by a balloon-borne instrument built at the Goddard Space Flight Center (GSFC). The High Energy Gas Cherenkov Spectrometer (HEGCS) measures the energy of incident cosmic rays by collecting the Cherenkov light which is generated in a volume of Freon gas. In flight, HEGCS made measurements in the 50 to 200 GeV/nucleon range. Because cosmic rays of this energy are rare, the instrument is large. The two scintillator mosaics used to measure incident charge are each 6 m^2 in area.

In 6 hours at the top of the atmosphere, HEGCS registered more than 10^5 cosmic ray events. Of these, approximately 30 were incident iron with energy above the 50 GeV/nucleon gas threshold. Analyzing these events, the index of the energy spectrum is found to be $2.65 + 0.12$, indicating that the energy spectrum of iron has continued to steepen at high energies, reaching the index characteristic of protons at much lower energies. This result is in contrast to particle measurements in extensive air shower studies and suggests the need to modify shower interpretation techniques.

Contact: Robert E. Streitmatter
Code 660

Sponsor: Office of Space Science and Applications

COUNTERPARTS OF GAMMA-RAY BURSTERS

Gamma-ray Bursters (GRB's) are mysterious objects which emit sudden intense flashes of gamma radiation, typically lasting a few seconds. GRB's were discovered 15 years ago, and since then no great progress has been made in understanding the nature of the GRB system. Recently, several models have been presented which depend on the presence of a neutron star in the system. The gamma-ray data alone, however, are not sufficient to decide between the competing models.

It has long been realized that the identification of a GRB counterpart in another energy range would go a long way towards distinguishing the correct model. This is because the source components could be seen more easily and their nature deduced from optical, radio, or infrared observations. Hence, much effort has gone into identifying a counterpart. The primary objective of the spaceborne interplanetary burst network, of which the Goddard Space Flight Center (GSFC) is a key member, has been to locate the GRB's accurately enough so that ground-based observations at other wavelengths could identify a counterpart.

The Low Energy Gamma-ray Group at GSFC has been on the forefront of activity in attempting to identify a counterpart. In addition to several observing trips to major ground-based observatories, data from the Infrared Astronomy Satellite (IRAS) have been examined for any infrared sources inside any of 23 known GRB error regions.

Unfortunately, despite the vast effort at GSFC and elsewhere, no GRB counterparts have been identified. All indications show that the counterparts of GRB's must be extremely faint in the optical, radio, and infrared regions. This negative result in itself can be used to eliminate many GRB models. The results have shown that any possible companion to a neutron star must be extremely faint. If GRB's are in our galaxy, then a companion could only be a very low mass object (e.g., a large planet). The strict brightness limits can also be used to limit the accretion rate onto the neutron star.

In order to pursue the search to higher precision, the GSFC Low Energy Gamma-ray Group and a group from the Massachusetts Institute of Technology (MIT) have developed a combined Explosive Transient Camera (ETC) and a Rapidly Moving Telescope (RMT) at GSFC, which will soon be installed on Kitt Peak, Arizona. The RMT will be attached to the ETC flash monitoring device, which will report whenever an optical flash from a GRB appears in the sky. Within a second after the flash is detected, the 7-inch telescope will swing around to observe the flash (hence its name). Observations of the flash will continue until it has faded to below fifteenth stellar magnitude. The RMT will be able to position sources with arcsec accuracy, sufficient to make unique identifications

with quiescent counterparts at the limiting magnitudes of the most sensitive ground-based telescopes.

Contact: Dr. Bradley Schaefer
Code 660

Sponsor: Office of Space Science and Applications

GAMMA RAYS, COSMIC RAYS AND NEUTRINOS FROM CYGNUS X-3

Recently, observations of the X-ray source Cygnus X-3 have been reported at radio, infrared, and ultrahigh gamma-ray energies. There are also uncertain reports of the detection of signals from the direction of Cygnus X-3 in underground proton decay detectors. Such signals may be from ultrahigh-energy cosmic-ray neutrinos or some new elementary particle.

The implications of these discoveries make Cygnus X-3 the first known source of ultrahigh-energy cosmic rays, and they have created widespread excitement in the scientific community. The observations have made the detailed study of the Cygnus X-3 system of prime importance. Recent scientific conferences have had entire sessions devoted to the observation and models of Cygnus X-3. The source is a binary system consisting of a relatively normal star and a highly collapsed star which may be a pulsar. The underlying energy source may be the pulsar or may be accretion of matter onto the collapsed star. Members of the Goddard High Energy Astrophysics Theory Office have been investigating the energetics of Cygnus X-3, acceleration of cosmic ray particles in the system, and the production of secondary subatomic particles such as neutrinos.

F. W. Stecker, A. K. Harding, and J. J. Barnard have examined the energetics and effects of a high-energy proton beam in the source and the subsequent production of secondary neutrinos, with particular regard to the stability and structure of the companion star. They find that the beam must heat a relatively small area of the star in order to avoid a higher mass loss from the system than is observed. They also point out that the beam will heat and compress the atmosphere of the companion star, and that the highest energy neutrinos produced by the proton collisions will be absorbed deep in the stellar interior. The subsequent heating of the core of the star from high-energy electrons and muons produced by the absorbed neutrinos could lead to a disruption of the star if the beam energy is too high. This sets upper limits on the beam energy in the Cygnus X-3 system.

D. Kazanas and D. Ellison suggest that acceleration in a shock formed in an accretion column or at the magnetic field boundary of a compact star can produce the required high-energy particles. This acceleration mechanism should be applicable to other binary systems. Indeed, several groups have detected ultrahigh-energy gamma rays from four other X-ray binary systems in the Galaxy and the Magellanic Clouds. They point out that, at these high energies, very energetic neutrons can be produced and escape from the vicinity of the collapsed star. Their model suggests that some of these neutrons may reach the Earth from Cygnus X-3 and may be detectable.

Visiting scientists G. Chanmugam and K. Brecher have alternatively suggested that the accretion disk region around the collapsed star can act as a giant dynamo, accelerating protons to very high energies. Subsequent proton-proton collisions, either with the gas accretion stream or with the companion star, would then give rise to the observed gamma rays, along with a neutrino flux.

Contact: Dr. Alice K. Harding
Code 660

Sponsor: Office of Space Science and Applications

A SEARCH FOR MEDIUM ENERGY GAMMA RAYS FROM ACTIVE GALAXIES

A number of Active Galactic Nuclei (AGN's) (i.e., quasars, Seyfert galaxies, BL Lac objects) have been detected in medium energy and hard X-rays, some with spectra which extrapolate to detectable gamma-ray fluxes. However, the only AGN detected in 100 MeV gamma rays has been the bright quasar 3C273. The gamma-ray and X-ray spectra for 3C273 indicate a "knee" or "break" somewhere between 1 and 10 MeV. The lack of detections of other AGN's in 100 MeV gamma rays requires that their spectra also must steepen somewhere between 0.1 and 10 MeV. For one relatively nearby Seyfert galaxy, NGC4151, there has been an unconfirmed

detection between 0.5 and 5 MeV, with a suggested knee at about 3 MeV. The detection of AGN's in the 1 to 20 MeV range, and the determination of the shapes of their "knees" would provide valuable insight into the high-energy processes in these exotic objects.

We are currently assembling a new gamma-ray telescope to study active galactic nuclei (as well as other objects) in the 1 to 20 MeV range. This instrument, the Advanced Compton Telescope (ACT), represents quite a different approach compared with earlier instruments in the same energy range. Although it utilizes the principle of Compton scattering as the detection mechanism, in other ways it differs significantly. The primary gamma-ray direction determination is made by a narrow-angle lead collimator, rather than the Compton event reconstruction, which contains ambiguities. The event reconstruction is carried out, but it is used as a background reduction technique by comparison with the known collimator pointing direction. Neutron background is suppressed by two methods: pulse shape digitization in the two sodium iodide main detectors, and a time-of-flight measurement which rejects the slower neutrons. A lead-scintillator sandwich covers the sides and bottom of the telescope to reduce background due to particles and gamma rays incident from wide angles. The collimator is rocked on and off a suspected source direction to provide a precise background subtraction.

The first observations using the ACT will be made during a balloon flight planned for FY86.

Contact: Dr. Robert C. Hartman
Code 660

Sponsor: Office of Space Science and Applications

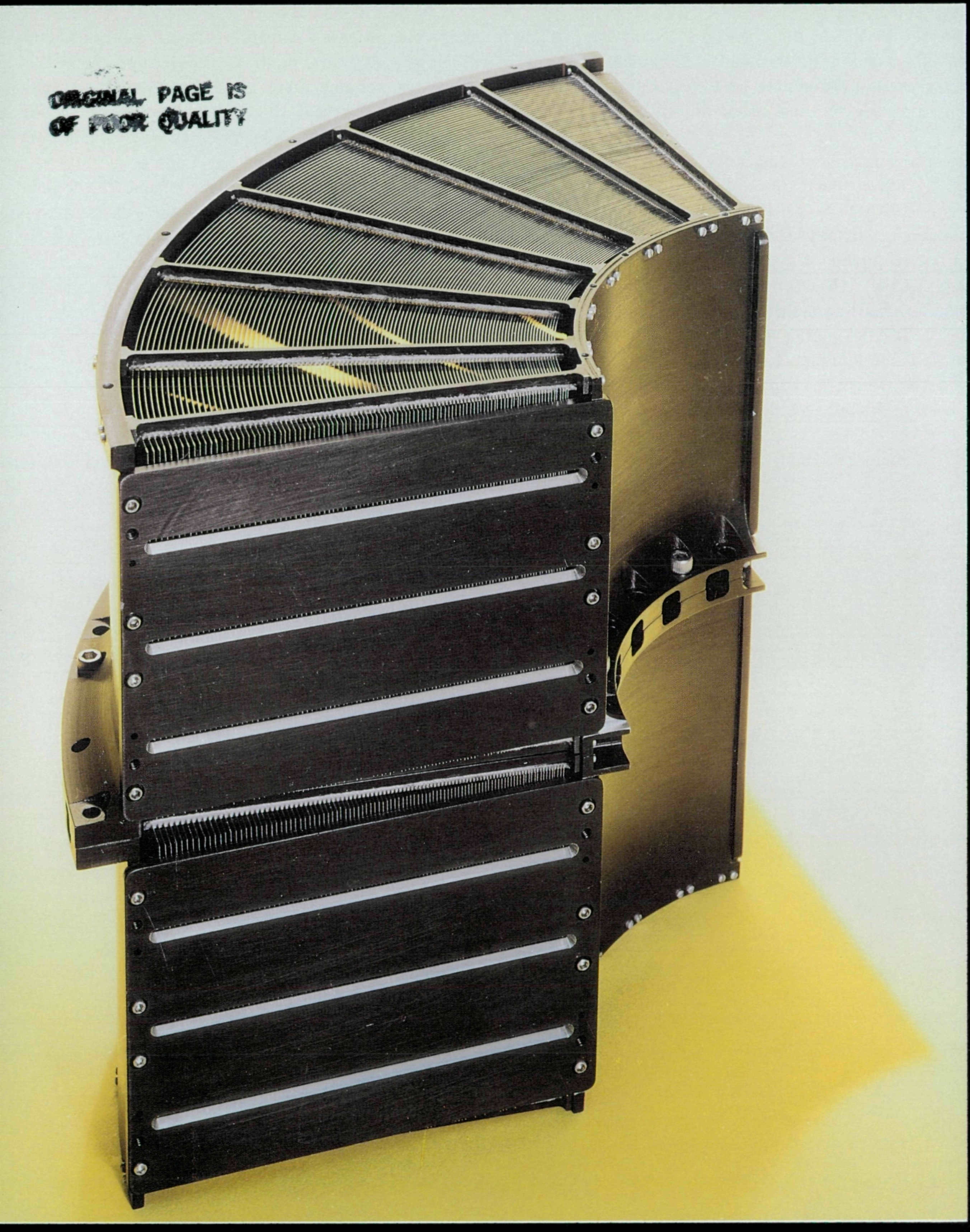
ORIGINAL PAGE IS
OF POOR QUALITY

Advanced technology programs at GSFC provide new capabilities in spacecraft subsystems, sensors, space communications and navigation, the acquisition of data from space missions, and the extraction of new information from that data.

SPACE TECHNOLOGY

HIGH-SPEED X-RAY IMAGING MIRRORS

The "speed" of an optical lens, i.e., its sensitivity to low light level sources, is a function of the surface area it uses to collect light. For X-rays, the analogue of a simple convex optical lens is the grazing incidence mirror. Conventional X-ray mirrors, usually referred to as Wolter-type mirrors, whose reflecting surfaces consist of precisely figured, conic sections of resolution, required thick backings for maintenance of their figure. Even if several of these mirrors are nested, such a system makes inefficient use of its aperture (the active collecting area comprises typically 10 to 20 percent of the aperture) and therefore is intrinsically slow.

A new kind of imaging mirror, the so-called conical mirror, represents a modification of the conventional X-ray mirror concept for improved speed. Simple cones are substituted for the precisely curved reflecting surfaces, eliminating the requirement for thick backings, and allowing the thick mirror elements to be replaced by a large number of thin metal foil reflectors. A typical conical system utilizes 50 percent of its aperture area, making it considerably faster than a typical Wolter mirror of the same aperture and focal length.

The inaugural use of the conical optics design for X-ray astronomy is in the Broadband X-ray Telescope (BBXRT), which will fly as an attached shuttle payload on the SHEAL-2 mission in late 1988. The BBXRT will have a pair of coaligned conical mirrors, each of which has a diameter of 40 cm, a focal length of 3.8 m, and consists of 118 reflector pairs. The individual reflectors are made from commercially available, high finish aluminum foil 0.127 mm thick. Preparation of a reflector involves coating a piece of foil with a thin layer of acrylic lacquer to mask surface imperfections, and then with a vacuum-evaporated layer of gold to provide reflectivity in the X-ray band. For ease of fabrication, the mirror is constructed in quadrants, one of which is shown in the accompanying photograph. Prototype mirrors have demonstrated X-ray imaging with arc-minute spatial resolution and X-ray reflection efficiency approaching the theoretical limit.

Efforts are currently under way to produce conical mirrors with spatial resolution of a few arc seconds. Additionally, techniques for mass-producing conical mirrors are being explored, a possibility suggested by the simple construction of the individual reflecting elements. In principle, such production could be automated to produce a large array of conical mirrors. An X-ray observatory incorporating such an array would provide astronomers an opportunity to study the spectral and spatial properties of the faintest, most distant X-ray sources.

Contact: Dr. Robert Petre
Code 660

Sponsor: Office of Space Science and Applications
GSFC Director's Discretionary Fund

LONG-LIFETIME CRYOGENIC REFRIGERATOR

Many space instruments require ultralow temperature cooling to perform their measurements. Several Goddard Space Flight Center technology programs are underway

◀ *Facing page: a quadrant of a conical X-ray imaging mirror for the BBXRT, consisting of 101 nested reflector pairs.*

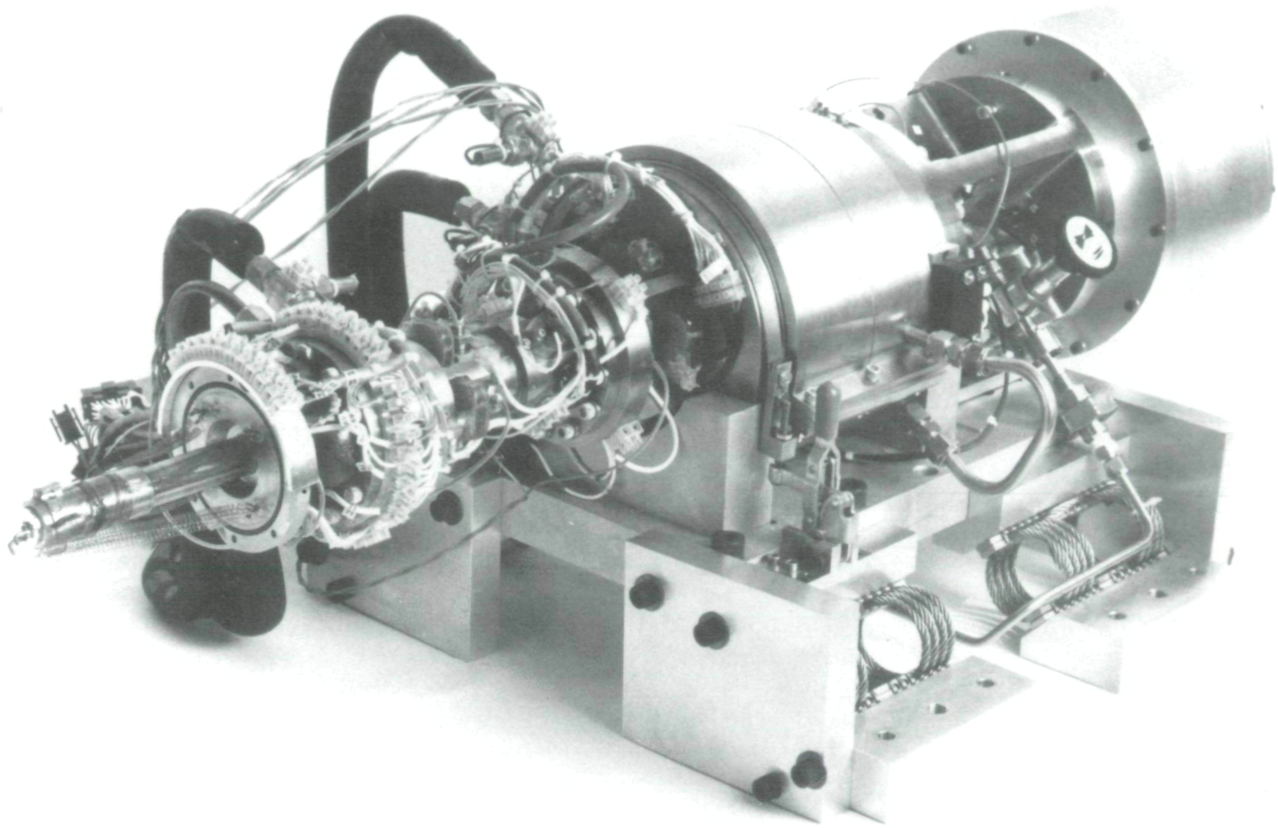

Proof-of-Principle Model Stirling Cycle Cryogenic Cooler on test stand.

to fulfill this need. One such program is to develop an ultralow temperature (cyrogenic) refrigerator that will operate in space for 3 to 5 years without maintenance.

The first unit of the new refrigerator, the Proof-of-Principle Model Stirling Cycle Cryogenic Cooler, successfully completed 2 years of operation in FY85. Running silently at an average speed of 25 cycles/sec, it generates 5 W of cooling power at a temperature of 65 °K when its compression heat is rejected at 300 °K. Its reciprocating components work without conventional bearings, seals, or lubricants because they are levitated and centered by magnetic bearings. A closed-loop servo system controls the position of the free-floating pistons. Moving magnetic linear motors of a new design provide linear motion because there is no friction and wear. The operating performance of the cooler has not changed during the 2 years of operation.

The second-generation cooler, the Technology Demonstration Model, is presently being fabricated; it is designed to survive shuttle launch and operation in space. The launch specifications necessitated improvements in electromagnetic bearings, axial and radial position sensors, structural design of the moving elements, and the axial counterbalance. As in the first-generation refrigerator, organic contamination has been eliminated by the use of all metal and ceramic construction. Reductions in system input power result from an integral permanent magnetic displacer spring/motor and more efficient linear motors and drive electronics.

Ferrite variable reluctance position sensors provide improved temperature stability of the magnetic bearing control system. Additional bearing improvements are realized through increases in gas film damping, C/DC force capabilities, and structural resonant freqencies. Improved Linear Variable Differential Transformers (LVDT's) provide high-frequency capabilities to the axial control systems. All clearance seal surfaces are specially treated with ion-plated titanium nitride to eliminate potential damage due to contact during launch and shipping. Transmitted

vibrations are minimized by 6-degree-of-freedom spring mounts between the refrigerator and spacecraft. The counterbalance, a tuned spring mass system driven by a linear motor and supported radially by magnetic bearings, cancels the unbalanced axial force generated during operation.

This cooler development has won two IR100 Invention-of-the-Year awards.

Contact: Max G. Gasser
Code 710

Sponsors: Office of Aeronautics and Space Technology
USAF Space Technology Center

LOW CURRENT SUPERCONDUCTING MAGNET FOR AN ADIABATIC DEMAGNETIZATION REFRIGERATOR

Ultrasensitive bolometers are being developed which require cooling to temperatures below 1 Kelvin (K). These bolometers will be used not only as infrared sensors for instruments on the Space Infrared Telescope Facility (SIRTF) and Large Deployable Reflector (LDR), but also as X-ray spectrometers for an instrument being developed for the Advanced X-ray Astrophysics Facility (AXAF). Since the Noise Equivalent Power (NEP) (the sensitivity figure-of-merit) is expected to vary as the absolute temperature to the -5/2 power, temperatures below that of space pumped liquid helium (>1.0 K) will allow much greater bolometer performance. Currently detectors are being fabricated which operate best at approximately 0.1 K. To achieve this temperature in space an Adiabatic Demagnetization Refrigerator (ADR) is required.

While laboratory ADR's have been used since the 1930's, various components must be developed to make them useful in space. Most of these improvements are related to the use of a superconducting magnet which powers the ADR. The ADR operates on an isothermal magnetization, adiabatic demagnetization refrigeration cycle. The refrigerant is a paramagnetic salt, and magnetizing field of a few tesla is provided by an electromagnet. For space applications, the magnet would be a superconducting solenoid because of the lower power and cooling requirements compared to a room temperature magnet. To maintain a relatively high duty cycle, the magnet must be capable of ramping up to full field and down to minimum field in a relatively short time (a fraction of an hour). For application on a space facility, there are a few more design requirements. So as not to interfere with surrounding instrumentation or spacecraft functions, the stray magnetic field must be minimized. To allow easy instrument insertion and removal, the magnet may not be able to be immersed in the liquid helium precoolant. Hence, it must be able to be cooled by conduction alone. Finally, to minimize the heat leak into the liquid helium dewar (exhaustion of the liquid helium determines the lifetime of the instrument or facility), the magnet leads must have minimum joule heating and thermal conductance. To meet this last requirement, minimizing the current required to produce a given field is the goal.

This investigation concentrated on the superconducting magnet requirements for space operation, in particular the need for operation in a vacuum instead of liquid helium immersion, low current draw, and small size and weight. The goal was to make a magnet with solenoid dimensions of 6 inches in length, 4.5 inches in outside diameter, and a 1.75-inch diameter clear bore for the salt pill. At the same time the magnet should have a central field of 3 tesla for a current of 3 amperes, with the field at least 2.25 tesla at a distance of 1.5 inches along the axis from the center. It was also sought to minimize the stray field in a localized area as, for example, around a bolometer, by using a trim coil in series with the main solenoid. Magnet detail design and construction was contracted, on a best-effort basis, with Cryomagnetics, Incorporated.

The magnet was constructed and preliminary tests were carried out by Cryomagnetics. The as-constructed size of the solenoid alone was 4.5-inch outer diameter, 1.75-inch clear bore, and a 4.125-inch length. The overall length of the magnet with trim coil and mounting flanges was 6.408 inches. The solenoid required over 100,000 feet of 0.005-inch diameter niobium-titanium wire, resulting in an inductance of 337 henries. This is believed to be the highest inductance superconducting solenoid ever made. Before winding, the wire was braided together for increased strength. High thermal conductivity epoxy provided thermal contact between windings and the mounting flange, which, in turn, was conduction cooled by attachment to a liquid helium reservoir.

The first test at Cryomagnetics was performed with the magnet immersed in liquid helium at 4.2 K. The performance met all specifications and even survived an inadvertent quench (sudden loss of superconductivity due to localized heating). The final factory test was performed in a vacuum with the magnet mounted to a 2 K cold plate. The measured results were: 3 tesla central field for an input current of 2.992 amperes (1.0025 tesla per ampere),

2.25 tesla or greater field in the bore of the solenoid extending 1.6 inches axially to either side of the center, a length of approximately 0.75 inch along the axis where the field is 0.005 times the central field or smaller due to the trim coil, and the current was achieved by ramping up the current at about 0.5 volt for about 30 minutes. No large temperature differences along the solenoid were observed.

At the GSFC, the magnet was again tested in vacuum. Tests were conducted at 4.2 K and 1.8 K. Measurements of current, voltage, and magnetic field confirmed the Cryomagnetics results. In addition, the magnet was subjected to a much more severe current ramp test. The current was decreased from 3 to 0.6 amperes in 10 minutes, simulating a typical demagnetization of a salt. The temperature drop along the solenoid remained small during this operation, indicating an eddy current heating was conducted away to the helium bath.

Contact: Michael DiPirro, Stephen Castles,
and Brent Warner
Code 710

Sponsor: GSFC Director's Discretionary Fund

CAPILLARY PUMPED LOOP HEAT TRANSPORT SYSTEM FLIGHT EXPERIMENT

Currently planned large space structures, such as the Space Station and its associated platforms, will operate at much higher power levels than previous smaller spacecraft. Such structures will consume tens of kilowatts and require transport over tens of meters. Conventional heat acquisition and transport systems, which involve circulation of a single-phase refrigerant through a closed loop, would be very large and massive if employed for this task. In recognition of these problems, efforts to develop more efficient two-phase heat acquisition and transport systems have been underway at the GSFC for several years. One type of system, which involves the use of capillary forces to pump a liquid refrigerant through a closed loop, has recently been flight-tested with great success. This type of heat acquisition and transport system is called a Capillary Pumped Loop, or CPL.

A capillary pump employs the surface tension of a fluid in a fine pore capillary wick to develop a pressure head. While small, this pressure head is sufficient to pump a refrigerant to an evaporating surface. In the evaporative process, the refrigerant's heat of vaporization is employed to absorb large heat fluxes (>7 W/cm^2 for the GSFC system). The resulting vapor is transported to a radiator for condensation, and then suctioned back to the wick (by the capillary pump), thus repeating the cycle. In previous work at the GSFC, a full-scale CPL capable of transporting approximately 7 kilowatts over 10 meters was fabricated and successfully ground tested. The results of that work were discussed in last year's annual Research and Technology Report.

Basic fluid and heat transfer mechanisms in microgravity are not well understood. Hence, it was necessary to demonstrate the CPL concept in the space environment, and a small, 14'' by 14'' by 4'' high experimental loop was fabricated. This mini-CPL loop and associated battery, data collection, and control electronics were designed to fit within a GAS canister. This small loop contained all essential elements of the full-scale CPL: multiple evaporators (two instead of the eight in the ground test loop), isolators between the evaporator inlets, transport tubing, a wicked reservoir for volumetric compensation and control of saturation temperature, and a radiator (a modified GAS top plate). Ammonia was the refrigerant. The photograph shows the (noninstrumented) mini-CPL test loop. Based upon extensive ground testing to determine performance envelope and other operating characteristics, the mini-CPL was then insulated and packaged in the GAS canister.

The CPL/GAS experiment was successfully flown on STS-51G in June 1985. A total of 13 power cycles of 6

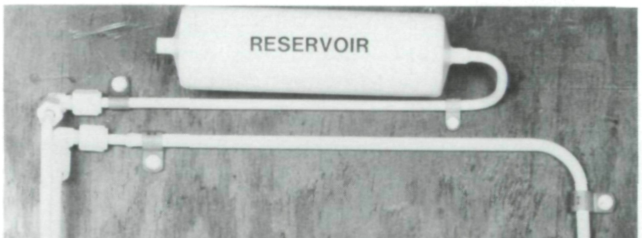

CPL/GAS Flight Experiment.

different profile types were run over the planned 124 hours. Most of the cycles involved the basic "100-watt zap" profile wherein both evaporators are cycled from full off, to 100-W on, to off. The results of this power profile test are shown in the first figure. Other power profiles tested included heat sharing (one evaporator on, the other off, see second figure), power stepdown (starting at the full 100 W per evaporator and then decreasing in steps to zero), low power (25 W/evaporator), steady state, and induced deprime (intentionally causing one evaporator to fail and observing time to recovery).

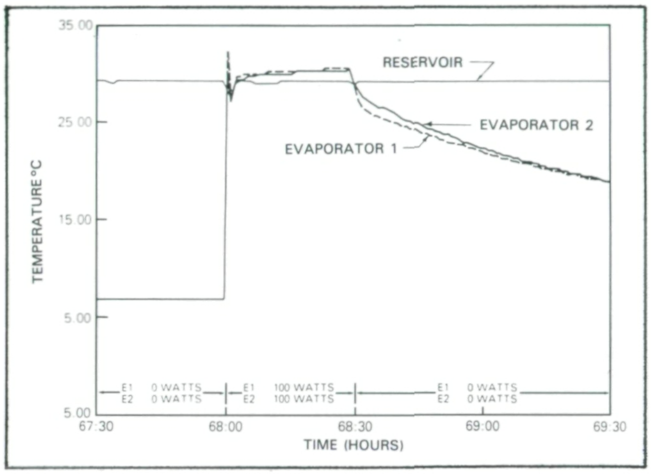

CPL "100-watt zap."

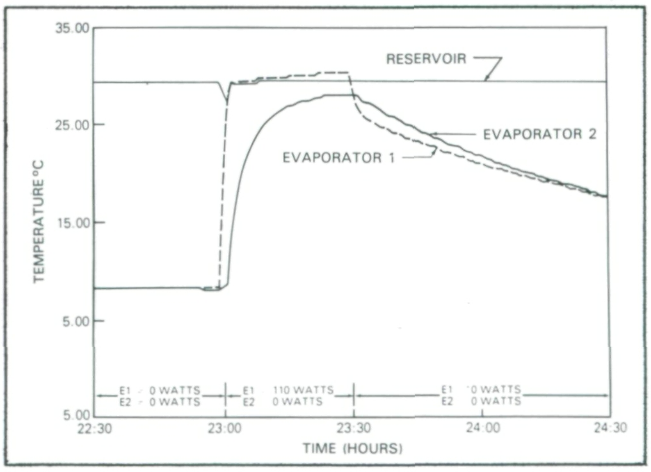

CPL heat sharing.

The results of this experiment are most encouraging. All power profiles worked as well or better than ground testing. Even the low-power cycle, which rarely worked on the ground, performed well in space. This experiment thus gives us confidence regarding the basic viability of this technology for space heat transport system. We are currently testing larger two-phase systems, of both the capillary and mechanically pumped type, and plan several larger space experiments.

Contact: Roy McIntosh
Code 730

Sponsor: Office of Space Science and Applications

PUMPED TWO-PHASE HEAT TRANSFER LOOP

New large space platforms, consuming tens of kilowatts of power, will require more advanced heat acquisition and transport systems. Two-phase systems, which utilize the heat of vaporization of a refrigerant, have been demonstrated to offer significant advantages for such applications. In addition to "passive" concepts employing the capillary pressures of fine wicks, two-phase systems utilizing a small mechanical pump have also been under development at GSFC. Mechanically pumped systems can accommodate much higher pressure drops than capillary pumped systems, thus allowing longer transport lengths and higher pressure drop components. Since heat acquisition is accomplished via vaporization of a refrigerant, the actual liquid flow rate is quite small (in comparison to a single-phase system), and the pump power requirements are negligible. An additional major advantage of two-phase heat transport systems is that the entire loop may be held within a very narrow temperature level. Hence, the sink temperature of each load is independent of the operation of other loads.

The key component in a mechanically pumped two-phase (PTP) heat transfer loop is the evaporator, which is generally called a cold plate. A one-foot-square development model cold plate has recently been fabricated by a vendor and tested at GSFC. This cold plate accepts liquid refrigerant (Freon or ammonia) from the pump and then evenly distributes it (via a system of wicks and capillary grooves) over one surface on the inside of the plate. Heat vaporizes the liquid film, and the vapor flows out an exit manifold to the vapor lines. As in the capillary pumped system, a radiator or other condenser cools and liquifies the vapor which is then pumped back to the plate. Unlike the capillary pumped system, however, capillary forces are only used to distribute the refrigerant, not pump it. Excess liquid not vaporized (due to nonpeak loads) is simply allowed to flow through the cold plate and become entrained in the vapor flow. The prototype version of this cold plate is shown in the photograph. Liquid enters from the right, is vaporized inside the plate

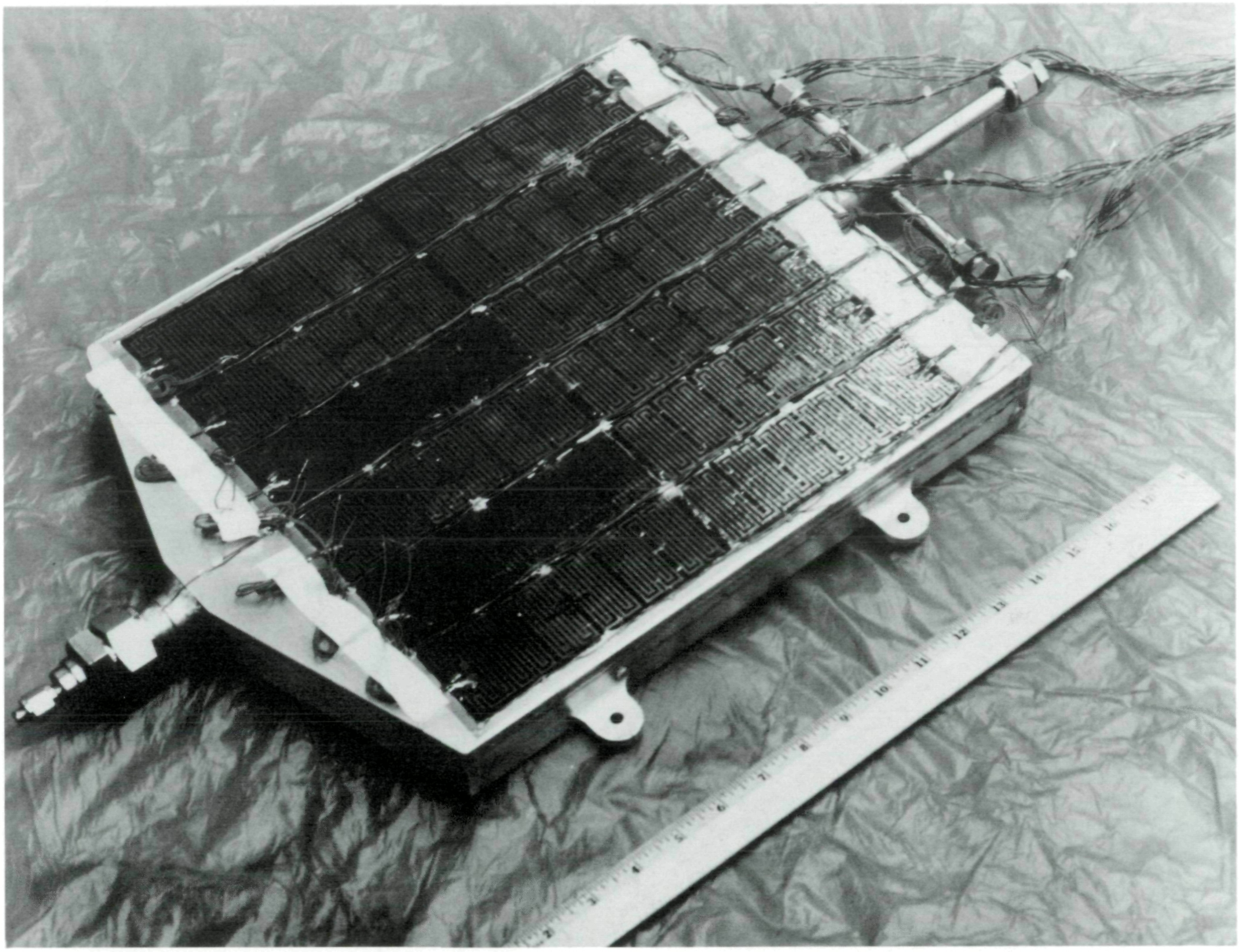

PTP cold plate.

(note heaters on top), and exits to the left as a two-phase fluid.

A development model of this cold plate has successfully demonstrated all design goals including: 3100 W dissipated over the entire plate with isothermality of less than 4°C; nonuniform heating accommodated with acceptable temperature differentials; local heat fluxes greater than 4.1 W/cm^2; heat transfer coefficients of almost 1.0 $W/cm^2/C°$; and operation in a condenser mode at over 400 W. These figures were obtained using R11 as a refrigerant. Ammonia is anticipated to provide higher values.

Based on the successful testing of the development unit, a prototype version has been fabricated, differing from the development unit in that it is of all welded construction and designed to operate with ammonia. Pending further success in ground testing with the prototype plate, a Hitchhiker-G PTP flight experiment will be flown in late FY86.

Contact: Ted Swanson
Code 730

Sponsor: Office of Space Science and Applications

ADVANCED OPTICS FOR SPACEBORNE INSTRUMENTS

Programs under active investigation in the Optics Branch at Goddard Space Flight Center are directed at solving near-term technology problems. Specific areas of research

include the development of diffraction gratings, glancing incidence optical components, far infrared filters, polarizers and beam splitters, and layered synthetic multilayer coatings.

Diffraction grating development is directed toward the investigation of new techniques, such as ion etching, to achieve highly efficient low-scatter gratings. Of particular interest is the development of low-scatter echelle gratings and the development of techniques for the fabrication of conical diffraction gratings. Progress has already been made in the fabrication of low-scatter, high-efficiency diffraction gratings for use in the vacuum ultraviolet region using holographic recording techniques. Aberration corrected gratings have also been successfully made to produce stigmatic images in Rowland type spectrometer designs in the extreme ultraviolet range.

Layered synthetic multilayer coatings have been investigated for use on near-normal incidence components in the extreme ultraviolet region and soft X-ray region. Coatings have been fabricated and measured. Fair agreement has been achieved with analytic models. Uncertainty concerning the optical constants of thin vacuum deposited materials is one area that must continue to be investigated to advance in this discipline. This technology holds promise for the development of high efficiency, narrowband, diffraction grating coatings in this spectral region.

Techniques for the fabrication of high-quality glancing incidence components are under active investigation. A computer-controlled polishing process has been developed which has a high level of confidence over the material removal process. Challenges in this area include the fabrication of components, which have a high rate of change in the full aperture axial slope, as opposed to the very minimal change characteristic of X-ray imaging components. Smoothing processes are the next area of material to be investigated, including the metrology to detect very small slope errors over relatively long spatial extent (microripple).

Components for use in far infrared instrumentation have been under continuing development. Since these components must operate in a cryogenic environment, additional development and measurement are involved. Wire grid beamsplitters and polarizers have successfully been fabricated for use on the COBE mission instrumentation. The development of efficient polarizers in the midinfrared with sharp cutoff properties is still under investigation. Also the production of highly efficient filters with high side band rejection characteristics is also a severe technology problem. Active investigation of material properties at cryogenic temperatures is a high priority activity in this area of technology.

Contact: John Mangus
Code E

Sponsor: National Physics Office
Small Business Innovation Research Program

LASER COMMUNICATIONS

Laser systems will play an increasing role in NASA's satellite communications during the late 1980's and beyond. Optical communications systems which use laser transmitters look very promising for high-speed communication links between low-Earth orbiting satellites and geosynchronous (GEO) satellites and between GEO satellites. Laser systems are attractive for these links due to their very high operating frequency, small size, and light weight. Additional advantages are high modulation bandwidth, very small beam divergences, and use of widely available spectral regions.

Although many different laser systems have been proposed as candidates for intersatellite communications systems, the recent dramatic improvement in semiconductor lasers makes them by far the best choice today. This is because they are extremely small and light; they can be directly modulated by current injection, and they have relatively high conversion efficiency of the electrical drive signal into optical power (10 to 20 percent).

For these applications, the laser diodes must emit high powers under high rate modulation, maintain diffraction

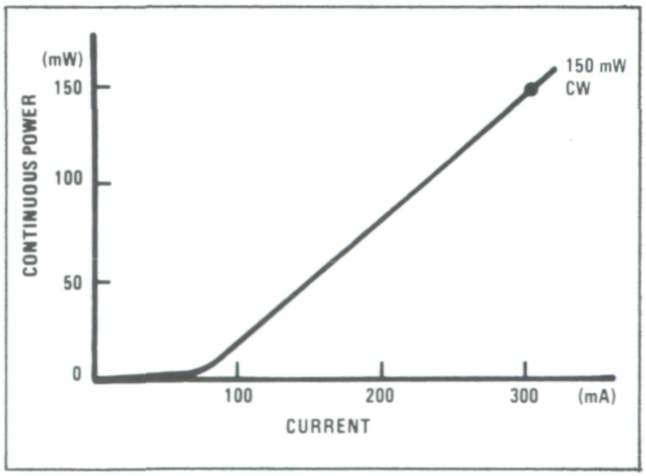

Semiconductor lasers can be directly modulated.

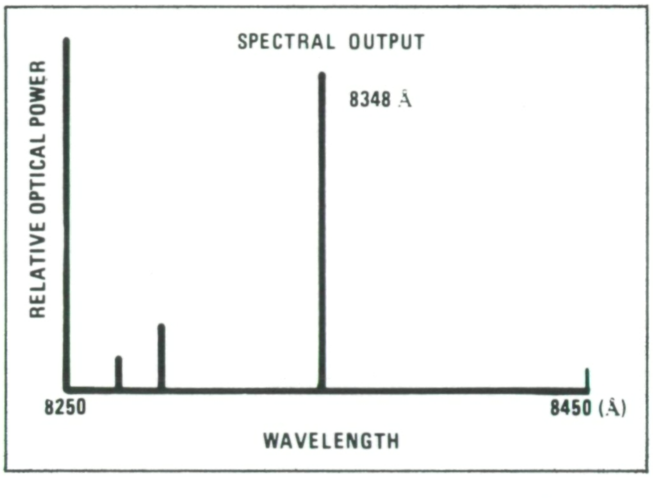

Semiconductor lasers have high conversion efficiency.

limited beam quality, and have long lifetimes. While present commercially available laser diodes emit from 30 to 50 mW CW, devices with four to eight times more power permit either much higher data rates, or smaller and lighter systems with the same data rate. Under a joint LaRC/GSFC program, RCA Sarnoff Labs has been developing Channeled Substrate Planar AlGaAs diode lasers which emit in the 800 to 880 nm region. Recent work has produced a single laser diode with 150 mW CW output power in a diffraction limited beam; this is the highest diffraction limited power yet reported from a laser diode. This same device structure has 300 psec rise and fall times, which permits 1 Gbit/sec data rates. From recent tests, it appears that selected devices at 100 mW power and good reliability will be available within the next 18 months. Ongoing work on nonabsorbing mirrors should increase this power in reliable devices once their development is complete.

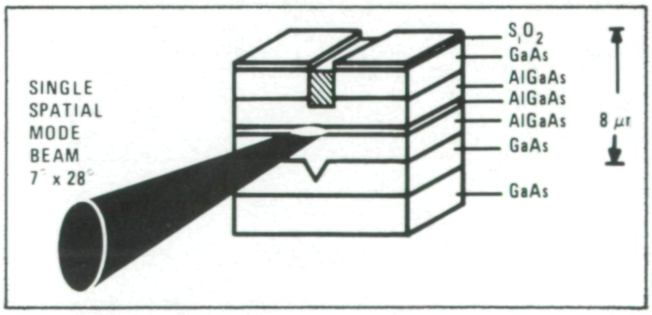

Channeled Substrate Planar AlGaAs diode lasers.

Contact: Jim Abshire
Code 720

Sponsor: Office of Aeronautics and Space Technology

400-MHz SURFACE ACOUSTIC WAVE OSCILLATOR

Data collection and search and rescue both utilize satellites to receive and retransmit signals from data collection platforms and from Emergency Locator Transmitters (ELT's). Platforms transmit at 401.650 MHz and ELT's at 406.025 MHz; both utilize 1.0 ± 0.1 radian phase modulation at 400 bits per second. Thus, the design of the transmitter for both applications is essentially the same, and if the design could be simplified by reducing the number of parts and eliminating the requirement for manual tuning and peaking of the transmitter, its cost should be reduced. Surface acoustic wave (SAW) oscillators require no frequency multiplication, manual tuning or peaking, and have the potential to be produced as an integrated circuit.

An integrated circuit 400-MHz transmitter with a ± 1.0 radian phase modulator is not yet commercially available. However, the first step toward this goal was taken when six prototype oscillators were delivered by Raytheon to the Johns Hopkins University Applied Physics Laboratory (APL) in September 1985. APL will test and document the frequency stability of the oscillators with respect to temperature, vibration, gravity, and long-term drift, before delivering them to Goddard. Goddard contracted with APL to develop the SAW oscillators, and APL contracted with Raytheon to fabricate and package the oscillators.

The first figure shows the size of a 400-MHz Surface Acoustic Wave (SAW) resonator in relation to a U.S. postage stamp. The second figure shows two sides of a prototype oscillator package, also in relation to a U.S. postage stamp. One side contains the SAW resonator; and the other side contains the oscillator circuit, which was fabricated using surface-mounted discrete components. The side containing the SAW resonator includes a small strip heater to stabilize the temperature of the SAW device at its turnover temperature. The temperature control circuit and the phase modulator are external to the prototype oscillator package.

Step 2 of this development will incorporate the phase modulator and temperature control circuit in the same package as the SAW oscillator, and step 3 will develop an integrated circuit to replace the discrete components in the temperature control and phase modulator circuits.

Contact: J. Turkiewicz
Code 670

Sponsor: Search and Rescue Satellite Aided Tracking (SARSAT) Project, Oceans Programs

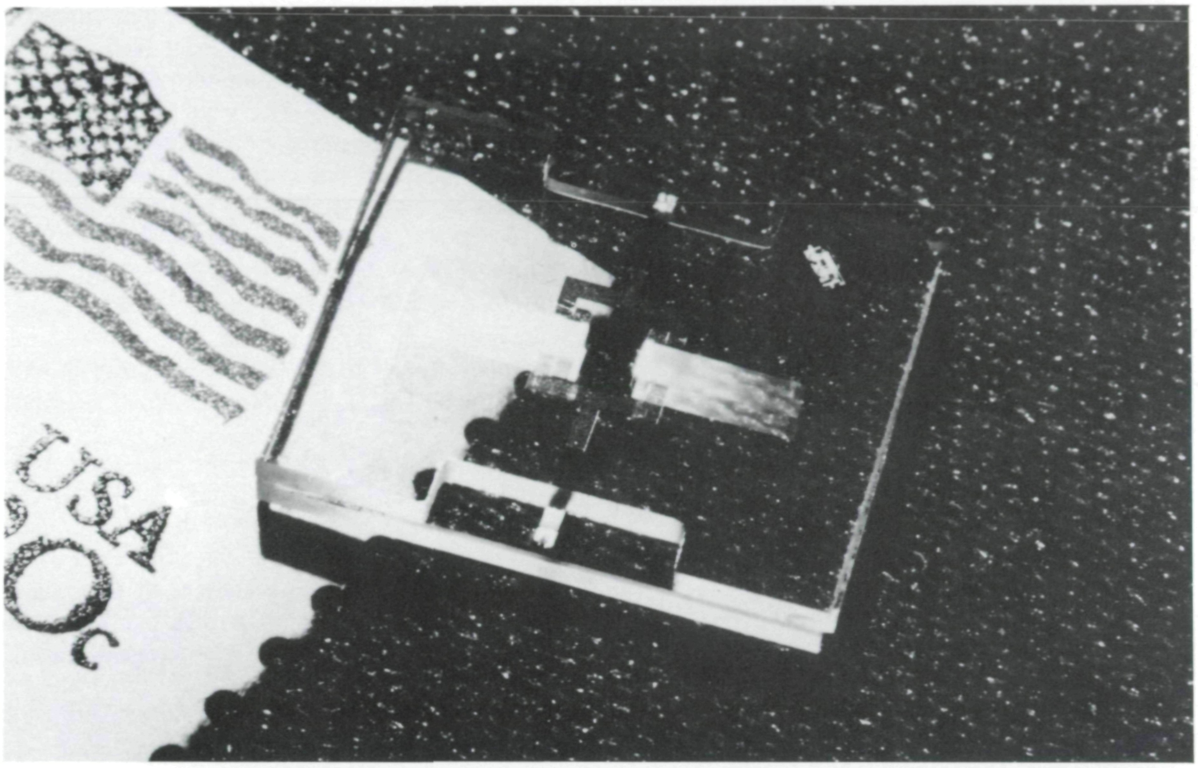

400-MHz Surface Acoustic Wave resonator.

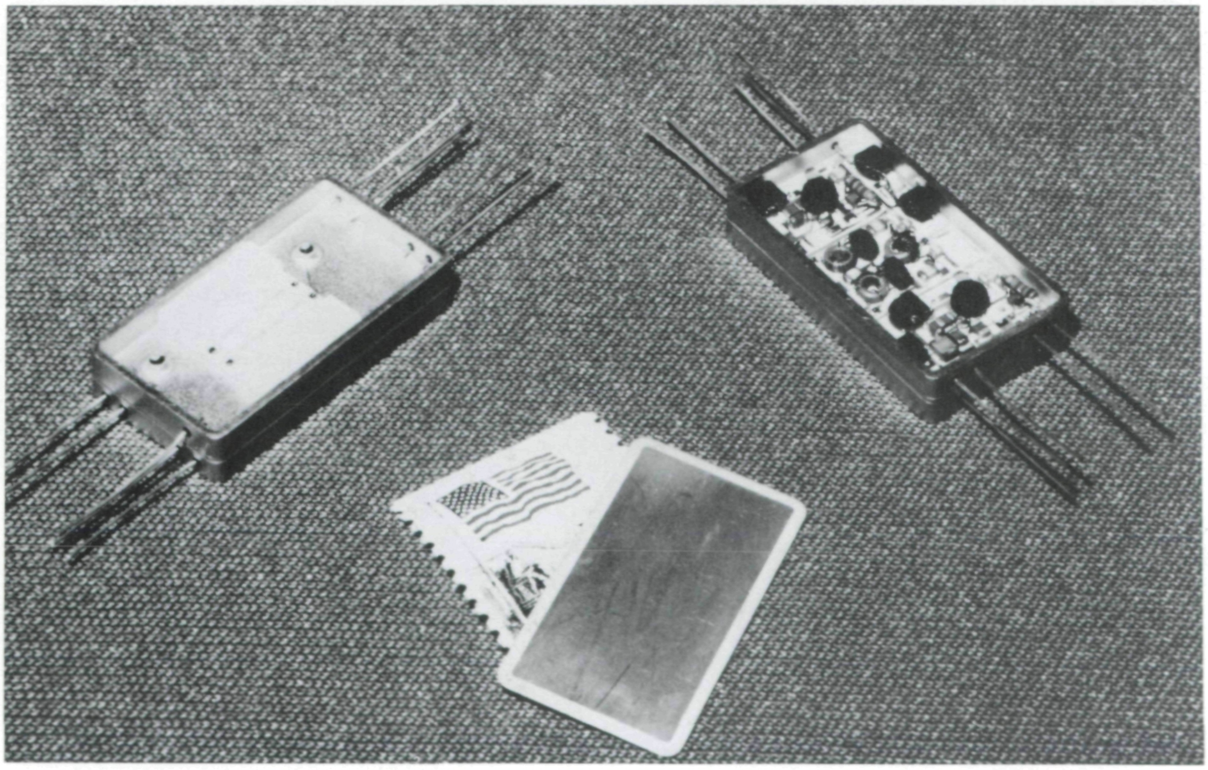

Prototype 400-MHz Surface Acoustic Wave oscillator.

60-GHz LOW-NOISE WIDEBAND RECEIVER

The frequencies around 60 gigahertz (GHz) are attractive from various standpoints to transfer data effectively at high rates between space vehicles. Two bands have been allocated by the World Administrative Radio Conference with 3.95 GHz and 5.0 GHz of bandwidth. As these frequencies are within the oxygen absorption band, interference to and from terrestrial sources is very unlikely, as is interception of these signals from ground stations.

High-performance spacecraft receivers capable of operating within these frequency bands will be required to implement any 60-GHz intersatellite communications system. To meet this challenge, an integrated receiver has been designed and fabricated utilizing printed circuit technology. Suspended stripline was used in order to demonstrate viability, low cost, and reproducibility.

This effort resulted in a low-noise, low-cost integrated receiver using printed circuit and gallium arsenide beam lead technology. The receiver operates at inputs from 59 to 64 GHz and includes a phase-locked Gunn oscillator at 51.5 GHz to produce an intermediate frequency (IF) output of 7.5 to 12.5 GHz. With the exception of the IF amplifier and radio frequency preselect filter, all circuits were fabricated using suspended microstripline. E-plane technology was used for the preselect filter.

Contact: John Chitwood
Code 720

Sponsor: Office of Aeronautics and Space Technology

KU-BAND HIGH-GAIN MICROSTRIP PLANAR ARRAY ANTENNA

A high-gain microstrip planar array antenna has been developed for operation in the Ku-band. The antenna is circularly polarized and employs a patch rotation scheme

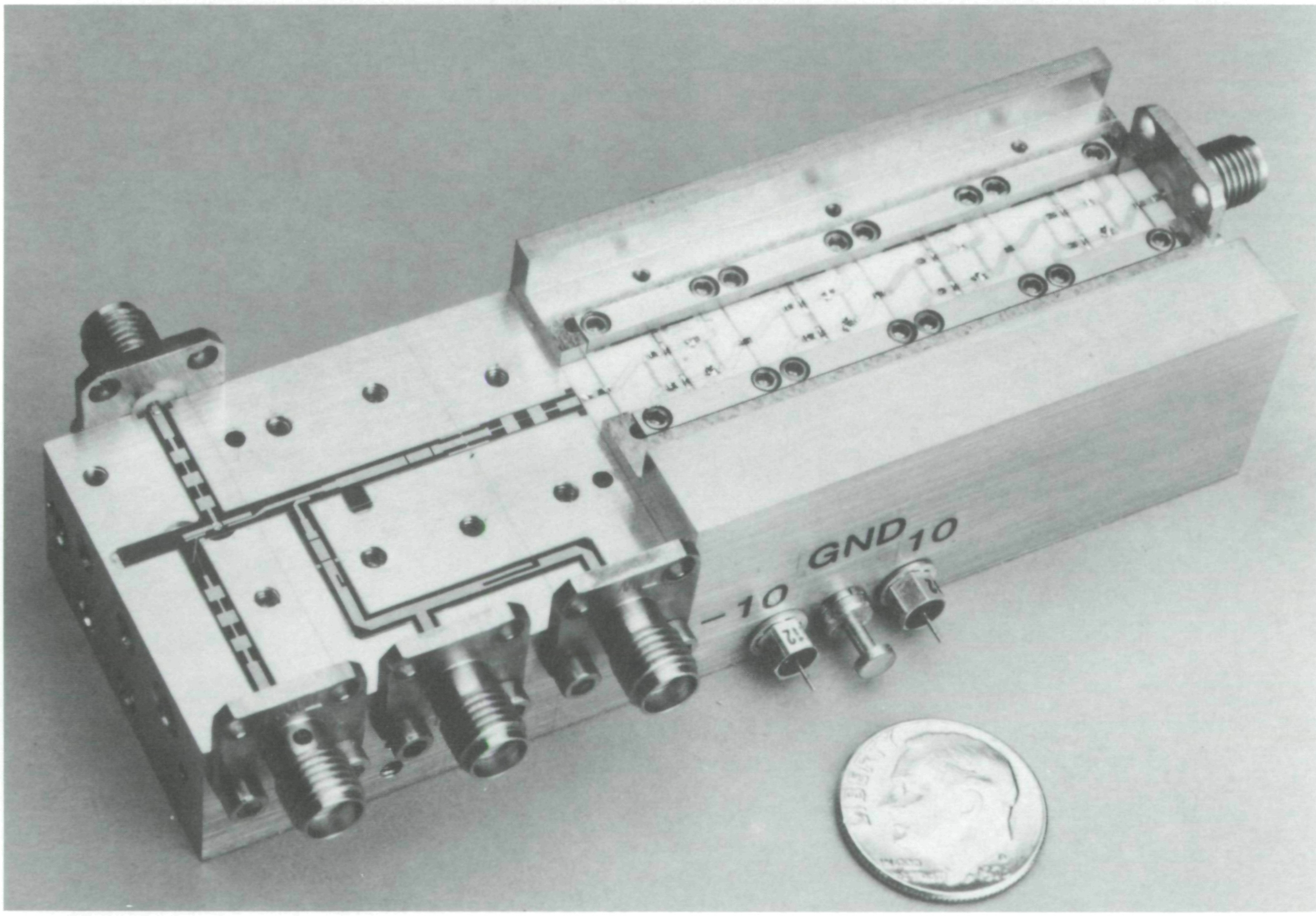

60-Gigahertz low-noise integrated receiver.

ORIGINAL PAGE IS
OF POOR QUALITY

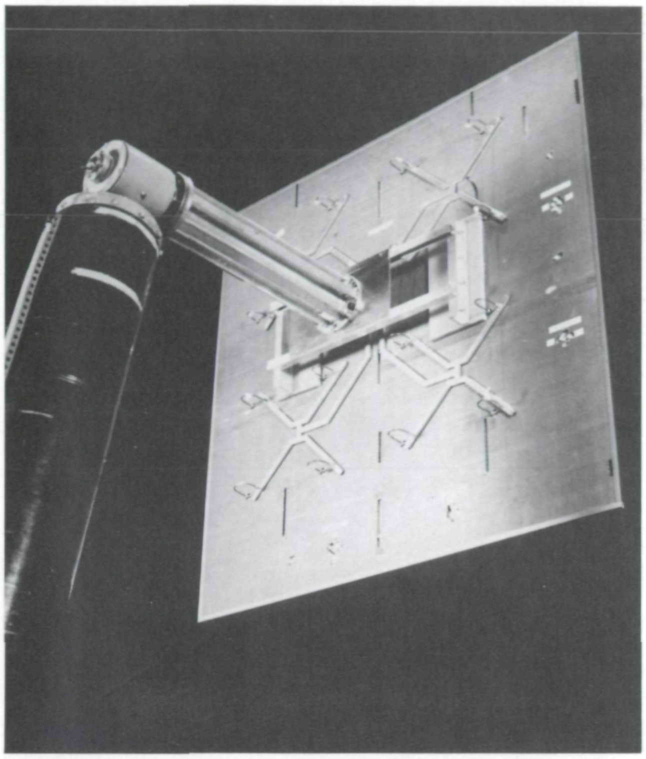

Complete Ku-band antenna in the anechoic chamber.

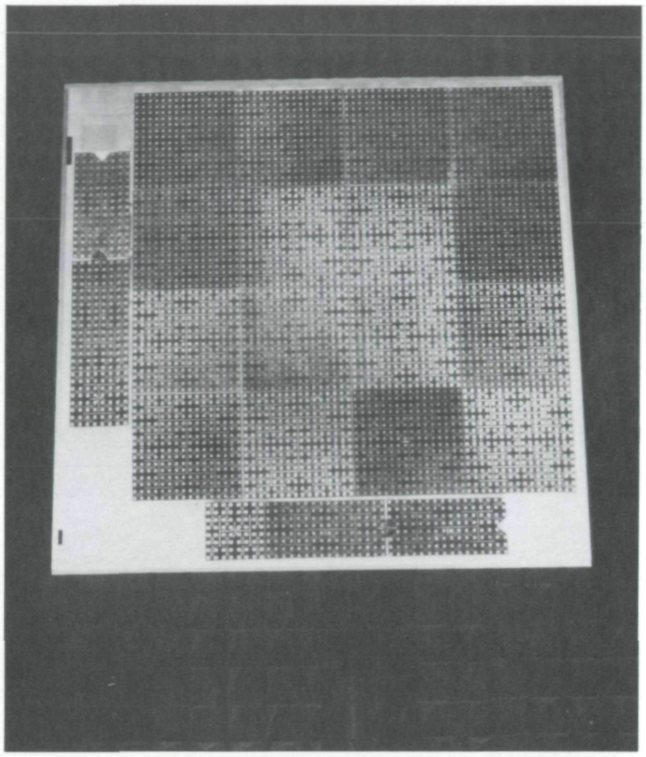

16-way waveguide power divider.

to more than double the 3-dB axial ratio bandwidth and the 2:1 VSWR bandwidth. A bandwidth of 4.5 percent was achieved on 0.015-inch Teflon—fiberglass material centered about 14.8 GHz.

The complete array is shown in the first figure. It is made up of a 4 × 4 array of subarray panels mounted on 0.25-inch honeycomb with 0.005-inch fiberglass backing. A monopulse tracking antenna, which is part of the overall assembly, is also shown. The system weighs approximately 12 pounds, is 51 inches square and approximately 2 inches deep, including the waveguide feed/power director which is shown in the second illustration. The feed system, which supplies the 16 subarray panels, consists of 5 four-way power dividers that are machined from a solid block of aluminum and interconnected with a WR-62 waveguide.

The waveguide is connected to the microstrip circuitry of the antenna via a coaxial cable whose length is adjusted to correct for build in phase errors.

The following data were measured on the first prototype antenna model: Bandwidth—640 MHz or 4.5 percent; center frequency—14.8 GHz; first side lobe level—12 dB down from peak of main beam; and, gain—39 dB ic.

The tracking scheme for this antenna utilized a coarse and fine monopulse sum and difference pattern in both the azimuth and elevation planes. The circularly polarized microstrip patch elements receive at a center frequency of 13.72 GHz. The coarse tracking is capable of pointing the transmitted beam to within ±5 degrees. Since the beamwidth of the main antenna is only 1 degree, a finer tracking system as part of a total Ku-band data system is provided and has the capability of pointing the antenna to within ±0.1 degree.

Contact: Carl L. Riffe
Code 720

Sponsor: Office of Space Tracking and Data Systems

STAR BUS FIBER OPTIC SPACECRAFT DATA SYSTEM

The Fiber Optic Data System (FODS) is an advanced, high-rate, packet-switched, distributed network data system for spacecraft. The 100-Mbs FODS, often termed "star bus," was demonstrated at the Sperry Corporation on June 19 and 20, 1985, to both government and industry.

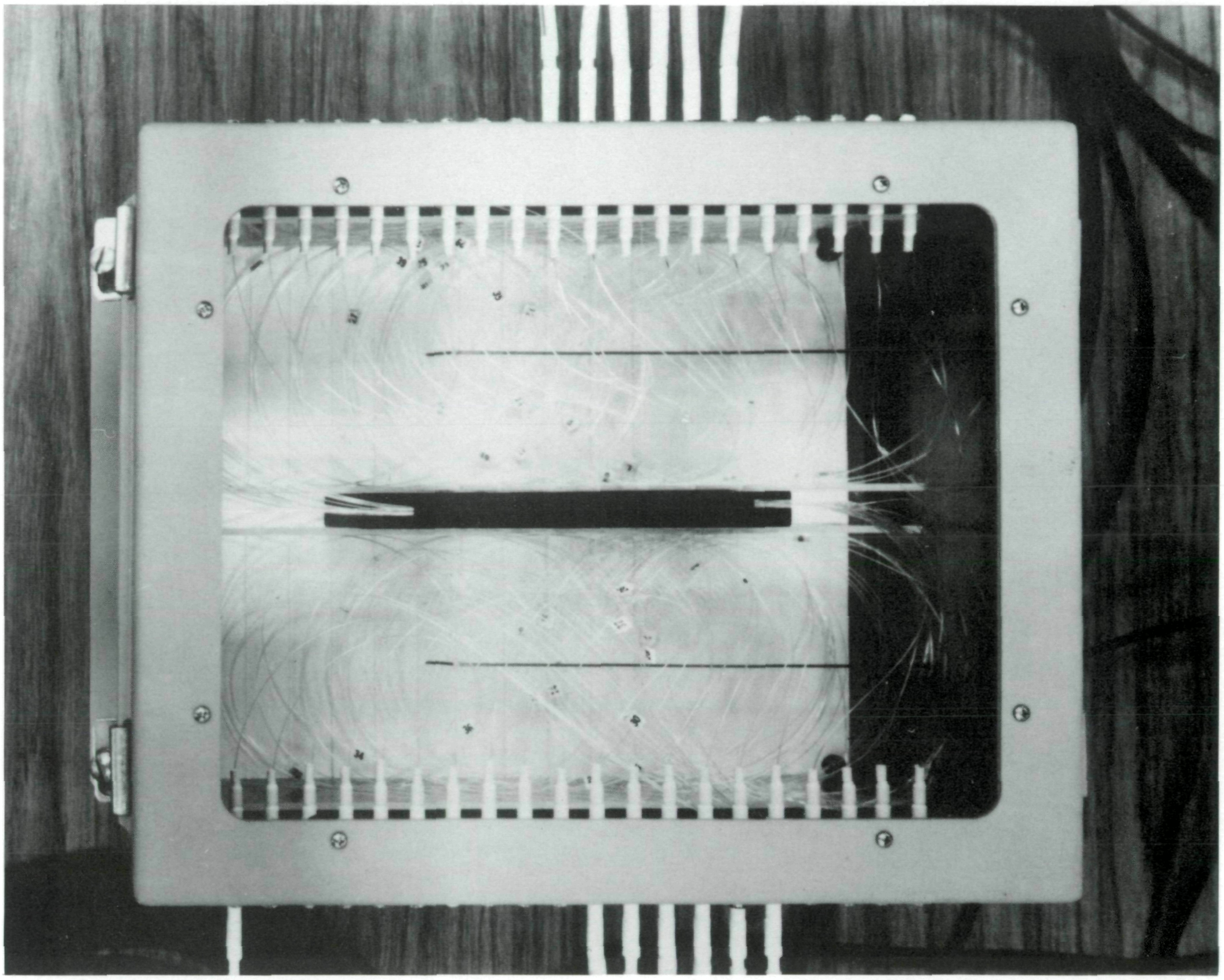

The Fiber Optic Data System.

The primary emphasis for FODS was to fully develop the first two layers of the ISO/OSI recommended architecture. Layer 1 is implemented using a passive fiber optic star coupler of high reliability and simplicity of function. This key element consists of fused 200 micron fibers. The FODS has been demonstrated utilizing redundant 20 × 20 couplers; however, the final system will be operating with redundant 32 × 32 couplers. Improvements to the Minimum Detectable Signal (MDS) strength of the optical receivers of approximately 5 dBm will allow the system to perform with the 32 × 32 full-up capability. This MDS improvement is considered to be easily attainable.

Other simple, reliable, optical components used are LED's and pin photodetectors. These components, presently being tested at the GSFC quality-testing facilitiies, should prove to be long-lived, low-power elements contributing to a reliable system.

Layer 2 of the ISO/OSI recommended architecture employs a bus access protocol termed "CSMA/CD/TS." This protocol is a self-starting, autonomous, bus loading-adjusting protocol exploiting the high-performance characteristics of a carrier-sensed multiple-access protocol for low-traffic intensity and the good performance of a time slot protocol for high-traffic intensity. Preliminary results corroborate the predicted analytical expectations of this new bus access protocol. Two other built-in familiar protocols can be utilized by the system for evaluation comparisons.

An important feature of the topology has been fully demonstrated whereby nodes in the network were disconnected with no effect in the operation of the other nodes.

Another vital characteristic of the system is the maximum attainable throughput, analytical results predict greater than 80 percent bus utilization with mean transfer delays in the order of milliseconds.

Future development involves implementing ISO/OSI Layer 3 and reducing input power by VLSI techniques in both HCMOS and gallium arsenide for the low-speed and high-speed circuit elements.

Contact: John Rende
Code 730

Sponsor: Space Station
Office of Aeronautics and Space Technology

20-MBS FLIGHT RECORDER

The 20-mbs flight recorder is a complete magnetic tape recorder/data storage system providing 10 to the 10th bits of storage capacity at data rates up to 20 mbs. The development of this system has been directed by GSFC with FCA, Government Communication Systems Division, Camden. The development of the 20-mbs recorder began in January 1983 and is expected to be complete in the third quarter of 1986.

Designed to operate unattended in the space environment, the 20-mbs system consists of two components: the Transport Unit (TU) and the Electronics Unit (EU). The system features serial input and output ports and provides for an auxiliary unit for adaptation to virtually any data I/O rate up to the maximum specified rate. An auxiliary cross strap unit can provide dual EU/TU redundancy.

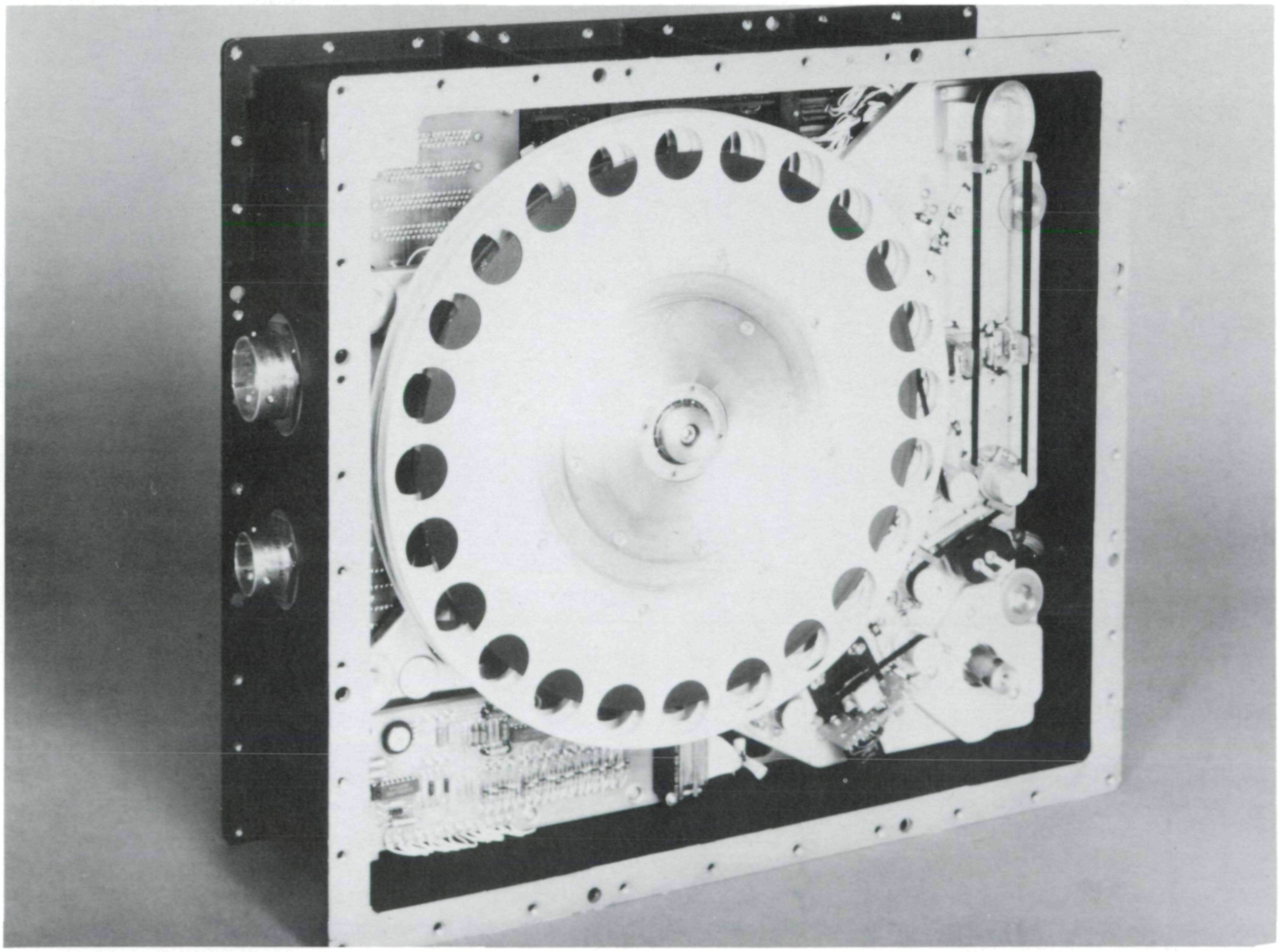

20-mbs flight recorder.

The 20-mbs system is designed for flexible mounting and operation. The EU and a TU can be mounted together or separately. The TU features negator-coupled reels housing 2780 feet of 1/4-inch magnetic tape. There is no edge guidance of tape, and redundant beginning and end of tape sensors are provided. A brushless dc motor drives the tape at the speed to accommodate the specified range of data rates and at constant bit packing density. A longitudinal, blocked data tape format is used with a sixteen-track head with twelve tracks allocated for data and four for error management. The tracks are recorded and reproduced by a single integrated head structure. Only the analog and motor drive electronics are located in the TU, and all elements of the TU are sealed in a pressurized container.

The EU is a vented sheet metal structure which houses five circuit boards to provide all the functions for data processing, command and control, telemetry, and power regulation and distribution. System command adaptability is provided by replacement of a single dedicated plug-in board.

The 20-mbs recorded prototype unit is currently in system checkout, and the major accomplishments this year were the implementation of LSI chips in the record, playback, and error detection/correction circuitry.

Contact: Tom Ratliff
Code 730

Sponsor: Office of Space Tracking and Data Systems

BALLOON GONDOLA DIAGNOSTICS PACKAGE

Numerous studies have been conducted in the past to develop a theoretical approach for predicting parachute-opening dynamics. Although this work has resulted in

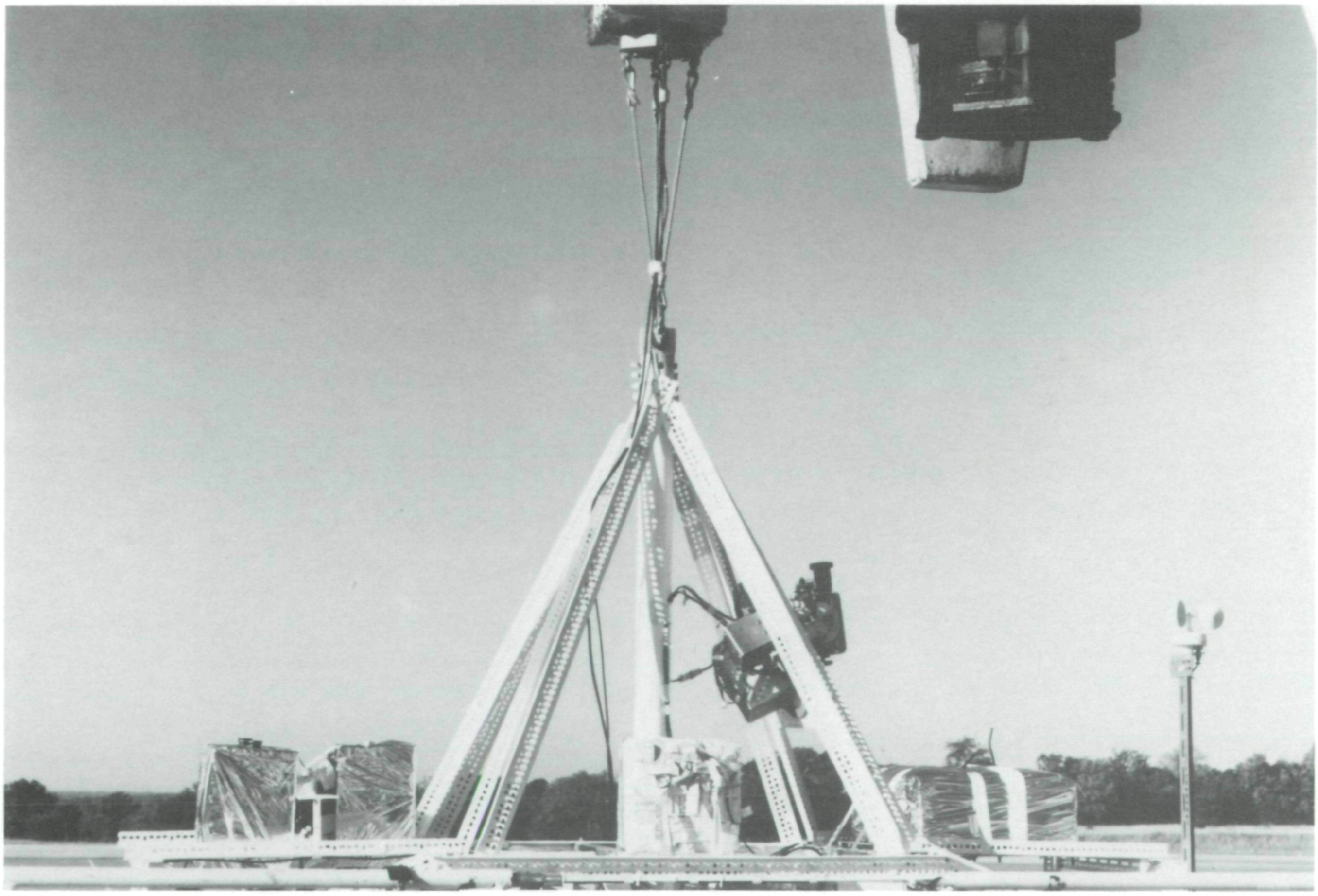

This view from on board the launch vehicle shows the GDP mechanical section held between the vehicle's arms prior to lift-off. The payload gondola suspended from the mechanical section holds, among other instrumentation, the lower electronics section (bottom right) with its telemetry antennas pointing toward the upper electronics section.

As the balloon is released from the launch spool, it ascends over the payload launch vehicle where the GDP mechanical section is released from the vehicle arms at the appropriate time to be lifted toward the stratosphere.

satisfactory models of the parachute-opening process for some applications, there remains a lack of analytical tools and meaningful data for scientific ballooning applications. Most of those studies concentrated on parachute openings from an undeployed state, at low altitude (less than 30,000 feet) or extremely high altitude with light payloads, and with a significant initial velocity. For some applications, multiple parachutes have been utilized to assure reliability. In scientific ballooning, a single deployed parachute is used, and it is flown as in integral part of the payload suspension system. The opening process occurs at a reasonably high altitude (normally 80,000 to 130,000 feet), with payloads up to 6,500 pounds, and with no significant initial velocity.

As part of the NASA Balloon Program, Goddard Space Flight Center/Wallops Flight Facility (GSFC/WFF) initiated a program to develop a lightweight, operational flight package, independent of the scientific payload and operational flight support equipment, capable of accurately measuring and recording parachute opening motions, forces, and accelerations. Given the name Gondola Diagnostics Package (GDP), the system actually consists of three sections: lower electronics section, mechanical section, and upper electronics section. The GDP can be flown on any payload launched by the National Scientific Balloon Facility (NSBF) with their primary launch vehicle in Palestine, Texas. The lower electronics package can be attached at any available location on the gondola. The upper electronics package is bolted directly to the mechanical section, which is installed in the flight train and serves as the interface between the parachute suspension and gondola rigging lines, as well as the launch restraint point.

The mechanical section consists of a launch fitting, similar to those normally used by the NSBF, modified to include a load cell. Loads measured by the load cell

are monitored by the top electronics package and this information, along with data on the motions of the top package, is telemetered to the lower electronics package. The lower electronics package measures gondola motions which, in addition to the information received from the top package, is stored on board. The lower electronics package also transmits all the data to ground-based telemetry stations.

Ground and flight testing of the system has been successfully concluded, and analytical methods have been developed for postflight data reduction and analysts. Operational use of the GDP on all flights at the NSBF will begin in early FY86. Results of the flight data will be used to develop a realistic structural specification for balloon gondolas and rigging, to evaluate existing and new balloon parachute deployment techniques, and to reduce balloon flight termination dynamics.

Contact: Robert S. Nock and I. Steve Smith
Code 840

Sponsor: NASA Balloon Program

SENSORS

RESEARCH OPTICAL SENSOR

During the last year, a concentrated effort has been carried out within the Laboratory for Terrestrial Physics to examine the present status of imaging radiometry from space, to project the scientific community's needs into the mid- to late-1990's and, after careful examination of recent developments in remote sensing technology, to design a multichannel imaging spectroradiometer capable of meeting these needs. The new system has been designated the Research Optical Sensor (ROS) and is viewed as the next logical step in land remote sensing science that has progressed from the Multispectral Scanner (MSS) of Landsats-1, -2, and -3 through the Thematic Mapper (TM) of Landsats-4 and -5. The major departure of the ROS design from those of MSS and TM is the utilization of linear detector arrays of several thousand elements for each of the spectral channels under consideration. This approach results in large increases in sensor sensitivity which can be used in numerous ways including increases in spatial resolution, spectral resolution, and/or radiometry sensitivity.

The use of linear array technology led to an ROS design capable of meeting current and future research requirements in terrestrial remote sensing. These requirements include the narrow spectral bands (20 nm) and wide spectral coverage (21 bands from the visible to thermal infrared) provided by the ROS design. This spectral resolution is needed for the sensing of mineral absorption bands in geologic studies and for the detection of subtle shifts in the spectral reflectance of vegetation in response to climatic and environmental factors. In conjunction with the spectral resolution, a high radiometric sensitivity is needed to infer terrestrial biophysical properties from the radiometric data and to account for atmospheric effects on the data. The absolute accuracy (2 percent), noise equivalent change in reflectance (0.5 percent), and data quantification (10 bits) of the ROS design provide the necessary sensitivity for the scientific studies.

Additional research requirements are addressed by the spatial resolution offered by the ROS design. Research is needed on the spatial dynamics of terrestrial biophysical properties and the relationship of the spatial dynamics to climate. The 10 m (visible and near infrared bands) and 20 m (shortwave infrared bands) instantaneous fields of view of the ROS design present the resolution needed to study, understand, and quantify the variation of certain terrestrial properties over surface area.

Another dimension of remote sensing research is addressed by the off-nadir pointing capabilities of the ROS design. Reflectance from terrestrial surfaces varies with the sensor viewing direction; that is, terrestrial surfaces reflect light anisotropically. The observation of reflectance anisotropy is under study as an enhanced approach to the remote determination of biophysical properties. Also, the total reflectance in all directions must be characterized to accurately calculate surface energy budgets. A single observation of the reflectance of nadir is usually insufficient for this purpose. The ROS design permits pointing of the sensor up to 40° off-nadir

C-2

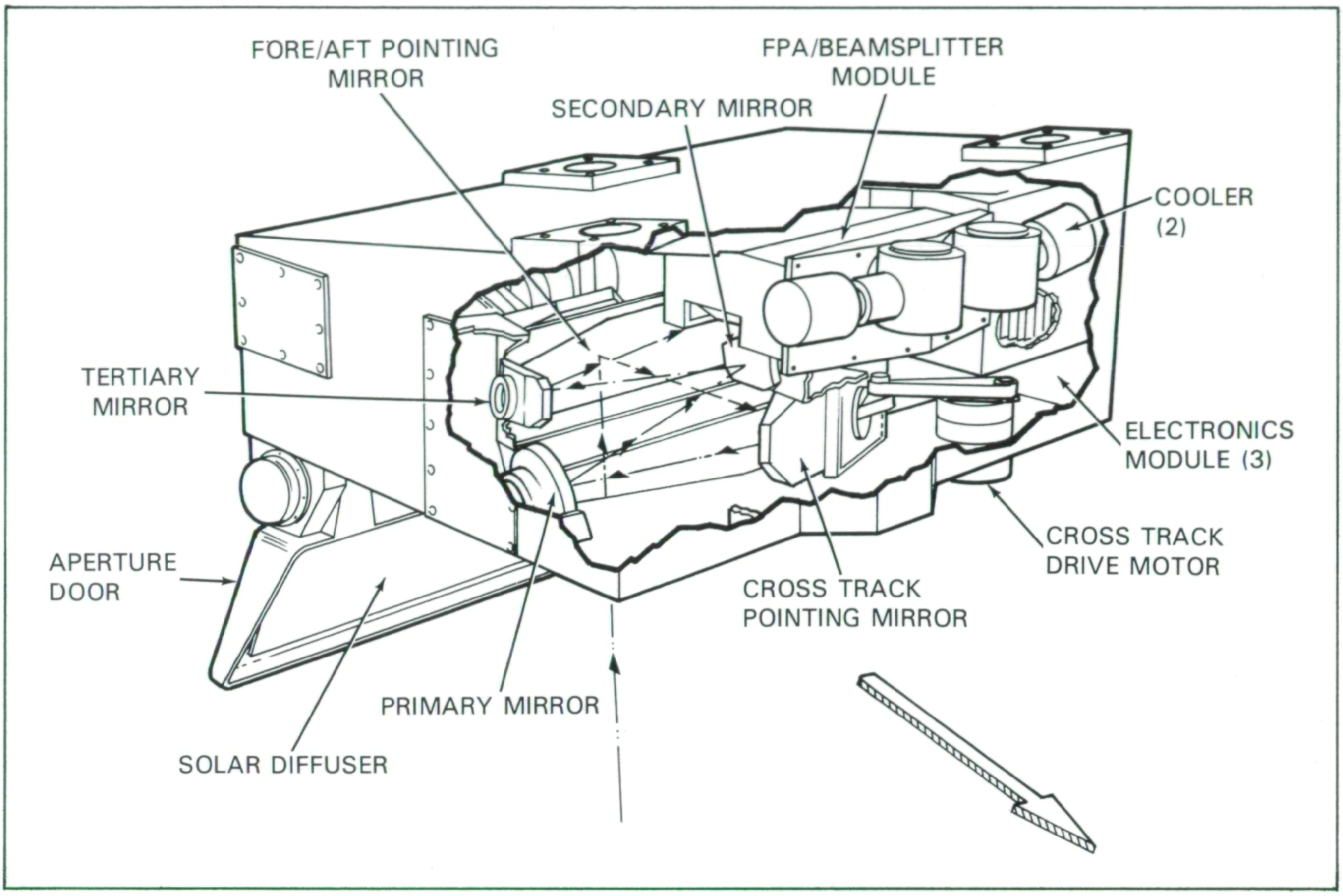

Research Optical Sensor Concept.

for the multiple direction observation of reflectance anisotropy.

The accompanying figure is a sketch of the ROS instrument. The fore/aft pointing mirror allows observation of any point on the Earth's surface within 40 degrees of nadir. The three-element, reflective optical system focuses the scene onto the Focal Plane Assembly (FPA)/Beamsplitter Module where the optical beam is split-off to the various detector arrays. The aperture door serves to protect the optics and also functions as a solar diffuser for calibration.

Much new technology was required to meet the scientific requirements for the ROS design. ROS new technology involves relatively wide field-of-view reflective triplet optics and electronically scanned two-dimensional detector arrays. The wider field-of-view optics is necessary to accommodate the increased spatial extent of the scene that is imaged. The ROS needs detector arrays to cover a rather large spectral range. As a result of the ROS activity, the visible (4-1.0 micrometers) and SWIR (1.0-2.5 micrometers) detector technology is well in hand. Although satisfactory MIR (4.0-7.0 micrometers) and TIR (7.0-12.0 micrometers) detector arrays are not yet available, substantial work in this area is under way in the detector community.

Contact: Harry F. Shaw
Code 620

Sponsor: Office of Space Science and Applications

LIDAR REMOTE SENSING OF THE ATMOSPHERIC PRESSURE PROFILE WITH TUNABLE ALEXANDRITE LASERS

Significant improvement in the measurement of the basic atmospheric parameters are required for improved weather forecasting, the prediction of climate change, and increased understanding of atmospheric processes. Measurement of the atmospheric pressure field is one of

the basic requirements. Previously, there have been no current remote sensing techniques for measurement of the pressure field. Thus, important forecasting tools such as maps of surface pressure and 500-mb height contours must be produced either by *in situ* measurement or by indirect methods.

We have recently developed and used a high-resolution tunable Alexandrite (chromium-doped beryllium oxide) laser system to make the first differential absorption lidar measurements of the atmospheric pressure profile. We also report on high accuracy measurements of laser spectral purity and the spectral line shape of the laser emission.

Our lidar system incorporates two solid-state Alexandrite lasers which are continuously tunable from 725 to 790 nm and have a bandwidth of 0.02 cm^{-1} using a birefringent filter and two etalons. We have measured the short-term frequency stability of the lasers to be better than 0.005 cm^{-1} and the Q-switched pulse length to be 100 to 130 nsec. One laser has a 100 mm $\times$ 5 mm diameter Alexandrite rod and a 150 mJ output energy. The tuning elements are electronically controlled and have a 3 cm^{-1} automatic spectral scanning capability. The second Alexandrite laser has a 75 mm $\times$ 5 mm rod and a 100 mJ output energy. Its tuning elements are manually controlled and it is typically used for the off-line measurement. Both lasers operate at a 10-Hz repetition rate and have a multimode spatial intensity distribution.

A 5-cm interferometer was used to make high-resolution (0.002 cm^{-1}) measurements of the laser line shape by observing Fizeau fringes in transmission. The laser output consists of three axial modes with an overall width of 0.026 cm^{-1}. The individual modes have a width of 0.004 cm^{-1} and are nonuniformly spaced with a ratio of 1 to 1.3.

Spectral purity is an important parameter in lidar absorption measurements since spectrally impure out-of-band radiation (e.g., amplified spontaneous emission) may be weakly absorbed whereas the narrowband component of the laser output may be strongly absorbed. For example, a 5 percent level of impurity can introduce a 100 percent error in a measurement with 95 percent absorption. We have shown that strong absorption lines can be used as a filter to reject the narrowband laser radiation. This allows the integrated out-of-band radiation of a pulsed laser to be easily measured. The spectral width of the rejection filter can be adjusted by varying the pressure of the absorbing gas. We have used this technique and found that the spectral impurity of our Alexandrite laser output is less than 0.01 percent. This is a thousandfold improvement in accuracy compared to other techniques which have been previously used.

Our ground-based lidar system has been used to make high-accuracy measurements of the atmospheric pressure profile utilizing the integrated absorption in the wings of lines in the O_2 A band. We use absorption troughs, regions of minimum absorption between two strongly absorbing lines, for these measurements. This technique greatly desensitizes the measurements to the effects of laser frequency instabilities.

The energy backscattered from the atmosphere is collected with a 45-cm telescope and detected with a photomultiplier tube. The receiver field of view can be made as small as 0.25 mrad with an adjustable field stop to provide rejection of daytime backgrounds. In addition, narrow bandwidth (1 nm) interference filters provide spectral background rejection. Separation of the on-line and off-line laser pulses is accomplished by introducing a 100-μsec time delay between the two laser pulses. A single detector channel is then used to observe both wavelengths. The analog signals from the photomultiplier are digitized to 10-bit accuracy at a 20-MHz sample rate by a transient waveform recorder. This function, as well as the system timing and computer interfaces to energy and spectral monitors, is implemented using CAMAC (IEEE 583) standard modules. An LSI-11/23 microprocessor controls system functions and monitors all operate adjustable parameters.

An example of upward-viewing profiling measurement made with our ground-based lidar system is shown in the illustration. The data were taken with a 1-mrad field of view. Interference filters were not used because of the low nighttime background levels. The lidar system was set up

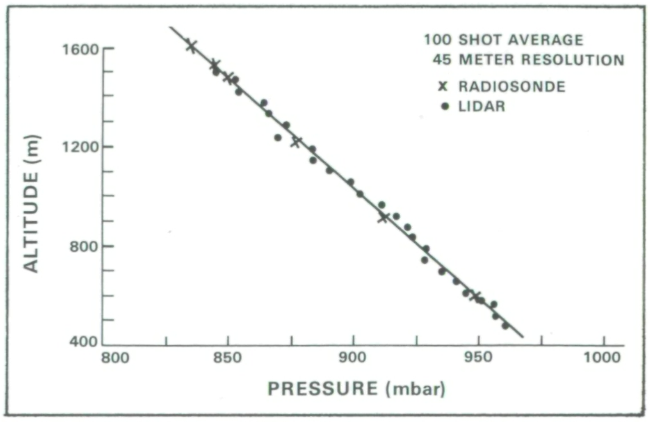

Ground-based pressure profile measurements.

to measure pressure with the on-line laser tuned to the absorption trough at 13153.8 cm^{-1} and with the reference laser tuned to a nonabsorbing frequency near 13170.0 cm^{-1}. The lidar signal returns were sampled with a 50-nsec range gate (7.5-m vertical integration) and averaged over 100 shots. The integrated absorption coefficient between the lidar and each altitude was calculated from these data. The pressure profile was then determined by relating the measured integrated absorption coefficient to the difference in the squares of the pressures at the measurement altitude and laser altitude. Uncertainties in the oxygen line parameters were corrected for by a calibration fit of the measured data to ground truth. The figure shows a comparison of the lidar-measured pressure profile above Goddard Space Flight Center (lat N 39.00°, long W 76.85°) to radiosonde data taken 1.5 hours earlier at Dulles Airport (lat N 38.98°, long W 77.46°). The data were averaged to a 45-m vertical resolution in order to improve the signal-to-noise ratio. The average deviation of the lidar pressure data from the radiosonde data is 0.3 percent.

In addition to pressure measurements, our system will also be used to investigate temperature profile measurements using the high J lines of the oxygen A band.

Contact: L. Korb
Code 610

Sponsor: Office of Space Sciences and Applications

AIRBORNE LASER BAROMETRIC ALTIMETER

The Airborne Laser Barometric Altimeter (ALBA) is an outgrowth of two-color laser ranging technology, which was originally developed under the OAST IR Lidar

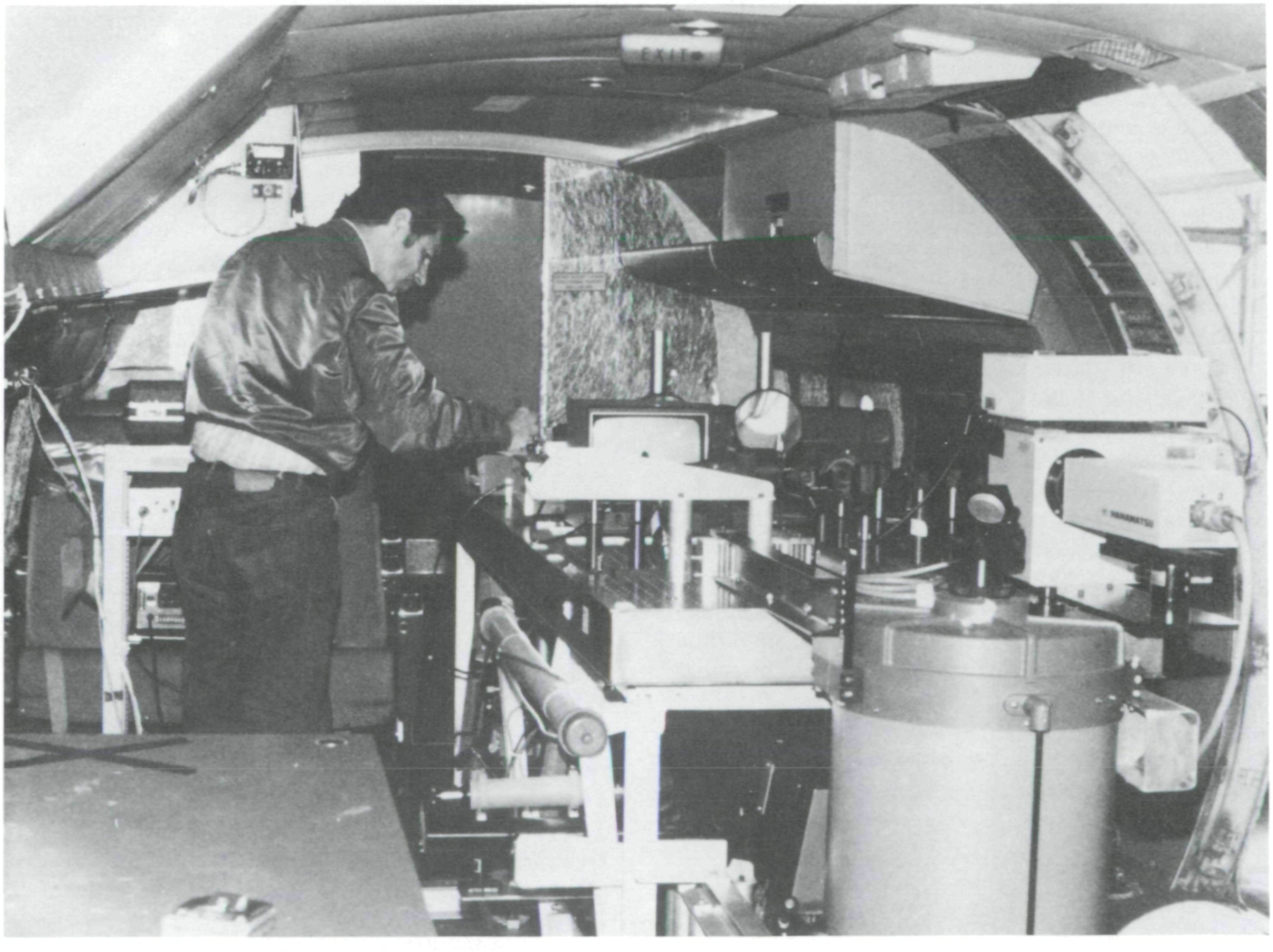

Laser barometric altimeter in Wallops Electra aircraft.

RTOP to support the NASA geodynamics program. In the original geodynamics application, ultrashort (30 picosecond) laser pulses at two wavelengths are emitted simultaneously by a Spaceborne Geodynamics Ranging System (SGRS) and travel through the atmosphere to a reflective ground target which, in turn, returns them to a telescope and a streak-camera-based range receiver colocated with the laser. The dispersive properties of the atmosphere cause the pulses to become separated in time. The induced temporal separation, which is proportional to the integrated air density in the path, is measured with a high-resolution (2 picosecond) streak camera. This permits the basic pulse time-of-flight data to be corrected for the refractive effects of the atmosphere to yield an absolute range accuracy on the order of several millimeters. These data provide subcentimeter accuracy measurements of long terrestrial baselines and permit the precise monitoring of the relative motion between tectonic plates.

With the ALBA instrument, we are investigating the potential for using this two-color laser ranging technology to provide the first active surface pressure measurements over oceans and to provide high-resolution measurements of sea surface and surface winds. In this mode, the instrument is in a nadir-viewing or altimeter mode, and small ocean surfaces normal to the propagating wavefront provide correlated high intensity signals or glints in the returning waveforms at the two wavelengths. The time delay between corresponding "glints" in the waveforms is proportional to the total integrated air density in the column between the aircraft and the sea surface. Operated from space, this would correspond to a measurement of surface pressure. In the first relatively crude experiment, the instrument clearly demonstrated a capability to remotely measure surface pressure with few millibar accuracy (0.3 to 0.7 percent) and a potential capability of one millibar accuracy. Since glints are generated by the crests and troughs of sea waves, the system can measure wave amplitudes as well. A Fourier transform of an individual waveform clearly shows centimeter amplitude capillary waves riding on the surface of the principal waves. Since capillary waves can be related to surface wind speed, the flight data are currently being analyzed to determine the instrument's potential for new, higher resolution measurements of surface winds.

Contact: John J. Degnan
Code 720

Sponsor: Office of Aeronautics and Space Technology

OCEAN TOPOGRAPHY EXPERIMENT RADAR ALTIMETER

The Ocean Topography Experiment (TOPEX) radar altimeter is being developed for the Jet Propulsion Laboratory's (JPL's) planned TOPEX spacecraft. It will be the fifth generation radar altimeter to have been flown in space dedicated toward the measurement of ocean topography. The 2-centimeter level of precision to be offered by the TOPEX radar altimeter, coupled with the accompanying precise orbit ephemerides to be made available by the project, make the TOPEX mission particularly attractive to the oceanographic community.

Over the past 3 years, the TOPEX Advanced Technology Model (ATM) radar altimeter breadboard electronics have been developed by The Johns Hopkins University/Applied Physics Laboratory (APL) in conjunction with the Goddard Space Flight Center. The stringent 2-centimeter precision requirement for ocean topography determination necessitated examining the applicability of existing radar altimeter designs for their use in TOPEX. As a result, a system configuration has evolved using some flight-proven designs in conjunction with needed improvements, i.e., a second frequency or channel to remove the range delay or apparent height bias caused by the electron content of the ionosphere, higher transmit pulse repetition frequencies for correlation benefits at higher sea states to maintain precision, and a faster microprocessor to accommodate two channels of altimetry data. In early 1985 at the subsystem level, the signal processor electronics package, completed last year, exceeded its bench-level checkout goal of $\leqslant 1$ centimeter measurement uncertainty with a simulated 2-meter significant waveheight test input, a convincing step toward the realization of an overall 2-centimeter precision radar altimeter for the TOPEX mission. Currently, all the breadboard electronics are undergoing final assembly with abbreviated system-level testing scheduled for completion in September 1985. Also, preliminary planning for the algorithms that will be used in the TOPEX mission ground data processing operation has been accomplished.

Detailed testing of the integrated ATM will be accomplished to fully evaluate and characterize the capability of the TOPEX ATM over the range of expected TOPEX ocean surface conditions. Additionally, the TOPEX 3-frequency feedhorn (2 linearly polarized 13.6 GHz, and 1 linearly polarized 5.3 GHz frequencies) will also be designed, developed, and tested. Electromagnetic compatibility testing will be conducted between the TOPEX radar altimeter (C-band 5.3 GHz) ionospheric correction channel frequency and the TOPEX radiometer

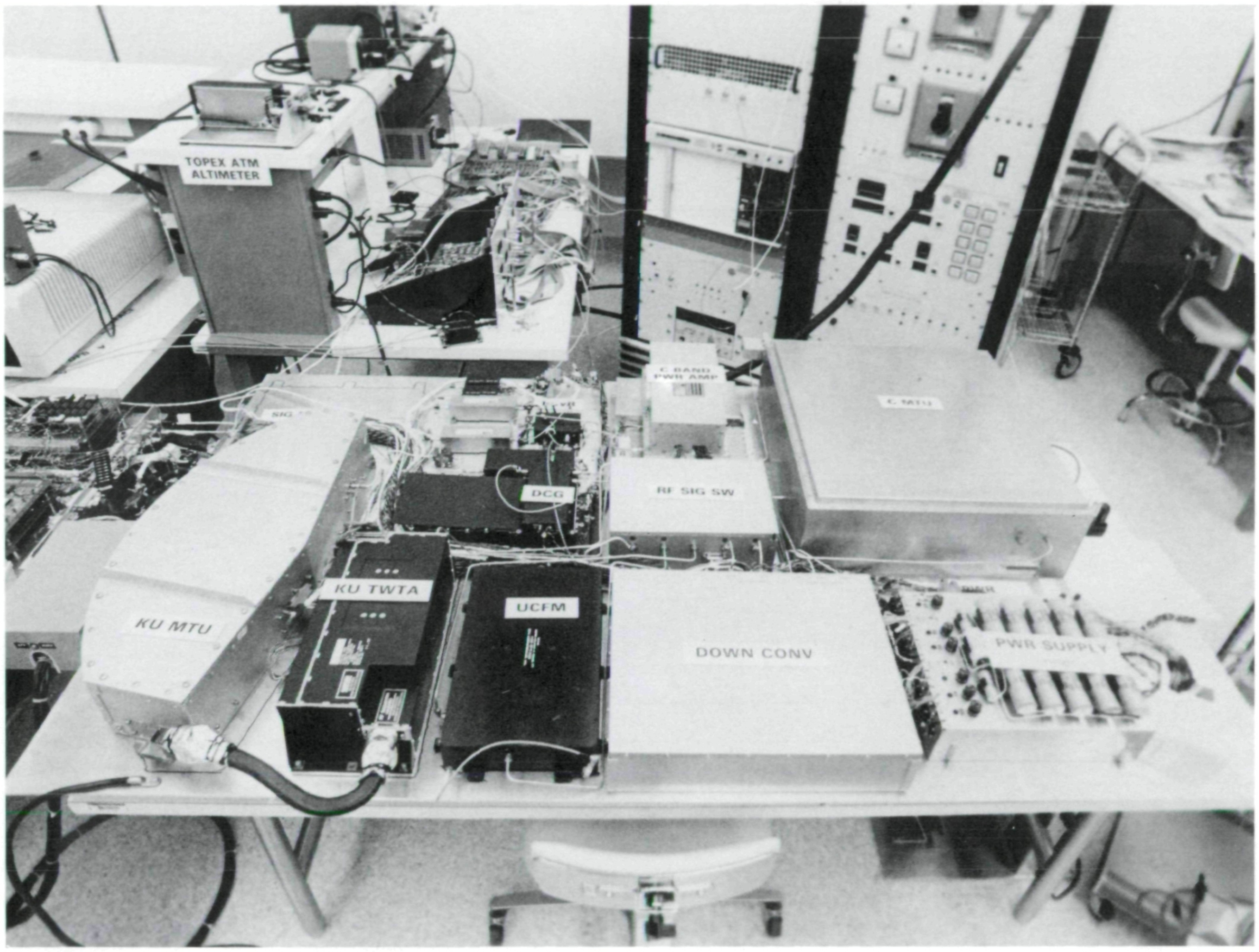

The Ocean Topography Experiment radar altimeter is being developed.

18-, 21-, and 37-GHz channels. The existing preliminary interface definition for the TOPEX radar altimeter will be expanded and refined for use by JPL.

Contact: Laurence C. Rossi
Code 670

Sponsor: Office of Space Science and Applications

GALILEO PROBE MASS SPECTROMETER (JUPITER)

The Jovian atmosphere is comprised primarily of 90 percent hydrogen and 10 percent helium. Remote measurements also indicate minor amounts of the inert gases neon, argon, krypton, and xenon, and noninert gases such as water, methane (CH_4), ammonia (NH_3), hydrogen sulfide (H_2S), acetylene (C_2H_2), and ethane (C_2H_6), as well as other trace constituents. A mass spectrometer in the Galileo Probe to be launched in 1986 will for the first time permit direct and repeated sampling of Jupiter's atmospheric gases at different altitudes as the Probe descends.

With its broad mass and sensitivity range, the instrument measures almost everything that enters it, making it ideal for this exploratory mission. The mass range of atmospheric gases to be analyzed will be from 1 to 150 atomic mass units (AMU's).

Ambient gases will enter into the mass spectrometer ion source through two sample inlet systems which are operated in sequence. The gas inlet ports will be sealed by metal-ceramic devices and kept under vacuum until

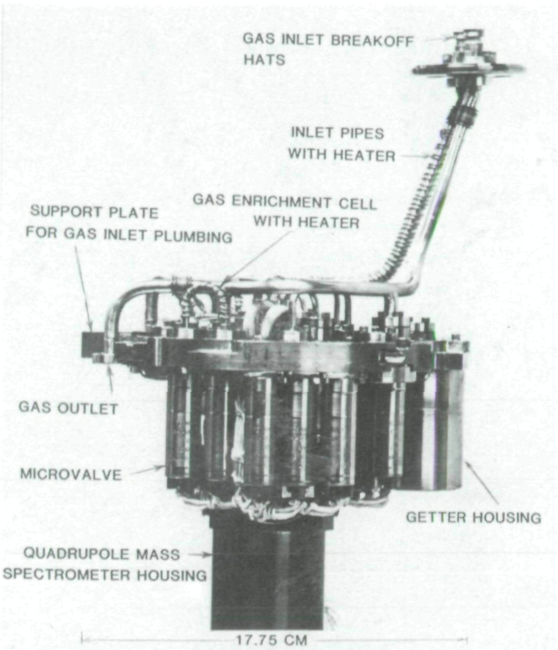

Galileo Probe Mass Spectrometer sample inlet system and quadrupole mass filter.

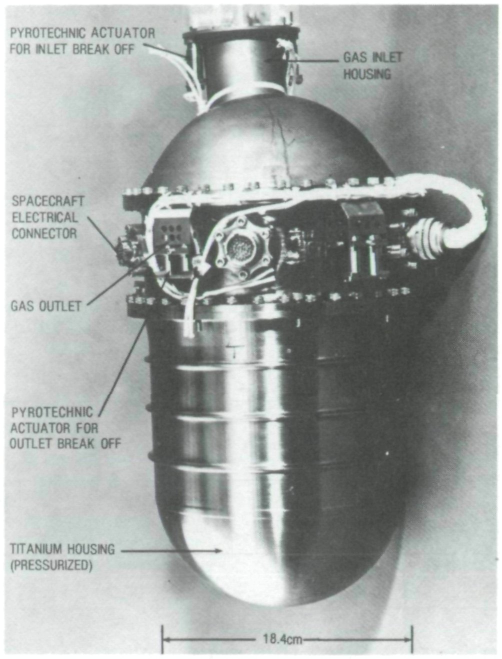

Galileo Probe Mass Spectrometer instrument housing.

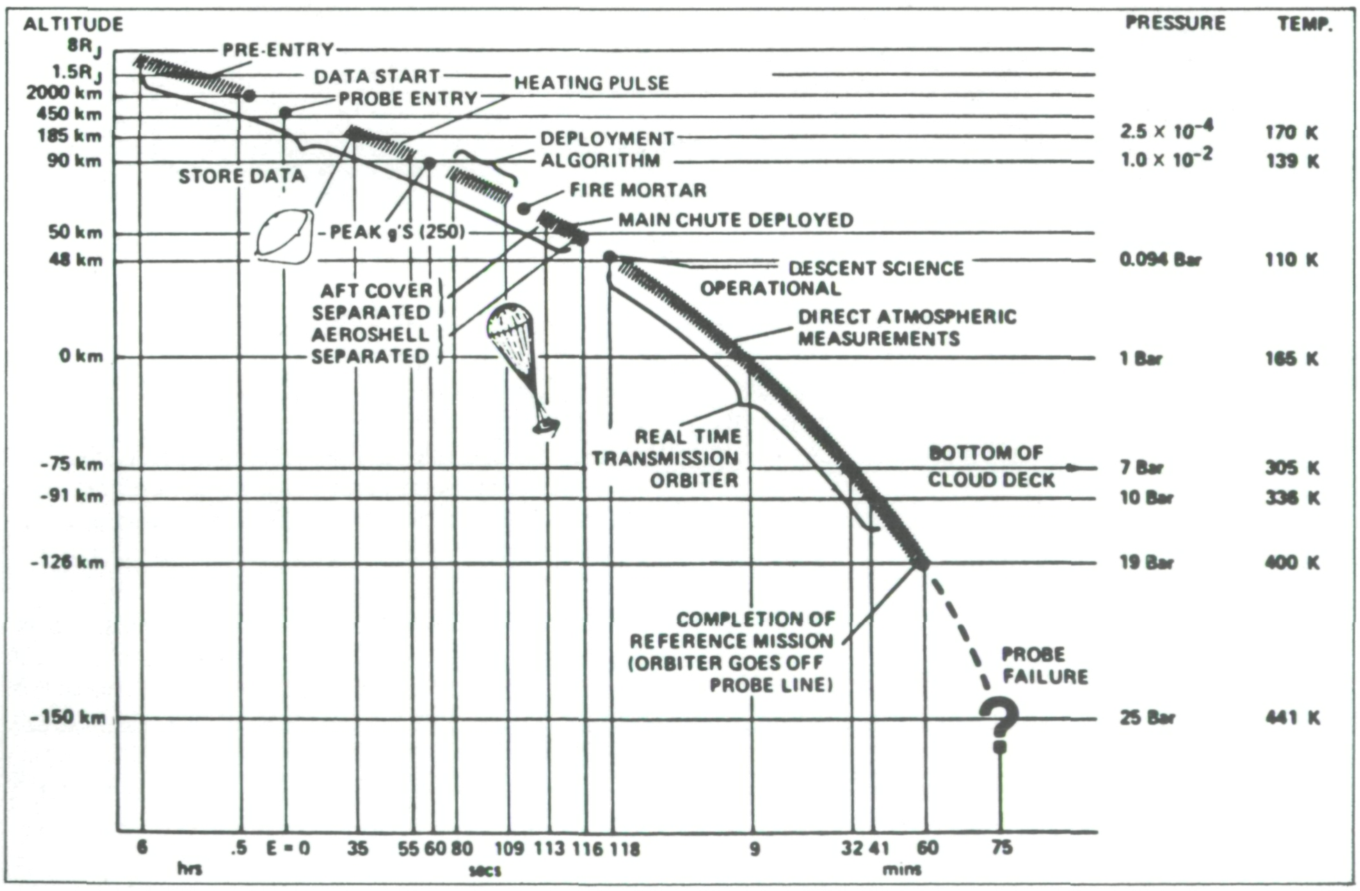

Entry probe descent events.

the Probe enters the Jovian atmosphere. Pyrotechnic devices will then release the covers, allowing atmospheric gases to enter the sample inlet system and sensor.

In addition, two sample enrichment cells will be used which separate hydrogen from the gas samples and adsorb trace gases such as hydrogen sulfide, phosphine, and complex hydrocarbons until only the noble gases remain. The noble gases are admitted to the ion source for analysis followed by the gases desorbed from the heated adsorption cell. Sample enrichment or sample detection threshold levels are enhanced by two to three orders of magnitude, depending on the adsorption properties of the molecular species.

The instrument was developed and built at NASA/Goddard Space Flight Center and is contained in a pressurized housing made of titanium and capable of withstanding 25 bar external pressure. The weight is 13 kilograms and approximately 25 watts are required for operation, about half of which is consumed in pumps and heaters in the sample inlet pumping system. The electronics system is designed and packaged 90 percent in hybrid form to minimize weight and size.

The flight unit instrument has successfully completed calibration and environmental tests and is now undergoing final checkout at JPL. The launch of the Galileo Orbiter/Probe is scheduled for the Space Transportation System (STS) in early 1986.

Contact: Dr. Hasso B. Niemann
Code 610

Sponsor: Office of Space Science and Applications

DESIGN AND SIMULATION OF VISIBLE AND INFRARED SENSORS

A computer model has been written to aid in the design of remote sensors that meet defined scientific requirements and at the same time minimize development costs. Although the computer model is still in an early stage of development, it is considered to be an important first step in the process of developing CAD/CAE techniques for sensor system development. Even after a remote sensor has been built and laboratory data have been analyzed, it is very difficult to determine if its scientific objectives can be achieved. It is also very difficult to predict how a complex sensor will perform before it is built. Sensor computer simulation and design models can be developed which are sufficiently accurate such that they can play an important role in each stage of the sensor conception and development process.

As remote sensors become increasingly more complex to meet challenging scientific requirements, costs also increase. It is desirable to be able to rapidly assess the performance of candidate sensor concepts before proceeding to hardware development. When sensor concepts are simulated on a computer, design variations can be assessed at a very modest cost. The other alternative is to prematurely commit to definite hardware designs with minimal simulation with the likely probability that changes will later be required and will be very expensive.

The software system under development takes scientific requirements and from them computes a preliminary set of sensor parameters. The scientific requirements may be defined in terms of resolution (temporal and spatial), number of spectral bands (wavelength and bandpass), plus figures of merit such as Modulation Transfer Function (MTF), signal-to-noise (S/N) ratio, noise equivalent delta reflectivity, or temperature. A more direct approach may be to optimize the sensor design based upon the accuracy of a retrieved parameter (e.g., Bidirectional Reflection Distribution Function (BRDF)) that is extracted from the sensor signal, but this technique presupposes a very mature state of algorithm development. Using MTF or S/N as a figure of merit has the advantage that they are both independent of the scientific parameter extraction algorithm. The simulation software or sensor model then operates on the scientific requirements and develops a preliminary set of sensor parameters, including major elements such as the optics (f-number, diameter, etc.), focal plane (detector type, number of detectors, temperature, etc.) scan configuration, etc.

The accompanying illustration shows the elements of a complete sensor system. It includes the scene being studied, the remote sensor itself with some onboard signal processing functions, the transmission link through which data are transmitted to the ground, and ground processing equipment that employs computer algorithms to analyze the sensor data and hopefully produce useful scientific results. At this time the sensor model incorporates the scene and intervening atmosphere, several forms of visible and infrared sensor systems, and some signal processing techniques. For the visible and near infrared range of wavelengths (0.4 to 2.1 micrometers) the scene radiance is determined by the reflectivity of the Earth's surface, the state of the atmosphere, and the location of the Sun. For the Short Wavelength Infrared

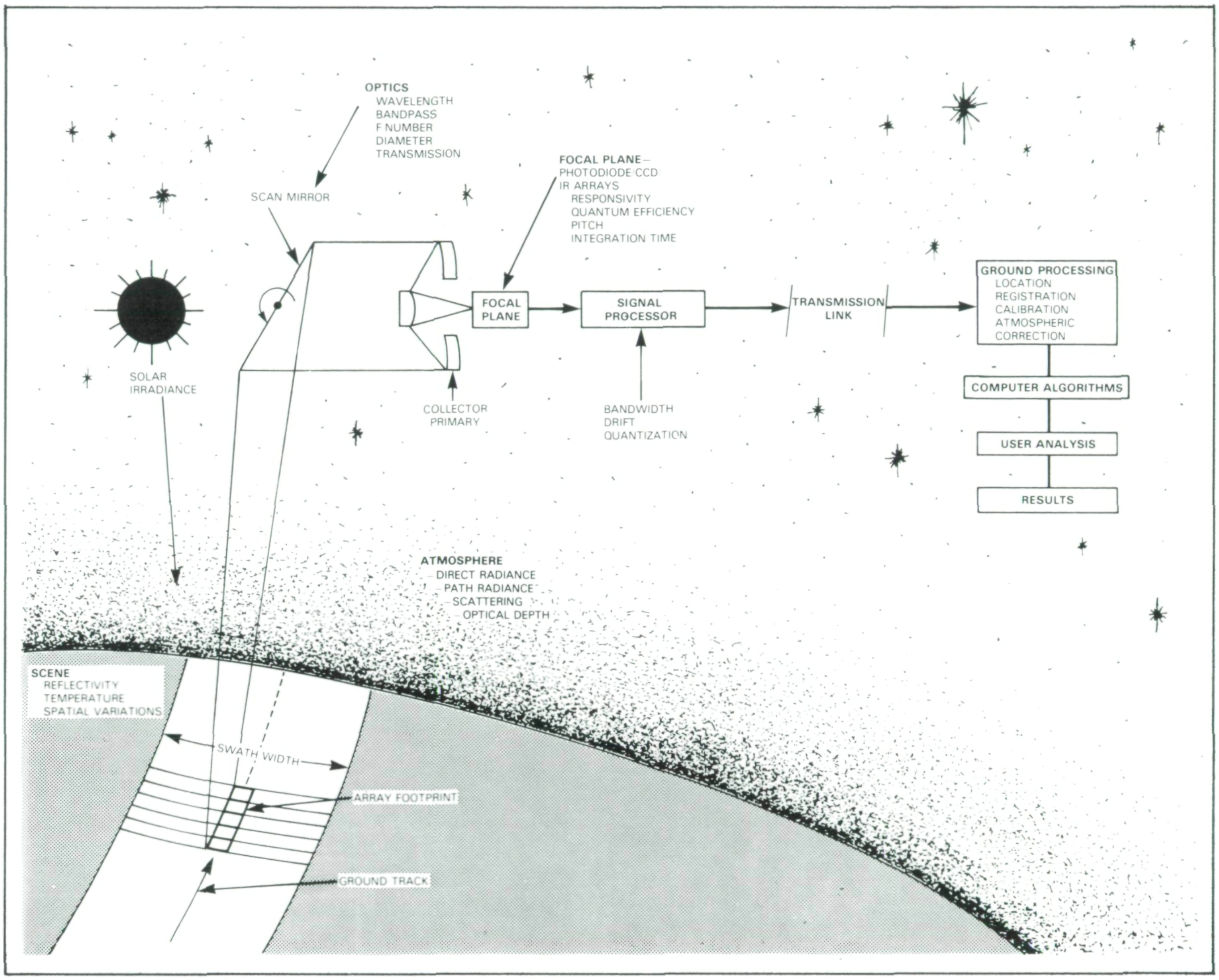

Parameters for sensor system design and simulation.

(SWIR) and Thermal Infrared (TIR) range of wavelengths (2.5 to 15.0 micrometers), the scene radiance depends upon the temperature of the Earth's surface and the atmosphere, and the optical depth of the atmosphere. The particular sensor shown in the figure, as an example, is termed a "whiskbroom scanner." The well-known MSS and TM sensors that flew on Landsat are also whiskbroom scanners. The sensor produces an image by means of the satellite moving across the scene while a rocking mirror moves an array of detectors, much like a whiskbroom, across the scene in synchronism with the satellite motion. In effect, the optical system maps the scene onto the focal plane where the detectors convert the photon flux into an analog electrical signal. The signal processor generates a digital signal which is transmitted to the ground for further signal processing and analysis.

The sensor computer model is presently being used to design two Moderate Resolution Imaging Spectrometer (MODIS) sensors which are candidates for flight on a future Earth Observing Satellite (EOS)/Space Station mission. In the future the model will be expanded to include a wider latitude of sensor platforms and scanning configurations. The model will also be used to test the effectiveness of various algorithms to extract scientific parameters and to understand the interaction between the algorithm and the remote sensor design.

Contact: Harry E. Montgomery
Code 620

Sponsor: Office of Space Science and Applications

WIDE-BANDWIDTH PHOTOCONDUCTOR MIXERS FOR THE FAR INFRARED

Heterodyne spectroscopy in the millimeter and the middle infrared spectral regions has been proven to be a powerful tool in the investigation of interstellar media, stars, planetary atmospheres, comets, the Sun, and the Earth's stratosphere. No adequate heterodyne receiver technology exists in the interesting spectral region for remote studies between 12 μm and 1 mm.

Mixers are one of the key components in heterodyne receivers. Heterodyne mixer technology is least developed in the 30-μm to 200-μm spectral region. Photoconductors present an alternative to GaAs Schottky diodes as mixers in the 100- to 200-μm region and, along with photodiodes, are perhaps the only useful mixers at wavelengths below 100 μm. Under Goddard support, adequate 30-μm HgCdTe photodiode mixers have been developed (D. Spears, MIT Lincoln Laboratory). This work showed that for available semiconductor material diode photomixers were not possible beyond 40-μm wavelengths because of strong electric field dependent tunneling that occurs in small energy gap (long wavelength) materials, which makes good rectification impossible. In photodiodes the electric fields in the junction depletion region are greater than 1000 V/cm. Photoconductors are quite different as they operate with uniform electric fields that are an order of magnitude lower than the space-charge fields of photodiodes. Tunneling, therefore, does not present a barrier to the operation of photoconductors in the far infrared. Photoconductors are, however, inherently two times less sensitive than heterodyne detectors as compared to photodiodes, since both generation and recombination noise are present in photoconductive detectors. Photoconductive gain in a device must be sufficiently high at high frequencies (wide bandwidth) to reduce the local oscillator power required to overcome the detector noise and to make it a useful photomixer. The gain is equal to the photocarrier lifetime, divided by the transit time between electrodes in the photoconductor. Photomixer bandwidth varies inversely with carrier lifetime, thus the transit time between electrodes (electrode spacing) must be short (small) in order to yield wide-bandwidth high-gain photoconductive mixers. To achieve high sensitivity, the detector surface area must be larger than a few signal-wavelengths-squared for optical matching and thicker than the signal photon absorption length (to absorb enough signal radiation).

Conventional photoconductor designs require relatively thick devices, thus relatively wide electrode spacing, yielding low photoconductive gain, limited bandwidths (especially at longer wavelengths), and relatively high bias and laser local oscillator power requirement for optimum (shot-noise-limited) performance. The resonant-optical-cavity interdigitated-electrode photoconductor structure developed at MIT Lincoln Laboratory by D. Spears and coworkers under this program addresses and overcomes the previously stated limitations of photoconductive mixers. The interdigitated-electrode structure as shown in the first figure provides for closely spaced electrodes so the carrier transit time is greatly reduced, resulting in wide bandwidth ($>$ 500 MHz), high photoconductive gain ($\sim$1), and low local oscillator power requirements ($\sim$50μW). The multiple electrodes can cover a large enough detector area for optical matching at long signal wavelengths λ (e.g., 125 μm diameter for λ = 28 μm). This structure requires a thin active region which is less than one absorption length at the wavelengths of the incident signal radiation. The resonant-optical-cavity structure, nevertheless, permits high absorption of incident photons, thus, high detection sensitivity. Adequate absorption is achieved by a layered structure consisting of a gold reflector on the device substrate and a thin HgCdTe active region sandwiched between two semiconductor spacers of germanium. When the total optical thickness of the structure at the detection wavelength is $m\lambda/4$ (m = odd integer), a resonant optical cavity is formed between the gold reflector and the device surface. The spacer thicknesses are adjusted such that the optical field peaks within the active HgCdTe layer enhancing the absorption coefficient by about 4n (n = index of refraction). For HgCdTe (n = 3.6) tenfold increase in absorption can be achieved. Calculations show that quantum efficiencies over 80 percent should be achievable at 30 μm and over 40 percent at 200 μm for devices made in this fashion.

The performance of a photomixer can be expressed in terms of its degradation from ideal $\Delta = \mathrm{NEP}/h\nu\Delta f$. The noise equivalent power (NEP) is in watts; Δf is the mixer noise bandwidth, and $h\nu$ is the photon energy. The second figure shows Δ as a function of wavelength for state-of-the-art far-infrared photomixers and the estimated performance for thin resonant-optical-cavity interdigitated-electrode HgCdTe photoconductor photomixers. A detector area equal to or greater than 2-wavelengths-square and doping levels that gave bandwidths in the range of 200 to 700 MHz were used in the calculations. In most cases local oscillator power of the order of 50 μW was required for maximum sensitivity. In the region of 100 μm, the projected performance is considerably better (20 times) than the best current devices, GaAs Schottky diodes. GaAs Schottky diodes

have demonstrated much higher bandwidths than attainable with HgCdTe photoconductors, but their sensitivity at 500 MHz is much lower than that projected for HgCdTe photoconductors. The shaded region in the figure illustrates the range of uncertainty in the calculations.

These results are significant for they provide the possibility of not only photomixers for sensitive heterodyne detection from 30 μm to 200 μm, but should significantly improve shorter wavelength devices. The resonant-optical-cavity configuration can also facilitate fabrication and enhance performance of superlattice detectors, blocked-impurity-band photoconductors, and can make a significant impact on a wide variety of coherent and direct detectors with applications from fiber optic communications to low background infrared astronomy. Photoconductor devices can be fabricated more uniform in performance than diodes and can be more easily

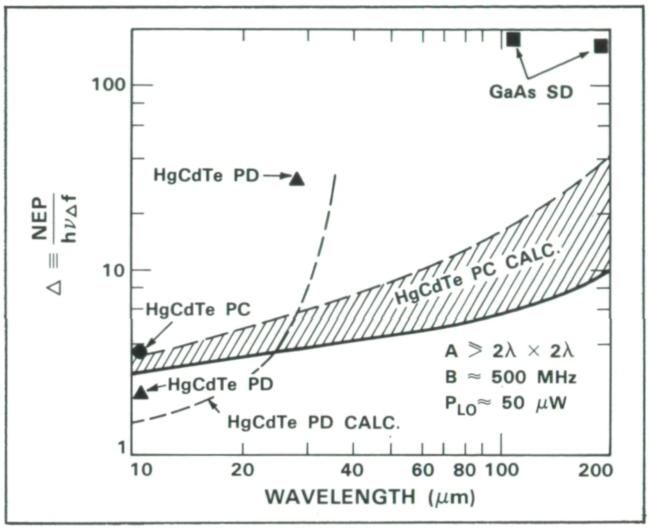

State of the art and projected performance of wide-bandwidth far-infrared photomixers.

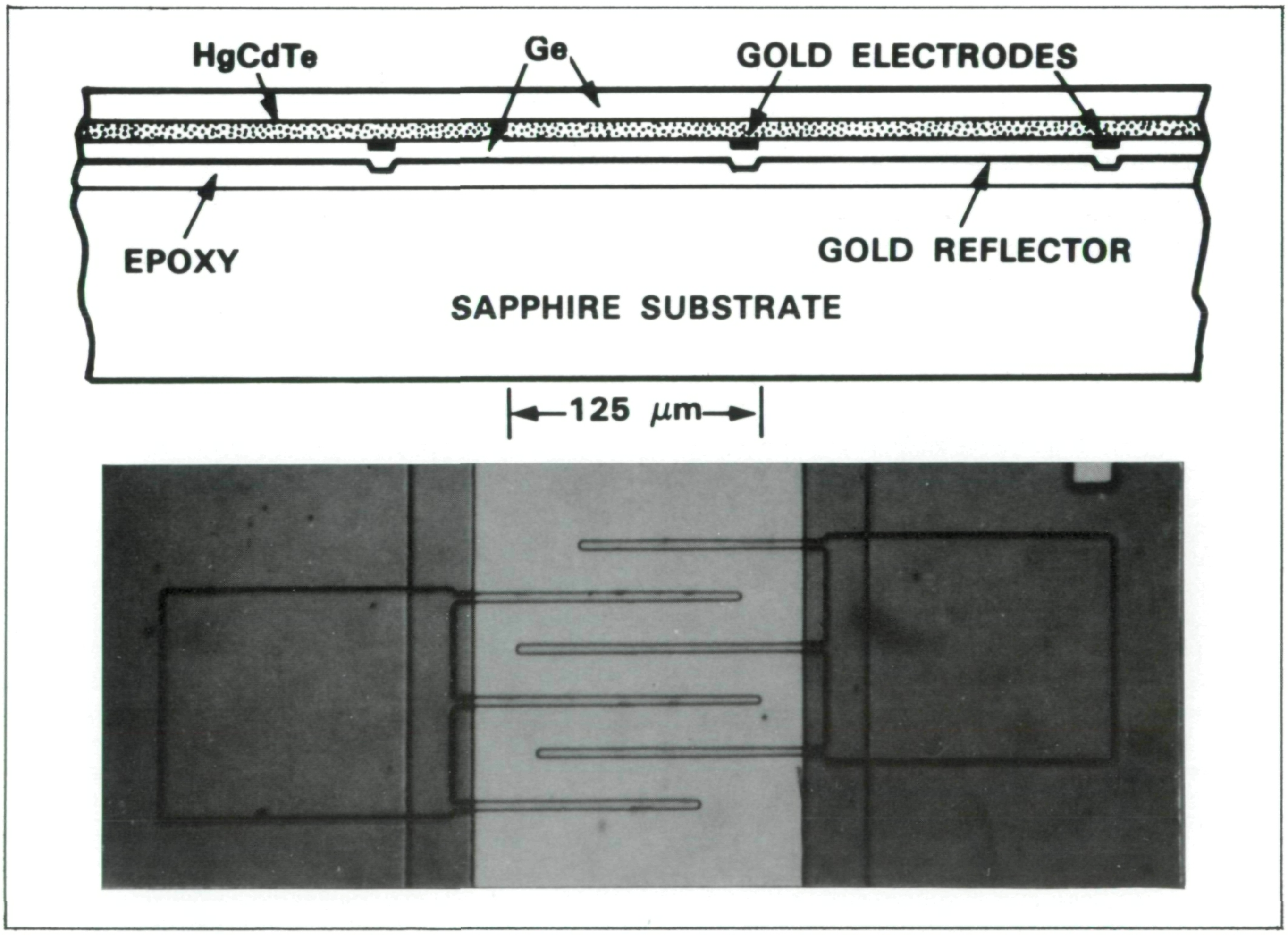

Resonant-optical-cavity interdigitated-electrode 28-μm HgCdTe photoconductor photomixer.

reproduced. The structure is extremely rugged and thus appropriate for space flight applications.

Contact: Dr. Theodor Kostiuk
Code 690

Sponsor: Office of Aeronautics and Space Technology

CRYOGENIC CALORIMETERS FOR HIGH RESOLUTION X-RAY SPECTROSCOPY

Microcalorimeters operating near 0.1 K are being developed at GSFC for use in the Spectroscopy Experiment under study for use with the proposed X-Ray Astrophysics Facility (AXAF). These detectors simultaneously offer high efficiency and high spectral resolving power, which makes them extremely attractive for X-ray astronomy.

Such a detector absorbs an X-ray, and its energy should be promptly converted to heat. The resulting temperature rise is proportional to the deposited energy. The fundamental limit to our ability to measure this temperature is set by thermodynamics; we can reduce the measurement uncertainty by reducing the detector heat capacity and its temperature. Tests at 0.1 K show that this thermodynamic limit is the limiting noise in actual detectors.

The limit to the resolution of these detectors is determined either by the uncertainty in temperature rise set by calorimeter noise or by noise in the thermalization of the X-ray. In different events, part of the X-ray energy can be trapped in charge in the semiconductor. The resolution of the spectrometer is limited by the more serious of these two effects.

Tests of a low-heat-capacity detector at 0.1 K has shown that the calorimeter thermal noise can be made very small. One device had a thermal resolution of 11 eV FWHM. The actual X-ray resolution in this device was ~250 eV, dominated by thermalization noise.

The best resolution achieved so far is shown in the accompanying illustration. This detector is an ion-implanted Si

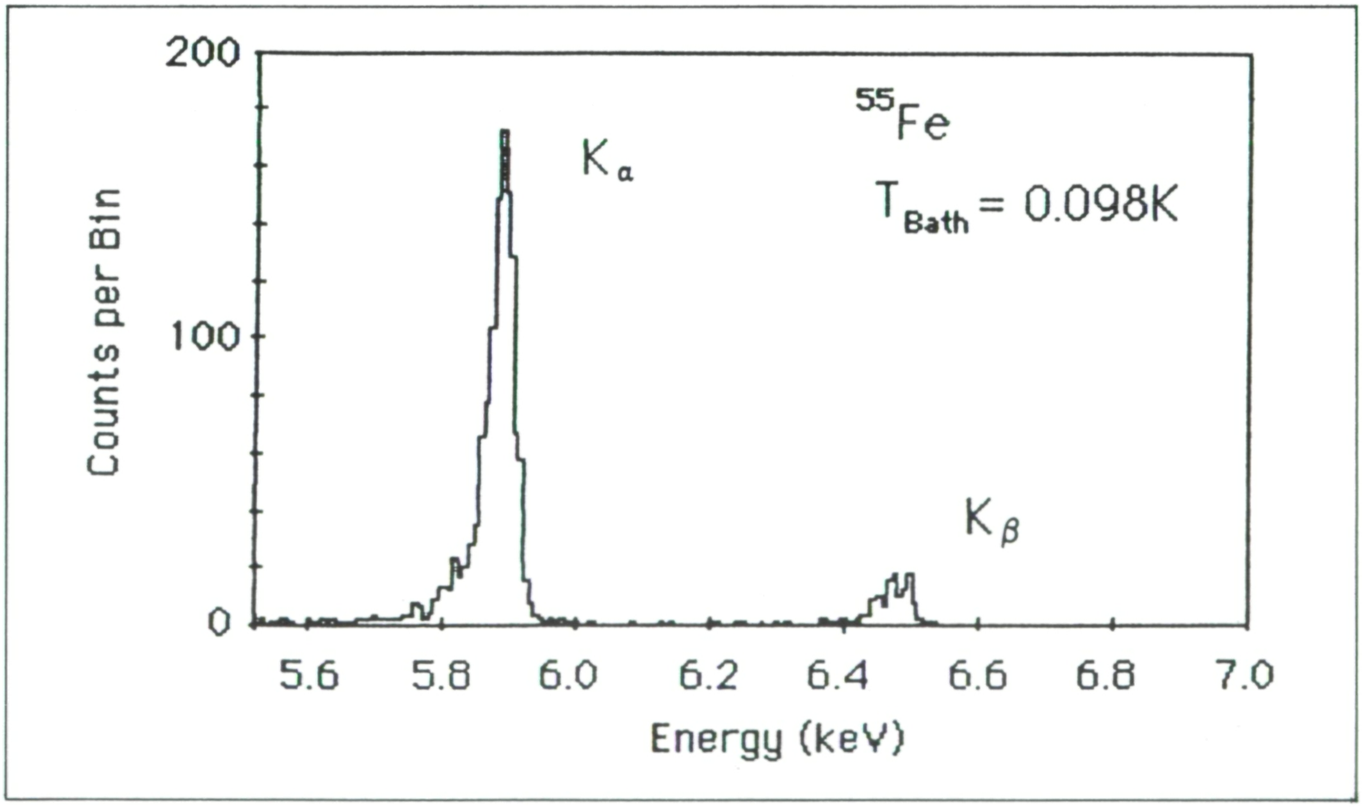

Spectrum showing ^{55}Mn K_α and K_β lines from the decay of a ^{55}Fe radioactive source. The X-rays were absorbed in a 2-μm-thick Bi layer on an ion-implanted Si bolometer made at GSFC. The resolution of the K_α line is 38 eV FWHM, corresponding to a resolving power ($E/\Delta E$) of approximately 150.

bolometer with a 2-μm-thick X-ray absorbing Bi layer. The resolution of 38 eV FWHM at 5.9 keV represents a substantial improvement over conventional nondispersive spectrometers.

Experiments carried out by D. McCammon and collaborators at the University of Wisconsin show that if the X-rays are absorbed in a metal film, there is little thermalization noise. Tests of this 0.3 K detector at GSFC resulted in a resolution of 57 eV FWHM at 5.9 keV.

Work is under way to study the X-ray conversion noise in a number of materials with heat capacities lower than metals. Our goal for the next year is to produce detectors with resolution near $<$20 eV FWHM.

Work described has been carried out in collaboration with D. McCammon, M. Juda, and J. Zhang of the University of Wisconsin. Some of the detectors tested were fabricated by the Microelectronics Fabrication Section at GSFC.

Contact: H. Moseley, A. Szymkowiak, and R. Kelley
Codes 690/660 and University of Maryland

Sponsor: Office of Space Science and Applications

TECHNIQUES

A MECHANICAL METHOD FOR APPLYING RAPIDLY SOLIDIFIED METAL COATINGS

In recent years, a great deal of research has been devoted to the development of new types of protective coatings based on the application of rapidly solidified (RS) metals. The RS metals, which are manufactured by quenching the melt at extremely fast cooling rates, are endowed with very desirable attributes, including superior corrosion resistance. Different methods have been tried to create RS metal coatings, such as electrodeposition and laser glazing, but they are rather costly and are not yet ready for industrial applications.

A new method has been developed at GSFC, which is both inexpensive and easy to use, for the application of RS metal coatings. This method is called peen plating; it is comprised of spraying a mixture of RS metal powder and peening particles at high velocity against the surface of the substrate. By the impact of the peening particles, the metal powder will be bonded to the surface and thus form a protective coating. The apparatus for peen plating can be easily adapted from the equipment commonly used for industrial shot peening.

Experimental work has been completed for several powder/substrate combinations, including RS tin and aluminum powders on copper and aluminum alloy substrates. The results showed that deposition of the powders on the substrates was readily achieved. Bend tests were conducted which showed that the coatings had adequate bonding on the substrate materials. It is well known that shot peening is beneficial to metals with respect to fatigue strength. However, initial results of recent tests indicated that specimens peen plated with RS metal coatings had even further improved fatigue properties as compared with specimens that were shot peened under identical conditions.

The present work has shown that peen plating is a simple and inexpensive process. It is a viable method for applying rapidly solidified metals as protective coatings.

Contact: Dr. Huai-Pu Chu
Code 310

Sponsor: Office of Aeronautics and Space Technology

FLIP-FLOP RECOVERY SYSTEM FOR SOUNDING ROCKET PAYLOAD

The "Flip-Flop" Recovery System was developed to protect forward-mounted instruments from ground impact during sounding rocket payload recovery operations. This development was driven in particular by the desire to reduce impact damage to two existing payloads that had flown several times previously. All of these flights were successful and were recovered; however, the sensitive forward-mounted mass spectrometers sustained substantial damage upon impact. These particular instruments were gold plated and costly to replace.

The following general restrictions and limitations were imposed on the recovery system design:

- To be adaptable and compatible to existing flight hardware
- To be as inexpensive as possible
- To be as simple as possible, yet highly reliable.

The new "Flip-Flop" Recovery System concept itself is a simple one; that is, the payload is rotated end-over-end at a predetermined time just after parachute deployment. The forward end of the payload then points upward, and the structurally stronger aft end can be used to absorb ground impact. Hence, the risk of damage to the sensitive forward portion of the experiment is greatly minimized. Payload rotation is accomplished with a stainless steel external cable that is attached to the forward end of the payload and parachute confluence point. During parachute deployment, the aft riser is severed with a dual-timed delay train pyrotechnic cutter. The cutter is mechanically actuated by the parachute as it deploys. The timed delay cutter allows adequate time for the parachute and payload to establish steady-state descent. The parachute canopy provides excellent energy dissipation as the payload is flipped over.

The first "Flip-Flop" Recovery System was launched on a Taurus-Orion Sounding Rocket from White Sands Missile Range in October 1984. This mission flight was fully successful, and the recovery system worked flawlessly. The "Flip-Flop" Recovery System provides a simple and inexpensive means of protecting sensitive forward-mounted instruments on sounding rocket flights. Future use may include a "Flip-Flop" Recovery System for the larger Black Brant vehicles.

Contact: Anel Flores, Jr.
Code 840

Sponsor: Office of Space Science and Applications

USER SPACE DATA SYSTEMS

INTERANNUAL VARIATIONS IN THE EARTH'S OUTGOING LONG-WAVE RADIATION

Six years of broadband Earth Radiation Budget (ERB) measurements taken by the Nimbus-7 ERB experiment have been archived. This period encompasses the 1982-1983 El Niño/Southern Oscillation event, which reached a peak near the beginning of the fifth data year (January 1983). A 41-month outgoing long-wave radiation subset of this data set, extending from June 1980 through October 1983, has been further processed to enhance the spatial resolution. This enhanced data set has been used to develop an atlas comparing the global outgoing long-wave radiation fields during the El Niño disturbance with those of the two preceding "normal" years. In addition, the Landsat Analysis System (LAS) in Goddard's Space Data and Computing Division has been used to display these radiation fields in false color maps. These color maps aid both scientists and laymen in following changes in the radiation fields from month to month and year to year. The ERB data provide the first broad spectral band glimpse of the terrestrial outgoing long-wave response to the El Niño event throughout the life cycle.

In the Nimbus ERB instruments, wide-field-of-view channels are used to measure both reflected-solar and emitted-terrestrial radiation in the spectral bands of 0.2 to 50 μm, 0.2 to 3.8 μm, and 0.7 to 2.8 μm. The calibrated output of the channels and their differences then yield total reflected shortwave, emitted long-wave, near-infrared reflected, ultraviolet and visible reflected, and total exitant irradiances. The net radiation is derived in a straightforward manner from these measurements.

These channels view the entire visible Earth disc at all times. Satellite-altitude (955 km) irradiance observations are taken at 4-second intervals throughout the 104-minute orbits. The actual connection between the radiances measured at satellite altitude and those emitted from the top-of-the-atmosphere is quite complex due to the nonuniform brightness over the large area viewed by these wide-field-of-view sensors. However, to simplify data processing, the measurements, in the archived data set, are reduced to the top-of-the-atmosphere by multiplying by a simple inverse square factor. The measurements are sorted into 2070 fixed target areas, each approximately 500 km by 500 km, which cover the globe. The principal archived data set consists of daily and monthly target are averages.

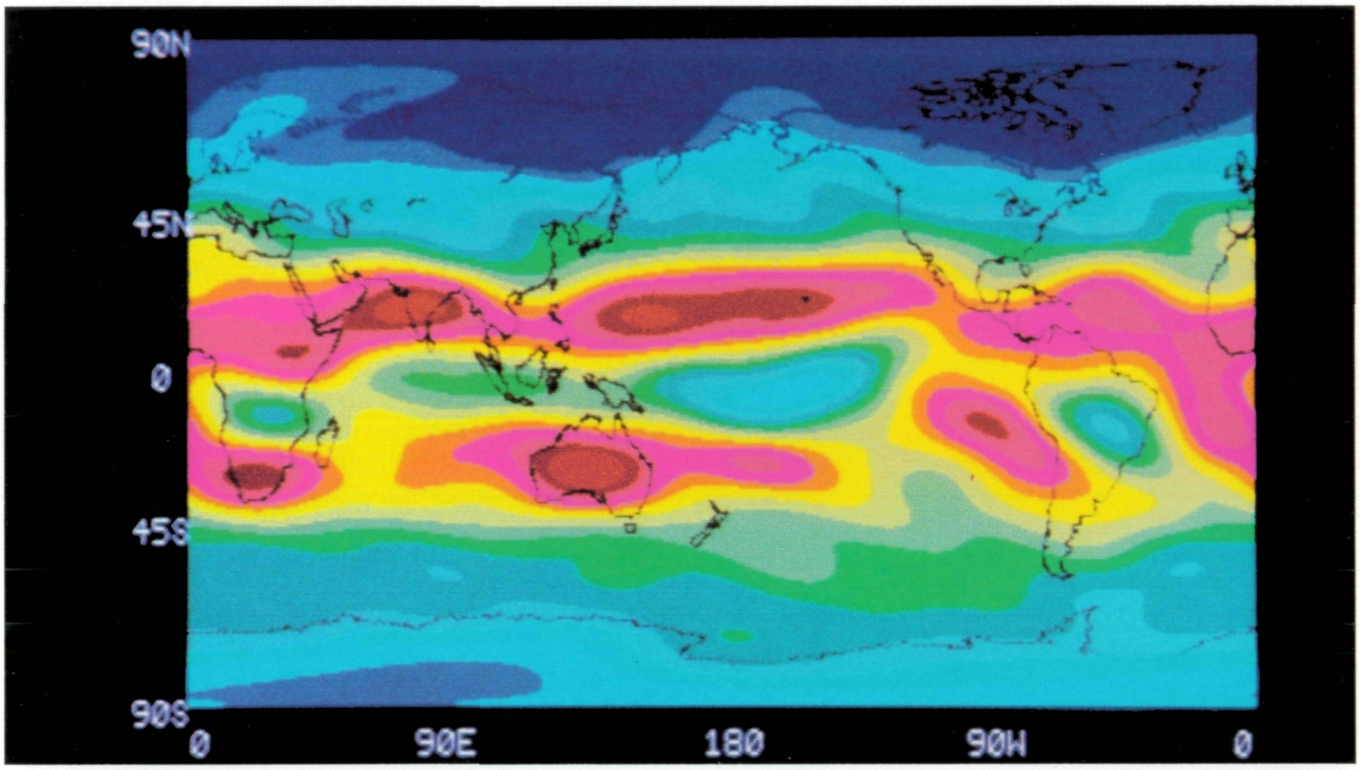

Resolution enhanced average outgoing long-wave radiation map for January 1981. The vertical scale is latitude, and the horizontal scale is longitude.

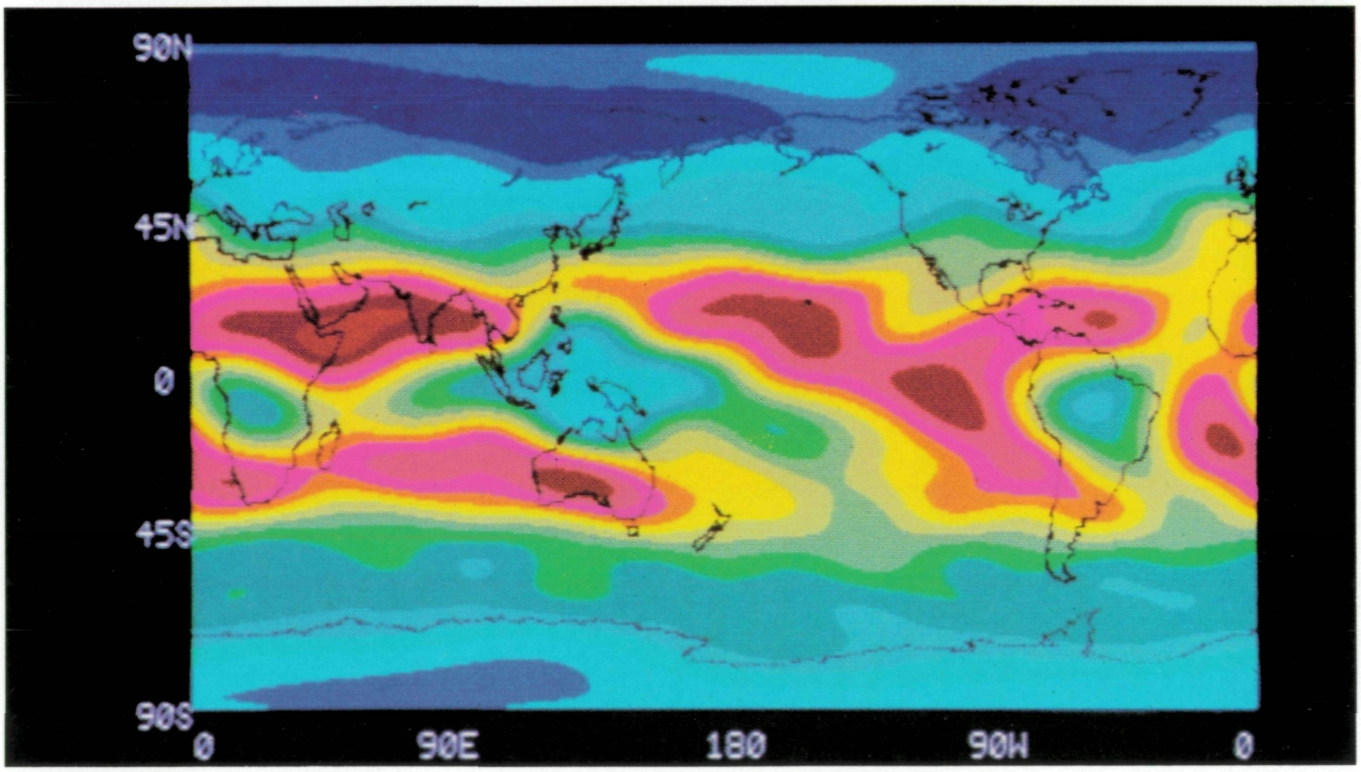

Resolution enhanced average outgoing long-wave radiation map for January 1983.

What distinguishes the 41-month data set from the six years of archived data is the extensive postprocessing which it has received. Through the use of additional information, already present but "hidden" in the data, it is possible to improve substantially both the time and space sampling of the data set. The technique used was developed by G. L. Smith and R. N. Green at the NASA Langley Research Center. A spectrally truncated 12th-degree spherical harmonic field is fitted to the archived target area averages on a global basis. By incorporating the known angular instrument response, the effective spatial resolution is doubled in latitude (along track) and considerably enhanced in longitude. For instance, the archived data set does not clearly resolve the equatorial cloud belt but the enhanced data set does. This enhancement can be performed on daily, 6-day or monthly averaged archived data. The present 41-month enhanced data set was developed from the monthly averaged measurements. It has been used to form both a black and white contour map atlas and a silent color movie.

Without question, the 1982-1983 El Niño event is associated with one of the largest-amplitude global climate perturbations in recent history. The meteorological ramifications of this event include: droughts in southern Africa, Indonesia, northern Brazil, and Australia; flooding in the central equatorial Pacific, Ecuador, southern Brazil, and Peru; intense tropical cyclones over French Polynesia and the Hawaiian Islands; and unusual storm activity across the southern United States from California to the Gulf of Mexico. The perturbations in the outgoing long-wave radiation (OLR) fields during El Niño arise principally from massive changes in the normal pattern of sea surface temperature and cloud cover in the tropics during this period.

As observed by the Nimbus-7 ERB, the annual cycles of global OLR fields were quite similar for the 2 years (June 1980 to May 1981 and June 1981 to May 1982). But by October 1982 it became evident that radiation fields would have a very different pattern during El Niño. The perturbations were pronounced in the October 1982 to May 1983 period with normal patterns slowly reasserting themselves thereafter. The most intense perturbations were noted in January 1983.

The global false color analysis maps for January 1981 and January 1983 are shown as illustrations of the types of changes observed. The red areas indicate intense outgoing long-wave radiation and are associated with hot surface areas that are either relatively cloud free or covered principally by low, warm clouds. The blue areas indicate cold radiative regions associated with either cold surface regions or high, thick cloud fields. Note that in January 1981 there is a cold (cloud) region over New Guinea and northern Australia. However, in January 1983 this region is broken up and the most intense portion moved far to the East. Similarly the hot regions near the coast of South America have also changed dramatically. Large-scale shifts can also be noted in the Indian Ocean.

Contact: Dr. H. Lee Kyle
Code 630

Sponsor: Office of Space Science and Applications

PILOT CLIMATE DATA SYSTEM

The Pilot Climate Data System (PCDS) is an interactive, scientific information management system for locating, obtaining, manipulating, and displaying climate-research data. The PCDS was developed—and continues to be enhanced—by the Data Management Systems Facility of GSFC's National Space Science Data Center (NSSDC) to manage a large collection of climate-related data of interest to the NASA-sponsored research community, and currently provides such support for 20 data sets. The PCDS enables researchers to locate data of interest, preview data using graphical and statistical methods, and extract subsets for further analysis at their own sites. The PCDS resides on a DEC VAX-11/780 computer system located in the NSSDC Computer Facility (NCF). Access to the PCDS is provided via dial-up and network terminals, as well as direct lines.

The PCDS provides these capabilities via the integration of several general-purpose software packages—some commercially available, others developed by different groups within GSFC—with specialized software for reading and reformatting the supported data sets. The result is a system that is powerful and easy to use but is also easily expanded either to provide support for additional data sets, or to provide additional functional capabilities.

Some of the accomplishments of the PCDS effort during FY85 are outlined as follows:

- The role of the PCDS in supporting NASA-sponsored research has greatly expanded through extensive discussions with the affected community. At the beginning of FY85, the first PCDS workshop was attended by about 100 members of the climate

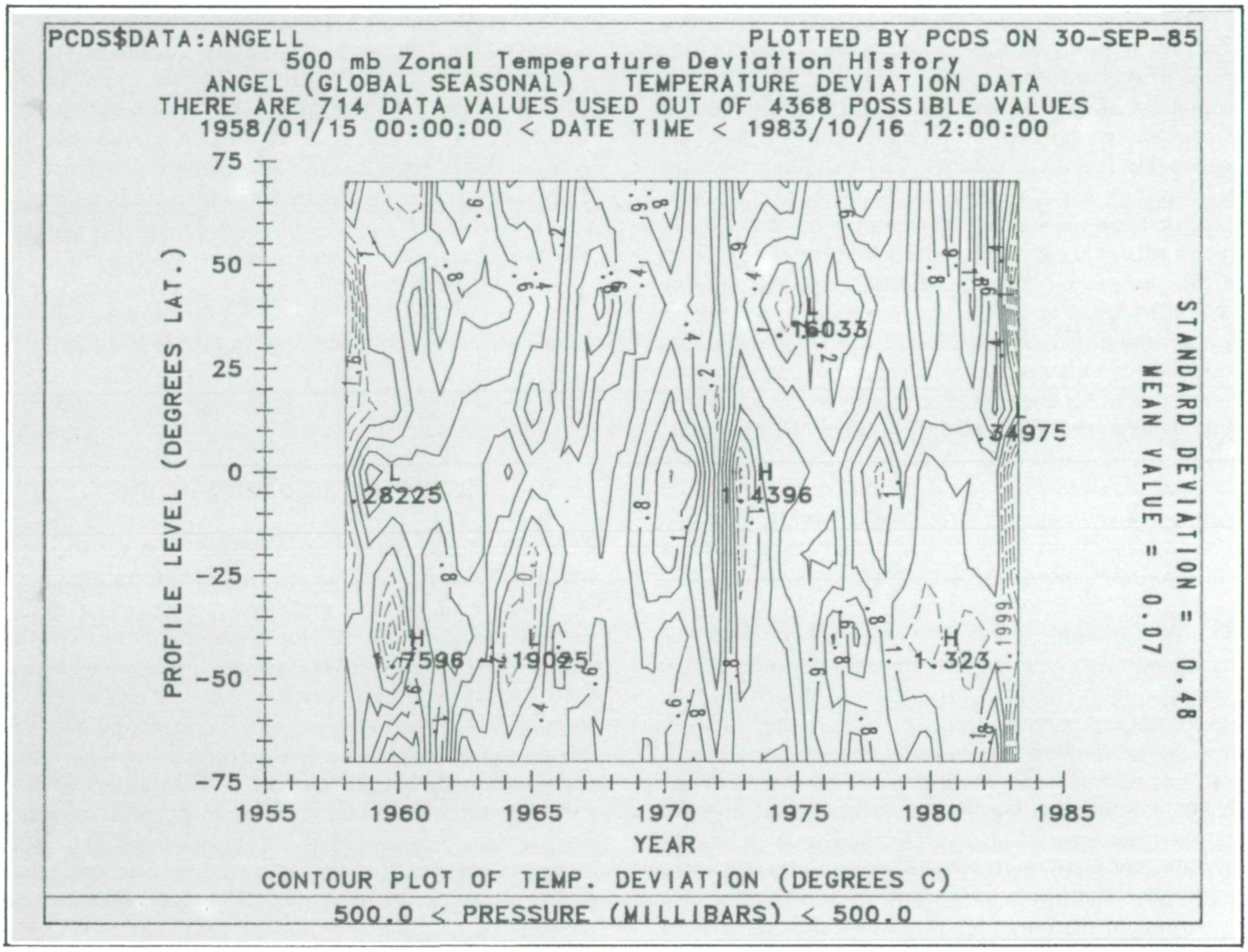

Typical PCDS graphical product.

research community. As a result of the workshop, additional scientists joined the user community; many researchers expressed a desire for the continued growth and support of the PCDS, and NASA Headquarters acknowledged the need for the PCDS. In May 1985, the first meeting of the PCDS Science Users Group, which consists of a core of representatives from each of the major research disciplines supported by the PCDS, took place. This meeting helped outline the direction for further development and support of the PCDS. In addition, cooperative use of the PCDS by other government agencies (e.g., NOAA and NSF), and NASA-sponsored foreign researchers (e.g., Peruvian studies of the E1 Niño phenomenon) have begun.

- The use of the PCDS is now expanding into universities for both classroom and research support. Initially this effort is being focused on the Pennsylvania State University and the University of Michigan, which will include a subset of the PCDS data-independent capabilities installed at those remote locations, networked to the central capability on the NCF.

- The availability of a data set independent format implemented as a data abstraction within the PCDS marks the first time such software technology has addressed the problems of scientific information management and analysis.

- Support of several data products of the International Satellite Cloud Climatology Project (ISCCP) has begun. In addition, efforts to manage and support the Earth Radiation Budget Experiment (ERBE) and the Global Solar Data Base (GSDB) have begun.

The PCDS supports mainly NASA-sponsored scientists, but is available to other research groups as resources allow. Since the PCDS provides a number of labor-saving utilities, significant research projects can be pursued via the PCDS even if they are supported with limited budgets.

Vital to the climate research community, the PCDS is easy to use and flexible. It frees the user from the burden of software generation. It provides state-of-the-art data management to support detailed scientific research, supports many large data sets from a variety of sources, and serves as a model for future information management systems in a variety of disciplines.

Contact: Lloyd A. Treinish
Code 630

Sponsor: Office of Space Science and Applications

DISTRIBUTED ACCESS VIEW INTEGRATED DATABASE SYSTEM

The objective of this project is to provide the fundamental research on the database uniformization problem so that NASA space data users can access any database independent of its physical distribution and specific organization. Our approach is to develop a solution to the database uniformization problem based on the recently developed framework called Database Logic.

The proposed Distributed Access View Integrated Database system (DAVID) will be constructed on top of existing databases/database management systems and will also provide facilities for the construction of new databases. Hence, DAVID can also be used as a stand-alone distributed homogeneous database management system. A functional breakdown of the DAVID system is given in the accompanying illustration.

Over the past year the following accomplishments have been made.

Several components of the GSQL Translation Package 2 were prototyped and tested. A preliminary version of the query decomposition has been produced through a grant with the Catholic University of America. A version of the definition generation module was developed through a grant to Stevens Institute. Modules for query logical optimization and report generation were produced through a grant to the University of Maryland. A module for DOAQ control was developed through a contract to Systems Applied Research.

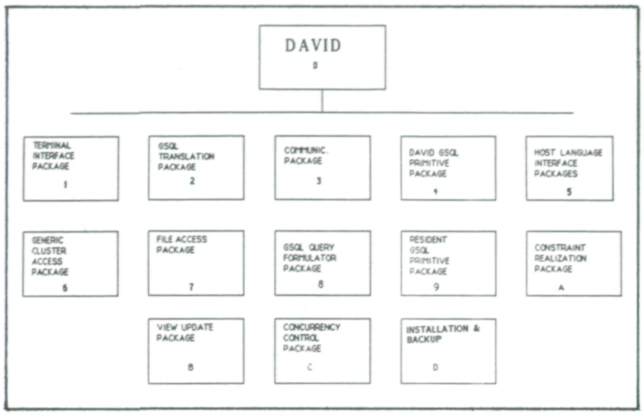

DAVID DBMS system overview.

Several components of the Resident GSQL Primitive Package 9 were also prototyped and tested. Preliminary versions of interface software were also developed: an interface to RAMIS by a grant to the University of Toledo; an interface to dBase II through a grant to Louisiana State University; an interface to IDMS by a grant to Brooklyn College of the City University of New York. Communications interface software was produced through a contract to Digital Analysis Corporation.

Contact: B. E. Jacobs
Code 630

Sponsor: Office of Aeronautics and Space Technology

OPERATIONS CONCEPTS IN TELESCIENCE

Many potential Space Station users have expressed a desire to perform the functions associated with flight planning, flight operations, and postflight analysis from their home institutions. This concept of distributed remote operations, referred to as "telescience," would allow researchers to plan and conduct experiments while being physically remote from centralized control institutions. This research has explored the implications that such a concept has on the command and control of Space Station user payloads.

A preliminary operations concept has been developed that attempts to meet Space Station requirements from both the customers' and NASA's perspectives. Many individuals have been consulted to identify the implications that a telescience concept has on payload command and control operations. The development of this operations concept is the initial phase in the identification of

the technologies that may serve as viable solutions to the problems and issues encountered. Specific technology solutions will be evaluated with prototyping (test-bedding) efforts and "proof-of-concept" studies. The development of operations scenarios will involve substantial user community participation and feedback.

The concept for payload operations involves the merging of both new and traditional technologies and methods of operations. Payloads would be required to operate within "operational envelopes" that would help to standardize a "language" for describing payload operations. Parameters contained in these envelopes describe payload requirements for resources, environmental requirements, and environmental impacts (on other payloads). Many of these boundaries would be enforced via a reactive, effect-oriented control system. This control system is one of several methods that would be used in successive layers to achieve compatible operations among payloads. Others include the payload design and manifesting process, and incentive-driven control (via premission contractual agreements between NASA and the customer), a simplified command checking function, and a payload safing capability for contingency and emergency situations. This concept offers the user-independence and remote operations capability required to support telescience operations.

Contact: Karen L. Moe
Code 520

Sponsor: Office of Space Station

GSFC/SPAN SYSTEM

The Space Physics Analysis Network (SPAN) is emerging as a viable method for solving an immediate communication problem for the space scientist. These scientists, located in universities, industry, and government institutions across the United States, need interactive communications among each other. Currently, SPAN provides low-rate communication capability with co-investigators and colleagues, and access to space science data bases, mission planning and information systems, and computational facilities. The SPAN utilizes up-to-date hardware and software for computer-to-computer communications, allowing binary file transfer and remote log-on capability to over 50 nationwide space science computer systems. New nodes on the network include six at MSFC, nine at JPL, two at UCSD, APL, UCLA, Lockheed, NSSDC, and ten at GSFC. GSFC is working with MSFC on the implementation and structure of SPAN.

SPAN is not discipline- or mission-dependent with participation from scientists in such fields as magnetospheric, ionospheric, planetary, and solar physics. The network is a test-bed system but functions such that the needs of the science users are addressed while maintaining a stable environment for facilitating correlative space science research and information exchange.

The SPAN system performance is evaluated by the Data Systems Users Working Group (DSUWG), which is made up of scientists and space data system managers from over 40 institutions. The DSUWG meets at least once a year for the purpose of SPAN evaluation and acts as the scientific steering committee providing guidelines for data storage, access, and data and software distribution over the network. All recommendations of the DSUWG are carried out including the development and update of the network users guide, development of network facilities and gateways, use of the standard network graphics metafiles, and the opening up of the data archives at the National Space Science Data Center (NSSDC). Currently the SPAN users guide has been distributed to over 500 scientists across the country.

SPAN is now managed by the NSSDC. The NSSDC is beginning to develop as the first major interactive regional data center providing facilities such as an on-line data catalog that directs users to the desired data archives and network-assisted coordinated data analysis workshops. In addition, the NSSDC is starting to serve as a software clearinghouse using the network to enhance software transportability and establishing standard practices for documentation and data format standards. The NSSDC is using SPAN to transmit data to remote space scientists from the International Comet Explorer spacecraft as it passes by Comet Giacobini-Zinner. Preencounter testing has been very successfully completed and is described elsewhere in this report.

It is anticipated that SPAN will grow rapidly over the next few years, not only from the standpoint of more network nodes; but as scientists become more proficient in the use of "telescience" (the use of telecommunications for the scientific purposes), more capability will be needed to satisfy these demands. Within the next 2 years all existing SPAN communications will be carried by the Program Support Communications (PSC) System being put in place at 14 NASA centers. The remote SPAN nodes will then become tail circuits physically connected to the closest SPAN/PSC center. The SPAN will use the PSC

as a communications backbone much like commercial systems. A backbone system with tail circuits affords SPAN users greater reliability, higher communication speeds, and additional gateways onto other networks such as the NASA Packet Switch System.

Contact: Jim Green
Code 630

Sponsor: Office of Space Science and Applications

TRANSPORTABLE APPLICATIONS EXECUTIVE

The Transportable Applications Executive (TAE) is an executive program that binds a system of applications into a single, easily operated whole, and supports user operation of programs through a consistent, friendly and flexible interactive user interface. TAE was developed to better serve the needs of the end user, the application programmer, and the system designer. For the end user, TAE provides a consistent user-computer interface, with both menu and command mode and easily accessed user-assistance in the form of on-line help, system messages, and program tutoring. For the applications programmer, TAE provides simplified but powerful user dialog and data access functions through a library of service subroutines. For the system designer, TAE provides a reusable framework and set of tools for flexibility in developing and ease in reconfiguring a system. TAE lowers the cost of system development, maintenance, and upgrade by providing software and structures for commonly recurring user requirements, by encouraging consistency in software development and documentation, and by allowing for experimentation in system design.

FY85 saw several significant accomplishments for TAE, in both user support and system development. TAE installations increased to over 40 facilities, located at 28 known sites, and has become the executive for at least 12 NASA scientific applications. Interest in TAE continues to grow. For instance, after an in-depth analysis of existing executive systems, the University Corporation of Atmospheric Research (UCAR) community selected TAE as their "shell" system onto which their university members will build meteorological applications. TAE is also being used by industry as a "de facto" standard (e.g., a commercial vendor is marketing an image-processing system which uses a customized version of TAE). The Fifth TAE Users Conference was held in June 1985, and this year 64 percent were from other government agencies, universities, and private research labs/companies. This is certainly an example of GSFC advanced technology being utilized by the external scientific community, as well as internally.

As TAE use expanded, so did cooperative development efforts with other TAE user sites. A working coalition with the USGS EROS Data Center (EDC) has proven to be highly successful. Joint support of an enhanced version of the Catalog Manager, EDC's installation and enhancements to the Display Management Subsystem (DMS), and the exchange of application software has been beneficial to both agencies. Cooperative development efforts have also been established with several universities, other NASA centers and GSFC's Data Systems Technology Division, which is using TAE to rapidly prototype a user interface language for Space Station applications. This has led to the prototyping of a graphics (e.g., windows and mouse) interface to TAE.

An enhanced version of TAE was released, incorporating new features requested by TAE users. TAE was successfully ported to the APOLLO Workstation and is now operational on SUN Workstation/UNIX, APOLLO Workstation/UNIX, Gould SEL/UNIX, VAX/VMS, and VAX/UNIX.

Several TAE subsytems, which augment the basic capabilities of TAE and can be installed at the option of a user site, were completed in FY85. The Display Management System (DMS) extends the TAE portability concept by allowing programs to be portable among raster-imaging devices. DMS abstracts the generic features of raster display devices and treats display functions in a device-independent manner. DMS supports the display functions of the Atmospheric and Oceanographic Information Processing System used in the Goddard Laboratory for Atmospheric Sciences and has been adopted by EDC for use in their multidevice image processing facility.

The prototype version of the Remote Communications Job Manager (RCJM), which provides TAE users with a uniform interface to a network, has become operational enabling scientists to work within a distributed processing environment. TAE with RCJM can be used by scientists to build and operate local applications, to initiate applications at remote sites, and to transfer data between participating workstations. RCJM will be enhanced and upgraded as efforts to develop efficient systems to support Space Station and "telescience" requirements continued.

The TAE Catalog Manager, a subsystem which institutes host-independent file naming and allows users to not have to remember different operating systems file naming conventions, was completed. It also gives users other useful features, such as ways to associate files with each other and flexibility in describing and cataloging files. The Catalog Manager supports the Land Analysis System (LAS) which is used by the Earth Science community.

The TAE Window Manager (WM) introduces the use of multiple virtual displays viewed through windows on a single physical device. TAE creates windows for its own use and as requested by application programs. The WM prototype was developed to support more intricate and varied user displays and user dialog such as in satellite control centers (e.g., NASA mission control centers) where multiwindow or even multidevice communications is common, and displays are updated simultaneously by one or more real-time processes and conversions to new architectures based on user needs.

Because of its open architecture, discipline independence, and suitability to many environments, the TAE system has become a cost-effective and easy tool for development of many scientific applications and research/prototyping projects.

Contact: Martha Szczur
Code 520

Sponsors: Office of Space Science and Applications
Office of Space Tracking and Data Systems

COORDINATED DATA ANALYSIS WORKSHOPS

Several important activities have occurred over the past year related to the Coordinated Data Analysis Workshop (CDAW) process that is conducted by the National Space Science Data Center (NSSDC) in conjunction with the scientific community. A new process, CDAW 7, was begun with the remote workshop held in late August 1984 in Edmonton, Alberta, Canada. This CDAW is concerned with determining whether an observed geomagnetic tail phenomenon is a plasmoid moving down the tail or is a tail lobe phenomenon. Further work must be done before the issue can be settled. The on-line data base for CDAW 7 consists of 12 data sets containing a total of 262 physical parameters.

The CDAW 6 process, begun in April 1981, reached a milestone with the publication of a set of papers, "Energy Transfer During Magnetospheric Substorms" in the Journal of Geophysical Research (Vol. 90, No. 2, February 1, 1985). There were 19 papers written by 48 authors from 24 different organizations. Eight were foreign organizations in Europe or Japan, showing the international effort of this endeavor. The average number of authors per paper was over 3, with papers ranging from single author to as many as seven authors. These numbers are not surprising considering the coordinated analysis involved. This set of papers significantly improves our understanding of the substorm process. Other papers are in process, and further study of this data base is being planned by the Japanese for the fall of 1985. The CDAW 6 data are broken into two data bases; the first has 64 data sets with 1315 parameters, and the second has 58 data sets with 1259 parameters.

After considerable effort the scientists participating in CDAW 8 have selected 7 time periods when ISEE 3 (now ICE) was in the deep geomagnetic tail from late 1982 to mid 1983 with the thought of concentrating on dynamical processes in the near and far magnetosphere. Because of the paucity of other satellite data relative to the International Magnetospheric Study time period, which was the period studied in all previous CDAW's, it is necessary to select a much larger set of intervals. Two important new satellites to join the process with CDAW 8 are Dynamics Explorers 1 and 2. Now that the NSSDC computer for handling CDAW's is a VAX, the use of the Space Physics Analysis Network (SPAN) will be stressed during CDAW 8. In addition, work has been done to demonstrate access to the system through both IBM and Macintosh PC's, as well as through dial-in modems. Consequently, from a system point of view, a participant will finally have all modes of access to the coordinated data base. This achieves a goal that NSSDC has aspired to for 6 years.

The CDAW process has continued to be used and to evolve during the past year; soon it should be a fully mature technique to further the goals of science.

Contact: James I. Vette
Code 630

Sponsor: Office of Space Science and Applications

SYNTHETIC APERTURE RADAR SIGNAL PROCESSING ON THE MASSIVELY PARALLEL PROCESSOR

A capability has been developed on the Massively Parallel Processor (MPP) to process Synthetic Aperture Radar

(SAR) signal (phase history) data into images and has been demonstrated using Seasat and Shuttle Imaging Radar-B (SIR-B) data. Typically, satellite-borne SAR's sense areas of several thousand square-kilometers in a few seconds, because the data collection time for a given satellite ground track distance depends only on the velocity of the satellite. Thus, SIR-B collects the signal data for a 100 km (along track) by 12 to 50 km (across track, depending on incidence angle) scene in approximately 15 seconds. Several digital processing systems have been developed for converting such signal data into interpretable images. The typical processing times in these systems, limited by conventional hardware, range from one to several hours. On the MPP the computational time has been reduced to only a few minutes.

The problem of processing signal data from space-borne SAR's has received considerable attention since 1978. While there are several approaches to this problem, the most widely used algorithms are based on the work by Cumming and Bennett ("Digital Processing of Seasat SAR Data," MacDonald, Dettwiler and Associates, Ltd.,

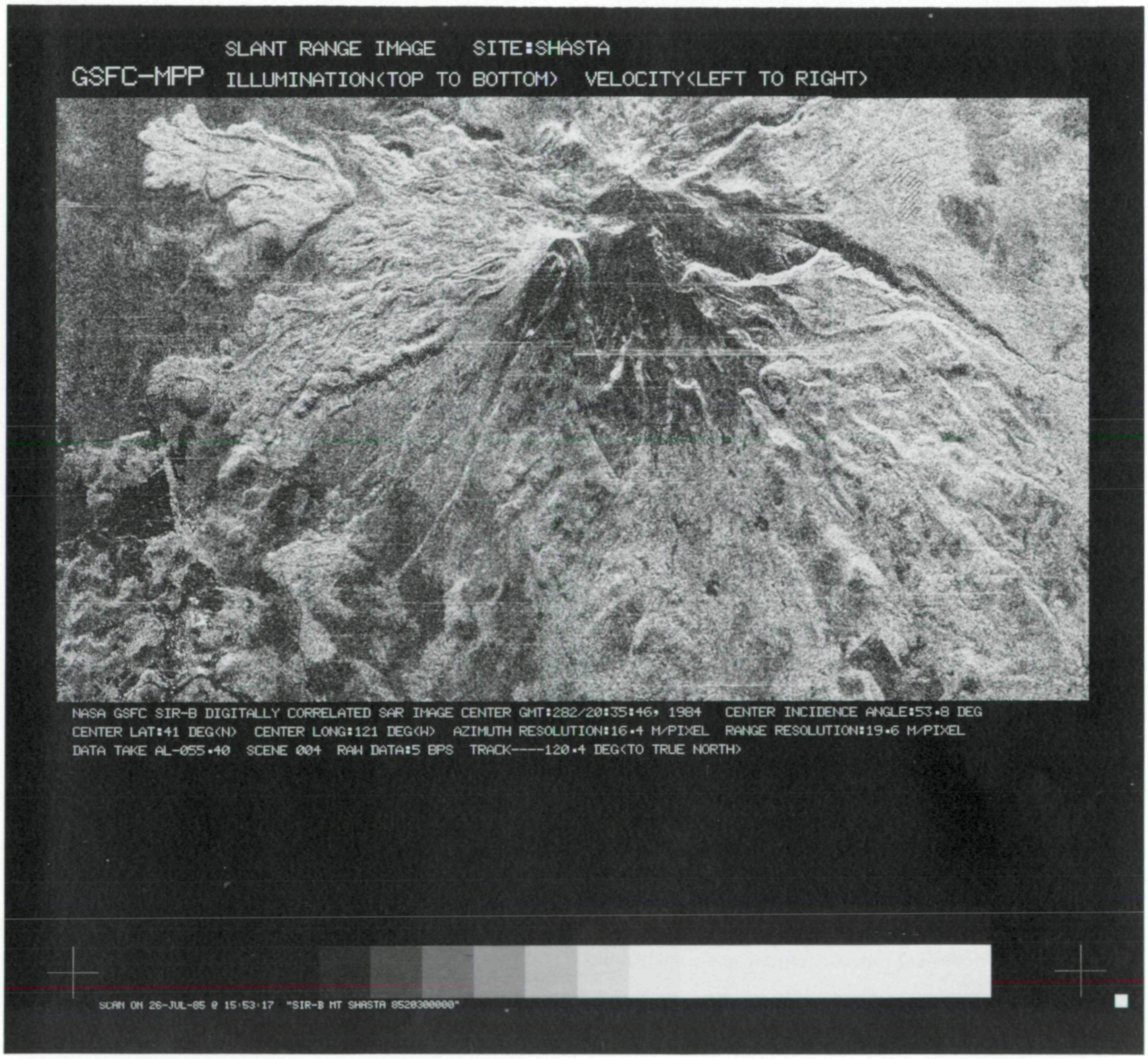

SIR-B image of Mount Shasta, California.

1979) and Wu ("A Digital Fast Correlation Approach to Produce Seasat SAR Imagery," proceedings of the IEEE International Radar Conference, 1980). It has been shown by them that the processing problem can be reduced, to a very good approximation, to two independent one-dimensional correlations, one in the across-track (range) direction and the other in the along-track (azimuth) direction. Further, these corelations can be implemented in the frequency domain using the Fast Fourier Transform (FFT) technique.

The primary time consuming steps in the processing are the I/O of the large volume of data (about 100 megabytes in and 10 megabytes out per SIR-B scene), the forward and inverse FFT's needed for the correlations (a total of about 91,000 for single-look processing per SIR-B scene), and the large matrix transpositions needed between the range and azimuth correlation steps. In the present MPP implementation, the primary attention has been to the computational step of the FFT's. Even with an unoptimized, high-level language subroutine, the MPP takes only 1.5 milliseconds per FFT of a 4096-long complex vector. This is 16 times faster than the corresponding FFT on the Floating Point Systems AP180V array processor (four of which are used in JPL's SAR production processor). This speed can be improved by a factor of 3 to 5 by optimization. The transposition step, which is a major time consumer in the present implementation due to disk I/O, will require virtually zero time with the expansion of the MPP Staging Memory from the present 2 megabytes to 16 megabytes. This expanded Staging Memory is on order and is expected to be on-line in early 1986.

The success of the MPP implementation has been demonstrated by processing both Seasat and SIR-B images. A SIR-B image of Mount Shasta, California, is shown in the accompanying figure. The computation time to generate this subset of the image, covering a 33-km by 12-km area was 79 seconds.

This development on the MPP constitutes a unique capability at GSFC permitting our entry into the SAR signal processing area. It offers the potential for producing a large number of images within reasonable time thus permitting experimentation with various processing techniques and parameters such as autofocusing options, number of looks, range attenuation compensation, and frequency domain weighting windows. This is significant in view of the number of SAR missions planned over the next several years by the U.S. and foreign governments. Continued development in this area will permit easy accessibility of data and experimentation facilities to GSFC scientists interested in analyzing and evaluating multisensor remotely sensed data for programs such as global habitability.

Contact: Dr. H. K. Ramapriyan
Code 630

Sponsors: Office of Space Science and Applications
Office of Aeronautics and Space Technology

NIMBUS-7 GEOPHYSICAL DATA SET DEVELOPMENT

The Nimbus-7 satellite is the last in the series of orbiting Earth observatories that have surveyed the atmosphere, mapped land and water characteristics, and observed weather and climate patterns. The Nimbus series of satellites have served as test platforms for the development of Earth observation techniques that are now used for operational monitoring of the Earth's weather, climate, and land characteristics.

Nimbus-7 is unique in that because of its longevity it has become the most significant source of experimental data from Earth-orbit relating to atmospheric and oceanic processes. The satellite is producing several data sets of unprecedented duration that relate to climate. All Nimbus data, when scientifically validated, are made available to the scientific community from federal archives. These data sets are in various stages of development and their status is presented as follows:

- Data from the Coastal Zone Color Scanner (CZCS) consisting of radiance, chlorophyll, sediment, and sea surface temperature, and covering 6 years, have been archived. Data production and validation continue.
- Solar and Earth radiation data covering 6 years from the Earth Radiation Budget (ERB) Experiment have been produced and archived.
- Limb Infrared Monitor of the Stratosphere (LIMS) Experiment data covering 7 months (LIMS cryogenic lifetime), and containing stratospheric temperature, ozone, water vapor, nitric acid, and nitrogen dioxide profiles, have been produced and archived, and are proving to be unique and invaluable for upper atmospheric studies.
- A 6-year data set of stratospheric aerosols in the polar regions from the Stratospheric Aerosol

ORIGINAL PAGE
COLOR PHOTOGRAPH

Measurement (SAM II) Experiment has been produced. Data production and validation continues.

- Observations of upper atmospheric temperature covering 3 1/2 years and 2 years of upper atmospheric methane and nitrous oxide have been made by the Stratospheric and Mesopheric Sounder (SAMS) Experiment. Due to instrument failure, this is the full extent of the SAMS data set. These data have been validated and archived.

- Six years of global ozone data, consisting of vertical concentration profiles and total burden concentration from the Solar Backscatter Ultraviolet (SBUV) and Total Ozone Mapping Spectrometer (TOMS) Experiment, have been archived.

- The production of the Scanning Multichannel Microwave Radiometer (SMMR) Experiment data continues and now extends into the seventh year of orbital data. The data consist of brightness

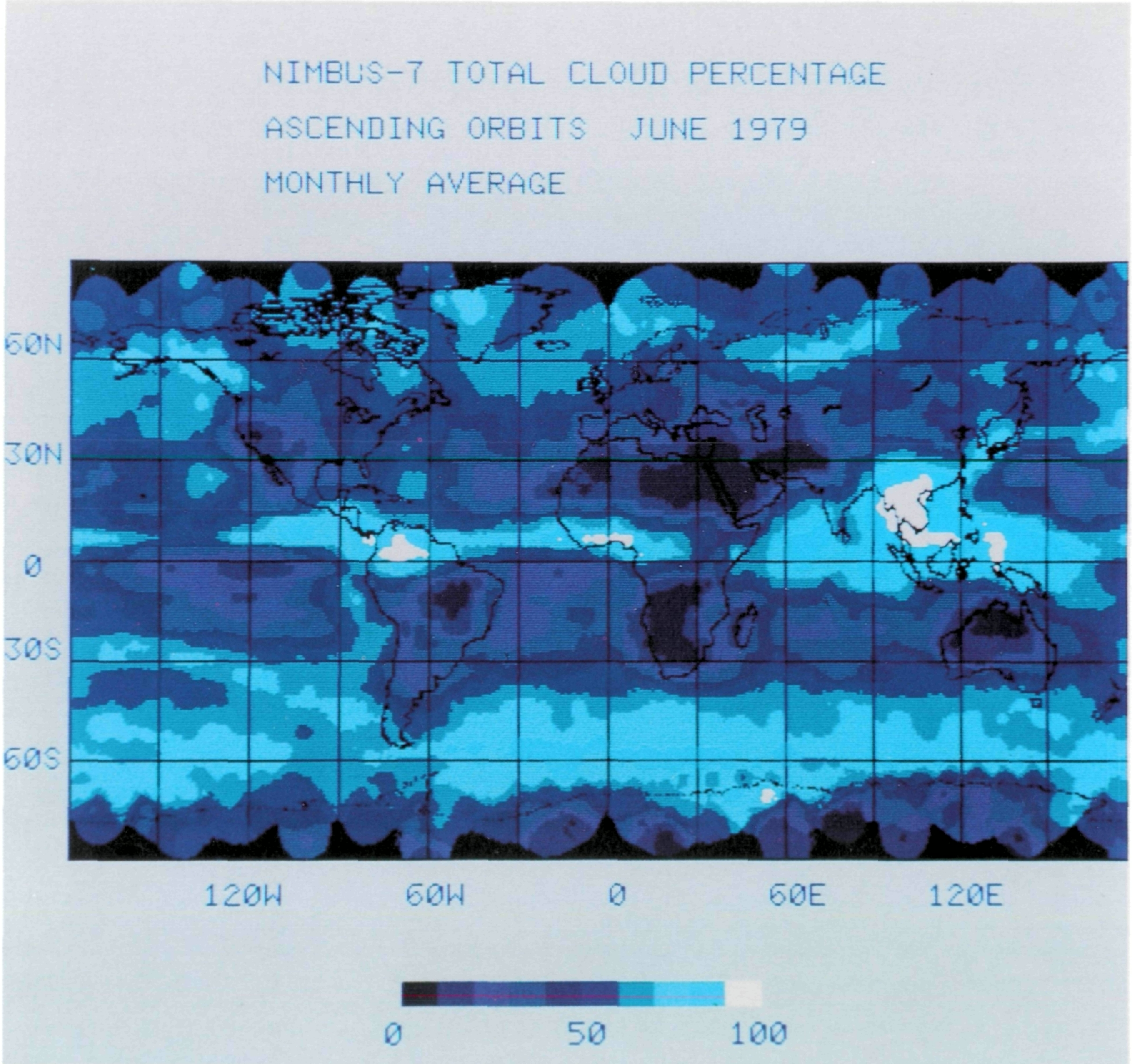

Sample of data generated by Nimbus-7, a most significant source of experimental data.

temperatures and the following derived products: sea ice (multiyear ice fraction and sea-ice concentration), total atmospheric water vapor over ocean, sea surface temperature, and sea surface wind speed. The first 5 years of data have been archived.

- A 6-year data set of infrared radiance observations from the Temperature Humidity Infrared Radiometer (THIR) Experiment has been archived. Additionally, a 6-year cloud climatology data set is under development using a combination of THIR and TOMS data. Two of the 6 years of cloud data consisting of low, middle, and high cloud amount have been produced and archived.

Contact: Dr. E. J. Hurley
Code 630

Sponsor: Office of Space Science and Applications

POWER SPECTRAL ANALYSIS FOR OCEAN PHYSICS

A problem which occurs often in most branches of science is that of choosing a spectral-domain representation for a limited set of imperfectly determined correlation-domain data. With increasing importance of correlation spectroscopy and aperture synthesis methods, this is particularly significant in seismology and radio-astronomy. While it is true that the two domains are linked by the Fourier Transform, it is only in the case of complete noiseless knowledge of the correlation function that the transform may be used to obtain the spectral function without imposing additional assumptions about the nature of both the data at hand and the unavailable data. A treatment of this problem by J. P. Burg, called the Maximum Entropy Method (MEM), appeared in the literature of the geosciences in 1967. Experiments, using data generated from processes with known spectral functions, have shown this method to be consistently superior, in some cases greatly so, to the traditional methods of Blackman and Tukey. The basic concept of the MEM is that given a limited set of autocovariance coefficients, the corresponding spectral analysis is based upon choosing that spectrum which corresponds to the most random or unpredictable time series whose autocovariance function coincides with the given set of coefficient values.

N. L. Bonavito and M. S. Bhatia have prepared a version of the Burg algorithm that guarantees the stability of the resulting prediction-error filter. In this spectral estimation, the power spectral density is expressed in terms of the coefficients of a (Wiener) Prediction-Error Filter and the prediction error power. A recursive procedure (Levinson) is used to compute the filter coefficients where the coefficients for the Mth order filter are computed from the lower order filter coefficients and the reflection coefficients. The set of reflection coefficients plays a central role in the design of prediction error filters. The developed algorithm uses the Final Prediction Error Criterion to choose the optimum filter order. It has been pretested with complex sinusoids of the form:

$$\underset{\sim}{x}(n) = \exp(j2\pi f_1 nT) + \exp(j2\pi f_2 nT + \underset{\sim}{\phi}) + \underset{\sim}{w}(n)$$

where f_1 and f_2 are two closely spaced frequencies, $\underset{\sim}{w}(n)$ is a complex white noise form, and $\underset{\sim}{\phi}$ is a random phase. For short data records ($n \sim 10$), the method super-resolves the peaks, whereas the Fast Fourier Transform (FFT) is unable to do so. For longer data records, both methods agree asymptotically.

A well known limitation on Fourier resolution techniques is that:

$$\text{Resolution} \geqslant \frac{1}{T_0}$$

where T_0 is the observation time spanned by n data samples. On the other hand, Bonavito and Bhatia have developed a theory which indicates that for the maximum entropy case, the limitation on resolution goes as T_0^{-2}. This result develops from the mean square displacement associated with the fluctuation of the variables under observation. This analysis indicates that the maximum entropy power spectrum is not quenched or curtailed as in the case of the FFT, and hence can be used to describe short time-scale physics, and the reversible (mechanical) behavior of physical systems.

These results are of considerable importance in the study of ocean wave generation and slope/surface elevation probability distribution. Drs. Norden Huaug and Steven Long of GSFC (670) have shown by comparing laboratory and field data, that the skewness of the surface elevation distribution is proportional to the significant slope of the wave field, where the proportionality constant is defined as the wavelength of the energy-containing waves. These results imply the presence of a mechanism to induce a long-range order or organizational element from among the weak nonlinear wave component interactions. Maximum entropy spectral analysis is thus viewed to be well suited to describe the dynamics both above and below the domains of turbulence. As is often the case, conditions for the onset of phase transitions require a multidimensional theory to predict such

behavior. In this regard, the research team has completed about 60 percent of a multichannel-multivariate maximum entropy program for the analysis of real signals. This will allow the processing of two dimensional, n nearest neighbor correlation terms for the same problems. At present, the team is in the process of utilizing MEM to spectrally analyze Wind-Wave Interaction Tank data from Wallops Island, Virginia, consisting of a time series of surface/slope data. These results will be presented in a later report.

Contact: Dr. N. L. Bonavito
Code 630

Sponsor: Office of Space Science and Applications

SPACE COMMUNICATIONS AND NAVIGATION

SPACE MISSION IN-FLIGHT COMMUNICATIONS PERFORMANCE UTILIZING THE CLASS SYSTEM

The Communications Link Analysis and Simulation System (CLASS) is a computerized space communications system performance analysis tool developed by the NASA network primarily for the prediction of user communications system performance through the Tracking and Data Relay Satellite System (TDRSS). The CLASS models all elements of the network systems, network user systems and communications channel environment, and is capable of providing a performance analysis of virtually all communications system performance measures of interest. The CLASS capability is not limited to TDRSS and, in fact, is readily extendable to the network design and evaluation of a broad range of space communication systems. Both end-to-end and system-by-system analysis can be accomplished through the CLASS, which is designed for convenient, reliable use by personnel with a wide range of communications system backgrounds and training in the use of simulation systems and the TDRSS.

One of the many capabilities is the prediction of the actual performance anticipated when the mission is supported in its normal flight configuration, considering all aspects of the communications system, channel and user operational plans and constraints, as well as network system constraints. This type of analysis is normally performed on a mission time line basis, during either premission simulation, mission time synchronous simulation or postmission analysis. Performance is evaluated on an end-to-end and/or on a system (or subsystem) basis.

This category also contains an automatic optimization feature such that when executed, optimization default algorithms check selected user and network parameters to determine if the performance of the system is optimum. Nonoptimum performance areas are noted, and suggested modifications to achieve optimum performance are provided. This capability can also be used as a mission design optimization tool as well as a network evaluation tool.

The primary uses of the CLASS in this category include the provision for determining communications system power requirements on a mission phase or statistical basis, orbit or trajectory optimization, and mission events time line optimization. Other uses include fault isolation or problem resolution during the mission and scheduling since areas of potentially poor communications performance can be identified. The outputs of the system can also be used to provide mission controllers with a current or selectable future prediction of the communications performance when executed in a mission time-synchronous mode.

Contact: Robert Godfrey
Code 530

Sponsor: Office of Space Tracking and Data Systems

DEVELOPMENT OF ALGORITHM FOR PRELIMINARY ORBIT DETERMINATION AND APPLICATION TO TDRSS

Traditionally, preliminary orbit determination has been performed using angular tracking measurements, or angular measurements in combination with ranging measurements, and many suitable techniques exist for these tracking types. In the Tracking and Data Relay Satellite System (TDRSS), however, accurate angular

measurements are generally not available because the antennas on each Tracking and Data Relay Satellite (TDRS) employ an open-loop pointing system based on predicted spacecraft positions. Since the antenna beam half-widths are relatively large (0.9 degrees for the S-band single-access mode, as illustrated in the first figure), it is possible to collect precise range and Doppler tracking for a spacecraft thay may soon drift out of the antenna beam pattern, following a maneuver or launch misfiring. Hence, there is a need for preliminary orbit determination based on the TDRSS range and Doppler tracking alone. It is necessary to determine the preliminary orbit with an error that is much smaller than the uncertainty implied by the width of the TDRS antenna beam, so that the resultant predicted orbit is sufficiently close to the center of the antenna beam in order that subsequent tracking can be obtained and routine orbit maintenance can be resumed.

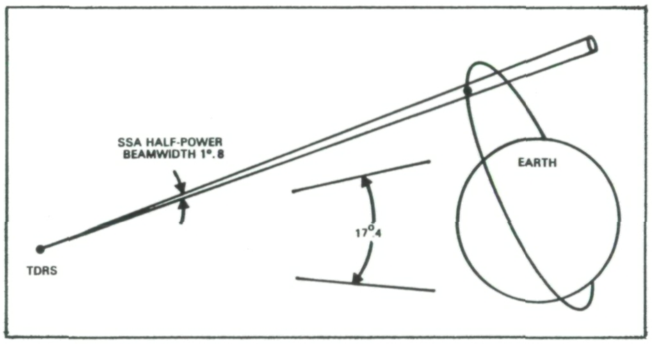

Relative angular size of the Earth and the TDRS SSA antenna beam.

The primary problem in preliminary orbit determination is obtaining a mathematical solution for a set of nonlinear equations when the *a priori* estimate of the solution is poor. The problem becomes very difficult in the case of range/Doppler-only tracking because no way is known to solve the problem in stages; for example, with angle tracking the determination of the orbit plane can often be first performed, followed by determination of remaining in-plane orbital parameters. With range/Doppler-only tracking the six orbital elements must be determined in a simultaneous solution. Since the *a priori* estimates of the orbit solution are poor, it is then necessary to have a reliable, wide-convergent method of solving the six nonlinear equations.

A continuation method was devised and applied to this problem. In a continuation method, a continuous solution path in a generalized space is defined and the path followed from the *a priori* estimate of the solution to one or more actual solutions for the problem. The particular

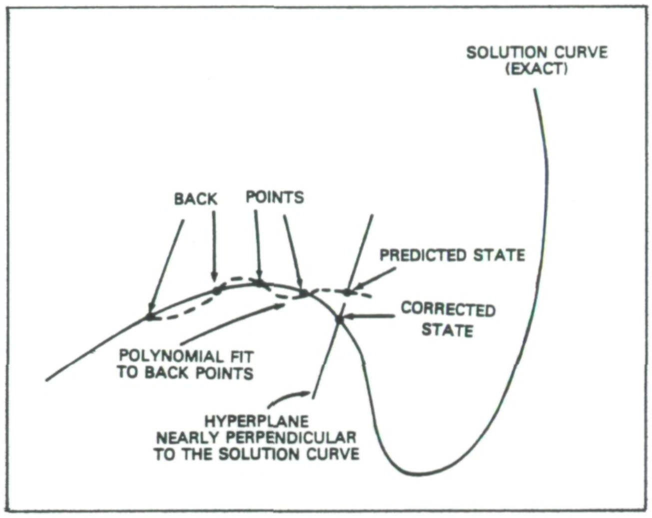

Numerical algorithm for following a solution curve.

formulation that was devised for this orbit determination problem can be shown to be a generalization of the classical Newton-Raphson method, but having a radius of convergence that is much larger. Physically, the formulation can be interpreted as continuously deforming the set of tracking measurements from an initial set, which is simply calculated from the *a priori* estimate of the orbit, to a final set, which is equal to the actual tracking measurements. The parameter λ is introduced to effect this deformation; $\lambda = 0$ corresponds to the *a priori* estimate, while $\lambda = 1$ corresponds to an actual solution. A numerical predictor-corrector algorithm, shown in the second figure, was developed to follow the solution curve in the generalized space, using the curve arclength, s, as the independent variable.

An example of an orbit determination solution curve obtained with the continuation method is shown in the third and fourth figures. This curve was obtained using actual TDRSS relay range and Doppler tracking. In this example the orbit was determined using a minimal set of six tracking measurements. The mathematical nature of the range/Doppler orbit determination problem leads to solution curves that are composed of one or more disjoint loops in the generalized space; the fourth illustration shows two z-symmetric loops, and in the third figure the two loops are actually superimposed. This particular example shows four mathematical solutions; the three spurious solutions can be discarded by checking the rough values of the TDRS antenna pointing angles. Using the developmental computer program on the DEC VAX 11/780 computer, computation of a solution loop using two-body orbital dynamic typically requires one minute of CPU time.

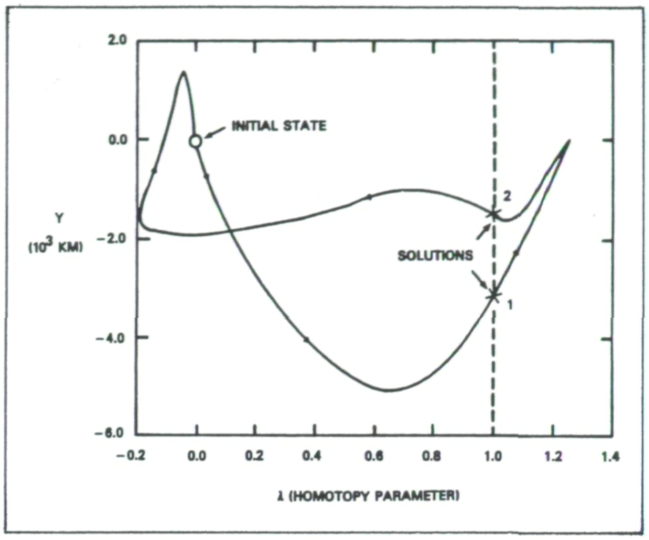

Projection of a Landsat-4 solution curve onto the Y-plane.

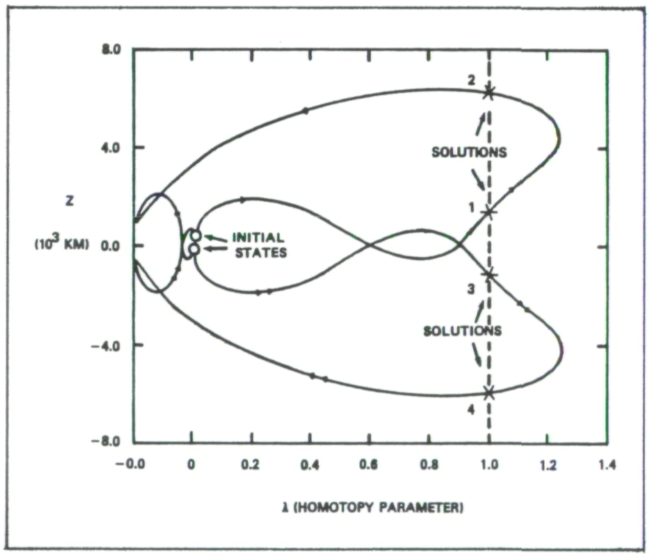

Projection of a Landsat-4 solution curve onto the Z-plane.

Although this continuation method was applied to the TDRSS range/Doppler problem, it is extremely general and flexible. It works equally well for other tracking measurement types, as well as for ground-based tracking, and, with minor modifications, the method can be extended to handle many trajectory targeting problems.

Contact: Ed Doll
Code 550

Sponsor: Office of Space Tracking and Data Systems

APPLICATION OF PSEUDO-NOISE CORRELATION AND BANDWIDTH SYNTHESIS TO ORBIT DETERMINATION

The ability to accurately determine the orbits of all satellites involved in any satellite communication system, whether they are in geosynchronous or low-Earth orbits, is crucial to successful operations. Today there is a growing need for low-Earth orbiting (LEO) satellites to provide more accurate, self-contained navigation capabilities.

As part of a Phase I Small Business Innovative Research (SBIR) project and a Phase II counterpart in progress, a new signaling and signal processing concept, the Pseudo-Noise Bandwidth Synthesis (PNBWS), has been introduced to support highly accurate satellite orbit determination. To date, its technical viability has been demonstrated through a combination of conceptual system architecture development, analysis, and computer simulation. The principal focus has been on geosynchronous satellite orbit determination (e.g., TDRS) with applicability to LEO satellite autonomous navigation to be explored later in Phase II.

PNBWS represents an extension of the bandwidth synthesis (BWS) technique that has been employed for many years in interferometric applications, and combines many of the benefits of conventional PN ranging, tone ranging and interferometry toward achieving time resolution down to the order of 1 nanosecond. This is accomplished by a novel combination of signal structure utilization and hardware/software signal processing. Especially significant is the achievement of wide-bandwidth time resolution via actual utilization of relatively little bandwidth. For example, the time resolution benefits of a 50-MHz bandwidth (<1 ns) may be achieved via actual application of only 5 to 10 MHz (i.e., a bandwidth utilization factor of 10 to 20 percent). In addition, in contrast to interferometric BWS, which requires the transfer of unprocessed, high rate data (e.g., >1 Mbps) among its ground sites, PNBWS depends on very low transfer rates (e.g., <1 kbps). This is a direct result of the fact that the PN signal structure may be taken advantage of at a given site to perform local signal processing and, hence, to locally arrive at a satellite-to-ground site range estimate; it is this *processed* (low rate) ranging data that is transferred to a central site for final orbit determination processing, instead of the *unprocessed* (high rate) data in interferometric applications.

In support of the PNBWS orbit determination concept, efforts to date have developed representative system implementations that include signal structure

characteristics and block diagram characterizations of the key signal processing components. An initial performance assessment has been conducted based on a combination of analysis and simulation. Attractive operational features associated with CONUS-based network geometry, low-complexity processing and satisfaction of space-to-ground flex density constraints have also been identified. In addition, key error sources (ionosphere, system clock biases, etc.) have been identified and qualitative means for self-calibration have been investigated.

For NASA, PNBWS offers the future potential for precision TDRS and follow-on TDRS orbit determination, as well as precision LEO satellite autonomous navigation. Bandwidth efficient, precision time and frequency transfer among a network of satellites and geographically remote sites also appears feasible via PNBWS.

Contact: John Coffman
Code 530

Sponsor: Small Business Innovative Research

AN INTEGRATED RECEIVER CONCEPT USING PROGRAMMABLE CHARGE-COUPLED DEVICES

The successful operation of any low earth orbiting (LEO) spacecraft mission — whether it be NASA, military, or commercial — depends heavily on the ability to perform accurate orbit determination, via both ground-based tracking and on-board spacecraft navigation. In fact, as the objectives of space-based research and operation become increasingly ambitious, the accuracy, speed, and efficiency requirements of the orbit determination process will grow, while cost reductions will be sought. Concurrent growth in communication and signal processing requirements can also be expected.

The orbit determination process typically originates with the key signal processing functions of pseudo-noise (PN) code acquisition/tracking and Doppler tracking. The criticality of PN code processing to orbit determination suggests that it be performed accurately and efficiently. Its importance grows when one also recognizes PN code centrality in possibly supporting several additional and simultaneous functions, such as flux density reduction, code division multiple access, and protection against jamming. Of special significance is PN code acquisition, which is a prerequisite for all subsequent hardware/software processing, including PN, carrier and symbol five synchronization, and data detection.

As part of a Phase I Small Business Innovative Research (SBIR) project, a fully integrated receiver concept has been introduced which incorporates a PN matched filter (PNMF), implemented by programmable Charge-Coupled Devices (CCD), for extremely rapid PN acquisition. Of particular significance is the fact that the CCD PNMF Integrated Receiver (CPIR) accomplishes PN/carrier/symbol acquisition and tracking, and does so in a unique, integrated fashion with all three functions interacting in a simultaneous and stable fashion.

A key component of the CPIR is the PNMF which provides the parallel processing feature that leads to dramatic reductions in PN acquisition time relative to conventional schemes. Also of significance is the fact that the PNMF is implemented by a programmable CCD which is exploited by the tracking and acquisition processing algorithms in novel ways to effect fully integrated and flexible operation.

In addition to the fundamental signal processing functions, the CPIR offers the potential for supporting other important functions not readily available via conventional receivers such as on-line correlation analysis. The Phase I study has also demonstrated that the CPIR may yield key performance monitoring and fault isolation information and enhance its potential future role as a microprocessor-based Autonomous Integrated Receiver System (AIRS) — a concept of considerable interest to NASA/GSFC.

In support of the CPIR concept, the Phase I study has developed initial design configurations that include block diagram characterizations and important concept options. In addition, a first level assessment of performance has been accomplished through a judicious mix of analysis and simulation that demonstrates both receiver acquisition and tracking capabilities.

Contact: Denver Herr
Code 530

Sponsor: Small Business Innovative Research

KA-BAND HYBRID MICROWAVE INTEGRATED CIRCUIT LOW NOISE RECEIVER

An advanced solid-state subsystem, the Ka-Band Hybrid Microwave Integrated Circuit Low Noise Receiver, which exhibited the lowest noise figure performance of any room temperature receiver ever reported at 30 gigahertz (GHz), was recently developed. This enhanced receiver

was fabricated during the second phase of a multiphase effort to develop a low cost, low noise receiver for spacecraft radiometer systems by utilizing Gallium Arsenide (GaAs) Field Effect Transistors (FET's) technology, exclusively. In addition to its low-noise specification, the receiver was required to be small, lightweight, and highly reliable.

State-of-the-art components were realized through a closely coupled device and circuit development effort, resulting in advances in materials, devices, and circuit technology. The significant program accomplishment was the development of the all-FET, low-noise receiver with 3.6 dB noise figure and 42 dB gain from 27.5 to 30.0 GHz. Some constituent parts of the receiver included a waveguide-to-microstrip transition, RF preamplifier, bandpass filter, dual-gate FET mixer, dielectric resonator-stabilized FET local oscillator, IF amplifier, and internally regulated direct current bias circuitry.

The key performance parameter in the above results, the noise figure, dramatically demonstrates the benefits to be obtained by using the FET devices and microwave integrated circuit (MIC) technology at millimeter wave frequencies. The noise performance of this receiver is 2 to 3 dB lower than the best single sideband mixer front-ends

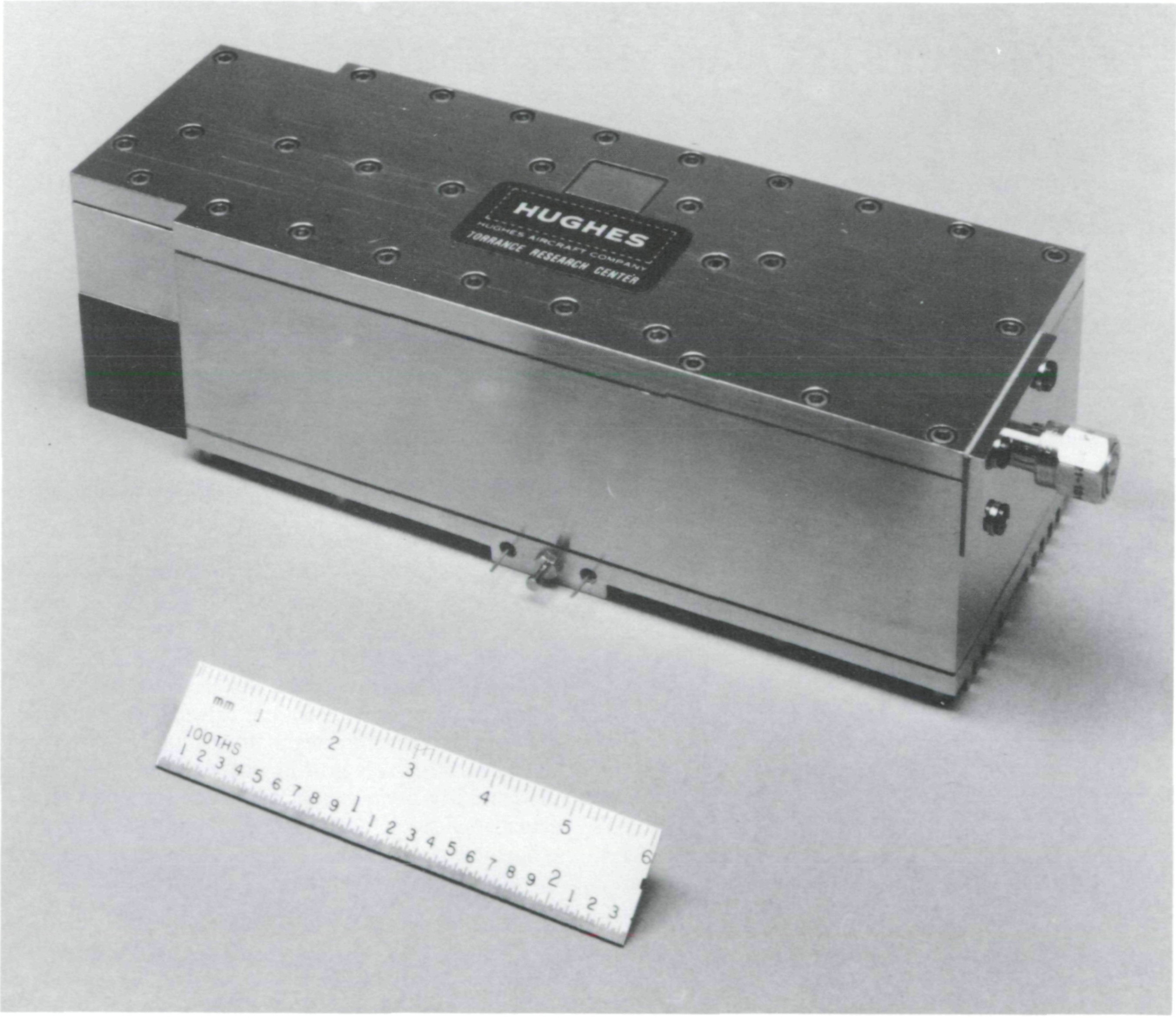

Ka-Band Hybrid Microwave Integrated Circuit Low Noise Receiver.

reported to date. Its dimensions are 1.25 × 1.75 × 6.0 inches, and its weight is 15 ounces (426 grams). Although the receiver was realized in a hybrid MIC format, components of this type will ultimately be developed using monolithic microwave integrated circuit (MMIC) technology as millimeter wave device and circuit technology matures.

Besides the aforementioned application of the low noise receiver for microwave radiometers, it can also be used to significantly improve the performance of microwave communication systems. The small size and weight of the integrated circuit receiver can be used to advantage by attaching it directly to the antenna, eliminating the need for lossy coaxial cables and rotary joints. Furthermore, the improved receiver sensitivity allows the communication system designer the additional flexibility of reducing the receiver antenna size and lowering the transmitter power.

Contact: Robert Jones
Code 720

Sponsor: Office of Aeronautics and Space Technology

SYSTEM AND SOFTWARE ENGINEERING

AN EXPERIMENT WITH ADA — THE GAMMA RAY OBSERVATORY ATTITUDE DYNAMIC SIMULATOR

Ada® is a new high-level software development language which holds great promise to improve programmer productivity and produce more reliable, maintainable software. In order to determine the applicability of Ada to projects at Goddard, several pilot implementation projects are being conducted. The largest initiated to date has been the Gamma Ray Observatory (GRO) Attitude Dynamic Simulator, a joint project of the Data Systems Technology Division and the Flight Dynamics Division. The goals of the project are to:

- Determine the impact of using Ada as a development methodology and language on productivity, reliability, maintainability, reusability, and portability.
- Characterize the development process using Ada and develop a set of measures for determining the advisability of utilizing Ada for portions of the Space Station project.

In 1985 the Data Systems Technology Division acquired several Ada environments and Ada training media from commercial and military sources for evaluation. A wide range of performance was seen and the best environment available was selected for the pilot applications.

The first phase of the GRO project was initiated in January 1985 with a seven person team from Goddard and Computer Sciences Corporation. Team members had to be thoroughly trained in Ada since Ada features such as strong data typing and concurrency which do not exist in the FORTRAN language. To properly utilize these new capabilities requires the use of new design techniques which were unfamiliar to most of the team members. Therefore, the training emphasized design methodologies to be used with Ada as well as the structure of the language itself. Training included classroom lectures, video tapes, computer aided instruction and textbooks. By far the most valuable learning mechanism was to apply the training to a sample project, a simple electronic message system.

After the team was thoroughly trained, the GRO Attitude Dynamics Simulator project was initiated. Due to current requirements potentially being biased to FORTRAN language implementation, the team reanalyzed the system requirements and entered the design phase. The project will be completed by the end of calendar year 1986 and is expected to generate nearly 40,000 lines of Ada code. The identical project is being implemented in parallel in the currently predominant language, FORTRAN, for actual application to the GRO Project. Both projects are being monitored to extract the amount of time being spent by each person on each stage of the project and to capture portions of the project which encounter any difficulties. The University of Maryland is analyzing the data acquired.

In addition to the results from the GRO Project, the team is already making a substantial contribution to the

understanding and use of Ada at NASA. Evaluation reports and recommendations for training have been produced. The team has synthesized a new object-oriented design methodology which has wide applicability and will be testing the methodology on the actual project implementation. Experience to date has been documented and has been presented to the Space Station Software Working Group.

When completed this Ada project will provide insight into the advantages and disadvantages of using Ada over FORTRAN on a medium-sized software system. It will also provide a firm basis of experience for future systems development in Ada.

Ada® is a registered trademark of the US government, Ada Joint Program Office.

Contact: Robert Nelson, and Ed Seidewitz, Code 550

Sponsor: Office of Space Tracking and Data Systems
Office of Space Station

DATA SYSTEMS TECHNOLOGY LAB

A Data Systems Technology Lab has been established in the Mission Operations and Data Systems Directorate to provide a test bed for the application of advanced technology, such as expert systems and VLSI components, to the design and development of future systems for spacecraft control, data capture, processing, and distribution. The facility includes the following major components:

- A VAX 8600 to support prototyping of telemetry data processing architectures, including control of pipeline and distributed VLSI components; modeling of alternative data system configurations; simulation of VLSI chip performance; and control and data management for a prototype optical disk subsystem.

- A VAX 11/785 to serve as a test bed for development of network scheduling algorithms and prototyping of control center and other interactive display techniques applying human factors and workstation technologies.

- A VAX 11/750 to serve as a gateway and preprocessing node for a satellite link to Stanford University. This link will support distributed control and processing software needed to develop and evaluate approaches for remote operation of science payloads, using plasma physics payloads as a test case.

- Ethernet and disk cluster interfaces and a Hyperchannel link to an IBM 4341 to allow the above systems to be configured in various distributed architectures for prototyping of protocols and multiprocessor system designs.

- The prototype optical disk subsystem is being developed by Storagetek Systems and includes a 4 gigabyte write-once optical disk, a 1 gigabyte commercial optical disk (Optimem), and a commercial 500 megabyte magnetic disk (DEC RA 81), all interfaced to a smart controller and dedicated bus to off-load data movement from the host processor.

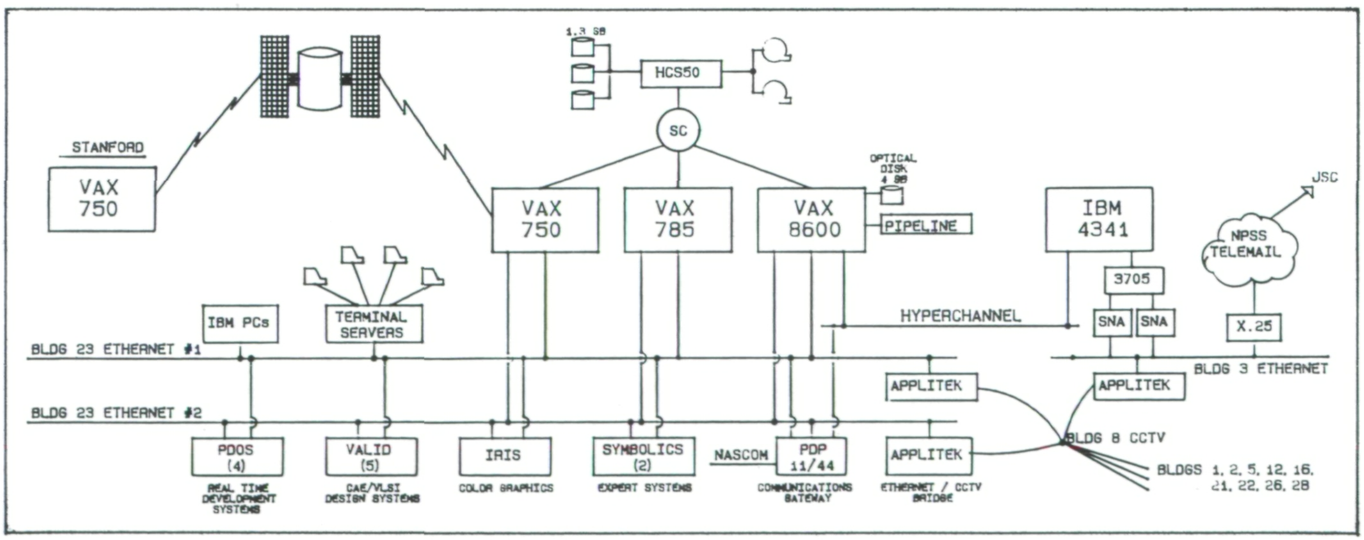

Data Systems Technology Laboratory.

Scheduled for delivery in summer 1986, this prototype system will be used to design and test hierarchical data storage and optical disk approaches for data capture, management, and distribution. The Optimem optical disk interface software is being coordinated with the National Space Science Data Center to allow the disk to serve as a medium for transferring mission data bases to active archives.

- Two Symbolics 3640 LISP machines are being used to develop prototype expert systems for automation of control center operations, scheduling, and system fault isolation.

- A Silicon Graphics IRIS workstation is being used to prototype advanced control center displays and user interfaces for remote science operations.

- The VALID design workstations and PDOS real-time development systems are being used to design gate arrays and circuit boards for data capture systems to provide a factor of 1000 improvement in cost-performance over conventional systems.

Contact: John T. Dalton
Code 520

Sponsor: Office of Space Tracking and Data Systems

NSSDC ON-LINE DATA CATALOG SYSTEM

Development of the NSSDC On-line Data Catalog System (NODCS), begun in 1984, is approaching completion. The system is intended to enable scientists throughout the space science community to quickly and easily find data relevant to their needs. The system is divided into two

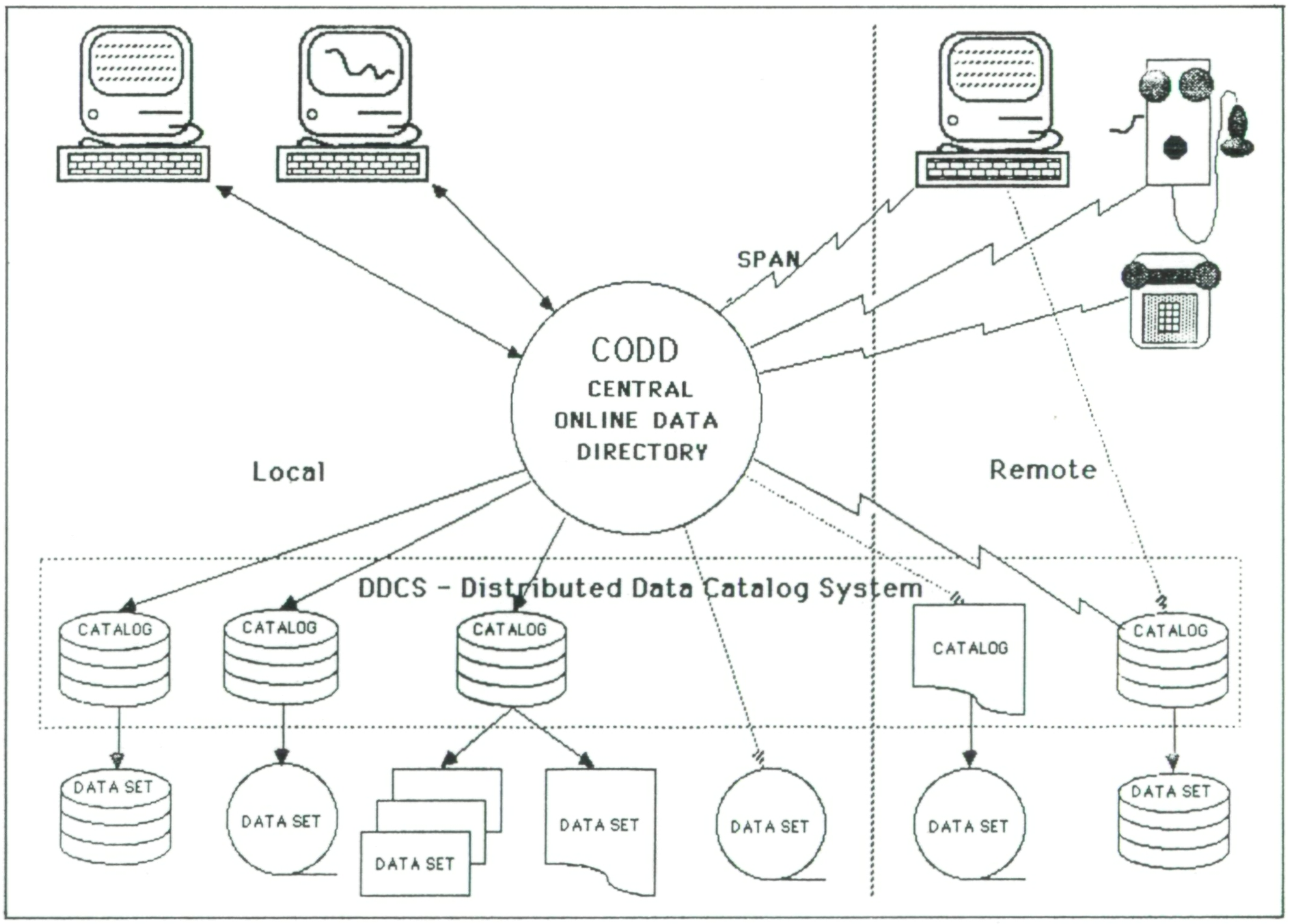

NSSDC On-line Data Catalog System.

parts, the Central On-line Data Directory (CODD) and the Distributed Data Catalog System (DDCS).

The CODD contains a user-friendly set of menus designed to allow a user with little or no experience to obtain information on data sets in their entirety, such as location, characteristics, and access procedures. This includes information on: the spacecraft, mission, or project; the instrument used; the data set quality, processing history, resolution, and parameters measured; the data set quality, processing history, resolution, and parameters measured; the names and places to be contacted concerning data information and content; etc. The CODD is accessible via computer networks (e.g., Space Physics Analysis Network (SPAN), dialup lines, or by using the facilities at NSSDC). Once the user has determined the data set or sets of interest he will be directed to a catalog within the DDCS which is associated with the data set, if one exists.

The DDCS encompasses all of the catalogs which are associated with the data sets and which contain more detailed information than the directory, usually concerning the individual segments of data within the data set. From this a scientist could determine, for example, if an instrument was operating at a particular time or place and what mode of operation was used at that time. A catalog normally resides with the data set and may be located at NSSDC or any other institution. The directory will provide the information needed to access the catalog and, in the future, may provide direct connection to online catalogs.

During the past year the initial directory has been modified in accordance with recommendations by a steering committee of scientists. In addition to being able to search for data sets by knowing the mission, experiment, or investigator name, the user will now be able to initiate a search based on selected keywords describing such things as the scientific discipline, phenomena of interest, quantities measured, measurement locations, general times, etc. A new and more complete user-friendly interface is in development. The data base has been transferred to version 4 of the Oracle Data Base Management System on the NSSDC VAX 11/780 computer. A system for new data entry has been developed using the Interactive Applications Processor within Oracle. The data base will initially be tested with data from the solar-terrestrial community.

Contact: James R. Thieman
Code 630

Sponsor: Office of Space Science and Applications

DIGITAL OPTICAL DISK

Emerging digital optical disk technology offers significant advantages over traditional magnetic tapes for the archiving and dissemination of large volumes of space and Earth science data. This technology also provides the ability of having very large data volumes online for immediate access by a broad community of users.

In order to better satisfy its traditional requirement of archiving/dissemination offline data, and to effectively satisfy a rapidly growing demand for online data and services, NSSDC has recently installed a 1-GB capacity Optimem optical disk system. The system is interfaced to a DEC PDP 11/23 computer running RSX-11M via an interface developed in association with the University of Texas at Dallas. The interface takes cognizance of the write-once nature of the optical disk, and sends directory information to an associated magnetic disk until the optical disk is almost full. An equivalent VAX/VMS interface to NSSDC is in process of development.

NSSDC is in its early learning phases with the new system. Data files are being transferred to and from the optical disk; files are in fact moving over SESnet, an Ethernet/CATV -based LAN at GSFC, from a VAX-11/780. Optimal data formats for data and directory files are being investigated. The initial test data files included data from Dynamics Explorer and ICE spacecraft.

As soon as it can be verified that this equipment is reliable, the optical disk will play a vital role in the NSSDC/NASA investigator program in data restoration.

Contact: Joseph H. King

Sponsor: Office of Space Science and Applications

Flight Projects and Mission Definition Studies

Flight Project activities during 1985 varied from the spectacular comet intercept mission of the International Cometary Explorer through the tail of Comet Giacobini-Zinner to the use on a Shuttle flight of the relatively simple workhorse space instrument carrier Spartan. A major thrust in support of the now-developing Space Station was implemented in FY85, highlighted by the accommodation of Spartan and the Solar Optical Telescope in the Space Station system. In addition, satellite servicing projects and planning and development of future free-flyers and Shuttle payload missions continued at a steady pace.

FLIGHT PROJECTS

SPACE STATION SPARTAN

The Space Station Spartan (3S) is intended to provide the scientific community with a cost effective short-duration free-flying carrier for a single instrument (or a single-purpose instrument cluster) operating from, and in conjunction with, the proposed Space Station. This carrier will support scientific investigations that have previously been flown on sounding rockets and balloons and will fulfill the diverse pointing and operational requirements often associated with such payloads. It will offer experimenters quick-turnaround schedules, and frequent flights of up to 3 months duration. Sounding rocket and Space Transportation System (STS) Spartan techniques and concepts with minimal redundancy will be used. The carrier is designed to be reusable, and the instruments can be changed while in space.

A study, initiated in January 1985 and completed in May 1985, developed the 3S concepts and defined the associated requirements and interfaces with the Space Station.

The carrier, replacement subsystem modules, and/or new instruments will be transported to space by the STS Orbiter. The Space Station will then function as a base for 3S operations. The Orbital Maneuvering Vehicle (OMV) will be used for the proximity operations of deployment and retrieval. After deployment the 3S onboard propulsion system will be used to place the carrier into its mission position (nominally 250 nmi) to the rear of Space Station. The 3S will then fly in formation with the Space Station. Once in position, the 3S will communicate by radio-frequency (RF) transmission via the Space Station to the ground. Thus an experimenter can gather data through real-time interaction with his instrument. Upon completion of the mission a similar operation, in reverse, will return the 3S to the Space Station. The 3S will then be fitted with new instruments, serviced, and stored until the next mission.

The needs of experimenters carrying out research within the ultraviolet and infrared astronomy, high-energy astrophysics, planetary studies, and solar physics fields using balloons and rockets have been considered paramount. Consequently, the STS/Spartan and 3S have been designed to accommodate these users.

An experimenter can fly a sounding-rocket type of instrument on a 3S carrier for up to 3 months of mission time. This duration is mostly limited by the quantity of propellant carried aboard and the type of Attitude Control System (ACS) used. The carrier is designed to hold an instrument measuring up to 44 inches in diameter and 14 feet in length, weighing up to 5,000 pounds. Three hundred watts of orbital average power will be available for the instrument. The basic three-axis ACS has been derived from the current STS/Spartan. The communications system will allow the experimenter to receive raw data in real time in order to select and verify targets from his ground-based control center.

The experimenter with extended observation requirements might prefer the 3S free-flyer to a Space Station attached

◀ *Facing page: Shuttle Pointed Autonomous Research Tool For Astronomy (SPARTAN) shown being removed from Orbiter by Remote Manipulator Unit.*

payload. He would have greater freedom in scheduling considerations because of minimal interfaces with the Space Station. His instrument would be free from attitude perturbations induced by other Space Station activities. Freedom from any potential contamination and electromagnetic interference sources from the Space Station might also be realized. As a free-flyer, no obstructions of view from other Space Station activities would exist, and an increase in continuous viewing time would be ensured.

The 3S derives its system and subsystem designs from successful spacecraft and existing Spartans. The 3S consists of ACS, Communications and Data Handling (C&DH), power, and propulsion replaceable modules and can be enhanced as future demands are identified.

For example, the ACS can evolve to serve various requirements. The basic ACS (derived from the STS/Spartan) will be modified to accommodate an up-to-3-month mission duration. This will fulfill the needs of current STS/Spartan instruments that can benefit from longer observing durations. An intermediate ACS, with improved jitter performance using reaction wheels, will accommodate high-resolution solar and stellar payloads. An enhanced ACS, similar to the Multimission Modular Spacecraft (MMS) ACS, will allow for very high resolution, narrow field ultraviolet, extreme ultraviolet, and X-ray astronomy payloads. The design of the 3S ACS as a replaceable module will allow upgrading of the basic carrier pointing capability without major modifications to the rest of the system.

The 3S is intended to be an evolution of and supplement to the present STS/Spartan concept and, as such, will conduct operations from the Space Station. Proven flight hardware and the simplicity of the 3S design will enable the 3S to meet a wide spectrum of experiment requirements at modest cost.

Contact: Sterling Smith
Code 420

Sponsor: Office of Space Science and Applications, Code E

SPACE STATION SCIENCE LABORATORY MODULE CONCEPT DEVELOPMENT

Major accomplishments in definition and concept development for the Science Laboratory Module (SLM) have occurred during FY85. Even though the original concept for the GSFC Work Package 3 (WP-3) laboratory module was essentially an extension of the Spacelab primarily to support life science research, the SLM concept has evolved to the extent that the laboratory will provide an integrated, generic facility. This facility, as currently envisioned, will support scientific research in many disciplines including planetology, technology development, plasma physics, monitoring and control of astronomy, Earth resources, solar physics and lidar experiments, and servicing of existing payloads, in addition to an extensive program in both human and plant/animal life science research. GSFC expects that many more uses will be found for the SLM capability in the future.

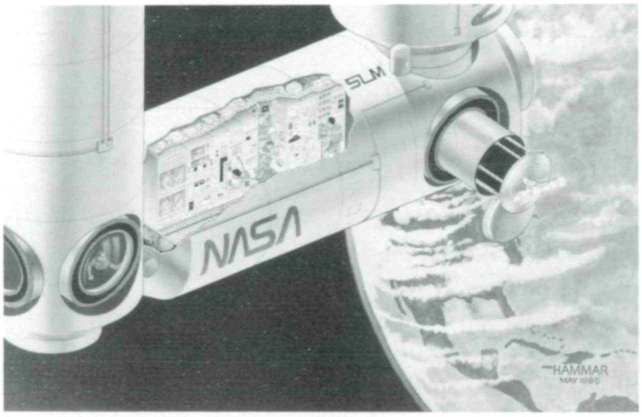

Space Station Science Laboratory Module (artist's concept).

The accompanying illustration shows an artist's concept for the SLM. As can be seen in this figure, the SLM will provide a shirt-sleeve environment, work benches, test facilities and storage for parts, tools and test equipment that can be used to repair free-flying satellites and platforms that have been returned to the Space Station for repair. In addition, optical windows and scientific airlocks are planned for the SLM enhancing generic capability of the laboratory.

The artist's concept illustrates a unique approach to module outfitting that utilizes submarine design and maintenance experience. The submarine outfitting experience was applied to evolve a low-cost concept that potentially optimizes human productivity, provides extensive equipment and stowage volume, and enables on-orbit outfitting and easy reconfiguration.

Contact: Dr. Mitchell Rambler
Code 400

Sponsor: Office of Space Station, Code S

SATELLITE SERVICING AT THE SPACE STATION

The Space Station will open up a new era in on-orbit servicing. It will give us the opportunity to use space in more rational, economical and imaginative ways than we have in the past.

Servicing has the primary objective of extending the operational life of satellites, platforms, or Space Station attached payloads by repair, refurbishment, resupply, replacement of failed or worn out units, or by changeout of payload instruments. Another important objective is the assembly in orbit of space systems too large, heavy, or costly to be integrated on the ground and launched on a single Shuttle flight.

The servicing facility defined by the NASA Initial Operating Capability (IOC) Reference Configuration is undergoing definition. Currently it consists of the following six principal elements.

- Servicing bay
- Satellite storage bay
- Refueling bay
- Instrument storage area
- Tool Orbital Replacement Unit (ORU) storage area
- Work station in pressurized lab module

The first figure is a drawing of the IOC Reference Configuration showing the servicing facility elements and their locations. These elements when taken together and supported by the Mobile Remote Manipulator System (MRMS), the Manned Maneuvering Unit (MMU), the Orbiting Maneuvering Vehicle (OMV), standard tools and Extravehicular Activity (EVA) support equipment, make up the Space Station servicing capability.

The servicing bay is approximately 9 m (30 ft) in diameter, and 21 m (70 ft) in length. The volume enclosed allows for berthing a 4.5-m (15-ft) diameter by 18-m (60-ft) long satellite with clearances for movement of EVA crew and placement of work stations. The bay is cylindrical in shape with a segmented retractable cover to allow partial to full opening for access as required. In addition, a separate small port at either end of the bay is envisioned for personnel and small equipment entry. The second diagram shows the servicing bay with cover partially open and the MRMS handling a payload.

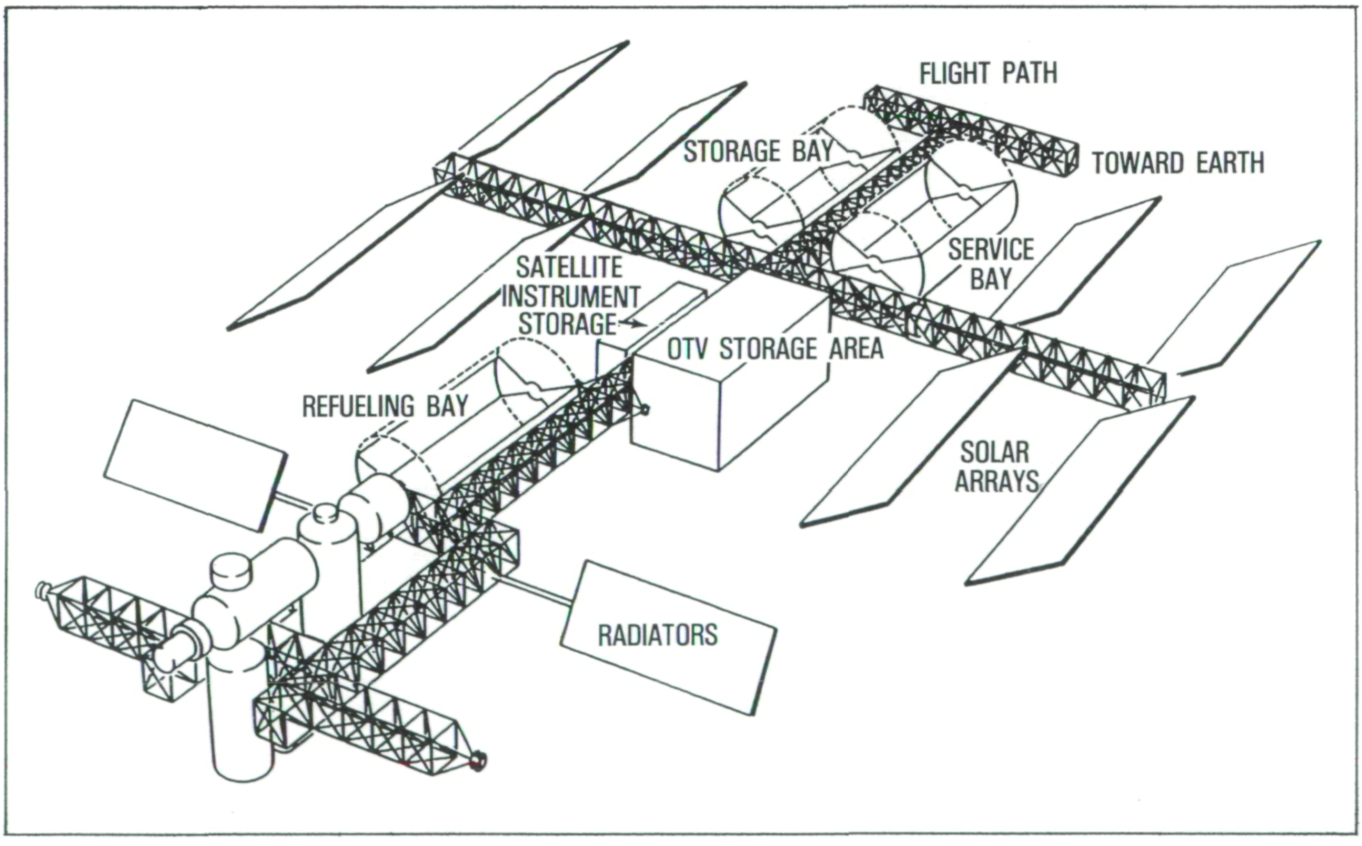

The Initial Operating Capability Space Station reference configuration.

The enclosed bay will provide environmental protection and contamination control. The bay will be outfitted with fixtures to hold satellites and payloads in fixed positions for servicing, and also a satellite positioning system allowing 90° tilt and ±180° rotation. A thermal control system with interfaces to the Space Station Active Thermal Control System will be utilized to control the internal temperature of the bay, as well as the temperature of the satellite being serviced. Power for the service bay is estimated to be 6 kW with 3.5 kW designated for satellite use. In addition to power control and distribution in the bay, the electrical system will include data processing and communication interfaces to the Space Station Information System. For support of servicing operations, the circuit television system facility monitors contamination and thermal sensors.

The storage bay is located adjacent to the servicing bay, but on the other side of the keel; it is identical in size and shape to the servicing bay and utilizes the segmented retractable cover. The storage bay will provide a safe haven for long-term storage of satellites, such as the Hubble Space Telescope, while repair procedures, equipment, or replacement units are being prepared on the ground for transfer to the Space Station.

The second figure also shows an instrument replacement using the servicing bay and storage bay on the main truss and illustrates how an instrument changeout, utilizing the MRMS, would be accomplished. Here the replacement instrument #2 is removed from the instrument carrier in the storage bay and the instrument #1 removed and placed back in storage.

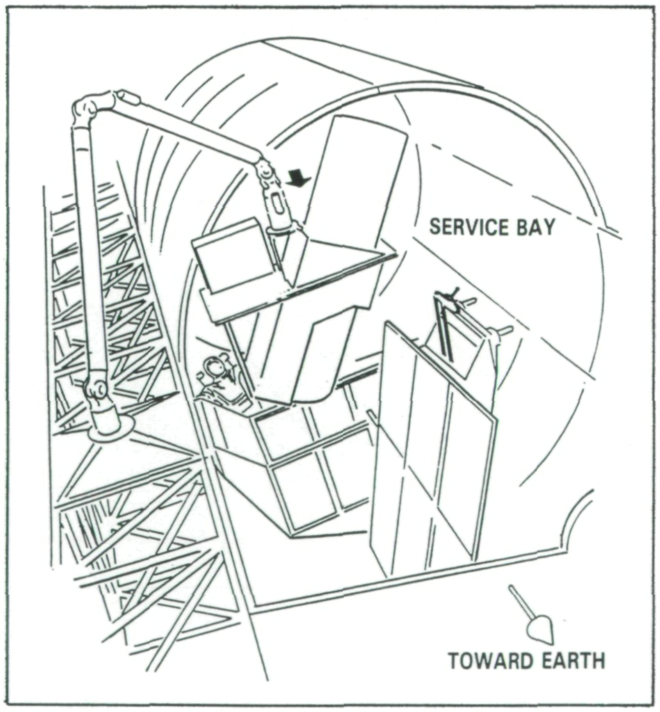

Space Station storage and servicing bays.

The refueling bay, as illustrated, will be identical in shape and size to the servicing bay and is located remote from the servicing and storage bays to prevent any contamination, that may occur from refueling, from reaching these bays.

Equipment will be provided to refuel satellite propulsion systems and to replenish cryogen systems for instruments. Other pressurants and fluids such as liquid nitrogen (LN_2) will be provided in this bay. A satellite retention/positioning system will be available to berth the satellite for refueling.

The power and data systems support satellite monitoring and caution warning system operations. The modular approach for the electrical system (power, data, etc.) will allow commonality with the servicing bay and will minimize cost. A thermal control system, contamination monitor and control system, and a crew EVA support system will be provided.

The instrument storage area is an enclosed volume located just below the solar array boom and is nominally 3 m x 6 m x 9 m (10 ft x 20 ft x 30 ft). It is used to store replacement instruments and other large modules awaiting installation or return to Earth.

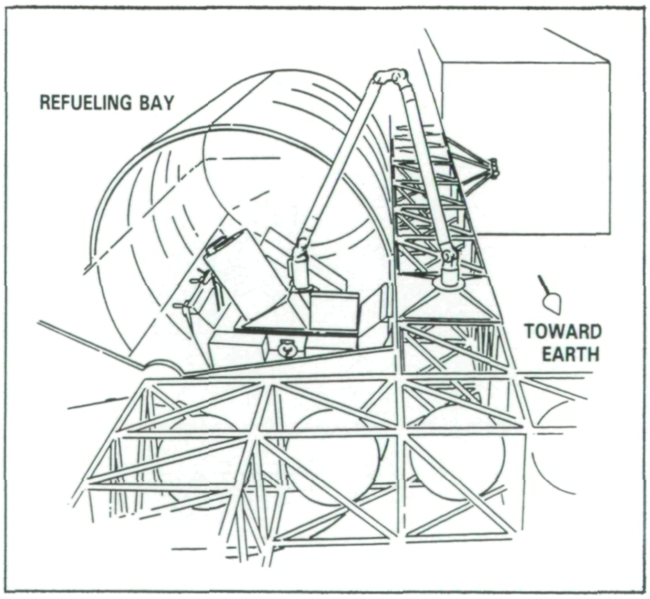

Space Station refueling bay.

Ten ORU storage lockers and four tool storage lockers, each 0.9 m x 1.5 m x 1.5 m (3 ft x 5 ft x 5 ft) are located across the center of the solar array mounting truss. These lockers have individual thermal control systems and covers. Power for all 14 boxes, holding fixtures for ORU's, and tools will be provided. Equipment for facility monitoring and EVA support is also included.

The work station in the Science Lab Module consists of a workbench and a control station. The workbench will be used for repair and replacement of items at the box level, which is two levels lower than the ORU level.

The control station will contain equipment to remotely monitor and control the customer servicing activities. The status of all facilities and viewing of the activities in each of the facilities will be provided via the Closed Circuit Television System.

Automation and Robotics (A&R) has the potential to improve signifantly the productivity of on-orbit assembly and servicing. A representative sample of the kinds of tasks for A&R are as follows:

- Removing and installing payloads and modules
- Performing precision mechanical assembly as in the buildup of an instrument system
- Servicing of manufacturing facilities such as materials processing systems
- Making electrical and fuel line connections using automatic mechanisms
- Testing and facility checkout of automated spacecraft

Contact: Francis Logan
Code 400

Sponsor: Office of Space Station, Code S

INTERNATIONAL COMETARY EXPLORER ENCOUNTERS COMET GIACOBINI-ZINNER

At 11:02 UT on September 11, 1985, the International Cometary Explorer (ICE) passed through the center of the ion tail of Comet Giacobini-Zinner at a distance of 7800 km from the comet nucleus, thus becoming the first spacecraft to ever encounter a comet. An overview of this encounter is presented in the accompanying illustration. The brief description of results presented here is based upon only a few days of looking at the data. Detailed analysis is expected to reveal a comprehensive picture of the interaction between the solar wind and a comet.

The plasma ion tail, which took approximately 20 minutes to cross, was characterized by a cold, dense plasma (the electron kinetic temperature was approximately 20,000 degrees Kelvin, and the electron density peaked at approximately 600 electrons/cubic centimeter; by contrast, the solar wind is typically 200,000 degrees Kelvin with a density<10 electrons/cubic centimeter). Plasma ion composition measurements in the tail showed predominantly water molecules, some carbon monoxide, and an unidentified molecule at mass 23 or 24 (possibly C_2). The tail was also found to have a two-lobed magnetic field structure with an embedded neutral sheet. This confirmed the theoretical picture, originally proposed by Alfvén in 1957, that a comet's plasma tail is formed from interplanetary magnetic field lines that are captured by the cometary atmosphere. The outward motion of the solar wind carrying these field lines causes the field lines to be wrapped around the nucleus like spaghetti bent over a fork. This results in a magnetic lobe composed of magnetic field lines of one polarity, which extends from the coma on one side of the plasma tail and a lobe of oppositely directed field lines on the other side of the tail. Such a pattern had previously been observed at Venus, but it was unknown prior to the ICE mission whether this model was correct for comets.

The interaction between the solar wind and a comet is unlike that with any other body because the cometary atmosphere, which is formed by sublimation of the comet icy material, is not gravitationally bound. Neutral gas leaving the comet nucleus ($\sim 5 \times 10^{28}$ neutral molecules/second at the time of the encounter) expands into a large volume. For example, the visible coma extends $\sim$60,000 km in diameter; the comet nucleus is thought to be only a few km in diameter. As they become ionized by solar ultraviolet and by charge exchange with the solar wind, molecules are "picked up" by the solar wind. For example, water molecules typically each absorb about 70 keV out of the oncoming solar wind. Prior to the encounter, it was speculated that this spatially distributed process of absorbing solar wind energy might inhibit the formation of a bow shock (bow shocks have been observed near Venus, Earth, Jupiter, and Saturn). The observations show that there is a turbulent interaction region near where the possible bow shock had been predicted (see the figure), but this region appears to be

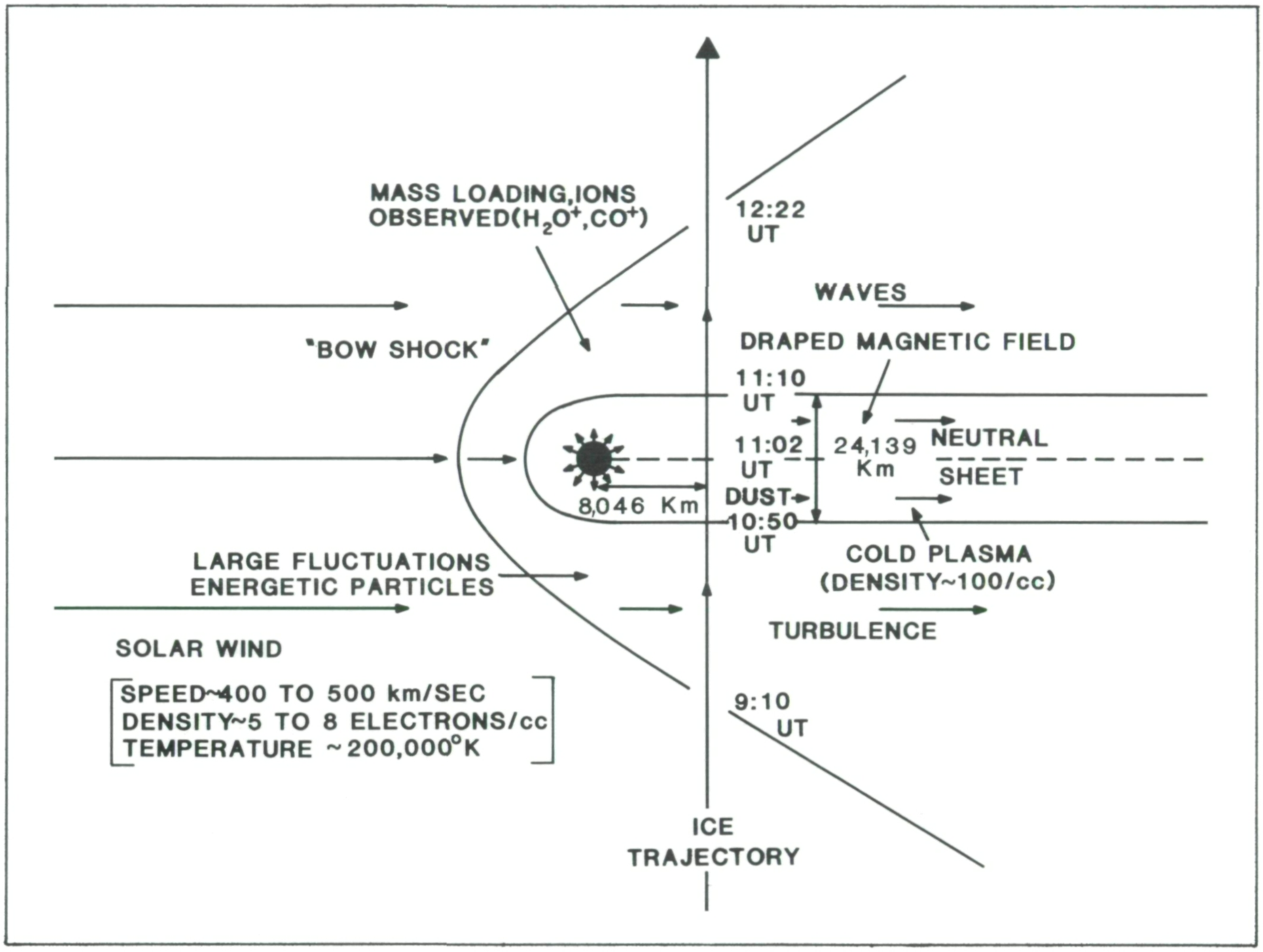

International Cometary Explorer encounter with Comet Giacobini-Zinner.

quite different from known bow shocks. Electron density changes by factors of 2-7 were observed to occur frequently on a time scale of minutes. "Pick-up" ions were seen at great distances from the center of the tail (apparently more than 2 million km). Electron plasma oscillations and ion acoustic waves were also detected far from the comet. Nearer to the "bow shock" bidirectional electron distributions, like those seen near the Earth's bow shock, indicated a flow of electrons away from the comet.

The ICE spacecraft was not originally intended to go to a comet, so the success of this mission depended more than usual upon cooperation and help from a great many groups. The comet and spacecraft trajectories had to be precisely determined and corrections to the spacecraft trajectory had to be computed. Commands were then sent from the ground to the spacecraft to activate the onboard hydrazine propulsion system. The resulting targeting error was approximately 600 km at a distance of 70 million km. This encounter distance was 50 times further from Earth than the spacecraft was designed to go. The Deep Space Network, augmented by ground stations at Arecibo, Puerto Rico, and Usuda, Japan, met the challenge of recovering a very weak telemetry signal from this great distance. Once received, the data were processed and distributed to the various experimenter groups, which then promptly analyzed their data for presentation to news reporters 2 days after the encounter.

Contacts: Tycho von Rosenvinge, John C. Brandt, and Robert Farquhar
Codes 660, 680, 550

Sponsor: Office of Space Science and Applications, Code E

HUBBLE SPACE TELESCOPE

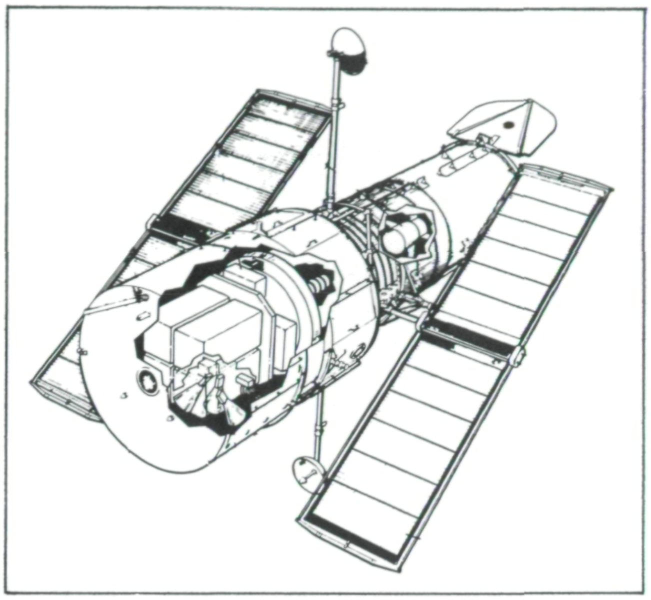

Hubble Space Telescope.

The objective of the Hubble Space Telescope (HST) Program is to establish and operate an astronomical facility consisting of an orbiting observatory and a ground system, which will greatly exceed the capability of even the best ground-based observatory, and to make the facility available for research in optical astronomy.

The Goddard Space Flight Center (GSFC) is responsible for the science and operations aspects of the HST. Specifically, the HST Project at the GSFC is responsible for managing the following:

- Design and development of the five Scientific Instruments (SI's) for use on the first launch of the HST;
- Design and development of the SI Control and Data Handling (SI C&DH) system;
- Verification and Acceptance Program (VAP) to integrate and test the SI's and the SI C&DH;
- System engineering of the total ground systems;
- Design and development of the Science Operations Ground System (SOGS);
- Establishment and operation of the Space Telescope (ST) Science Institute (ST ScI), located on the Johns Hopkins University campus in Baltimore, Maryland, which will conduct the science operations; and
- Operation of the total observatory.

In addition, the GSFC Mission and Data Operations Directorate is responsible for the design, development, and maintenance of the Data Capture Facility, the Payload Operations Control Center, and other institutional support.

The European Space Agency is providing the HST solaı array, one scientific instrument, and participation in science operations.

During FY85, the remaining SI's were delivered to Lockheed Missiles and Space Company (LMSC). After individual receiving and inspection testing, all instruments were electrically integrated into the Optical Telescope Assembly and then tested with the SI C&DH. In late FY85, an observatory level functional test was performed on the HST.

The ST Operations Control Center (STOCC) is the facility used for controlling the HST when it is placed into Earth orbit in 1986. The STOCC is located at GSFC and is operated by the LMSC.

The ST ScI has been created to administer the HST science research program for NASA and to plan and conduct the actual HST science observations. The ST ScI is operated by the Association of Universities for Research in Astronomy under contract to NASA.

The SOGS, a complex network of computers and image processing terminals, is being developed by TRW under contract to NASA. This system will schedule observations to be made by the HST and will process the resulting data and provide products which are useful to astronomers. The SOGS hardware has been deployed to site with two VAX computer systems residing at the GSFC and four VAX computer systems residing at the ST ScI. A significant portion of the SOGS software has also been delivered to site, and system integration and testing is now being performed. The remainder of the SOGS software will be completed and installed at site in FY86. SOGS will continue undergoing extensive operational testing in preparation for launch of the HST.

Contact: Frank A. Carr
Code 400

Sponsor: Office of Space Science and Applications,
Code E

ORIGINAL PAGE IS
OF POOR QUALITY

COSMIC BACKGROUND EXPLORER

The Cosmic Background Explorer (COBE) has been specifically designed for studying the Big Bang, the primeval explosion that started the expansion of the Universe, and for measuring the diffuse infrared and microwave background radiation, which includes the primary remnant of the explosion. In addition, COBE instruments will determine the spectrum of the radiation and the variances between different points of the sky with far better sensitivities than can be achieved with other techniques.

The COBE Observatory will carry three instruments: the Differential Microwave Radiometer (DMR), the Far Infrared Absolute Spectrophotometer (FIRAS), and the Diffuse Infrared Background Experiment (DIRBE). Using standard microwave receivers, the DMR will measure the anisotropy of the cosmic background radiation at wavelengths of 3.3, 5.7, and 9.5 mm, with an angular resolution of 7°. The FIRAS will measure the spectrum (the intensity as a function of wavelength) over a wavelength range of 100 microns to 1 cm, with a 5 percent spectral resolution and a 7° angular resolution; it is a cryogenically cooled polarizing Michelson interferometer. The DIRBE will measure the brightness of the sky at wavelengths from 1 to 300 microns with a 1° angular resolution in 10 bands; it is a cryogenically cooled, off-axis, Gregorian telescope.

The three COBE instruments will be pointed away from the Earth to survey the cosmos—FIRAS along the spin axis, and DMR and DIRBE 30° off the spin axis. These instruments are located inside a large radio frequency (RF)/thermal shield to protect against thermal and electromagnetic radiation from the Sun, the Earth, and

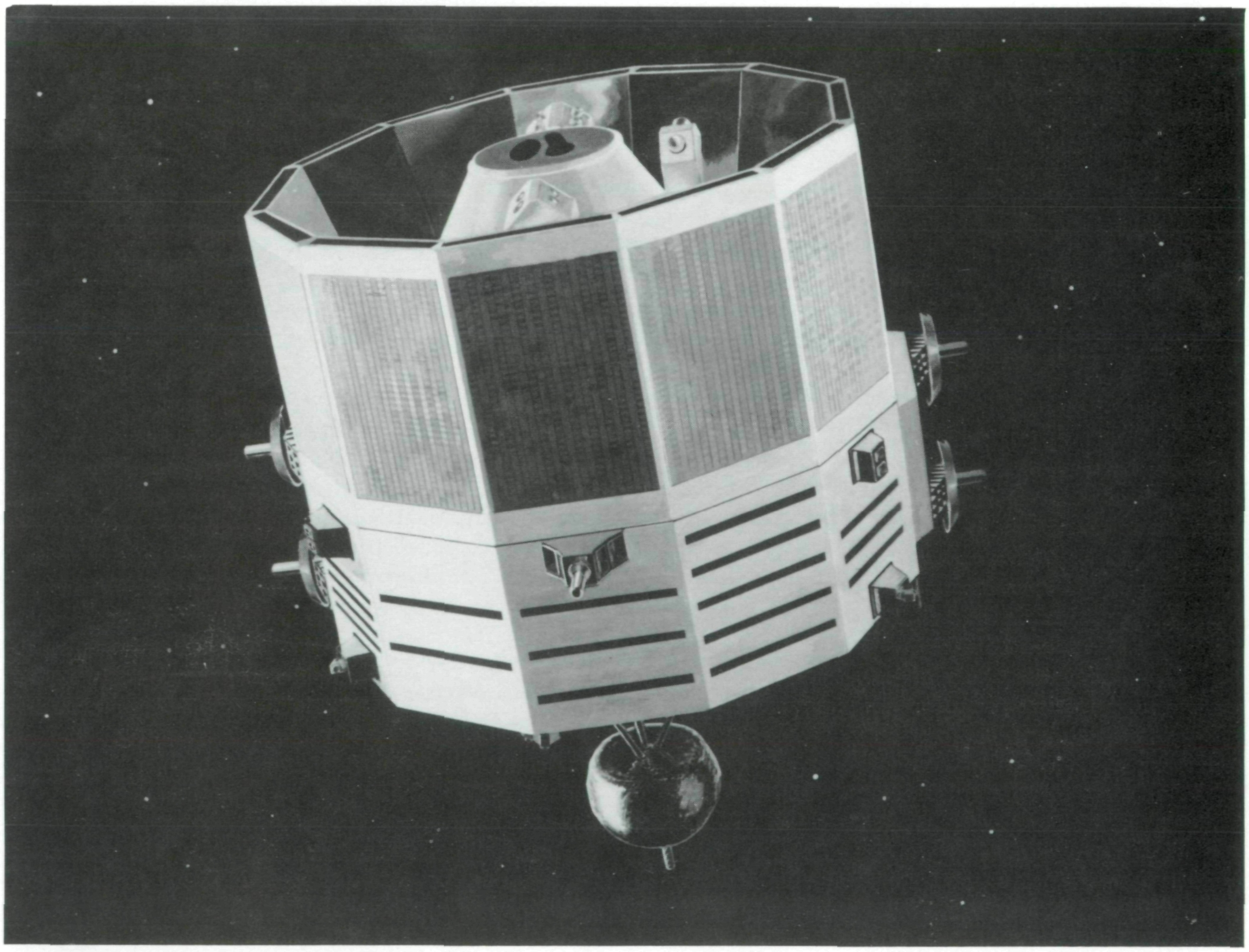

Cosmic Background Explorer (artist's concept).

the Observatory telemetry transmitter. Within the RF/thermal shield is a liquid helium dewar, similar to that flown on board the Infrared Astronomical Satellite. To satisfy the requirements of two of the COBE experiments, the Observatory will rotate at approximately 1 rpm.

Science and ancillary data will be continuously stored on board one of the two Observatory tape recorders, which will be played back once per day to the ground system. The Tracking and Data Relay Satellite System will be used to provide telemetry and commands for Observatory safety and health monitoring.

The COBE is being designed, integrated, and tested by engineers and scientists at Goddard Space Flight Center. Certain major subsystems, however, will be procured from selected contractors. The COBE Observatory, which will weigh approximately 4,536 kg, will be launched in 1988 from the Western Missile and Space Center by the Shuttle into a parking orbit of approximately 300 km, 99° inclination. An onboard propulsion system will place the Observatory into a 900-km altitude, Sun-synchronous orbit. The planned lifetime for COBE is 1 year.

The flight structure completed fabrication and assembly and is currently being prepared for test activity in the test and evaluation facility at the GSFC. The flight dewar has been assembled and successfully completed testing at Ball Aerospace Systems Division (BASD), and it is scheduled to be delivered to the GSFC in November 1985. Both the FIRAS and DIRBE test units have been assembled. The DIRBE test unit is currently in the liquid helium test dewar at the GSFC in preparation for functional testing at liquid helium temperature. The DMR 31-GHz flight radiometer is in final stages of assembly and will be entering the test phase shortly. The COBE science data room completed a systems concept review in the early part of the year and will be going through a preliminary design review early next year.

Contact: Roger Mattson
Code 400

Sponsor: Office of Space Science and Applications,
Code E

UPPER ATMOSPHERE RESEARCH SATELLITE MISSION

The objectives of the Upper Atmosphere Research Satellite (UARS) Mission are to understand the mechanisms that control upper atmosphere structure and variability, assess man's impact on the Earth's ozone layer, assess the potential effect of stratospheric change on weather and climate, and develop an effective strategy for stratospheric monitoring. Meeting these objectives requires coordinated measurements on a global scale of atmospheric chemistry, winds, and energy input. These data will be acquired by a single observatory containing 10 scientific instruments and orbiting the Earth at an altitude of 600 km and an inclination of 57°. The UARS observatory will be a 3-axis stabilized, Earth-oriented satellite and will use the Multimission Modular Spacecraft (MMS) for attitude control, communications, and power storage. Since analysis of coordinated measurements is essential to the mission, a Central Data Handling Facility (CDHF) will be implemented at the GSFC for data processing and storage. Computer-based remote terminals will be located at each of the Principal Investigator's facilities for communication with the CDHF and for performing data analysis.

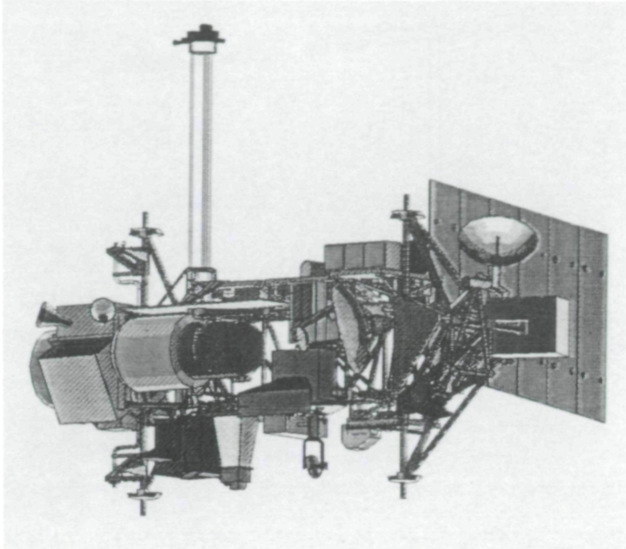

Upper Atmosphere Research Satellite system assembly.

Execution phase contracts and institutional agreements for development of the flight instruments have been under way for approximately 2 years. Preliminary instrument designs have been completed, and final (critical) design reviews will be conducted during FY86. The observatory development contract was awarded to General Electric in March 1985, and the observatory system concept review was completed in September 1985. Contracts for development of the CDHF hardware and software are scheduled for award early in FY86.

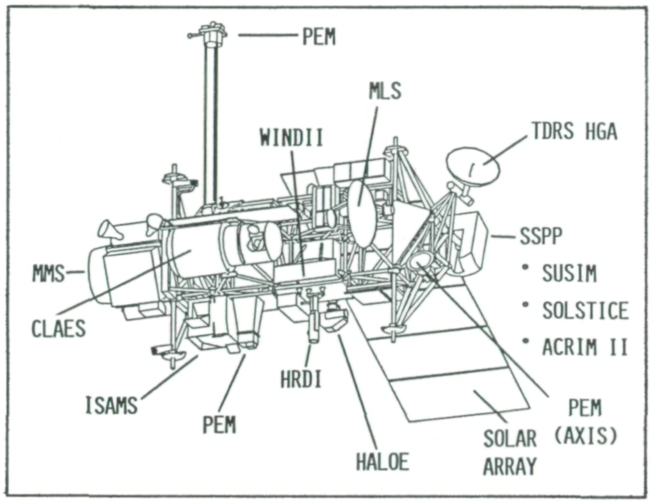

Upper Atmosphere Research Satellite instrument configuration.

Current project planning is based on launch of the observatory in the fall of 1989, 18 months of flight operations, and 12 additional months of data processing and analysis.

Contact: Peter T. Burr
Code 430

Sponsor: Office of Space Science and Applications,
Code E

GODDARD'S HITCHHIKER (SHUTTLE PAYLOAD OF OPPORTUNITY CARRIER)

Hitchhiker-Goddard (HH-G) is a newly developed modular system capable of physically and operationally supporting up to six different customer payloads on a given Shuttle flight. HH-G is a long-awaited addition to the growing family of attached payload carrier systems. Its closest cousins include the highly successful Get Away Special (GAS) and Spartan programs, which are also conducted by Goddard Space Flight Center (GSFC). Other family members include the Spacelab and Hitchhiker-M programs, which are managed by Marshall Space Flight Center. The Hitchhiker programs fill a gap in the attached carrier stable by combining some of the simplicity and rapid turnaround capability of the GAS program with some of the additional services such as real-time command and telemetry afforded by Spacelab. The goals of the Hitchhiker programs are to provide reduced flight lead time, provide increased reflight opportunities, reduce integration costs, and maximize Shuttle load factor.

As the name Hitchhiker implies, the plan is to permit the relatively late selection and manifesting of customer payloads. It is expected that payloads may be identified as late as 8 months before flight and that the final payload complement may be selected as late as 6 months prior to flight. This short selection-to-flight time is possible only by providing standardized payload-to-carrier interfaces and limiting payload activities, which impact the preplanned flight design, such as crew activity and pointing maneuvers. Large resource margins must also be maintained and, as always, primary payloads have priority over secondary payloads when competing for flight resources. HH-G is to be manifested twice per year thus allowing representative mass, volume, and energy requirements to be factored into the mission flight design prior to the selection of the actual payload complement. Additional HH-G flights are possible on an opportunity basis.

The HH-G system is based on the Shuttle Payload of Opportunity Carrier (SPOC) developed by the Applied Engineering Division at GSFC. SPOC is a modular system that can be combined in a variety of physical configurations. This flexibility allows the carrier to be adapted to a particular payload complement or, if required, the carrier may be configured to suit Shuttle manifest limitations. The primary components of the SPOC system are the SPOC payload mounting plates and the SPOC avionics package. Two additional essential elements of the SPOC system are standard 5 cubic foot sealed and opening-lid GAS canisters. These GAS canisters are modified electrically to be compatible with the SPOC system. GAS adapter beams are utilized to present a standardized interface to the Shuttle for the SPOC plates, as well as the GAS canisters. Even the mounting location in the Orbiter has been standardized. HH-G payloads will be accommodated on the starboard sidewall in the forward portion of the cargo bay. A typical Hitchhiker configuration might consist of a SPOC plate and two GAS canisters or two SPOC plates. The SPOC avionics package may be mounted on a SPOC plate or in the space normally occupied by a single GAS canister. A minimum configuration might consist of the SPOC avionics package and a single GAS canister mounted together on the same GAS adapter beam.

The first Hitchhiker (HG-1) is manifested aboard STS 61-C, which is scheduled for launch December 1985. HG-1 (photo G85-03975) will support three diverse payloads which represent three of the types of payloads that HH-G will carry. The Particle Analysis Cameras for Shuttle (PACS) is sponsored by the USAF Geophysics Laboratory. PACS is mounted to a SPOC plate with the

ORIGINAL PAGE IS
OF POOR QUALITY

SPOC avionics package and will provide film images of the environment around the Shuttle in support of future Department of Defense missions. Shuttle Environment Effects on Coated Mirrors (SEECM) is provided by the Perkin-Elmer Corporation. SEECM is mounted on the upper edge of the SPOC plate near PACS and will investigate molecular contamination, atomic oxygen erosion effects, and atomic oxygen cleaning effects. The third customer payload, Capillary Pumped Loop (CPL), is contained in a standard GAS canister located in the cargo bay adjacent to the SPOC plate. CPL is a NASA Space Station Advanced Development Program experiment, which will investigate the priming of an experimental heat transport system. CPL is developed by the Applied Engineering Division at GSFC.

HH-G promises to be highly successful if interest by the payload community is a valid indicator. Several potential customers have filed a Request for Flight Assignment (STS Form 100) requesting the HH-G carrier. Numerous other customers have shown varying degrees of interest generally reflective of their funding status. A variety of

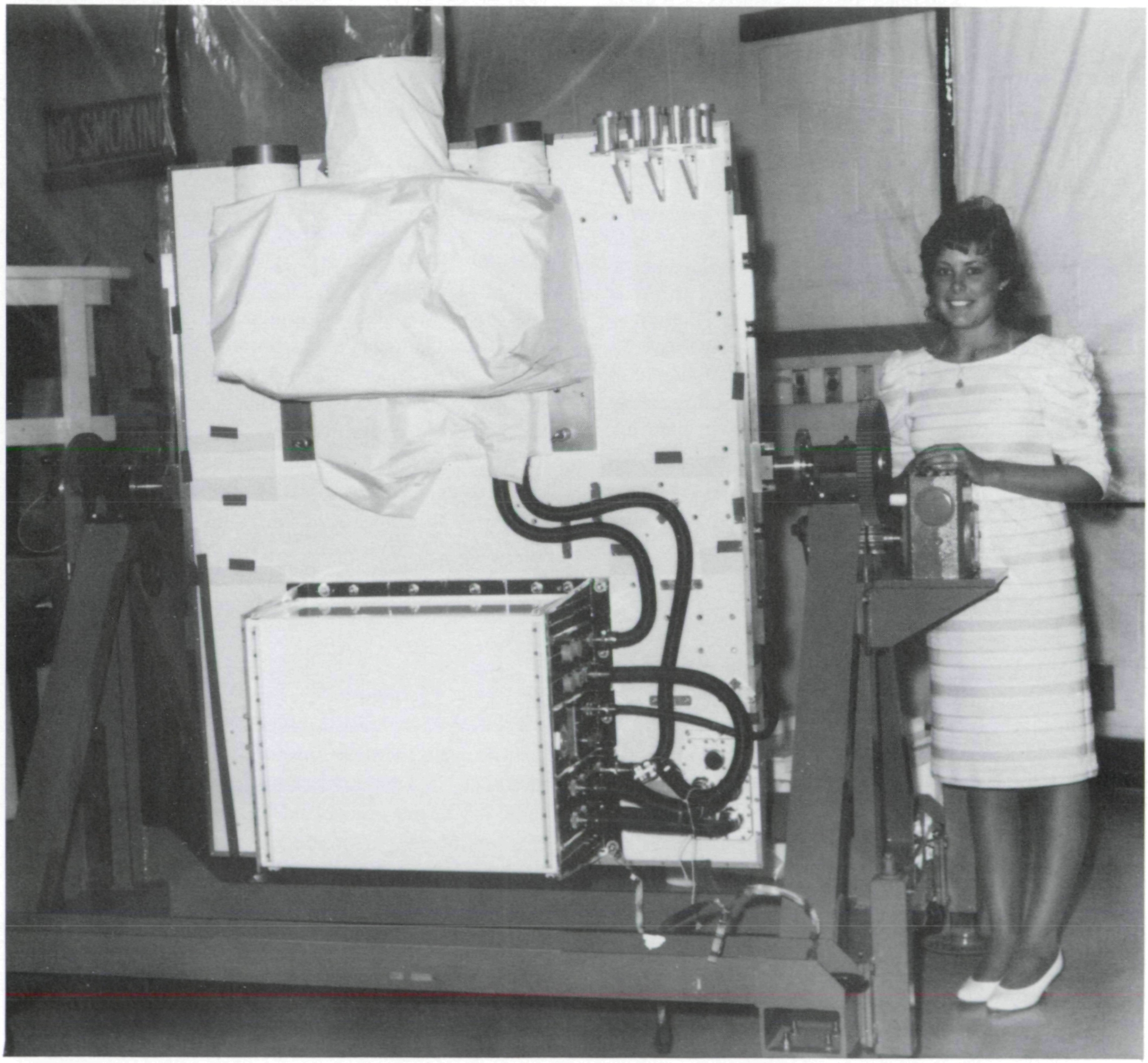

Hitchhiker G-1 shown mounted on Shuttle Payload Opportunity Carrier (SPOC).

scientific payloads have been proposed that are sponsored by various U.S. government agencies in the internal or university development mode. Many forms of Space Station advanced technology experimentation and development will be conducted in this manner. Various advanced communication techniques may be demonstrated on HH-G. The Life Sciences Division at NASA Headquarters requested and received a presentation on HH-G capabilities.

Carriers such as the HH-G also open up opportunities for domestic and foreign commercial endeavors. This is an exciting new thrust for NASA and is directly related to administration policies regarding space commercialization. Preliminary technical meetings have been conducted with several potential commercial users. More than half of these inquiries are from foreign corporations.

The practical limitations, which are imposed by the Hitchhiker program guidelines, result in the program's obvious unsuitability for certain types of attached Shuttle payloads. For example, the Shuttle High Energy Astrophysics Laboratory (SHEAL) has pointing requirements well beyond the scope of a Hitchhiker mission. However, the SPOC carrier will be used in a non-Hitchhiker, "charter flight" mode. SHEAL missions will utilize up to four dedicated SPOC plates and a SPOC avionics package along with a large instrument pointing system to gather data on a wide range of X-ray sources.

Contact: Theodore C. Goldsmith
Code 730

Sponsor: Office of Space Flight, Code M

SOLAR OPTICAL TELESCOPE

The Solar Optical Telescope (SOT) will conduct detailed observations of the solar disc in order to determine the densities, temperatures, magnetic fields, and nonthermal velocity fields in numerous solar features on the scale at which many basic physical processes are occurring. Recent observations show that the plasma in the solar chromosphere and transition region often exhibit a scale on the order of a few tenths of an arc second. Thus, to understand the flow of energy and mass on a global scale over the surface of the Sun, it is necessary to investigate structures only slightly larger than the photon mean-free-path of about 100 km.

The SOT Observatory consists of two major parts: the Telescope Facility, scheduled to be designed and built by the Perkin-Elmer Corporation, which remains essentially unchanged from mission to mission; and the Science Instruments (SI's), which, depending on the science objectives, may vary for each mission.

Two science instruments are to be flown on the first SOT mission. They are: the Coordinated Filtergraph Spectrograph which consists of a narrow band, visible tunable filtergraph, and a visible and ultraviolet (UV) spectrograph. The cameras for both systems use large charge-coupled-device (CCD) arrays. The instrument will study hydrodynamic and magnetic processes on spatial scales rarely, if ever, resolved from the ground. The instrument will have an active image motion stabiliziation system to enable diffraction-limited performance and a dedicated experiment processor for experiment control and data flow management. Near-simultaneous visible and ultraviolet observations will follow the flows, energy, and magnetic fields continuously from the low photosphere into the corona.

The Photometric Filtergraph, consists of a pair of high-speed film cameras behind broad pass band continuum filters. The Photometric Filtergraph will be combined with the Coordinated Filtergraph Spectrograph into one focal plane package for the SOT, and the integrated instrument will be built by Lockheed Palo Alto Research Laboratory. The instrument will record high-resolution images of the solar atmosphere on photographic film. Filtergraphs will be recorded in the visible and as far down into the UV as practicable. The recorded data will be used to study granulation, surface flows, sunspots, and solar flares.

The SOT Observatory remains Shuttle-attached throughout the mission. It utilizes the Spacelab-provided Instrument Pointing System during inorbit operations, and is mounted via a payload clamp assembly in the Orbiter cargo bay during launch and landing. Mission Operations are conducted by interactive control either from the Payload Specialist station in the Orbiter Aft Flight Deck or from ground-based stations in the Payload Operations Control Center.

Contact: George D. Hogan
Code 420

Sponsor: Office of Space Science and Applications,
Code E

ORIGINAL PAGE IS
OF POOR QUALITY

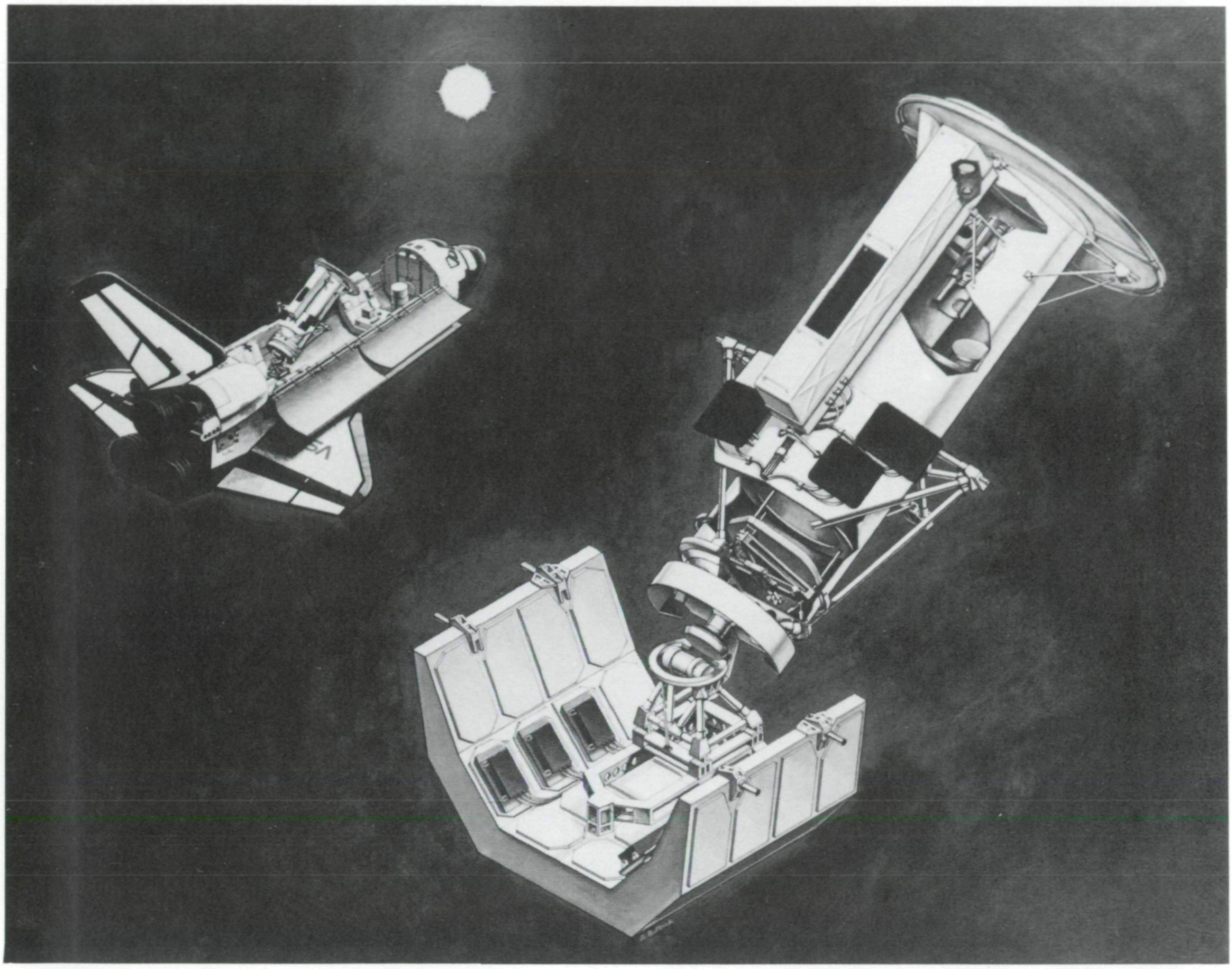

NASA/Perkin-Elmer Solar Optical Telescope Observatory (artist's conception).

ACCOMMODATION OF THE SOLAR OPTICAL TELESCOPE ON THE SPACE STATION

The Solar Optical Telescope (SOT-1), currently under development as a Spacelab instrument, is also a candidate for the Space Station. The primary goal of both missions is to study physical processes that occur on the Sun using unprecedented angular resolution and stability, corresponding to an atmospheric density scale of 70 km or 0.1 arc-sec. These studies require continuous interval measurements for short, intermediate, and long-term periods of time; thus, the Spacelab and Space Station flights will provide scientists with complementary sets of data.

The SOT missions are designed to help resolve a number of fundamental problems in solar physics including: the small-scale structure of the Sun's magnetic field and its origin, growth, and decay; the nature of the solar dynamo that generates the magnetic field; the heating of the outer solar atmosphere; the velocity fields in the subcoronal solar atmosphere and their influences on the solar winds. In contrast to the SOT Spacelab missions, the Space Station accommodation of the SOT will enable the design of experiments to study the fine-scale, local manifestations of solar phenomena which evolve and endure for periods of weeks or even months.

The SOT will be accommodated on either the upper boom of the Space Station or the transverse boom which also contains the solar arrays. An instrument pointing system, mounted between the SOT and the boom-mounting plate

will provide the required pointing during sunlit portions of the orbit. The instrument will be controlled remotely from the ground or, in the event that the system is not in communication with ground control, automatically or manually from the Space Station. All instrument data will be transmitted to ground (GSFC) for processing and subsequent distribution to participating investigators.

The Space Station will orbit the Earth at a nominal altitude of 500 km circular at an inclination of 28.5 degrees. The design range of 463 to 555 km altitude allows for orbit decay and system reboost via onboard propellants approximately every 3 months. The low orbital inclination allows about 1 hour of sunlight per orbit, thereby permitting more than 900 hours of operation of the SOT over a 6-month period of time.

The SOT will be delivered to the Space Station via the Orbiter and transferred at the lower keel extension by means of a Mobile Remote Manipulator System (MRMS), which also is used to transport the SOT to upper or transverse boom via the Space Station keel. Electrical, mechanical, and other interface connections are made automatically or with mission specialist assistance.

The SOT observatory flight weight is approximately 4000 kg, with an additional 1400 kg needed for the instrument pointing system, and an estimated 1200 kg requirement for the cradle mounting assembly. Less than 4000 W of power are required continuously and about 6000 W peak power anticipated. The observatory envelope size is 4.4 m by 7.5 m diameter. The observatory consists of the following components: a coordinated filtergraph/

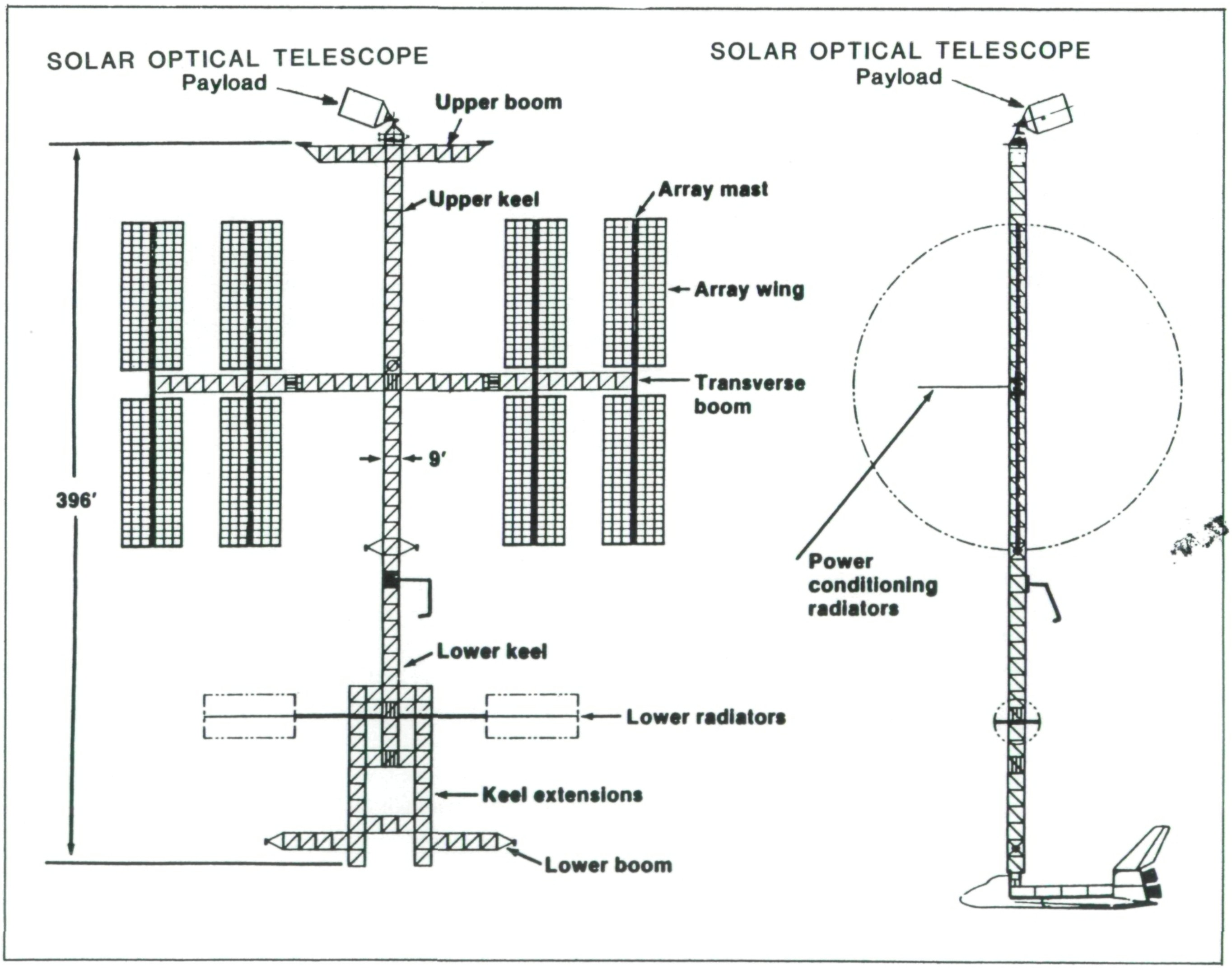

Solar Optical Telescope attached payload on Space Station upper boom configuration.

spectrograph, and a photometric filtergraph instrument, both contained in a Coordinated Instrument Package (CIP); and the basic SOT facility with a Gregorian optical system consisting of a series of four mirrors all suitably mounted on the cylindrical telescope structure.

A concept study conducted by the Advanced Missions Analysis Office in conjunction with other Goddard elements indicates that the SOT can be feasibly accommodated on the Space Station to provide valuable solar data.

Contact: Dr. Enrico P. Mercanti
Code 400

Sponsor: Office of Space Science and Applications,
Code E

Index

Index (Continued)

NASA

National Aeronautics and
Space Administration

Goddard Space Flight Center
Greenbelt, Maryland 20771

Office of the Director